

Dissertation zur Erlangung des akademischen Grades  
Doctor rerum naturalium (Dr. rer. nat.)

**Field theory of interacting polaritons under  
drive and dissipation**

vorgelegt von

**Christian Høj Johansen**

geboren am 24. Januar 1992 in Odder

Fakultät Physik

Technische Universität Dresden

und

Max-Planck-Institut für Physik komplexer Systeme

wissenschaftlicher Betreuer:

Dr. Francesco Piazza

---

Erstgutachter:	Prof. Dr. Jan Michael Rost
Zweitgutachter:	Prof. Dr. Walter Strunz
Drittgutachter:	Prof. Dr. Oded Zilberberg
Abgabedatum:	October 10, 2022
Datum der Disputation:	January 19, 2023

---

# Abstract

This thesis explores systems that exhibit strong coupling between an optical cavity field and a many-particle system. To treat the drive and dissipative nature of the cavity on the same footing as the dynamics of the many-particle system, we use a non-equilibrium field theoretic approach.

The first system considered is an ultracold bosonic gas trapped inside a cavity. The dispersive coupling between the cavity field and the atoms' motion leads to the formation of a polariton. We show how a modulation of the pump laser on the energy scale of the transverse cavity mode splitting can be used to create effective interactions between different cavity modes. This effective interaction results in the polariton acquiring a multimode nature, exemplified by avoided crossings in the cavity spectrum. As the laser power is increased, the polariton softens and at a critical power becomes unstable. This instability signals the transition into a superradiant state.

If the multimode polariton contains a cavity mode with an effective negative detuning, then the transition does not happen through a mode softening but at a finite frequency. To investigate this, classical non-linear equations are constructed from the action and from these we derive the critical couplings and frequencies. It is shown how the superradiant transition happening at a finite frequency is a consequence of a competition between the negatively and the positively detuned cavity modes making up the polariton. The finite-frequency transition is found to be equivalent to a Hopf bifurcation and leads to the emergence of limit cycles. Our analysis shows that the system can exhibit both bistabilities and evolution constricted to a two-torus. We end the investigation by showing how interactions among the atoms combined with the emerging limit cycle open new phonon scattering channels.

The second system considered in the thesis is inspired by the recent experiments on gated Transition-metal dichalcogenides (TMD) monolayers inside cavities. An exciton within the TMD can couple strongly to the cavity and, due to the electronic gating, also interact strongly with the conduction electrons. To treat the strong interactions of the excitons with both cavity and electrons, we solve the coupled equations for the correlation functions non-perturbatively within a ladder approximation. The strong interactions give rise to new quasiparticles known as polaron-polaritons. By driving the system through the cavity, we show how the competition between electron-induced momentum relaxation and cavity loss leads to the accumulation of polaritons at a small but finite momentum, which is accompanied by significant decrease of the polariton linewidth. Due to the hybrid nature of the polaron-polariton, we show that this behavior can be qualitatively modified by changing the cavity detuning.

---

# List of publications

Chapter 3 in this thesis is based on the author's own publication:

C.H.J, J. Lang, A. Morales, A. Baumgärtner, T. Donner, and F. Piazza. Multimode-polariton superradiance via Floquet engineering, *SciPost Physics*, 12(094), 2022

Besides the published paper there are two papers that are in preparation. The first is based on chapter 4:

C.H.J, J. Lang, and F. Piazza. Multimode-polariton limit cycles.

The second is based on chapter 5:

C.H.J, T. Wasak, J. Lang, and F. Piazza. Driven-dissipative steady states of polaron-polaritons.

---



# Contents

<b>1</b>	<b>Introduction</b>	<b>1</b>
<b>2</b>	<b>Non-equilibrium field theory</b>	<b>5</b>
2.1	Quantum mechanics . . . . .	6
2.2	The time contour . . . . .	8
2.2.1	Evolution along the contour . . . . .	9
2.3	The free action and propagators . . . . .	12
2.4	Beyond the free theory . . . . .	17
2.4.1	Classical equations of motion . . . . .	17
2.4.2	Self-energies and Feynman diagrams . . . . .	19
2.5	Spectral properties . . . . .	24
2.5.1	Quasiparticle picture . . . . .	26
2.6	Occupation of the spectrum . . . . .	28
2.7	Combinatorics for non-equilibrium diagrams . . . . .	33
2.8	Open quantum systems . . . . .	35
2.8.1	Linearly coupled environment . . . . .	37
2.9	Summary . . . . .	41
<b>3</b>	<b>Multimode polaritons</b>	<b>43</b>
3.1	Introduction . . . . .	43
3.2	Model and Hamiltonian . . . . .	44
3.3	Non-equilibrium action . . . . .	51
3.4	Self-energies . . . . .	55
3.4.1	Stark shift . . . . .	56
3.4.2	Cavity self-energy . . . . .	57
3.4.3	Sideband picture . . . . .	64
3.5	Multimode polaritons . . . . .	66
3.5.1	Single mode polariton . . . . .	66
3.5.2	Including phase modulation . . . . .	68

3.6	Multimode superradiance . . . . .	72
3.7	Summary and discussion . . . . .	75
<b>4</b>	<b>Polariton limit cycles</b>	<b>76</b>
4.1	Introduction . . . . .	76
4.2	Minimal model . . . . .	78
4.3	Classical equations of motion . . . . .	81
4.4	Linear stability of the normal phase . . . . .	83
4.4.1	Normal-phase fixed point . . . . .	84
4.4.2	One-mode cavity . . . . .	88
4.4.3	Two-mode cavity . . . . .	92
4.4.4	Four-mode cavity . . . . .	96
4.4.5	Phase diagram . . . . .	98
4.5	Beyond the normal phase . . . . .	103
4.5.1	Conserving system of real equations for the center manifold . . . . .	104
4.5.2	Double Hopf bifurcation and Stuart-Landau equations . . . . .	106
4.5.3	Stuart-Landau equations the for multimode polaritons . . . . .	113
4.5.4	Double Hopf normal form . . . . .	114
4.5.5	Symmetry breaking of the steady states . . . . .	119
4.6	Atom collisions . . . . .	120
4.6.1	Linear stability with a weakly interacting BEC . . . . .	120
4.6.2	Beyond linear stability . . . . .	124
4.7	Summary and discussion . . . . .	128
<b>5</b>	<b>Polaron-polaritons</b>	<b>130</b>
5.1	Introduction . . . . .	130
5.2	Model . . . . .	132
5.2.1	Non-interacting constituents . . . . .	132
5.2.2	Interactions . . . . .	135
5.3	Dyson equations . . . . .	141
5.3.1	Trion . . . . .	143
5.3.2	Excitons and the dilute limit . . . . .	147
5.4	Self-consistent convolution method . . . . .	149
5.4.1	Spline interpolation and the temporal Fourier transform . . . . .	152
5.4.2	Hankel transform . . . . .	155
5.4.3	Structure of a self-energy computation . . . . .	159
5.4.4	Subtraction schemes . . . . .	161
5.5	Results . . . . .	165

5.5.1	Polarons . . . . .	166
5.5.2	Undriven polaron-polaritons . . . . .	172
5.5.3	Driving of polaron-polaritons . . . . .	176
5.6	Summary and discussion . . . . .	183
<b>6</b>	<b>Conclusion</b>	<b>184</b>
<b>A</b>	<b>Action for a free theory</b>	<b>187</b>
A.1	Propagators for the free system . . . . .	189
A.1.1	Keldysh rotation . . . . .	193
<b>B</b>	<b>Kramers-Kronig relation for the retarded propagator</b>	<b>198</b>
B.1	Derivative relation . . . . .	199
B.2	Relation to Fourier transform . . . . .	201
<b>C</b>	<b>Lehmann representation of contour propagators</b>	<b>202</b>
<b>D</b>	<b>Contour configurations of diagrams: An algorithm</b>	<b>204</b>
<b>E</b>	<b>Stuart-Landau components</b>	<b>211</b>
<b>F</b>	<b>Spline interpolation</b>	<b>215</b>
F.1	Cubic spline . . . . .	215
F.2	Quintic spline . . . . .	217
<b>G</b>	<b>Hankel transform</b>	<b>220</b>
G.1	Hermite Interpolation of the Bessel function . . . . .	220
G.2	Oscillating integrals . . . . .	223
	<b>Bibliography</b>	<b>225</b>



# Chapter 1

## Introduction

Understanding the interaction between light and matter has led to a long list of technological advances. A few recent examples are LEDs which are high-efficiency light sources, optical fibers, which allow high-speed information transfer, and solar cells, which makes it possible to convert the light from the sun into electricity. One promising path to improve our technology further is to exploit strong light-matter coupling on a quantum level, which is the regime explored in this thesis.

The foundation for light-matter interaction on a quantum level is quantum electrodynamics (QED) [1–7]. QED is a relativistic quantum theory, and its theoretical development was a breakthrough that led to Tomonaga, Schwinger, and Feynman receiving the Nobel prize in 1965. In QED, the electron is a freely moving particle that moves at such speed that a relativistic description is necessary. In this thesis we consider systems at low energy where the electron is not moving freely but confined inside matter, either by being bound to an atom or embedded in a solid material. Due to the confinement and the low energy, the electron moves much slower than the speed of light, and a relativistic theory is no longer necessary.

Part of the success of QED is that the interaction strength between light and matter is small, which allows for a perturbative treatment. To generate the strong light-matter coupling we seek, one approach is to increase the intensity of the light field. Lasers are the best example of tuneable and intense light which creates a strong field at a well-defined frequency and position. The laser makes it possible to probe the low energy excitations around the ground state [8]. With slightly higher intensities and shorter laser pulses it is possible to go beyond probing and use the laser to switch between different meta-stable states of the quantum material and trigger non-equilibrium phase transitions [9, 10]. The high level of control over the laser even makes it possible to change properties of the phases. One example is that by tuning the laser to excite specific phonon modes in Fullerenes a similar response as superconductivity was found but at five times the critical

temperature [11].

The high intensity of the laser makes quantum fluctuations negligible, so that the field is essentially a classical electromagnetic field. Another approach to strong coupling between light and matter is to confine the light within a small volume using an optical cavity. The effect of confining the light is that the field is quantized, and more importantly, a strong coupling between a single light quantum, a photon, and the quantum material can be achieved [12–15]. The coupling arises as a photon is absorbed by a mode in the material that possesses a dipole momentum, transferring the material to an excited state. Strong coupling between a cavity photon and quantum emitters is the foundation for cavity QED, for which Haroche was awarded the Nobel prize in 2012 [16]. The regime of strong coupling between a photon and a single emitter was first studied in the highly celebrated Jaynes-Cummings model [17], and its predictions have been experimentally verified [18–21]. Experimentally this strong coupling regime has been made more accessible as a result of the advances in engineering high-quality cavities [22, 23].

In the strong coupling regime the energy is coherently transferred between the material and the the cavity field. The coherent exchange of energy means that the system's quantum state is partly photonic and partly matter. This quantum superposition of light and matter is known as a polariton. While the concept was first considered as a superposition between a photon and an atomic excitation the polariton concept has a much broader scope as it applies to any system where photons are strongly coupled to a matter excitation. The diversity within the polariton concept is exemplified by more than 70 different polaritons having been proposed so far [24]. The matter part of the polaritons range from a single electronic transition like in the Jaynes-Cummings model to collective modes of solid state materials [25, 26].

Polaritons are interesting because of the fundamentally different nature of photons and matter. Photons are fast and only interact weakly with each other, making them ideal information carriers. They are promising candidates for realizing intriguing new technologies such as quantum computers [27, 28], or a quantum internet [29]. However, these technologies hinge on manipulating the photon state and implementing photon-photon interactions in order to perform quantum information processing. In particular these interactions need to strong on the single-photon level.

In turn, effective photon-photon interactions can only be mediated by matter, and thus rely on the formation of polaritons [30]. This is the basis not only for light-based quantum information processing but also for the whole field of quantum nonlinear optics. Progress in this direction has been made also in solid state systems, where both strong effective interactions [31] and highly controllable photon state preparation [32] have been experimentally demonstrated.

---

Polaritons have a wide range of technological applications, but due to their variety, they also require a broad spectrum of different theoretical techniques to be described. The polaritons which will be considered in this thesis are formed within quantum correlated matter. Besides accounting for the correlations within the matter it is also necessary to account for the fact that light confinement is never perfect, which means that photons can be lost. To overcome the cavity loss, the system has to be driven externally and is no longer in thermal equilibrium. Strong correlations within the many-body system is native to condensed matter physics whereas the driven-dissipative nature of the cavity is well described known in quantum optics. A framework that allows us to merge these two fields is non-equilibrium field theory. This framework makes it possible to treat the driven-dissipative nature of the polariton together with the interactions within the matter. In chapter 2 we lay the theoretical foundation for the thesis by explaining the construction of the non-equilibrium field theory and how one can use it to derive different approximations.

Using the framework of non-equilibrium field theory, we explore two different driven and dissipative polariton systems with the common feature that both matter components have a macroscopic number of particles. In chapter 3 we investigate an ultracold gas inside a cavity driven by a time-periodic laser. The matter component of the polariton is the motion of the atoms, and we show how the atom cloud, driven by a modulated laser, gives rise to effective interactions between the cavity modes resulting in a polariton composed of multiple cavity modes. The interactions between multimode polaritons give rise to an intriguing phase diagram containing symmetry-broken phases with order parameters that oscillate in time. In chapter 4 we use the insight generated in chapter 3 to construct a minimal model. With this model, we derive the classical equations that govern the broken symmetry phase and find that the multimode nature of the polariton gives rise to different types of polaritonic limit cycles. Both of these chapters mainly investigate the polariton from the perspective of quantum optics, focusing on how the matter degree of freedom mediates effective interactions between the different modes of the cavity field. In chapter 5, we consider a different type of polariton where the matter component is an exciton interacting strongly with electrons within a two-dimensional semiconductor. The strong interactions between the excitons and electrons lead to quasiparticles known as polarons, and the polaritons emerging from coupling to the cavity are polaron-polaritons. The strong coupling between excitons and electrons requires a fully non-perturbative theoretical approach. We develop a new numerical method for solving self-consistent Dyson equations on the real-time contour defined in chapter 2 and show how the properties of the polaron-polariton can be understood through an intricate interplay between the driven-dissipative nature of the cavity and the many-body nature arising from exciton-

electron scattering.



# Chapter 2

## Non-equilibrium field theory

This chapter will describe the structure of non-relativistic quantum field theory for non-equilibrium systems, which we will use to describe the low-energy systems throughout this thesis.

The focus of this chapter is on how to construct a non-equilibrium field theory and what properties it has. This theory will be the basis for all calculations in this thesis and we, therefore, emphasize its relation to physical observables and how these can be computed. To facilitate this, many details will be skipped, and for those, the interested reader is referred to [33–36].

In section 2.1 we will give a very brief overview of the main elements of quantum mechanics, but for a more comprehensive description, the reader is referred to any textbook on the topic, for example [37,38]. With the quantum dynamical equations established, we seek a method that makes it possible to compute correlation functions without having to solve the full many-body problem. The first step is establishing the proper time contour in section 2.2, consisting of a forward and a backward propagating branch. The contour gives us a convenient way of time-evolving quantum-mechanical expectation values. In section 2.3, this time contour is used to construct a field theoretic formulation of these expectation values for a free theory. The free theory is non-trivial to construct because the non-equilibrium nature of the systems leads to correlations between forward and backward time propagation. With these correlations incorporated in the free theory, we discuss in section 2.4 how to include interactions in a many-particle system. Specifically we focus on two different methods to compute the expectation values from the action of the field theory. One method is to derive the classical equation and the other is through Feynman diagrams. Having discussed the equation of motion for interacting systems, sections 2.5 and 2.6 are dedicated to the physical content of the correlations functions in the quantum field theory. We will see that the non-equilibrium nature can give rise to a substantial number of different Feynman diagrams, and in section 2.7 we introduce an algorithm for

sorting and eliminating redundant diagrams. Finally, we consider a specific situation of a system coupled to an environment in section 2.8. We show how the coupling gives rise to an effective description of the system's degrees of freedom and relate it to the standard open quantum systems approaches.

## 2.1 Quantum mechanics

For a closed quantum system, the first postulate of quantum mechanics is that physical states are described by state vectors  $|\psi(t)\rangle$ , which are vectors in a Hilbert space. The evolution of a state is governed by the Schrödinger equation [38]

$$i \frac{d}{dt} |\psi(t)\rangle = H(t) |\psi(t)\rangle, \quad (2.1)$$

where we are working in units where  $\hbar = 1$ . This will be done throughout the thesis.

The Hamiltonian operator  $H(t)$  is a Hermitian operator, meaning that  $H(t) = H(t)^\dagger$ , where the dagger is the conjugation and transposition operation. Given an initial state of the system,  $|\psi(t_0)\rangle$ , one can formally solve this differential equation with the time evolution operator [37]

$$|\psi(t)\rangle = U(t, t_0) |\psi(t_0)\rangle. \quad (2.2)$$

The time evolution operator must satisfy the differential equation

$$\frac{d}{dt} U(t, t_0) = -iH(t)U(t, t_0), \quad (2.3)$$

with the initial condition  $U(t_0, t_0) = \mathbb{1}$ . As a direct consequence of the Hermitian Hamiltonian, one finds  $U$  to be unitary such that  $UU^\dagger = \mathbb{1}$ , where  $\mathbb{1}$  is the identity operator. Formally  $U$  can be written as

$$U(t, t_0) = \mathcal{T} \exp \left( -i \int_{t_0}^t H(t') dt' \right), \quad (2.4)$$

where  $\mathcal{T}$  is known as the time-ordering operator. It orders operator products such that operators at earlier times are to the right of operators at a later time [39]. Using eq. (2.4) to evolve the system directly is only possible for systems that can be exactly diagonalized. This is not generally the case for systems with many degrees of freedom, which makes it necessary to look for alternative ways of acquiring information about the interacting system. A feature of  $U$  that proves useful is that it has the semigroup property [40]

$$U(t_2, t_0) = U(t_2, t_1)U(t_1, t_0), \quad (2.5)$$

such that it is possible to split the entire time evolution into many small steps.

The system's state at time  $t$  is fully described by  $|\psi(t)\rangle$ . However, it does not directly contain information about a specific experimental measurement outcome. The second postulate of quantum mechanics states that physical observables are governed by Hermitian operators. Therefore, the state vector and the appropriate Hermitian operator  $A$  describing the observable must be known to predict a measurement outcome. The quantum states are probabilistic in nature, and repeating the same measurement process on identically prepared systems does not generally lead to identical outcomes. Instead, predictions can only be made about the average result after many measurements. A measurement result can be predicted by computing the expectation value of  $A$  and is computed by taking the inner product with the state vector

$$\langle A \rangle(t) = \langle \psi(t) | A | \psi(t) \rangle. \quad (2.6)$$

Besides the inherently probabilistic nature of quantum mechanics, a classical probabilistic effect can also arise due to incomplete knowledge of the system. Incomplete knowledge means that the system can be in different states with different probabilities. In this case, there are no quantum correlations between the two states. To describe both quantum correlations and classical probability effects simultaneously, one can define the density matrix

$$\rho = \sum_n p_n |\psi_n\rangle \langle \psi_n|, \quad (2.7)$$

where  $p_n$  is the classical probability of being in state  $|\psi_n\rangle$ . The general properties defining  $\rho$  are that it is Hermitian, positive and normalized. To satisfy these conditions, all eigenvalues of  $\rho$  must be real, greater than or equal to 0, and sum up to 1. These properties allow us to interpret the eigenvalues of the density matrix as the probabilities for the different eigenstates. Computing the expectation value of an observable is done by taking the trace

$$\langle A \rangle(t) = \sum_n p_n(t) \langle \psi_n | A | \psi_n \rangle = \text{Tr} (A\rho(t)). \quad (2.8)$$

The time evolution of the density matrix follows from the Schrödinger equation eq. (2.1) such that its evolution is governed by

$$\frac{d}{dt}\rho(t) = -iH(t)\rho(t) + i\rho(t)H(t) = -i[H(t), \rho(t)]_-, \quad (2.9)$$

where  $[\cdot, \cdot]_-$  is the commutator. This equation is known as the Von Neumann equation. Knowing the initial condition  $\rho(t_0)$  of the system, eq. (2.9) is again solved by the time

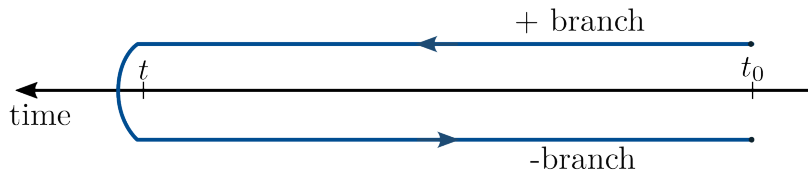


Figure 2.1: *The closed time contour used to describe the partition function. The blue line is the contour along which the initial state evolves. It can be considered as two different branches defined by the direction of propagation. The + branch propagates the system forward in time while the – branch propagates backward in time. Notice that the orientation of the time axis is chosen to align with the direction in the partition function eq. (2.11).*

evolution operator eq. (2.4)

$$\rho(t) = U(t, t_0)\rho(t_0)U^\dagger(t, t_0). \quad (2.10)$$

All information about the quantum system is encoded in the density matrix. However, even storing the full density matrix becomes intractable with growing system size. Therefore, finding a solution for the full density matrix for all times for a general, interacting many-body system is, in all but a few cases impossible, and approximations are needed to make further progress. One widely used approach considers the entire system split into two parts: an environment and a subsystem with a small number of degrees of freedom. By enforcing different approximations on the environment and its interaction with the subsystem, an equation of motion for only the subsystem can be constructed [40]. The resulting equations can then be solved using methods like exact diagonalization or tensor network methods [41–44]. These approaches are limited in the size of the subsystem Hilbert space and the range of the quantum correlations.

Instead of decreasing the effective system size, we will follow a different path. As computing the full density matrix is not tractable, we will focus on computing only specific observables, which can be done efficiently even in the thermodynamic limit. These methods are thus well suited for considering collective macroscopic phenomena.

## 2.2 The time contour

As seen from eq. (2.8), a given expectation value is computed by tracing over the density matrix and the observable. With this in mind, the natural starting point is to define a partition function through the trace of the density matrix

$$\mathcal{Z} = \text{Tr} [\rho(t)] = \text{Tr} [U^\dagger(t, t_0)U(t, t_0)\rho_0]. \quad (2.11)$$

The first property of the partition function is that it directly corresponds to the normalization of the density matrix and, therefore, must always equal one. We have seen that  $U$  is time-ordered, which in turn means that  $U^\dagger$  is anti-time-ordered. To handle this correctly, one can use the time contour sketched in fig. 2.1 and evolve the density matrix around this contour [45,46]. Starting on the upper branch at the initial time  $t_0$ , the state is evolved forward using  $U(t, t_0)$  until the final time is reached. The system is then evolved backward with  $U^\dagger$ . Because the direction of propagation is reversed, anti-time ordering is guaranteed by construction.

Consider the specific case, where at some initial time far back in the past, the system was in a simple non-interacting thermal state. Formally, this is done by letting  $\rho_0$  be a thermal state and taking  $t_0 = -\infty$ . This corresponds to adiabatically turning interactions on and off along the forward and backward contour, respectively. The contour can also be extended into the future using  $U^\dagger(\infty, t)U(\infty, t) = \mathbb{1}$ . It is worth mentioning that instead of the adiabatic onset of interactions, one can append an imaginary time evolution to the contour [47]. This can be useful if one considers dynamics, but arbitrary initial states can also be constructed without the imaginary time addition.

We will now develop a field theory that allows us to compute correlation functions based on the  $t(t_0) \rightarrow (-)\infty$  version of the contour in fig. 2.1. The correlations functions we consider will be of the two-point type meaning that they will be of the form

$$\langle A(t')B(t) \rangle = \text{Tr} (AU(t, t')BU(t, t_0)\rho_0U^\dagger(t, t_0)U^\dagger(t', t)). \quad (2.12)$$

One can derive the same equations of motion for the correlation functions by using an analytic continuation to put the correlation functions on the contour directly [48–50]. Which approach one uses to derive the equations for the correlation functions is mainly a matter of preference. The action approach is convenient for our calculations because it makes it straightforward to derive classical equations and trace out different parts of the system.

### 2.2.1 Evolution along the contour

For the field theory approach, we exploit the previously mentioned semigroup property of the evolution operator in eq. (2.5). This property can be used to slice each branch of the time contour into  $N$  small pieces. The full evolution operator is then partitioned into evolutions over each of these small intervals

$$U(t, t_0) = \prod_{n=1}^N U(n\Delta + t_0, (n-1)\Delta + t_0), \quad \Delta = (t - t_0)/N, \quad (2.13)$$

where  $\Delta$  is the length of each time slice. At this point, each evolution operator is still a complicated object which includes the time-ordering operator. However, for a large number of slices, each time interval becomes sufficiently small such that the Hamiltonian effectively does not change during the course of one interval, and consequently, both the time-ordering and the integral in eq. (2.4) become trivial. The simplified evolution operator then describes evolution over one small time step

$$U\left((n+1)\Delta + t_0, n\Delta + t_0\right) = \exp\left(-i\Delta H(n\Delta + t_0)\right), \quad (2.14)$$

under the constraint that  $\Delta$  is small enough such that

$$H(n\Delta + t) \approx H\left((n+1)\Delta + t\right), \quad \forall t. \quad (2.15)$$

Even though the evolution operator has been simplified to a product of operator exponentials, it is still necessary to diagonalize the Hamiltonian for all times to find the spectral representation of the exponential operators. Alternatively, one can use the smallness of  $\Delta$  to expand the evolution operator in eq. (2.14)

$$U(n\Delta + t_0, (n-1)\Delta + t_0) = 1 - i\Delta H(n\Delta + t_0) + \mathcal{O}(\Delta^2). \quad (2.16)$$

This expansion is often used in digital quantum simulators [51] and is known as a Trotter decomposition [52, 53]. The leading-order term is of  $\mathcal{O}(1)$  because the full evolution contains  $N$  factors of evolution operators, which exactly cancels the factor of  $1/N$  contained in  $\Delta$ . The higher-order terms scale inversely with  $N$  such that, in the limit where  $N \rightarrow \infty$ , only keeping up to first order in  $\Delta$  becomes exact.

The evolution of the density matrix has been split into small tractable steps. Because quantum mechanics is not deterministic, the system can be in different possible states at each step, and the system can evolve along all possible paths simultaneously. This idea is explicitly implemented in the contour by inserting identities between each time slice. Such an approach to quantum mechanics was pioneered by Feynman and is referred to as the Feynman path integral approach to quantum mechanics [54]. Feynman's path integral was originally described in the position and momentum basis analogously to the classical action in Lagrangian mechanics. While this works well for single particles or even bosonic systems, it is not suitable for most many-body electronic systems because they obey fermionic statistics. Instead of working with position and momentum operators, one can directly incorporate the statistics of the constituents (fermionic or bosonic) into the basis by working in second quantization [39]. In brief, the idea is to describe the system's state by the number of excitations it contains. These excitations are identified by different

degrees of freedom (momentum, spin, site, electromagnetic mode, etc.). One can define operators that create (annihilate) an excitation in a specific state, and these operators satisfy either bosonic or fermionic statistics.

One can add an infinite number of excitations into a specific bosonic mode, while fermions obey the Pauli exclusion principle and can only contain zero or one excitation. For bosons, the operators are defined through their commutation relations

$$[b_k, b_q^\dagger]_- = \delta_{k,q}, \quad [b_k^{(\dagger)}, b_q^{(\dagger)}]_- = 0, \quad (2.17)$$

where the annihilation operator ( $b_k$ ) removes an excitation from a mode defined by its quantum number  $k$ . Note that this can be a composite number corresponding to a combination of several degrees of freedom. For fermions, the exclusion principle is ensured by having the operators defined through the anti-commutator

$$[c_k, c_q^\dagger]_+ = \delta_{k,q}, \quad [c_k^{(\dagger)}, c_q^{(\dagger)}]_+ = 0, \quad (2.18)$$

which is defined as  $[A, B]_+ = AB + BA$ .

Any physical operator can be expressed through the annihilation and creation operators, the simplest example being the number operator  $a_k^\dagger a_k = n_k$ , which counts the number of excitations in the  $k$ 'th state. Even though the annihilation operator is non-Hermitian, the right eigenstate of this operator can still be defined. This state is known as the coherent state, and its defining feature is that it is unchanged by having an excitation removed from it.

For a compact representation, it is convenient to work with the unnormalized coherent states [34], which for a single bosonic mode takes the form

$$b|\phi\rangle = \phi|\phi\rangle, \quad |\phi\rangle = e^{\phi b^\dagger}|0\rangle. \quad (2.19)$$

Because of the non-Hermiticity of  $b$ , the eigenvalues  $\phi$  are not real but complex numbers. The non-Hermitian nature of the coherent state also means that the overlap between different coherent states belonging to the same mode is not orthogonal

$$\langle\theta|\phi\rangle = \sum_{m,n} \frac{\bar{\theta}^m(\phi)^n}{m!n!} \langle 0|b^m(b^\dagger)^n|0\rangle = \sum_n \frac{(\bar{\theta}\phi)^n}{n!} = e^{\bar{\theta}\phi}. \quad (2.20)$$

The coherent states thus constitute an over-complete basis. To account for this over-counting, the appropriate identity relation includes a correction factor

$$\mathbb{1} = \int d[\bar{\phi}, \phi] e^{-|\phi|^2} |\phi\rangle \langle\phi|, \quad (2.21)$$

Here the integral measure is to be understood as  $d(\operatorname{Re} \phi) d(\operatorname{Im} \phi) / \pi$  such that the integral's domain is the entire complex plane. From this identity resolution, the trace of any operator can be computed in the coherent state basis as

$$\operatorname{Tr} [\mathcal{O}] = \int d[\bar{\phi}, \phi] e^{-|\phi|^2} \langle \phi | \mathcal{O} | \phi \rangle. \quad (2.22)$$

To define the coherent states for a fermionic operator, one has to use the algebra of anti-commuting numbers to ensure the anti-commutation relations are fulfilled. These numbers are known as Grassmann numbers (or the exterior algebra) [33, 34, 55] and using them, the coherent state for a single fermionic mode is

$$|\psi\rangle = |0\rangle - \psi |1\rangle = (1 - \psi c^\dagger) = e^{-\psi c^\dagger} |0\rangle, \quad (2.23)$$

where  $\psi$  is a Grassmann number. The overlaps appear identical to the bosonic coherent states in eq. (2.20) with the complex numbers replaced by Grassmann numbers. Compared to the bosonic case, one important difference is that the numbers  $\psi$  and  $\bar{\psi}$  are unrelated. This means that the identity

$$\mathbb{1} = \int d[\bar{\psi}, \psi] e^{-\bar{\psi}\psi} |\psi\rangle \langle \psi|, \quad (2.24)$$

can not be written with an absolute value, and the measure is to be understood simply as  $d\psi d\bar{\psi}$ . Lastly, due to their anti-commuting nature, one finds that the trace acquires a change of sign

$$\operatorname{Tr} [\mathcal{O}] = \int d[\bar{\psi}, \psi] e^{-\bar{\psi}\psi} \langle \psi | \mathcal{O} | -\psi \rangle. \quad (2.25)$$

As we will be deriving the formalism simultaneously for bosons and fermions, we will denote the coherent state as  $|\phi\rangle$  for both bosons and fermions. The difference between the two will lead to sign-changes due to the anti-commutation relations. We will follow the notation that whenever two different signs are written, the upper one is for bosons, and the lower one is for fermions. Initially, we focus on the simple case of a single mode to showcase the main structure of the action. As we progress, more degrees of freedom will be added, and it will be clear that they are generally straightforward to include.

## 2.3 The free action and propagators

Having defined a contour and a suitable basis, we are now ready to construct the action for the theory. After the partition function in eq. (2.11) is placed on the contour and



coherent state identities have been inserted between the time slices, it takes the form

$$\begin{aligned} \mathcal{Z} = & \int \left( \prod_{j=1}^N d[\bar{\phi}_j^+, \phi_j^+] d[\bar{\phi}_j^-, \phi_j^-] e^{-|\phi_j^+|^2 - |\phi_j^-|^2} \right) \\ & \times \langle \phi_1^- | U_{-\Delta}(t_0) | \phi_2^- \rangle \dots \langle \phi_{N-1}^- | U_{-\Delta}(t_{N-1}) | \phi_N^- \rangle \langle \phi_N^- | \mathbb{1} | \phi_N^+ \rangle \\ & \times \langle \phi_N^+ | U_{+\Delta}(t_{N-1}) | \phi_{N-1}^+ \rangle \langle \phi_{N-1}^+ | \dots | \phi_1^+ \rangle \langle \phi_1^+ | \rho_0 | \pm \phi_1^- \rangle. \end{aligned} \quad (2.26)$$

The trace leads to the two boundary fields ( $\phi_1^-$ ) being identical, apart from a sign depending on whether the system is bosonic or fermionic, according to the trace formulas in the previous section. The sliced evolution operator from eq. (2.16) is

$$U(t_{n+1}, t_n) = 1 - i\Delta H(t_n) = U_{+\Delta}(t_n), \quad (2.27)$$

were  $t_n = n\Delta + t_0$ . The contour is closed by the identity (as a jump from one branch to the other requires no evolution along the time axes) and by the initial state. These end overlaps lead to correlations between the + and - fields and are important as they preserve the normalization of the density matrix. So even though they only account for four of the infinitely many points on the contour, it is essential to include them in the construction.

To evaluate the overlaps, one can always write  $H$  with all annihilation operators to the right of the creation operators, a form known as the normal-ordered form of  $H$ . Evaluating overlaps of normal ordered operators is particularly simple, as each annihilation/creation operator in the overlap, due to the definition of the coherent states, is just replaced by the complex/Grassmann number defining the coherent state. The form of one overlap in eq. (2.26) is then given as

$$\begin{aligned} \langle \phi_n^\pm | U_{\pm\Delta}(t_n) | \phi_{n\mp 1}^\pm \rangle &= \langle \phi_n^\pm | \phi_{n\mp 1}^\pm \rangle \left( 1 \mp i\Delta H(\bar{\phi}_n^\pm, \phi_{n\mp 1}^\pm, t_n) \right) \\ &\approx \exp \left( \bar{\phi}_n^\pm \phi_{n\mp 1}^\pm \mp i\Delta H(\bar{\phi}_n^\pm, \phi_{n\mp 1}^\pm, t_n) \right). \end{aligned} \quad (2.28)$$

With these overlaps, the partition function can be written as

$$\begin{aligned}
\mathcal{Z} &= \int \left( \prod_{j=1}^N d[\bar{\phi}_j^+, \phi_j^+] d[\bar{\phi}_j^-, \phi_j^-] \right) \\
&\times \exp \left[ i \sum_{n=2}^N \Delta \left( i \bar{\phi}_n^+ \frac{\phi_n^+ - \phi_{n-1}^+}{\Delta} - H(\bar{\phi}_n^+, \phi_{n-1}^+, t_n) \right. \right. \\
&\quad \left. \left. - i \bar{\phi}_n^- \frac{\phi_n^- - \phi_{n-1}^-}{\Delta} + H(\bar{\phi}_{n-1}^-, \phi_n^-, t_n) \right) \right] \\
&\times \exp \left( i \bar{\phi}_1^+ \phi_1^+ + i \bar{\phi}_1^- \phi_1^- - i \bar{\phi}_N^- \phi_N^+ \right) \langle \phi_1^+ | \rho_0 | \pm \phi_1^- \rangle.
\end{aligned} \tag{2.29}$$

The goal is to write  $\mathcal{Z}$  in a continuum form, i.e.

$$\mathcal{Z} = \int \mathcal{D}[\bar{\phi}^\pm, \phi^\pm] \exp(i\mathcal{S}) \tag{2.30}$$

where  $\mathcal{S}$  is called the action and is a functional of the coherent fields in the limit of  $\Delta \rightarrow 0$ . The first exponential, containing the sum over  $n$ , can directly be written in such a continuum form where

$$\begin{aligned}
\mathcal{S}_{+-} &= \int dt \left( \bar{\phi}^+(t) i \partial_t \phi^+(t) - H(\bar{\phi}^+(t), \phi^+(t), t) \right. \\
&\quad \left. - \bar{\phi}^-(t) i \partial_t \phi^-(t) - H(\bar{\phi}^-(t), \phi^-(t), t) \right).
\end{aligned} \tag{2.31}$$

Because the boundary overlaps in the last line of eq. (2.29) can not be included in this form, it can not preserve the normalization of the partition function.

To find a self-contained continuum action, we first consider the simple case of a free theory with an initial thermal state. In this case, both the Hamiltonian part and the expectation value of the initial state are quadratic in the fields. The theory can be solved exactly as all correlation functions are derivable from the two-point functions. The two-point correlation functions are often referred to as the Greens functions or the propagators of the theory. They are defined through

$$\begin{aligned}
G^{\alpha,\beta}(t, t') &= \langle \phi^\alpha(t) \bar{\phi}^\beta(t') \rangle \\
&= \int \mathcal{D}[\bar{\phi}^\pm, \phi^\pm] \phi^\alpha(t) \bar{\phi}^\beta(t') \exp(i\mathcal{S}),
\end{aligned} \tag{2.32}$$

with  $\alpha, \beta \in \{+, -\}$  and  $\mathcal{S}$  now being the action, that does contain the contour coupling which we seek to find. If a free theory is considered, then  $\mathcal{S}$  is quadratic, and the Gaussian functional integral has a closed form solution. The full discrete action can then be written as a matrix from which the discrete propagators can be computed. Afterward, this can be

promoted to a continuum theory by taking the limit  $\Delta \rightarrow 0$ . This is done in appendix A where we show that if one rotates the fields on the contour into a mixed basis through the transformation

$$\begin{pmatrix} \phi^c \\ \phi^q \end{pmatrix} = \frac{1}{\sqrt{2}} \begin{pmatrix} 1 & 1 \\ 1 & -1 \end{pmatrix} \begin{pmatrix} \phi^+ \\ \phi^- \end{pmatrix}, \quad (2.33)$$

then the correlations of the contour endpoints in eq. (2.29), can be included in the quadratic part of the action. The field  $\phi^c$  is referred to as the classical field,  $\phi^q$  as the quantum field, and the rotation in eq. (2.33) is known as the Keldysh rotation. The rotated fields will be referred to as the Keldysh basis, while the original fields on the  $\pm$  branches will be referred to as the  $\pm$  basis.

For bosons,  $\phi$  and  $\bar{\phi}$  are related by complex conjugation, which forces the bar fields to be transformed by the complex conjugate version of eq. (2.33) which has the same form. As this is not the case for the fermionic fields, one can choose a different transformation for the bar fields [33]. Whenever we work with fermions, they will also interact with bosonic particles; therefore, it is convenient to use the same contour transformation for all kinds of particles such that the action always takes the same form. Note that the name classical and quantum fields are meaningless for fermions as they have no classical analog.

Using the rotation in eq. (2.33), it is shown in appendix A that the continuum action for the free theory takes the form (see eq. (A.37))

$$\mathcal{S} = \int dx dx' \begin{pmatrix} \bar{\phi}^c(x) \\ \bar{\phi}^q(x) \end{pmatrix}^T \begin{pmatrix} 0 & (G^A)^{-1}(x, x') \\ (G^R)^{-1}(x, x') & P^K(x, x') \end{pmatrix} \begin{pmatrix} \phi^c(x') \\ \phi^q(x') \end{pmatrix}. \quad (2.34)$$

The two-point propagators related to these new fields are

$$\begin{aligned} i\mathbf{G}(x, x') &= \left\langle \begin{pmatrix} \phi^c(x)\bar{\phi}^c(x') & \phi^c(x)\bar{\phi}^q(x') \\ \phi^q(x)\bar{\phi}^c(x') & 0 \end{pmatrix} \right\rangle \\ &= i \begin{pmatrix} G^K(x, x') & G^R(x, x') \\ G^A(x, x') & 0 \end{pmatrix} \end{aligned} \quad (2.35)$$

The three different types of propagators are known as the retarded ( $R$ ), the advanced ( $A$ ), and the Keldysh ( $K$ ) propagator.

The retarded and advanced elements appearing in the action in eq. (2.34) is directly related to the retarded and advanced propagators through an inversion, while the Keldysh propagator is defined by the element  $P^K$  in eq. (2.34)

$$G^K(x, x') = -G^R(x, y)P^K(y, z)G^A(z, x'), \quad (2.36)$$

where the repeated arguments are contracted over. For the free theory,  $P^K = P_0^K$  is an element with infinitesimal weight as shown in eq. (A.41).

While the elements in eq. (2.34) are changed by interaction, eq. (2.35) can be taken as the definition of the propagators and is completely general also for interacting systems. Even though we do not yet know how to construct the action for an interacting system, eq. (2.35) gives rise to some general defining properties of the propagators. For the case of the retarded propagator, its definition is related to the expectation values of the creation and annihilation operators, introduced in eq. (2.19), which can be seen by undoing the Keldysh rotation

$$\begin{aligned}
G^R(x, x') &= -i \langle \phi^c(x), \bar{\phi}^q(x') \rangle \\
&= -\frac{i}{2} \langle \phi^+(x) + \phi^-(x), \bar{\phi}^+(x') - \bar{\phi}^-(x') \rangle \\
&= -\frac{i}{2} \left( \langle \mathcal{T} a(x) a^\dagger(x') \rangle - \langle \mathcal{T}_- a(x) a^\dagger(x') \rangle + \left\langle [a(x), a^\dagger(x')]_{\mp} \right\rangle \right) \\
&= -\frac{i}{2} \begin{cases} \langle a(x) a^\dagger(x') \rangle \mp \langle a^\dagger(x') a(x) \rangle + \langle a(x) a^\dagger(x') \rangle \mp \langle a^\dagger(x') a(x) \rangle, & t > t' \\ \pm \langle a^\dagger(x') a(x) \rangle - \langle a(x) a^\dagger(x') \rangle + \langle a(x) a^\dagger(x') \rangle \mp \langle a^\dagger(x') a(x) \rangle, & t < t' \end{cases} \\
&= -i\theta(t - t') \left\langle [a(x), a^\dagger(x')]_{\mp} \right\rangle,
\end{aligned} \tag{2.37}$$

where  $\mathcal{T}$  is the time-ordering operator discussed in eq. (2.4) and  $\mathcal{T}_-$  is the anti-time-ordering operator. Rotating  $G^A$  and  $G^K$  into the  $\pm$  basis leads to

$$\begin{aligned}
G^A(x, x') &= i\theta(t' - t) \left\langle [a(x), a^\dagger(x')]_{\mp} \right\rangle, \\
G^K(x, x') &= -i \left\langle [a(x), a^\dagger(x')]_{\pm} \right\rangle.
\end{aligned} \tag{2.38}$$

This gives the propagators the properties

$$G^A(x, x') = (G^R(x, x'))^\dagger, \quad G^K(x, x') = -(G^K(x, x'))^\dagger. \tag{2.39}$$

These relations are often referred to as the causal structure of the propagators. For equal times they lead to the generic relation

$$\begin{aligned}
G^R(t, t; \alpha, \alpha') + G^A(t, t; \alpha, \alpha') &= -i\theta(0) \left( \left\langle [a(t, \alpha), a^\dagger(t, \alpha')]_{\mp} \right\rangle \right. \\
&\quad \left. - \left\langle [a(t, \alpha), a^\dagger(t, \alpha')]_{\mp} \right\rangle \right) = 0.
\end{aligned} \tag{2.40}$$

Due to the (anti-)commutation relations, the difference between the two propagators must

satisfy

$$G^R(t, t; \alpha, \alpha') - G^A(t, t; \alpha, \alpha') = -i\theta(0) \left( \left\langle [a(t, \alpha), a^\dagger(t, \alpha')]_{\mp} \right\rangle + \left\langle [a(t, \alpha), a^\dagger(t, \alpha')]_{\mp} \right\rangle \right) = -i\delta_{\alpha, \alpha'}. \quad (2.41)$$

## 2.4 Beyond the free theory

We have derived some general properties of the two-point propagators but have only shown how to construct the action for a Gaussian theory. We have discussed how the coupling between the two branches of the contour that arise from the thermal initial state and the trace can be included in the bare propagators.

To take advantage of the non-interacting structure, the Hamiltonian is split into a quadratic part ( $H_0$ ) and a non-quadratic part ( $H_I$ )

$$H = H_0 + H_I \quad (2.42)$$

This Hamiltonian is put on the contour in fig. 2.1 using the action in eq. (2.31), simply by normal ordering it and replacing creation and annihilation operators by complex/Grassmann fields. The non-interacting (quadratic) part immediately gives rise to the bare propagators

$$(G_0^R)^{-1}(x, x') = \delta(x - x') \left( i\partial_t - \frac{H_0(\bar{\phi}^q(x), \phi^c(x), x)}{\bar{\phi}^q(x)\phi^c(x)} \right). \quad (2.43)$$

The interactions, which are not included in the bare propagator, are then rotated into the Keldysh basis. In this thesis, two approaches will be used to compute the propagators, either construct an effective theory for the propagators or derive a set of classical equations.

### 2.4.1 Classical equations of motion

For bosonic fields, one can derive classical equations of motion directly from the action. The action is a functional that takes a specific space-time configuration as an argument and outputs a number with the dimension of energy  $\times$  time. This number is related to how a trajectory/path has changed over time. In a quantum system, all possible paths are followed simultaneously, which is why the partition function is a functional integral over all possible field configurations, weighted by the exponential of the action. A classical system can only take one specific path and follows the one along which the action is

stationary [56]. By requiring that the variation of action vanishes, four different types of equations emerge

$$\frac{\delta\mathcal{S}[\phi^c, \phi^q]}{\delta\phi^c(t)} = 0, \quad \frac{\delta\mathcal{S}[\phi^c, \phi^q]}{\delta\bar{\phi}^c(t)} = 0, \quad \frac{\delta\mathcal{S}[\phi^c, \phi^q]}{\delta\phi^q(t)} = 0, \quad \frac{\delta\mathcal{S}[\phi^c, \phi^q]}{\delta\bar{\phi}^q(t)} = 0. \quad (2.44)$$

A crucial feature of the Keldysh action is that the action always has to be at least linear in the quantum fields. This is necessary for the normalization of the density matrix to be preserved and means that  $\mathcal{S}[\phi^c, \phi^q = 0] = 0$ . The equations originating from taking functional derivatives with respect to the classical fields are, therefore, always solved by  $\phi^q = \bar{\phi}^q = 0$ . The classical equations are then given by only two types of equations

$$\left. \frac{\delta\mathcal{S}}{\delta\phi^q(t)} \right|_{\bar{\phi}^q=\phi^q=0} = 0, \quad \left. \frac{\delta\mathcal{S}}{\delta\bar{\phi}^q(t)} \right|_{\bar{\phi}^q=\phi^q=0} = 0. \quad (2.45)$$

The physical interpretation of the non-trivial solutions  $\Phi$  to these equations is that the field has obtained a finite coherent occupation value. When a bosonic state described by annihilation operator,  $a$  acquires a high occupation  $N \gg 1$  in a coherent state, then

$$\langle\phi|aa^\dagger|\phi\rangle = \langle\phi|a^\dagger a|\phi\rangle + \langle\phi|\phi\rangle = \langle\phi|\phi\rangle N + \langle\phi|\phi\rangle, \quad (2.46)$$

and it becomes a good approximation to assume that commutator vanishes such that

$$\langle\phi|aa^\dagger|\phi\rangle = \langle\phi|a^\dagger a|\phi\rangle. \quad (2.47)$$

Due to Pauli's exclusion principle, a fermionic coherent state can not contain more than one fermion, and there is no limit in which the anti-commutation can be ignored. Consequently, the classical approach can not be used directly for fermions. It is, however, useful for fermionic systems because a bosonic quasiparticle can arise joining an even number of fermions, an example being that of a Cooper pair [57]. A composite bosonic particle emerges at a phase transition, where the composite bosonic mode acquires a finite occupation once the phase transition is crossed. The occupation of this mode is the order parameter describing the phase, and one can derive a classical equation for this order parameter. The critical point of the phase transition occurs when the solution has a finite value of the order parameter.

Using the action as a starting point does not just give a rigorous way to derive a classical theory but also allows one to derive semiclassical equations in different ways. By including fluctuations around the initial state, one can derive the Truncated Wigner approximation [58]. Another example is that the inclusion of dissipation directly leads to semiclassical equations that are stochastic equations of the Langevin form [59], which

will be shown in chapter 4.

## 2.4.2 Self-energies and Feynman diagrams

One is enforcing multiple approximations using the saddle-point approximation to derive the classical equations. It is assumed that the system has a classical limit, that the quantum fluctuations are negligible, and that the expectation values of a product of operators are equivalent to the product of their individual expectation values. As mentioned, one can improve the classical equations by relaxing some assumptions, but it will never be ideal for a generic interacting quantum system. Furthermore, the classical equations can not capture interaction-induced perturbations to the spectrum of fermionic particles.

Instead of relying on a variation of the action, one can derive equations for the retarded and Keldysh propagator. To this extent, we assume that an expansion around the free theory converges and writes the full propagator as

$$\begin{aligned} iG^{\alpha,\beta}(x, x') &= \langle \phi^\alpha(x) \bar{\phi}^\beta(x') \rangle = \int \mathcal{D}[\phi^c, \phi^q] \phi^\alpha(x) \bar{\phi}^\beta(x') e^{i\mathcal{S}_I} e^{i\mathcal{S}_0} \\ &= \int \mathcal{D}[\phi^c, \phi^q] \phi^\alpha(x) \bar{\phi}^\beta(x') \sum_{n=0}^{\infty} \frac{(i\mathcal{S}_I)^n}{n!} e^{i\mathcal{S}_0}, \end{aligned} \quad (2.48)$$

where the exponential containing the interaction is written as a power series. The straightforward approach of truncating the sum at a specific order is problematic because the higher order terms can dominate as the number of new terms can increase faster than  $1/n!$  [34]. To overcome this problem, it is necessary to go to infinite order in  $n$ . For the retarded propagator, this resummation was first discussed by Dyson [7] and generalized by Schwinger [60]. The idea is to define a specific element known as the self-energy  $\Sigma$ . The self-energy is derived from the interaction, such that the series expansion of the retarded full propagator, from eq. (2.48) with  $\alpha = c$  and  $\beta = q$ , can be written as

$$\begin{aligned} G^R(x, x') &= G_0^R(x, x') + G_0^R(x, y) \Sigma^R(y, z) G_0^R(z, x') \\ &\quad + G_0^R(x, y_1) \Sigma^R(y_1, y_2) G_0^R(y_2, y_3) \Sigma^R(y_3, y_4) G_0^R(y_4, x') + \dots \end{aligned} \quad (2.49)$$

The factor of  $G_0^R(x, y) \Sigma^R(y, z)$  can be taken out from all the terms containing the self-energy

$$\begin{aligned} G^R(x, x') &= G_0^R(x, x') + G_0^R(x, y) \Sigma^R(y, z) \\ &\quad \times (G_0^R(z, x') + G_0^R(z, y_1) \Sigma^R(y_1, x') + \dots). \end{aligned} \quad (2.50)$$

The last factor corresponds to the full propagator in eq. (2.50), such that we can write

$$G^R(x, x') = G_0^R(x, x') + G_0^R(x, y) \Sigma^R(y, z) G^R(z, x'). \quad (2.51)$$

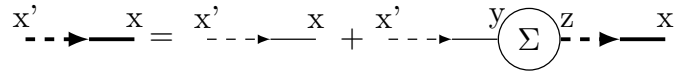


Figure 2.2: *The graphical representation of the Dyson equation for the retarded propagator in eq. (2.53). Dashed lines represent a quantum field, and solid lines a classical field. The thin lines are the bare propagators, while the thick lines are the full propagator. The arrow points away from particle creation and towards particle annihilation. The LHS reads: create a particle in a quantum field at  $x'$  and remove a particle in a classical field at  $x$ .*

To make progress, one can contract eq. (2.51) with the inverse bare propagator from the left and gather the terms involving the full propagator

$$\left( (G_0^R)^{-1}(x'', x) - \Sigma^R(x'', x) \right) G^R(x, x') = \delta(x'' - x'). \quad (2.52)$$

Applying the inverse of the left factor, the full propagator is found by inverting the difference between the bare propagator and the self-energy

$$G^R(x, x') = \left( (G_0^R)^{-1} - \Sigma^R \right)^{-1}(x, x'). \quad (2.53)$$

This equation will be referred to as the Dyson equation for the retarded propagator. For a non-equilibrium theory, the action acquires a matrix structure. Due to causality, the inversion of the retarded and advanced propagators follow by the inversion of a single element in the action. However, the matrix structure leads to an additional coupled equation for the Keldysh propagator, which is in general independent from the retarded and advanced propagators. For the Keldysh component in the action, the resummation leads to a change of  $P^K$

$$P^K(x, x') = 2i0^+ F_0(x, x') - \Sigma^K(x, x'), \quad (2.54)$$

where  $0^+$  is a positive infinitesimal and  $F_0$  is related to the initial state eq. (A.40). As soon as a finite self-energy contribution is added, one can neglect the infinitesimal contribution from the free theory. An important feature of the self-energy is that it satisfies the same causality as the propagators such that  $\Sigma^R = (\Sigma^A)^\dagger$  and  $\Sigma^K = -(\Sigma^K)^\dagger$ , which is essential because any allowed form of the self-energy must preserve the causality of the propagators [33].

To construct the self-energy, it proves advantageous to introduce a graphical representation of the equations. This provides a clear physical interpretation of the processes included in the self-energy and can make the calculation more transparent, as identifying the multiplicity of corresponding diagrams is typically easier than identifying equivalent



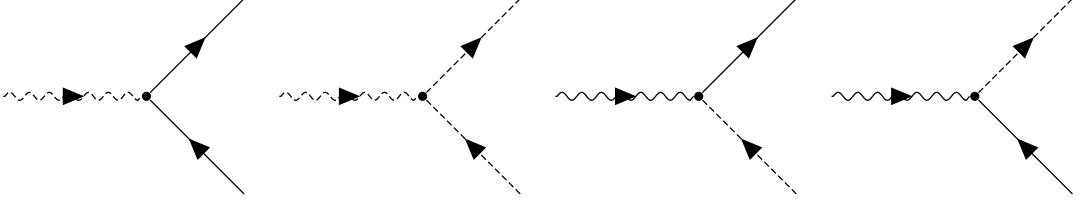


Figure 2.3: Four of the eight vertices generated by the interactions in eq. (2.56). The wavy line represents the  $\phi_a$  fields, and the straight lines are the  $\phi_b$  fields. The remaining four diagrams correspond to the ones shown here with all the arrows flipped. Similarly to fig. 2.2, the dashed lines represent quantum fields while the solid lines represent classical fields.

terms in a complicated sum. The full retarded propagator is shown in its graphical representation in fig. 2.2. The construction of the self-energy is initiated by defining a vertex for each term in  $S_I$ . For example consider a system described by the Hamiltonian

$$H = \omega_b b^\dagger b + \omega_a a^\dagger a + b^\dagger b (g a + \bar{g} a^\dagger), \quad (2.55)$$

where  $b(b^\dagger)$  and  $a(a^\dagger)$  are bosonic annihilation(creation) operators and  $\omega_b$  ( $\omega_a$ ) is the energy required to create a single excitation in the  $b$  ( $a$ ) mode. The coupling  $g$  is a constant. The interacting part of the action is

$$\mathcal{S}_I = -\frac{1}{\sqrt{2}} \int dt g \begin{pmatrix} \bar{\phi}_b^c \phi_b^q + \bar{\phi}_b^q \phi_b^c \\ \bar{\phi}_b^c \phi_b^c + \bar{\phi}_b^q \phi_b^q \end{pmatrix}^T \begin{pmatrix} \phi_a^c \\ \phi_a^q \end{pmatrix} + \text{H.c.}, \quad (2.56)$$

where  $T$  denotes transposition. For this interaction, one can write down eight different vertices, four for the term written in eq. (2.56) and four for its Hermitian conjugate that are also implicitly written in eq. (2.56). The first four are drawn in fig. 2.3. To build the self-energy, one has to go to a specific order in the interaction. This means constructing all diagrams which include a specific number of vertices.

The self-energy always has two external legs, and in the non-equilibrium formalism, the type of leg (quantum or classical) determines which of the three blocks of the action the self-energy belongs to. In the Keldysh basis, the self-energy is written as

$$\Sigma = \begin{pmatrix} 0 & \Sigma^A \\ \Sigma^R & \Sigma^K \end{pmatrix}. \quad (2.57)$$

To find  $\Sigma^R$ , the left external leg has to be a classical field, and the right external leg has to be a quantum field. For  $\Sigma^K$ , both external legs have to be quantum fields.

Considering an interaction where all vertices have  $N$  legs and to order  $n$  in the inter-

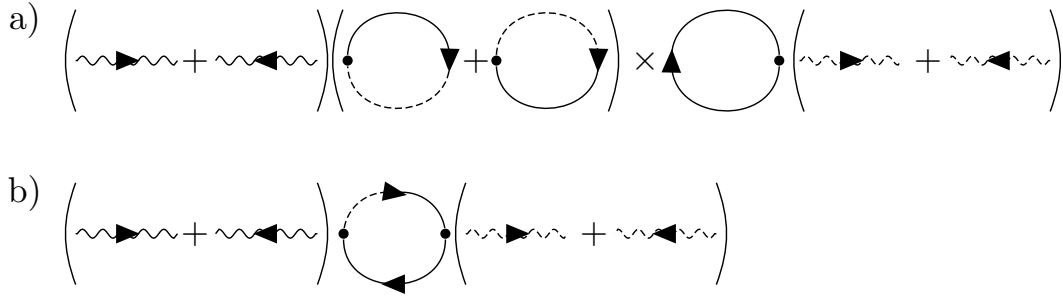


Figure 2.4: The diagrams contributing to the retarded self-energy for  $a$ -fields with the interaction in eq. (2.56) when two vertices are considered. The wavy  $\phi_a$ -fields can propagate in both directions, and both have been included here inside a parenthesis. Both the a) line and the b) line, therefore, consists of a sum of four diagrams. The  $\phi_a$  field connects to a vertex indicated as a black dot. The diagram in a) consists of disconnected diagrams, and the  $\times$  indicates a product. The disconnected diagrams are only evaluated at the diagonals, while the diagram in b) is of the particle-hole type and depends on the non-diagonal part of the propagators of the  $b$ -fields.

action, the two external legs are constrained, meaning that there are  $nN - 2$  free legs left. These should be connected in all possible ways. Each time two legs are connected, this can be identified as a specific propagator. As an example consider the three-legged vertices in fig. 2.3 and consider  $n = 2$ . The retarded diagrams for the  $a$ -field are constructed with two vertices. As the left external leg has to be a classical  $a$ -field, the first vertex has to be one of the last two shown in fig. 2.3. The right external leg must be a quantum field and can be the conjugate of either of the two first vertices in fig. 2.3. Connecting the internal legs, one arrives at the diagrams shown in fig. 2.4. In the considered case, both vertices must be directly connected to the external legs. In general, one can draw diagrams where parts are not connected to external legs, known as disconnected diagrams. It is a feature of the non-equilibrium formalism that these always evaluate to zero [33], which means that the self-energy only contains connected diagrams. This is a consequence that follows directly from the normalization of the partition function.

A shared feature of the diagrams for the  $a$ -fields is that the interaction gives rise to anomalous propagators because the arrow of the  $a$ -field propagator can go in both directions without changing the diagram. This gives rise to a Nambu structure for the self-energy, which we will explore in more detail in chapter 3.

For the diagrams shown in fig. 2.4a the  $a$ -field interacts with a  $b$ -field through the propagator  $G_b^R(x, x) + G_b^A(x, x)$  which vanishes due to eq. (2.40). The only diagram that is important for the self-energy at  $n = 2$  is therefore the loop diagram in fig. 2.4b. To compute the diagram, it must be translated into an equation which can be done through a well-defined algorithm that will now be described.

Inspecting the action in eq. (2.56) one sees that each vertex has a prefactor of  $-g/\sqrt{2}$  and furthermore the series expansion in eq. (2.48) gives each vertex a additional factor of  $i$ . The factor of  $1/n!$  in eq. (2.48) is used to re-exponentiate the result and therefore does not enter the self-energy. For more complicated diagrams, there may be several ways of generating the same diagram, and a combinatorial factor must be included in the diagram's value. Each line, that is connected at a vertex in both ends, can be identified with a specific propagator through  $\langle \phi_{n,x}^\alpha \bar{\phi}_{m,x'}^\beta \rangle = iG_{n,m}^{\alpha,\beta}(x, x')$ .

To include the self-energy in the action, the external legs are removed, an overall factor of  $-i$  is included, and due to the self-energy sign-convention, one also multiplies with  $-1$ . One last important rule is that for each closed loop of fermionic particles, a factor of  $-1$  must be included. This arises from the anti-commutation of the fermions [61].

Apart from sign convention, the same procedure works for adding effective interaction terms (not quadratic in the fields) to the action. For the diagram in fig. 2.4b we find the expression

$$\begin{aligned} \Sigma_a^R(z, y) &= (-1)(-i) \left( \frac{ig}{\sqrt{2}} \right)^2 iG_b^R(z, y) iG_b^K(y, z) \\ &= i \frac{g^2}{2} G_b^R(z, y) G_b^K(y, z). \end{aligned} \quad (2.58)$$

Usually, one relies on the smallness of some parameter in the interaction compared to the bare energy scales, such that the self-energy only contains relatively simple diagrams. Alternatively, the self-energy can be chosen such that it captures a specific physical process that is believed to be important. By doing the Dyson resummation, one captures these processes to infinite order. To avoid over-counting in this process, it is important that the self-energy only includes diagrams that cannot be built by other diagrams already included in the self-energy. These diagrams are called one-particle irreducible and are identified by the fact that by cutting any line, the diagram remains a connected diagram.

One thing not generated through this method is the insertion of self-energies into each other. This can be achieved by using a self-consistent theory. The idea is that in the self-energy, one promotes all the propagators to full propagators (equivalent to promoting all lines in the self-energy to bold lines according to fig. 2.2). The self-energy then becomes a functional of the propagator. By this conceptually simple procedure, one includes a vast amount of additional diagrams. This procedure also has the important property that if the self-energy is derived from a so-called  $\Phi$ -functional and all lines are bold, then the solution will satisfy the conservation laws arising from the full action [62]. Besides being computationally much more demanding, it does have the disadvantage of being an uncontrolled approximation. The effect is that many effects are included, but one can not say that all effects up to a specific order are included. In the worst-case scenario, one is generating processes that should cancel out against other processes at the same order,

but the latter are not being generated through the diagrams included in the self-energy. Still, the fact that conservation laws are respected makes self-consistent approximations very desirable in general. The self-consistent approach has also been found to give good quantitative results in highly non-trivial cases. An example relevant for the present thesis is the BCS-BEC transition in a three-dimensional two-component Fermi-gas [63].

## 2.5 Spectral properties

Given an approximation for the self-energy, we can compute the propagators with interactions included. It is then essential to understand what physical information these propagators contain. The most transparent situation is when one considers a time-independent system in its steady state. This means that the propagators only depend on the relative time  $\tau = t - t'$ . For a generic situation, one can rewrite the propagators with absolute ( $t_a$ ) and relative time

$$\begin{pmatrix} t \\ t' \end{pmatrix} = \begin{pmatrix} 1 & 1/2 \\ 1 & -1/2 \end{pmatrix} \begin{pmatrix} t_a \\ \tau \end{pmatrix}. \quad (2.59)$$

We will call these coordinates the center of time (COT) coordinates. As the transformation is linear, the Jacobian is given by the absolute value of the determinant of the transformation matrix, which for this rotation is unity. Therefore, the action takes the same form with all  $t, t'$  replaced by  $t_a, \tau$  in eq. (2.59). In COT coordinates the propagator  $G^\alpha(t, q; t', q')$ <sup>1</sup> is written as

$$G^\alpha(t_a, \tau; q, q') = G^\alpha(t_a + \tau/2, q; t_a - \tau/2, q'), \quad (2.60)$$

which propagates the state  $q'$  at  $t'$  to the state  $q$  at  $t$ . The Fourier transform is then used to go between the relative time and frequency domain

$$f(\omega) = \int_{-\infty}^{\infty} e^{it\omega} f(t) dt, \quad f(t) = \frac{1}{2\pi} \int_{-\infty}^{\infty} e^{-i\omega t} f(\omega) d\omega, \quad (2.61)$$

giving the propagator  $G^\alpha(t_a, \omega; q, q')$  and the causal structure from eq. (2.39) takes the form

$$G^A(t_a, \omega; q, q') = \bar{G}^R(t_a, \omega; q', q), \quad G^K(t_a, \omega; q, q') = -\bar{G}^K(t_a, \omega; q', q). \quad (2.62)$$

It was observed in eq. (2.37) that the retarded propagator is only non-zero for  $\tau \geq 0$ . As shown in appendix B this means that the real and imaginary parts of  $G^R(t_a, \omega, q', q)$  are dependent of each other. The imaginary part can be computed from  $\text{Re} G^R(t_a, \omega, q', q)$

---

<sup>1</sup>with  $\alpha \in \{R, A, K\}$

using the Kramers-Kronig relations

$$\text{Im } G^R(t_a, \omega, q', q) = \mathcal{P} \int \frac{d\omega'}{\pi} \frac{\text{Re } G^R(t_a, \omega', q', q)}{\omega - \omega'}, \quad (2.63)$$

and

$$\text{Re } G^R(t_a, \omega, q', q) = \mathcal{P} \int \frac{d\omega'}{\pi} \frac{\text{Im } G^R(t_a, \omega', q', q)}{\omega' - \omega}. \quad (2.64)$$

This motivates defining a quantity that is related to the imaginary part of the retarded propagator

$$\begin{aligned} A(t_a, \omega, q, q') &= i (G^R(t_a, \omega, q, q') - G^A(t_a, \omega, q, q')) \\ &= i (G^R(t_a, \omega, q, q') - \bar{G}^R(t_a, \omega, q', q)), \end{aligned} \quad (2.65)$$

where  $A(t_a, \omega, q, q')$  is known as the spectral function. Due to the properties of the retarded propagator in eq. (2.41) the spectral function obeys a sum rule

$$\int \frac{d\omega}{2\pi} A(t_a, \omega, q, q') = \delta_{q, q'}. \quad (2.66)$$

The normalization of the  $q, q$  part makes it possible to give a physical interpretation of the spectral function. To facilitate this consider a system with a single mode, like in appendix A, with an arbitrary non-zero self-energy split into its real and imaginary parts  $\Sigma^R(t_a, \omega) = \sigma(t_a, \omega) + i\gamma(t_a, \omega)$ . The propagators and self-energies are then scalar-valued functions, and the corresponding spectral function is

$$\begin{aligned} A(t_a, \omega) &= -2\text{Im}G^R(t_a, \omega) = -2\text{Im} \frac{1}{\omega - \omega_0(t_a) - \Sigma^R(t_a, \omega)} \\ &= \frac{-2\gamma(t_a, \omega)}{(\omega - \omega_0(t_a) - \sigma(t_a, \omega))^2 + \gamma(t_a, \omega)^2} \\ &= -2 \text{Im} (\Sigma^R(t_a, \omega)) |G^R(t_a, \omega)|^2, \end{aligned} \quad (2.67)$$

which is a type of generalized Lorentzian. In the non-interacting case, both self-energy terms vanish, and  $-\gamma$  is substituted with an infinitesimal positive number. In this case the infinitely narrow Lorentzian turns into  $\delta(\omega - \omega_0)$ . The interpretation is that the system can only be excited at  $\omega = \omega_0$ . As the excitation is an eigenstate, it has an infinite lifetime, which leads to the peak having zero width.

For the interacting case, the bare creation operation does not create an eigenstate. The consequence is that the real eigenstate is a superposition of many bare states. Due to the sum rule, the diagonal parts describe a probability measure for how the spectral weight of the free modes is distributed into the interacting states. Practically it means that from the spectral function peak positions, we learn about the energies of the new single-particle excitations (at  $\omega_0 + \sigma(\omega)$ ), and the peak widths contain information about

how good single-particle eigenstates the bare states are (their lifetime). From eq. (2.67), we can directly carry over this interpretation to the retarded self-energy. The real part of the retarded self-energy shifts the energy of the single-particle states, while the imaginary parts give rise to a finite lifetime as the free state can spread out into the interacting states. Experimentally the spectral function is accessible because it is related to the linear response of the system. In cavity systems it can for example be investigated using pump-probe [64] or transmission techniques [65], while for electronic systems it can be probed with scanning tunnel microscopy [66, 67] or angle-resolved photoemission spectroscopy [68, 69].

Lastly, note that the spectral function can be defined in a basis independent form as

$$A = i(G^R - G^A), \quad (2.68)$$

which for an interacting or non-equilibrium system can be written like

$$A = iG^R \circ (\Sigma^R - \Sigma^A) \circ G^A, \quad (2.69)$$

where  $\circ$  denotes contraction. This rewriting follows directly from the Dyson equation, in eq. (2.53), for the retarded and advanced propagators.

### 2.5.1 Quasiparticle picture

We have relied on well-defined peaks in the spectral function for these interpretations of the interacting system. This assumption hinges on  $\gamma(\omega)$  being a small value, and under this condition, one can put this qualitative description on a more rigorous footing. The idea is to describe the interacting theory through single-particle excitations with renormalized parameters. This concept was first used by [70] in the context of Fermi-liquids. The starting point is the retarded scalar propagator

$$G_n^R(t_a, \omega) = \frac{1}{\omega - \omega_n(t_a) - \sigma_n(t_a, \omega) - i\gamma_n(t_a, \omega)}, \quad (2.70)$$

where  $n$  defines different bare modes, and the self-energy is split into real and imaginary parts. The real part of the pole of  $G^R$  can be approximated as the solution  $\omega_{n,p}(t_a)$  to the equation

$$\omega_{n,p}(t_a) = \omega_n(t_a) + \sigma(t_a, \omega_{n,p}). \quad (2.71)$$

If solutions are found, then one can expand around them to define the new quasiparticles for the theory at absolute time  $t_a$ . For this expansion to be valid,  $\gamma$  must be small. This is necessary because the true poles of the retarded propagator are not on the real axis but

in the lower half of the complex plane. To linear order in  $\omega$ , one finds the propagator

$$G_n^R(t_a, \omega) \approx \left( \omega - (\omega_n(t_a) - \sigma_n(t_a, \omega_{n,p})) - \omega \partial_\omega \sigma_n(t_a, \omega_{n,p}) - i\gamma_n(t_a, \omega_{n,p}) - i\omega \partial_\omega \gamma(t_a, \omega_{n,p}) \right)^{-1}. \quad (2.72)$$

In its current form, the imaginary  $\omega$  dependence makes it impossible to rewrite eq. (2.72) as something that has the same form as a free particle. A similar form as the free particle can be found if we assume that  $\partial_\omega \gamma(\omega_{n,p})$  is negligible. With this approximation, the propagator takes the form

$$G_n^R(t_a, \omega) \approx \frac{Z(t_a)}{\omega - \tilde{\omega}_n(t_a) - i\tilde{\gamma}_n(t_a)} \quad (2.73)$$

where the quasiparticle weight is defined as

$$Z(t_a) = (1 - \partial_\omega \sigma_n(t_a, \omega_{n,p}))^{-1}, \quad (2.74)$$

and the renormalized dispersions and decay rates are given by

$$\begin{aligned} \tilde{\omega}_n(t_a) &= Z(t_a)\omega_{n,p}(t_a), \\ \tilde{\gamma}_n(t_a) &= Z(t_a)\gamma_n(t_a, \omega_{n,p}). \end{aligned} \quad (2.75)$$

Note that this approximation relies heavily on the smallness of the imaginary part of the decay rate. Additionally, the quasiparticle spectral function violates the sum rule in eq. (2.66). This is a direct consequence of not keeping equal orders in the expansion of the real and imaginary parts of the self-energy. By computing the integral over the spectral function, one finds that the result is given by  $Z$  instead of 1.  $Z$ , therefore, contains information about how much of the spectral weight is put into the quasiparticle when exciting a mode with the bare creation operator. The remaining part  $1 - Z$ , is spectral weight that is added to other types of excitations. In other words,  $Z$  is related to the overlap between the excitation of a bare mode in the real interacting basis and the quasiparticle approximation.

As the self-energies have the same causal structure as the propagators, the real and imaginary parts of the self-energies are also connected by the Kramers-Kronig relations derived for the propagator in eq. (2.63). Using this connection, it is possible to include real and imaginary parts at the same order, as shown in [71], thereby restoring the sum rule for the quasiparticle approximation. The disadvantage of this approach is that the interpretation becomes less obvious. For this reason, we stick with the quasiparticle

approximation defined in eq. (2.73).

## 2.6 Occupation of the spectrum

We have access to the spectral information of the system through the retarded propagator, and in this section, we will show that the information in the Keldysh propagator is related to the occupation. In COT coordinates, the Keldysh propagator is connected to the creation and annihilation operators by eq. (2.38)

$$iG^K(t_a, \tau; q, q') = \left\langle \left[ a_q(t_a + \tau/2), a_{q'}^\dagger(t_a - \tau/2) \right]_{\pm} \right\rangle. \quad (2.76)$$

Consider first the diagonal part of eq. (2.76) at  $\tau = 0$

$$\begin{aligned} iG^K(t_a, 0; q, q) &= i \int \frac{d\omega}{2\pi} G^K(t_a, \omega; q, q) = \left\langle [a_q(t_a), a_q^\dagger(t_a)]_{\pm} \right\rangle \\ &= 1 \pm 2 \langle a_q^\dagger(t_a) a_q(t_a) \rangle = 1 \pm 2 \langle n_q(t_a) \rangle = 1 \pm 2 \langle n_q(t_a) \rangle, \end{aligned} \quad (2.77)$$

As the excitation is removed and added in the same mode, this relates to the expectation value of the number operator for the  $q$ th mode. For the off-diagonal part, the commutation and anti-commutation relations lead to

$$iG^K(t_a, 0; q, k) = \pm 2 \langle a_q^\dagger(t_a) a_k(t_a) \rangle, \quad (2.78)$$

which does not contain the constant vacuum term seen in eq. (2.77).

Generally,  $G^K$  is derived from the action using the relation in eq. (2.36). Including the self-energy as in eq. (2.54), it takes the form

$$G^K = G^R \circ (-P_0^K + \Sigma^K) \circ G^A \quad (2.79)$$

where the indices have been suppressed, as the general structure is independent of the chosen representation.

If the system is non-interacting, all self-energies vanish, and the system becomes time-translation invariant. The bare infinitesimal term  $P_0^K$  derived in appendix A then defines how the Keldysh propagator is inverted. In appendix A we find

$$\begin{aligned} G_0^K(\omega, k) &= - \left| G_0^R(\omega, k) \right|^2 P_0^K(\omega) = -i A_0(\omega, k) (1 \pm 2n_{B/F}(\omega)) \\ &= -i 2\pi \delta(\omega - \epsilon_k + \mu) (1 \pm 2n_{B/F}(\omega)), \end{aligned} \quad (2.80)$$

where  $\epsilon_k$  is the bare dispersion defined by the quantum number  $k$ , corresponding to the



non-interacting Hamiltonian  $H_0$ . The chemical potential is denoted as  $\mu$  and  $n_{B/F} = (e^{\beta\omega} \mp 1)^{-1}$  is the Bose-Einstein or Fermi-Dirac distribution, with inverse temperature  $\beta$ .

If the system is interacting, but one is still able to diagonalize the retarded propagator and  $\Sigma^K$  simultaneously, then the contractions in eq. (2.79) simplify, and the steady state solution for  $G^K(\omega, k)$  becomes

$$G^K(\omega, k) = |G^R(\omega, k)|^2 \Sigma^K(\omega, k) = -\frac{A(\omega, k)\Sigma^K(\omega, k)}{2 \operatorname{Im} \Sigma^R(\omega, k)}. \quad (2.81)$$

To facilitate physical interpretation, it is helpful to remove the constant vacuum contribution in eq. (2.77), which can be done by writing the Keldysh propagator as

$$G^K = G^R - G^A + \delta G^K = -iA + \delta G^K, \quad (2.82)$$

where the occupied propagator  $\delta G^K$  is defined through

$$\delta G^K = G^R \circ \delta \Sigma^K \circ G^A, \quad (2.83)$$

which, in the steady state, gives a relation similar to eq. (2.81).

Setting this equal to eq. (2.79) and neglecting all the infinitesimal terms, one finds that the self-energies are connected by the relation

$$\delta \Sigma^K = \Sigma^K - (\Sigma^R - \Sigma^A). \quad (2.84)$$

The diagonal part of  $\delta G^K$  is then proportional to the occupation of the different modes and, for a non-interacting system in equilibrium, directly corresponds to eq. (2.80) and is therefore given by

$$\delta G_0^K(\omega, k) = \mp i 2\pi \delta(\omega - \epsilon_k + \mu) 2n_{B/F}(\omega). \quad (2.85)$$

For general out-of-equilibrium interacting systems where  $G^R$  and  $G^K$  can be simultaneously diagonalized, it takes the form

$$\delta G^K(\omega, k) = -\frac{A(\omega, k)\delta \Sigma^K(\omega, k)}{2 \operatorname{Im} \Sigma^R(\omega, k)}. \quad (2.86)$$

Causality requires  $\delta G^K$  to be anti-Hermitian such that  $\delta G^K$  must be purely imaginary in the diagonal representation. Because  $A$  and  $\operatorname{Im} \Sigma^R$  are real,  $\delta \Sigma^K$  is also purely imaginary. To connect with equilibrium field theory, it can be useful to parametrize  $\delta G^K$  by the spectral function

$$\operatorname{Im} \delta G^K(\omega, k) = -A(\omega, k)\delta F(\omega, k), \quad (2.87)$$

which at this point defines  $\delta F$ . To highlight the properties of these functions, consider a closed but interacting single-mode system in its steady state. To understand the generic properties of the propagators, we will use the Lehmann representation [39, 61]. The explicit calculations are shown in appendix C. Let the Hamiltonian be defined through its eigenstates  $H|\alpha\rangle = E_\alpha|\alpha\rangle$  and the density matrix be diagonal in this basis  $\rho = \sum_\alpha c(E_\alpha)|\alpha\rangle\langle\alpha|$ . Using the bare creation ( $a^\dagger$ ) and annihilation ( $a$ ) operators the spectral function is

$$A(\omega) = 2\pi \sum_{\alpha,\beta} (c(E_\beta) \mp c(E_\alpha)) |\langle\alpha|a^\dagger|\beta\rangle|^2 \delta(\omega - E_\alpha + E_\beta), \quad (2.88)$$

where the sign depends on the statistics of the excitation. Because  $c(E_\alpha)$  is an eigenvalue of the density matrix, it must always be a real number between 0 and 1. Consequently, the spectral function can have sign changes for bosons but is always positive for fermions. In the Lehmann representation,  $\text{Im} \delta G^K(\omega)$  is found to be

$$\text{Im} \delta G^K(\omega) = \mp 2\pi \sum_{\alpha,\beta} 2c(E_\alpha) |\langle\alpha|a^\dagger|\beta\rangle|^2 \delta(\omega - E_\alpha + E_\beta), \quad (2.89)$$

which can never change sign for bosons or fermions. As shown in appendix C, this is not true for  $\text{Im} G^K$ , which can change sign for fermions.

Using eq. (2.83) one sees that the sign of  $\text{Im} \delta \Sigma^K(\omega, k)$  must always be identical to the sign of  $\text{Im} \delta G^K(\omega, k)$  such that for bosons

$$\text{Im} \delta G^K = |G^R|^2 \text{Im} \delta \Sigma^K \leq 0, \quad (2.90)$$

while for fermions

$$\text{Im} \delta G^K = |G^R|^2 \text{Im} \delta \Sigma^K \geq 0. \quad (2.91)$$

Additionally, the steady state solution for  $\delta F$  can immediately be found from eqs. (2.90) and (2.91) by rewriting  $|G^R|^2$  in terms of the spectral function as in eq. (2.69)

$$\delta F(\omega, k) = -\frac{\text{Im} \delta \Sigma^k(\omega, k)}{-2 \text{Im} \Sigma^R}. \quad (2.92)$$

Using the Lehmann representation,  $\delta F$  is written as

$$\begin{aligned} \delta F(\omega) &= -\frac{\text{Im} \delta G^K(\omega)}{A(\omega)} \\ &= -\frac{\mp \sum_{\alpha,\beta} 2c(E_\alpha) |\langle\alpha|a^\dagger|\beta\rangle|^2 \delta(\omega - E_\alpha + E_\beta)}{\sum_{\alpha,\beta} [c(E_\alpha - \omega) \mp c(E_\alpha)] |\langle\alpha|a^\dagger|\beta\rangle|^2 \delta(\omega - E_\alpha + E_\beta)}. \end{aligned} \quad (2.93)$$

Because  $\text{Im } \delta G^K$  cannot change sign, it requires that if  $\delta F$  changes sign, so does  $A$ . This is explicitly seen in the Lehmann representation but also directly built into eq. (2.92) because the sign of both  $A$ , through 2.67, and  $\delta F$  is fully determined by the sign of  $-\text{Im } \Sigma^R$ .

For fermions eq. (2.88) proves that  $\delta F$  can not change sign and because  $A > 0$  it follows that  $-\text{Im } \Sigma^R(\omega, k) > 0$ , which forces  $\delta F(\omega, k) \leq 0$ . Furthermore, the Pauli exclusion principle means that  $0 \leq c(E_\alpha) \leq 1$ . From eq. (2.93) it then follows that  $\delta F$  is bounded from below such that  $\Delta F \geq -2$ . Combining these aspects, we arrive at an inequality between the retarded self-energy and  $\delta \Sigma^K$

$$-4 \text{Im } \Sigma^R \geq \text{Im } \Sigma^K \geq 0. \quad (2.94)$$

This relation can be valuable for identifying errors in numerical calculations.

For bosons,  $A$  can be sign-changing, which means that  $\delta F$  can also be sign-changing. Furthermore, there is no bound on the absolute value of  $\delta F$  as there is no exclusion principle for bosons. When the signs of  $A$  and  $\delta F$  differ, then the occupation of the specific mode has become unstable such that it grows exponentially. The quadratic part of the theory will then no longer be bounded because the Gaussian integrals are no longer well-defined. As a consequence, the theory breaks down. The physical interpretation is that the fluctuations start dominating the bare contribution, which renders the expansion around the bare modes ill-behaved. This instability means that the system has transitioned into a new steady state. That is, the system has experienced a phase transition.

The technical solution to this problem is to expand around the new equilibrium. This is done by separating the unstable mode from the theory and treating it as a macroscopically occupied field. The occupied part of this mode can then be described by the classical equations discussed in section 2.4.1. This way, the unbounded quadratic part is removed from the theory, and the macroscopically occupied mode appears in the vertices as a classical source field.

As an example consider a state in thermal equilibrium:  $c(E_\alpha) = \frac{e^{-\beta E_\alpha}}{\mathcal{N}}$ , where  $\mathcal{N} = \text{Tr } e^{-\beta H}$ . Plugging this into eq. (2.93) one finds the Bose-distribution as in the free theory

$$\delta F(\omega) = \frac{1}{e^{\beta\omega} - 1}. \quad (2.95)$$

Notice that this result is independent of the interactions in the system. Consequently, it is sufficient to know the spectrum in thermal equilibrium as the distribution function act as a proportionality factor for the occupation. This fundamental connection between the occupation and spectral function for a system in thermal equilibrium is known as the fluctuation-dissipation theorem [72, 73]. On a technical level it is seen that it is a

consequence of the eigenvalues of the density matrix satisfying  $c(E_\alpha - \omega) = c(E_\alpha)c(-\omega)$ . The equilibrium theory [39, 61, 74] relies on this such that it is sufficient to compute only spectral properties of the system, whereas, in our non-equilibrium formalism, both the Keldysh propagator and the retarded must be computed.

For the current example, consider a free spectral function given by

$$A(\omega) = 2\pi\delta(\omega - \epsilon_0 + \mu), \quad (2.96)$$

where  $\epsilon_0$  is the ground state energy. The spectral function cannot change sign and is always positive. As  $\text{Im } \delta G^K$  is negative for bosons,  $\delta F(\omega)$  must be positive. However, when  $\omega < 0$  then  $\delta F(\omega < 0)$  changes sign. As long as  $\epsilon_0 - \mu > 0$  then  $A(\omega < 0) = 0$  and the sign change of  $\delta F$  has no effect as  $\delta G^K(\omega < 0) = 0$ . If  $\mu > \epsilon_0$ , then the spectral function has a positive weight at frequencies where  $\delta F$  is negative, which gives rise to  $\delta G^K$  having an unphysical sign. At this point, the bosons condense into the ground state mode of the system, which means that the ground state field has to be separated from the action.

In thermal equilibrium, the fluctuation-dissipation theorem holds, which means that all instabilities and phase transitions appear in the spectrum. This means that the instability occurs in the retarded propagator. The retarded propagator becomes unbounded if the steady state solution has the pole in the positive imaginary plane, as this corresponds to the mode growing exponentially in time. Away from thermal equilibrium, the occupation and the spectrum are completely independent. Consequently, when the system is out of equilibrium, the quadratic part of the action can become unbounded both due to an instability in the retarded propagator and through an instability in  $\delta\Sigma^K$  [75].

The parametrization of  $\delta G^K$  in terms of the spectral function in eq. (2.87) relied on being able to simultaneously diagonalize  $G^R$  and  $\delta\Sigma^K$ . Even when this is not possible, one can still define a "distribution" function through the basis independent parametrization

$$\delta G^K = G^R \circ \delta F - \delta F \circ G^A. \quad (2.97)$$

Due to the causal structure in eq. (2.39),  $\delta F$  will always be Hermitian. Finally, it is worth pointing out that our definition of  $\delta G^K$  in eq. (2.82) is directly related to the commonly used lesser propagator [34, 39, 48, 49, 61] by

$$G^<(t, q; t', q') = \pm \frac{\delta G^K(t, q; t', q')}{2}. \quad (2.98)$$

For the discussion of the occupation, we have mainly focused on the stationary state of a time-translation invariant system, while for the previous discussion of the spectral

function, we discussed the system in absolute and relative time. The general two-time inversion of the Keldysh propagator leads to

$$(G_0^R)^{-1} \circ \delta G^K - \delta G^K \circ (G_0^A)^{-1} = \Sigma^R \circ \delta G^K - \delta G^K \circ \Sigma^A + \delta \Sigma^K \circ G^A - G^R \circ \delta \Sigma^K, \quad (2.99)$$

which describes the two-time evolution of the Keldysh propagator [49]. As we are mainly concerned with stationary-state properties, we will not discuss this here but will point out that the propagators are much less constrained during time evolution. Because of the fewer constraints, the signs are allowed to change throughout the evolution, which makes the two-time evolution of generic systems challenging.

## 2.7 Combinatorics for non-equilibrium diagrams

In this section, we will return to the diagrams used to build the self-energy in 2.4.2. We do this because the Keldysh structure leads to a differentiation of diagrams that topologically look identical. The differentiation happens because the internal propagators can be different combinations of retarded, advanced, or Keldysh propagators, even for topologically equivalent diagrams. For a diagram topology with many internal lines, the different combinations of retarded, advanced, and Keldysh can lead to a large number of diagrams. However, the causal structure of the internal propagators means that many of these are either zero or cancel out against each other. In appendix D, we construct a generic algorithm to derive only the diagrams that can be non-zero. In the current section, we will not discuss the algorithm's structure but will focus on how cancellations and vanishing diagrams are identified.

We have discussed two types of self-energies, the retarded self-energy, and the Keldysh self-energy. For a retarded self-energy, the incoming line (that is not drawn) has to be a classical field and the outgoing a quantum field, while for the Keldysh self-energy, both the incoming and outgoing line has to be a quantum field due to eq. (2.79). By constricting the incoming and outgoing line, one constricts the possible configurations of the first and last vertex in the diagram. In the following, we will focus on a retarded diagram, but the techniques discussed work in exactly the same way for a Keldysh self-energy diagram.

As an example, we will consider a diagram with the topology in fig. 2.5. This diagram can contribute to the self-energy in a Bose-Fermi mixture with intra-species contact interaction, such as the situation discussed in chapter 5. The system contains three different kinds of particles  $D$ ,  $W$ , and  $S$ . The arrows indicate a particle carrying energy and momentum  $p_n = (\omega_n, k_n)$ , and the line style differentiates the particle type. We will also use the index  $p_n$  to refer to the specific propagators in the diagram. A line with a double-arrow for particle type  $D$  (for double-arrow), a wavy line for particle type  $W$  (for wavy/wiggly),

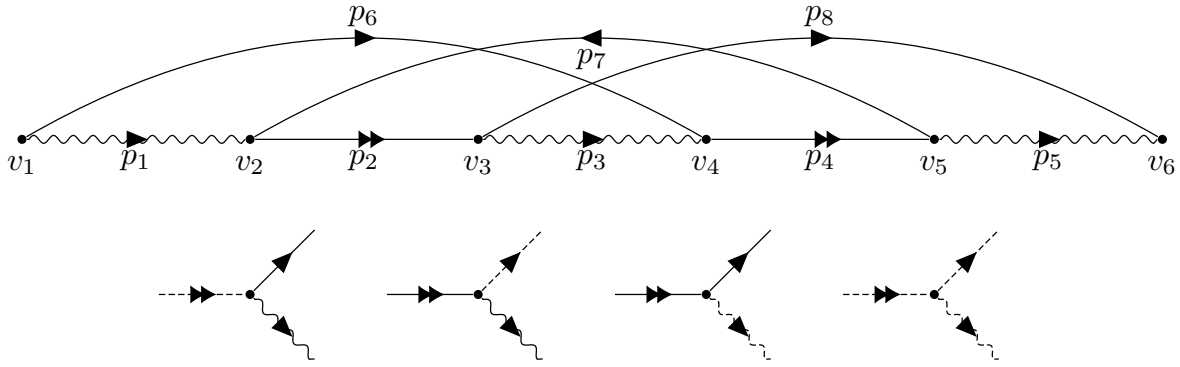


Figure 2.5: *The topology of a diagram for interaction between three different types of fields (differentiated by the arrow and line type) that contributes to the self-energy. It consists of six vertices, each labeled by  $v_i$  and eight propagators labeled by  $p_i$ . Below the diagram is the four possible types of vertex structures arising from the contour degree of freedom. Due to causality, a configuration with only classical legs is impossible.*

and a straight line with a single arrow for particle type  $S$  (for straight/single). The contact interaction allows particle  $D$  to break into particle  $W$  and  $S$  at vertex  $v_n$ . During such a process, the energy and momentum must be conserved. To construct this diagram, one first chooses which sort of self-energy one wants to construct. The type is determined by the incoming left line (which is not drawn) on vertex  $v_1$  and the outgoing right line on  $v_6$ . In the considered case, the vertex must have three lines connecting it, and each line must be of a different particle type. The diagram in fig. 2.5 therefore contributes to the self-energy of the  $D$  particle as there is no double-arrow line connected to the vertex  $v_1$  and  $v_6$ . The Keldysh structure leads to there being a total of eight different vertex configurations. Four of these are shown below the diagram in fig. 2.5. The remaining four are found by flipping the direction of all the arrows. In these vertices, the same notation as in 2.4.2 is used, where a quantum field has a dashed line, and a classical field is a solid line.

This diagram consists of  $N_v = 6$  vertices and  $N_p = 8$  internal propagators. For the retarded self-energy, one needs the left incident line on  $v_1$  to be a classical field and the right incident line on  $v_6$  to be a quantum field. If one constructs all possible Keldysh configurations in fig. 2.5, this gives rise to 1024 versions for the retarded diagram, which all have different retarded, advanced, and Keldysh propagators inside the diagram. All diagrams containing a  $q - q$  propagator vanish, leaving a more manageable 84 diagrams.

The behavior of the vacuum contribution in each  $G^K$  is better treated separately since often the vacuum contribution cancels out with other diagrams. This will for example be seen in chapter 5. To make the vacuum appear directly in the diagram, one can write out the Keldysh propagator using eq. (2.82).

So far, causality has only been used through the q-q propagator vanishing, but causality also means that diagrams where  $G^R(\tau)G^A(\tau)$  appear, vanish because the two propagators have no shared support. In complicated diagrams with several internal loops, such simple products do not appear, but as discussed in appendix D, this can be generalized and semi-automated for more complicated diagrams like that in fig. 2.5. When an internal propagator is evaluated at equal times ( $t = t'$ ) cancellations due to eq. (2.40) can also happen.

For the example in fig. 2.5 using the causality cancellation and writing out the vacuum contribution, the number of different configurations increases to 220. In the specific case, it increases because many of the internal lines are of the Keldysh type. In such a case, many diagrams will vanish if parts of the system are not occupied as all the  $\delta G^K$  propagators belonging to the unoccupied particles are zero. In the considered case, the  $S$  propagators  $p_{\{6-8\}}$  can be the particles of the medium which are thermally occupied, while the  $W$  particles  $p_{\{1,3,5\}}$  are unoccupied. In that case, the  $D$  propagators  $p_{\{2,4\}}$  are the composite particles due to an attractive interaction between the medium and the  $W$  particle. So if there are no  $W$  particles, there also will be no occupation of the  $D$  particles. Removing all diagrams containing a  $\delta G^K$  for both  $D$  and  $W$  leaves us with nine configurations that must be computed. So even though writing out the vacuum contribution initially led to more diagrams, the fact that parts of the system were unoccupied decreased the number from 84 to 9.

In summary, non-equilibrium leads to a drastic increase in the number of different diagrams one has to compute, but many of them are zero due to the casual structure of the theory. The process of finding all the non-zero diagrams can be done by implementing the algorithm discussed in appendix D. Due to their sharp features, the vacuum parts are usually numerically challenging. In those cases, it is advantageous to cancel as many of such diagrams as possible, which can be done by separating the vacuum contribution in  $G^K$ .

Having determined the relevant diagrams is only the first step. The second and usually much harder step is to compute their value. To do this efficiently, one has to consider the specific diagram and physical situation. This means there is no generic algorithm to compute the diagrams that is stable, accurate, and fast enough to be universal.

## 2.8 Open quantum systems

So far, we have been thinking about closed systems, but if a subsystem is coupled to a large environment, one can effectively split the full system into two parts, the subsystem, and the environment. The interaction with the environment means that the subsystem

itself cannot be described as a closed system. If the subsystem is much smaller than the environment, then the modification of the state of the environment due to the subsystem is small or even negligible. In this case, one can hope to construct an effective description of the subsystem without explicitly considering the back-action onto the environment. Using such an effective description in general means that the time-evolution operator is no longer unitary as environment-induced dissipation and driving are included in the description. The subsystem is then referred to as an open system. One of the common methods to derive the effective non-unitary description of the subsystem is to assume that the environment state is entirely independent of the subsystem state and that the interaction between environment and subsystem is weak enough that one only has to treat the effect of the interaction to second order. A controlled expansion in the subsystem-environment coupling leads to the well-known and widely used Born-Markov master equation describing the evolution of the subsystem. From here on, the subsystem is referred to simply as the system, which is the degrees of freedom that remain after having traced away the environment, whereas when we say total system we mean system including the environment. Here, the derivation of the Born-Markov master equation will not be presented. Instead, we refer the reader unfamiliar with the derivation to section 3.3.1 in [40]. A particular Markovian master equation is the Lindblad equation (or Gorini-Kossakowski-Sudarshan-Lindblad equation) [76, 77]. Its advantage is that the system's evolution is completely positive and trace preserving (CPTP) and its most general form is [78]

$$\partial_t \rho = -i [H_s(t), \rho] + \sum_i^{N^2-1} \gamma_i(t) \left( L_i(t) \rho L_i^\dagger(t) - \frac{1}{2} \{ L_i^\dagger(t) L_i(t), \rho \} \right), \quad (2.100)$$

Where  $H_s(t)$  is the effective unitary evolution of the system with dimensionality  $N$  and  $\rho(t) = \text{Tr}_E \chi(t)$  is the density matrix for the system after having traced away the environment degrees of freedom from the total state  $\chi(t)$ . The Hamiltonian includes the bare system evolution and a renormalization of the internal energy levels known as the Lamb shift. The second term is non-unitary and accounts for drive and dissipation. The rate of the physical process described by the jump operator  $L_i(t)$  is given by  $\gamma_i(t)$ . For this equation to be a CPTP mapping for all  $t$ , it is necessary that  $\gamma_i(t) \geq 0 \forall t$ . The Lindblad approach, as it is CPTP, guarantees a physical density matrix throughout the entire evolution. For other master equations, the range of validity has to be checked such that it is not violated.

The advantage of master equation methods is that the resulting effective dynamics of the system can be treated with high accuracy and with few approximations either using exact diagonalization or tensor network methods [41–44]. Furthermore, the master equa-



tion gives access to the systems density matrix, and all system properties can therefore be computed. For master equations, a big challenge is tackling the exponentially increasing Hilbert space dimension. This is more challenging than for a closed system because it is necessary to work with density matrices instead of states. Therefore, the effective dimension of the space one has to consider is of dimension  $N^2$ . Questions regarding large interacting systems are thus challenging for master equation approaches.

Using the field theoretic approach to compute the propagators, we only have information regarding the expectation values of removing and adding a particle instead of the full density matrix. One can derive a theory for higher-order correlation functions, but this significantly increases the complexity of the computation. The advantage gained is that we can treat interacting systems that are macroscopic in size.

### 2.8.1 Linearly coupled environment

Having discussed the standard approach to an open system, we will now focus on the specific case of an environment that couples linearly to the system and treat it with our field theoretic approach. We will derive the self-energies that arise from this coupling and use them to model the loss of cavity photons, due to imperfect mirrors, in all considered systems in chapters 3 to 5 and in chapter 5 also use it to describe incoherent driving. For this reason, we focus on a bosonic quantum harmonic oscillator, described by annihilation (creation) operator  $a$  ( $a^\dagger$ ), embedded in an environment consisting of non-interacting bosonic quantum harmonic oscillators, with annihilation (creation) operator  $b_k$  ( $b_k^\dagger$ ). We consider the interaction to be bilinear, such that a single excitation between system and environment is transferred while conserving the total particle number.

The total system is described by

$$H = H_a + H_b + H_I, \quad (2.101)$$

with

$$\begin{aligned} H_b &= \sum_k \epsilon_k b_k^\dagger b_k, \\ H_I &= \sum_k g_k a b_k^\dagger + \bar{g}_k b_k a^\dagger, \end{aligned} \quad (2.102)$$

where  $H_b$  is the Hamiltonian describing the environment with dispersion  $\epsilon_k$ , and  $H_I$  describes the coupling between system and environment with strength  $g_k$ .  $H_a$  is left completely general, albeit for a single mode. This assumption simplifies the following discussion, but the derivation for a multimode case follows the same steps. The final result will therefore be straightforward to generalize to the multimode case.

The first step is to write down the action. As the initial state information is lost due

to coupling to the environment, the stationary state is independent of the actual choice of the initial state. The most convenient choice is a thermal state at inverse temperature  $\beta$ . As the contour adiabatically turns on the interactions the initial state is a product state between the system and environment such that the total initial state can be written as

$$\rho_0 = \rho_{a,0} \otimes \rho_{b,0}. \quad (2.103)$$

After rotating into the Keldysh basis, the action takes the form

$$\begin{aligned} \mathcal{S} = & \int \frac{d\omega}{2\pi} \begin{pmatrix} \bar{a}^c(\omega) \\ \bar{a}^q(\omega) \end{pmatrix}^T \begin{pmatrix} 0 & (G_a^A)^{-1}(\omega) \\ (G_a^R)^{-1}(\omega) & P_a^K(\omega) \end{pmatrix} \begin{pmatrix} a^c(\omega) \\ a^q(\omega) \end{pmatrix} \\ & + \sum_k \int \frac{d\omega}{2\pi} \begin{pmatrix} \bar{b}^c(\omega, k) \\ \bar{b}^q(\omega, k) \end{pmatrix}^T \begin{pmatrix} 0 & (G_b^A)^{-1}(\omega, k) \\ (G_b^R)^{-1}(\omega, k) & P_b^K(\omega, k) \end{pmatrix} \begin{pmatrix} b^c(\omega, k) \\ b^q(\omega, k) \end{pmatrix} \\ & + \sum_k \int \frac{d\omega}{2\pi} g_k \begin{pmatrix} \bar{b}^c(\omega, k) \\ \bar{b}^q(\omega, k) \end{pmatrix}^T \sigma_1 \begin{pmatrix} a^c(\omega) \\ a^q(\omega) \end{pmatrix} + \text{H.c.}, \end{aligned} \quad (2.104)$$

where the same symbols for the complex fields as for the operators in the Hamiltonian have been used. To arrive at this, we have taken advantage of the Hamiltonian being time-independent, such that the COT representation is independent of absolute time, and Fourier transformed the relative time. The environment propagators are the bare propagators similar to those in eq. (A.40) with the appropriate dispersions

$$\begin{aligned} G_b^R(\omega, k) &= \frac{1}{\omega - \epsilon_k + i0^+}, \\ G_b^K(\omega, k) &= -2i\pi \left(1 + 2n_B(\omega)\right) \delta(\omega - \epsilon_k), \end{aligned} \quad (2.105)$$

The interaction between the environment and the system has four possible vertex configurations, shown in fig. 2.6a. From this interaction, one can only construct one topology for the self-energy. The retarded and Keldysh self-energies are shown in fig. 2.6(b,c), and as there is no internal loop, we can directly read off their values

$$\begin{aligned} \Sigma_a^R(\omega) &= \sum_k |g_k|^2 G_b^R(\omega, k) = \sum_k |g_k|^2 \frac{1}{\omega - \epsilon_k + i0^+}, \\ \Sigma_a^K(\omega) &= \sum_k |g_k|^2 G_b^K(\omega, k) = -2i\pi \sum_k |g_k|^2 \coth\left(\beta \frac{\omega - \mu}{2}\right) \delta(\omega - \epsilon_k). \end{aligned} \quad (2.106)$$

The fact that there is only one topology of the self-energy, without any internal loops, is a manifestation of having the system coupling linearly to the environment. For such coupling, one can perform the Gaussian functional integral exactly. By using the self-energies

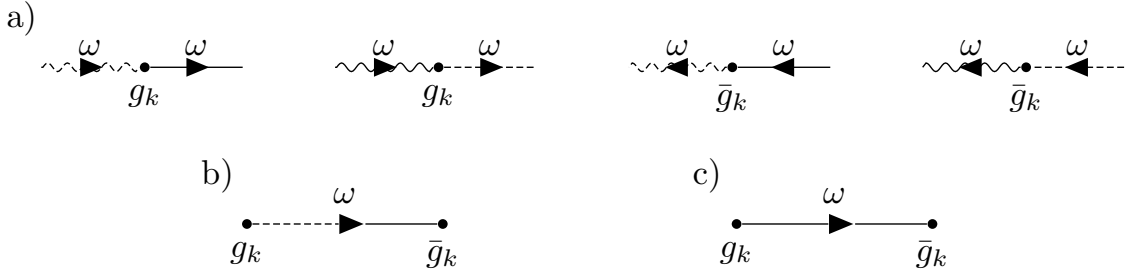


Figure 2.6: a) The different vertices arising from the interaction in eq. (2.104). The wavy line symbolizes the  $a$ -field, and the straight line the  $b$ -field. Here we have explicitly shown the vertex factor to highlight the connection to the Hermitian conjugation. The vertex is energy conserving as there is the same incoming and outgoing energy. b) The retarded self-energy for the system ( $a$ -field) and c) the Keldysh self-energy.

in eq. (2.106) and solving the Dyson equations in eq. (2.53) and eq. (2.81), one finds an exact solution for the propagators. Because the solution is exact, it also means that all non-Markovian effects are captured, which can be understood by considering the infinite Dyson series for the environment propagator. Here one sees that solving the Dyson equation is equivalent to using the fully dressed propagator for the environment. To capture the effect of the environment to the second order as in a Born-Markov approximation, we (would) use only the first term in the geometric series of the  $G^R$  in eq. (2.53), i.e.

$$G_a^R(\omega, k) \approx G_{a,0}^R(\omega, k) + G_{a,0}^R(\omega, k) \Sigma_a^R(\omega, k) G_{a,0}^R(\omega, k). \quad (2.107)$$

Computing the self-energies is straightforward as the environment is treated as a free system, making its spectral function a  $\delta$ -function. The sum over states is then equivalent to an integral over the spectral density

$$J(\omega) = \sum_k |g_k|^2 A_b(\omega, k) = \sum_k |g_k|^2 \delta(\epsilon_k - \omega). \quad (2.108)$$

The retarded self-energy is given by

$$\begin{aligned} \Sigma^R(\omega) &= \int_{-\infty}^{\infty} d\nu \frac{J(\nu)(\omega - \nu - i0^+)}{(\omega - \nu)^2 + (0^+)^2} \\ &= -i\pi J(\omega) + \mathcal{P} \int d\nu \frac{J(\nu)}{\omega - \nu}, \end{aligned} \quad (2.109)$$

with the details of the derivation shown in appendix B. As the self-energies have the same causal properties as the propagators, we can check that the retarded self-energies satisfy the Kramers-Kronig relation. Using the imaginary part in eq. (2.109) and eq. (2.64), one

finds that the real part of the retarded self-energy should be

$$\mathcal{P} \int \frac{d\omega' - \pi J(\omega')}{\pi \omega' - \omega} = \mathcal{P} \int d\omega' \frac{J(\omega')}{\omega - \omega'}, \quad (2.110)$$

which is exactly equal to the real part in eq. (2.109).

We have discussed that including the full self-energy in the Dyson equation leads to an exact solution. To get an effective theory at the same level as in the Lindblad equation, one can use the quasiparticle approximation in eq. (2.73) to zeroth order. In this case, the quasiparticle weight is one, and the self-energies simply lead to constant shifts of the real and imaginary part of the pole in the system's propagator. By truncating at zeroth order, we have effectively assumed that the self-energies are completely flat around the system's characteristic energy  $\omega_0$ . That is, the self-energies can be replaced with the zeroth order term

$$\Sigma_a^R(\omega) = \Sigma_a^R(\omega_0) + \mathcal{O}(\omega) = \sigma - i\gamma + \mathcal{O}(\omega), \quad (2.111)$$

where both  $\sigma$  and  $\gamma$  are real-valued. The imaginary part of the zeroth order term is equivalent to the vacuum rate for the non-unitary part in eq. (2.100), that one would compute from a Lindblad equation using the same approximations. Notice that the retarded self-energy has a negative imaginary part, and we define

$$\gamma = -\text{Im} \Sigma_a^R = \pi J(\omega_0) > 0. \quad (2.112)$$

The real part is equivalent to the Lamb shift, which is included in the effective Hamiltonian appearing in the unitary evolution of eq. (2.100).

For the Keldysh self-energy, we find

$$\begin{aligned} \Sigma_a^K(\omega) &= -i2\pi \int d\nu (1 + 2n_B(\omega)) J(\nu) \delta(\omega - \nu) \\ &= -i2\pi J(\omega) (1 + 2n_B(\omega)) \\ &= i2\gamma (1 + 2n_B(\omega_0)) + \mathcal{O}(\omega), \end{aligned} \quad (2.113)$$

where, in the last line, the thermal distribution function is expanded around the same energy as the retarded self-energy in eq. (2.111). Here we recognize the vacuum part and a contribution proportional to the environment's occupation at the system energy scale. We note that the corresponding broadening induced by the retarded self-energy is independent of the occupation of the environment. The physical understanding is that even when there is no occupation in the environment, it still gives rise to a decay channel

for the system. All the stimulated effects are thus captured through  $\delta\Sigma_a^K$

$$\begin{aligned}\delta\Sigma_a^K(\omega_0) &= \Sigma_a^K(\omega_0) - i2 \operatorname{Im} \Sigma_a^R(\omega_0, k) = i2\gamma(1 + 2n_B(\omega_0)) - i2\gamma \\ &= i2\gamma(2n_B(\omega_0)).\end{aligned}\tag{2.114}$$

As stated at the start of the section, we will use these results to model the optical cavity's decay into the electromagnetic vacuum field outside the cavity. For optical cavities, the typical resonant energies are on the order of hundreds of THz [79–81], which corresponds to  $10^{14}\text{s}^{-1}h/k_B \sim 5000\text{K}$ , with  $h$  ( $k_B$ ) being Planck's (Boltzmann's) constant. As the experiments are performed below or at room temperature, the background electromagnetic environment will, therefore, be unoccupied at the relevant frequencies.

Until now, only a fully flat spectral density has been considered. If the coupling to the environment is weak, one can take the  $\omega$  dependence of the imaginary part of the self-energy into account within the quasiparticle picture. This is consistent if the coupling is small enough such that  $\partial_\omega \operatorname{Re} \Sigma_a^R(\omega) \ll 1$  such that unit quasiparticle weight is still a good approximation. As shown in appendix B the Kramers-Kronig relation between the imaginary and real part of the self-energy implies

$$\partial_\omega \operatorname{Re} \Sigma_a^R(\omega) = \mathcal{P} \int \frac{d\nu}{\pi} \frac{\operatorname{Im} \Sigma_a^R(\omega) - \operatorname{Im} \Sigma_a^R(\nu)}{(\omega - \nu)^2}.\tag{2.115}$$

Therefore, it is justified to model a structured environment, such as the weak incoherent laser drive in chapter 5. To do this in practice, we choose a physical retarded self-energy, (one that obeys the causality structure), absorb the real part into our definition of the bare energies, and can then promote  $\gamma \rightarrow \gamma(\omega)$ . One can then check the validity of the approximation using the integral in eq. (2.115).

The microscopic derivation presented here has shown how to include dissipation and driving due to a linearly coupled environment. A pragmatic approach is to choose the rates and jump operators in the Lindblad equation phenomenologically, which also can be done for the self-energies. Lastly, it is worth pointing out that from a Lindblad master equation, one can directly derive a non-equilibrium action for the system [82].

## 2.9 Summary

In this chapter, we have described the structure of the quantum field theory for systems out of equilibrium. The fluctuation-dissipation relation between the retarded and the Keldysh propagator cannot be assumed a priori like in thermal equilibrium but instead results from the solution of two coupled, independent Dyson equations when the system is thermal.

From the non-equilibrium action, we have shown how one can directly derive the classical equations of motion for bosonic systems.

When the classical equations are not appropriate, we have explained how one can derive self-energies through diagrams and how the self-energies allow one to do infinite-order perturbation theory through the Dyson equation. It has been shown that the number of Feynman diagrams to be considered out of equilibrium is, in general, much larger, but the causality structure of the non-equilibrium field theory makes it possible to reduce this number and simplify the structure.

Lastly, we have discussed how effects like incoherent drive and dissipation can efficiently be included in the theory.

# Chapter 3

## Multimode polaritons

### 3.1 Introduction

This chapter investigates a cloud of ultracold bosonic atoms inside a cavity. The chapter is based on the work in [83]. We propose a method to generate polaritons consisting of multiple photonic modes. On the one hand, this is of fundamental interest because a macroscopic number of modes makes it possible to study thermodynamic phases of photons and complex types of order [84–94]. On the other hand, this is challenging because the necessary strong light-matter coupling is either achieved by confining the light in a cavity or using Rydberg atoms [95]. In both cases, the strongly coupled light modes are near-resonant with the excitations in the matter system. Achieving strong coupling to several modes requires a near-degenerate set of light modes. There are methods to achieve a set of near-degenerate cavity modes by fine tuning the cavity geometry [96,97], using a photonic crystal [98] or considering low dimensional systems [99] as we will do in chapter 5. All these methods are either experimentally challenging or possess limited tuneability.

Here we will overcome the large frequency splitting of the cavity modes by engineering the pump laser, which is already an essential element of the experimental setups considered here [81]. This idea has been demonstrated experimentally via Floquet engineering of Rydberg levels in a linear cavity without degenerate modes [100]. They consider a single cavity mode resonantly coupled to an atomic transition driven by an external laser. The strong coupling gives rise to a polariton where the matter component is the transition between the ground and the excited state of the atom. By modulating the laser, new effective atomic transitions are generated that are split by the modulation frequency. The splitting is chosen such that one of these transitions is near resonance with a second cavity mode. The interactions in the systems are then inherited from the atomic component of the polaritons. In their scheme, the matter component is an atomic transition dressed by

a Rydberg excitation. The large dipole moment of the Rydberg states leads to nonlinear mediated interactions between the photons [101].

We are interested in a different kind of polariton, namely one that emerges from coupling a cavity mode to the spatial motion of the atom cloud [102]. The matter part of this system is qualitatively different from that of ref. [100]. The qualitative difference becomes apparent by the fact that the ultracold gas, even in a single cavity mode setup, can exhibit a phase transition to a self-ordered state. The self-ordered state of the atoms is dual to the cavity field entering a superradiant state. The system is well-studied both experimentally [81, 103, 104] and theoretically [105–109] and possesses a large degree of tune-ability. Extending the system to many cavity modes [110, 111] can make it possible to explore an even larger plethora of phenomena, including quantum droplets [112], and quantum liquids [113]. Even including just a few cavity modes can lead to intriguing new features such as supersolid-like phases [114, 115], quasicrystals [116] and two-mode Dicke models [117].

Here we investigate how a phase modulation of the pump laser can make it experimentally possible to couple several cavity modes and how this affects the nature of the polariton below the superradiant threshold. We find that the phase modulation of the laser allows one to write down an effective model coupling many transverse cavity modes via their interaction with the atomic motion. The effective coupling between the modes and their detunings can be designed by tuning the phase modulation. This allows one to hybridize several cavity modes leading to multimode polaritons. The key to making this possible is a large separation of energy scales between the energy scale of the atomic motion and the energy scale of the cavity mode splitting.

## 3.2 Model and Hamiltonian

The system under consideration consists of a planar cavity with a cloud of ultracold atoms inside and is sketched in fig. 3.1.

The atoms are modeled in the simplest possible way, namely as two-level systems (TLS). The TLS approximation is valid because the frequency of the pump that drives the system is only close to one specific electronic transition.

The spatial extension of atoms is on the order of  $10^{-10}\text{m}$  [118], which should be compared to the pump wavelength. The pump is chosen to be close to resonance with the internal electronic transition from the ground state  $|g\rangle$  to the excited state  $|e\rangle$ , which requires a pump wavelength of the order of  $c2\pi/\omega_c \sim 10^{-7}\text{m}$ , with  $c$  being the speed of light in free vacuum. Therefore, we can assume a spatially constant pump field over the extent of one atom [119]. As the system is non-relativistic, we work in the Coulomb



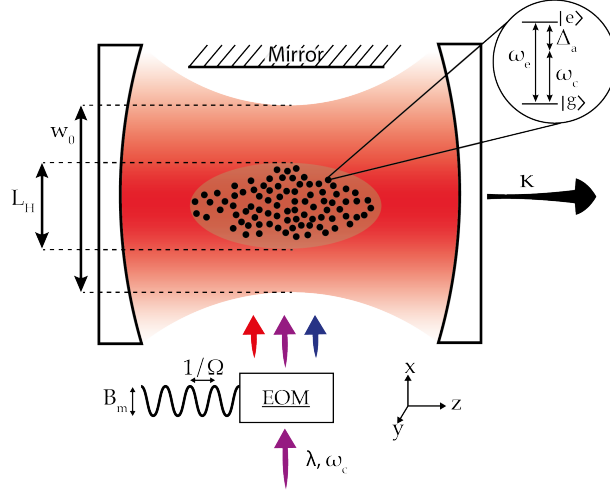


Figure 3.1: A sketch of the considered setup. It is composed of a linear cavity with a waist of  $w_0$ , filled with a cigar-shaped atom cloud with a diameter  $L_H$ . The atoms are modeled as two-level systems with energy splitting  $\omega_e$ . The cavity mirrors give rise to a loss of photons with the rate  $\kappa$  and to mitigate this loss, a transverse pump laser drives the atom cloud with a carrier frequency of  $\omega_c$  and an effective coupling to the atoms  $\lambda$ . The carrier frequency is detuned from the atomic transition by  $\Delta_a$ . Before impinging on the atoms, the pump is sent through an electro-optical modulator which generates a phase-modulation of the pump with frequency  $\Omega$  and amplitude  $B_m$ .

gauge, where the divergence of the electromagnetic vector field is zero. In this gauge, the atom-field interaction takes the form [37, 120]

$$H_{a-EM} = q_e \hat{\mathbf{r}} \cdot \mathbf{E}(\mathbf{r}_0, t), \quad (3.1)$$

where  $q_e$  is the charge of the electron,  $\hat{\mathbf{r}}$  is the operator for the electron position in relation to the position of the nucleus  $\mathbf{r}_0$  and  $\mathbf{E}(\mathbf{r}_0, t)$  is the time-dependent electric field at the position of the atom. This approximation is known as the dipole approximation and is the starting point for how we describe light-matter interaction throughout this thesis.

Because the atoms are modeled as independent TLSs, each atom's Hilbert space is described by a complete set of operators in the  $SU(2)$  group, and we choose the specific representation

$$\sigma^z = |e\rangle \langle e| - |g\rangle \langle g|, \quad \sigma^- = |g\rangle \langle e|, \quad \sigma^+ = |e\rangle \langle g|, \quad \mathbf{1} = |e\rangle \langle e| + |g\rangle \langle g|. \quad (3.2)$$

Experimentally the most commonly used atoms are those in the first group of the periodic system, such as Rubidium-87 [81]. These all possess spherically symmetric ground states, whereas the excited states are not spherically symmetric. Because the position operator

is odd, it can only have off-diagonal elements it does not couple states with the same symmetry [121]. Additionally, the position operator is Hermitian, and the off-diagonal components can be chosen as real; therefore, they must be identical. The representation of the dipole operator in the ground and excited state basis is then

$$q_e \hat{\mathbf{r}} = \mathbf{d} (\sigma^- + \sigma^+), \quad (3.3)$$

where  $\mathbf{d} = q_e \langle e | \hat{\mathbf{r}} | g \rangle = q_e \langle g | \hat{\mathbf{r}} | e \rangle$ .

The electric field is a sum of the pump and cavity fields. The pump field contains a macroscopic number of photons, making quantum fluctuations negligible. Under this approximation, the pump field is essentially classical and can be written as

$$\mathbf{E}_p(\mathbf{r}, t) = \mathbf{t} E_0 \eta_p(\mathbf{r}) \cos(\omega_c t + f(t)), \quad (3.4)$$

where  $\omega_c$  is the carrier frequency,  $E_0$  is the pump power,  $\mathbf{t}$  is a unit vector describing the pump polarization, and  $\eta_p$  is the pump's spatial profile. The phase modulation of the pump is described by  $f(t)$ , which is considered periodic with period  $T$  such that  $f(t+T) = f(t)$  and real.

We can not assume a large occupation for the cavity field and therefore have to consider the field's quantum nature. The quantized cavity field can be written as [37]

$$\mathbf{E}_c(\mathbf{r}, t) = \sum_{\mathbf{p}} \mathbf{t}_{\mathbf{p}} \sqrt{2\pi\omega_{\mathbf{p}}} (a_{\mathbf{p}}(t) + a_{\mathbf{p}}^\dagger(t)) u_{\mathbf{p}}(\mathbf{r}), \quad (3.5)$$

where  $a_{\mathbf{p}}$  ( $a_{\mathbf{p}}^\dagger$ ) is the bosonic annihilation (creation) operators for the  $\mathbf{p}$ 'th cavity mode with frequency  $\omega_{\mathbf{p}}$  and polarisation  $\mathbf{t}_{\mathbf{p}}$ . The cavity geometry determines the mode function  $u_{\mathbf{p}}$ . Here we consider a cavity in a near-planar configuration. This configuration is symmetric, as illustrated in fig. 3.1, and the radius of the mirrors  $R$  is large compared to the distance between the mirrors. When the mirrors are radially symmetric in the transverse plane ( $(x, y)$ -plane in fig. 3.1), the paraxial equation leads to the solution [79]

$$u_{q,j,p}(z, r, \theta) = \cos\left(\frac{qz}{L_z}\right) \text{LG}_{jp}(r/w_0, \theta), \quad (3.6)$$

where  $q$  is an integer that defines the number of longitudinal nodes, and  $L_z$  is the distance between the two mirrors. The waist of the cavity is given by  $w_0$  as sketched in fig. 3.1. The transverse degrees of freedom are described in polar coordinates with radius  $r$  and

angle  $\theta$ , and  $\text{LG}_{jp}(r, \theta)$  are the Laguerre-Gauss modes

$$\text{LG}_{jp}(r, \theta) = e^{-r^2 + ip\theta} \sqrt{\frac{j!}{(p+j)!}} (\sqrt{2r})^{|p|} L_j^{|p|}(2r^2), \quad (3.7)$$

where  $L_j^{|p|}(x)$  is the associated Laguerre polynomial of order  $j$ . The radial form of the mode is set by  $j$  while the angular distribution is determined by  $p$ , which represents the angular momentum of the field. The near-planar cavity has a large energy spacing between different longitudinal modes. This spacing is known as the free spectral range  $V_F$  and is set by the length of the cavity [80]

$$V_F = \frac{\pi c}{L_z}. \quad (3.8)$$

In comparison, the energy difference between different transverse modes is

$$\omega_T = 2V_F \sqrt{2L_z/R}, \quad (3.9)$$

which in the near-planar limit,  $L_z \ll R$ , is much smaller than  $V_F$ . The energy of the paraxial cavity modes can be written as a sum of these two energies [79]

$$\omega_{q,j,p} = V_F q + \omega_T (2j + p). \quad (3.10)$$

In this project, we seek to understand if coupling between different transverse modes is possible. To simplify the problem, the pump will later be approximated as not carrying any momentum similar to other works on similar systems [105–109, 122]. In these works, the higher-order transverse modes are not important because  $\omega_T$  ranges from hundred of MHz [81] to a few GHz [123], while the intrinsic energy scale of the atomic system is set by the recoil energy of the atoms which is on the order of tens of kHz [81, 123]. We will make the higher-order transverse modes energetically relevant through the pump modulation. However, because the pump mode is assumed spatially uniform, we will later explicitly show that it is only possible to couple between transverse modes with the same angular momentum. For our calculations, the transverse modes of interest will only be those with zero angular momentum described by  $\text{LG}_{j0}(r, \theta)$ . As they carry zero angular momentum, they are radially symmetric, and the first four transverse mode profiles are shown in fig. 3.2a. Their characteristic feature is that at the center ( $r = 0$ ), they are all unity and then decay for  $r > 0$ . The lowest-order mode is a Gaussian with a width determined by  $w_0$ , while the higher-order modes have an additional node for each higher order. For a near-planar cavity, the nodes in the higher-order modes lead to a narrow center peak and higher energy. The increased energy leads to the spectrum of the cavity

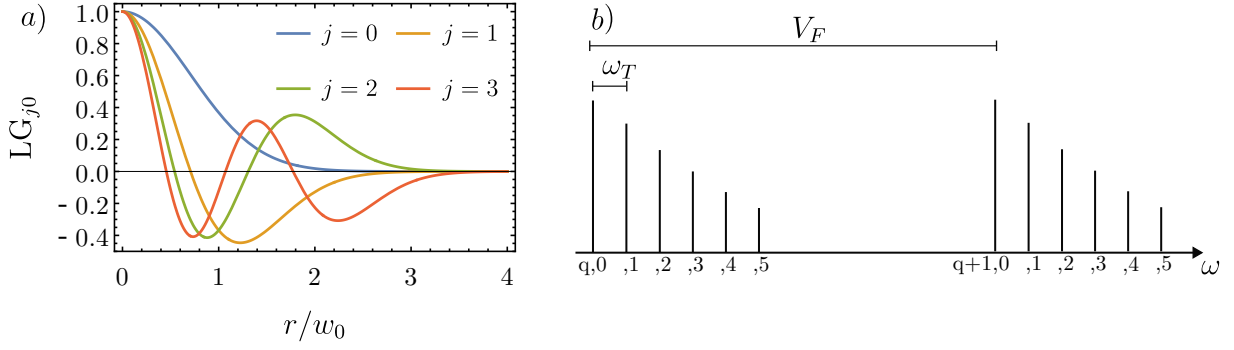


Figure 3.2: a) The radial dependence of the four first transverse cavity modes with zero angular momentum. b) The frequencies of the mode functions with  $q$  denoting the longitudinal mode and the second index, the transverse cavity modes.

having the lowest-order mode at the energy  $qV_F + \omega_T$  and higher-order modes sitting slightly higher in energy at  $qV_F + 2j\omega_T$  as shown in fig. 3.2b. The transverse splitting is  $2\omega_T$  because of the zero angular momentum nature of the modes as seen in eq. (3.10).

With both the electric field and the atomic dipole operator defined, the Hamiltonian for a single atom is

$$\begin{aligned}
 H = & \omega_e \sigma^+ \sigma^- + \sum_{\mathbf{p}} \omega_{\mathbf{p}} a_{\mathbf{p}}^\dagger a_{\mathbf{p}} \\
 & + (\sigma^+ + \sigma^-) \left( \lambda \eta_p(\mathbf{r}_0) e^{i\omega_c t + i f(t)} + \sum_{\mathbf{p}} g_{\mathbf{p}} u_{\mathbf{p}}(\mathbf{r}_0) a_{\mathbf{p}} + H.c. \right), \quad (3.11)
 \end{aligned}$$

where  $\lambda = E_0 \mathbf{d} \cdot \mathbf{t}$  is linear with the strength of the pump field and  $g_{\mathbf{p}} = 2\mathbf{d} \cdot \mathbf{t}_{\mathbf{p}} \sqrt{\omega_{\mathbf{p}} / L_z w_0^2}$  scales inversely with the square of the cavity volume. The composite index  $\mathbf{p} = (q, j, p)$  has been introduced to ease the notation.

The cavity mode functions have been explicitly included in the Hamiltonian, meaning that the only mode dependence in  $g_{\mathbf{p}}$  is due to the frequency of the cavity field and the polarization. Consistent with assuming the mirrors to be radially symmetric and perfectly aligned, we assume that the cavity modes can have any polarization. Together with our assumption of having  $|g\rangle$  being an S state and  $|e\rangle$  being a P state, this means that the cavity polarization will be set by the polarization of the pump  $\mathbf{t}_{\mathbf{p}} = \mathbf{t}$ . In that case, the coupling  $g_{q,j,p}$  is well approximated as independent of the transverse mode indices  $j, p$ . This approximation is valid because the energy scale of the cavity field is set by the frequency of the pump, which has its energy scale set by the splitting of the atomic energy levels. If we consider Rubidium-87 as an example, the relevant energy splitting is that of the D1 transition at 377 THz [118], which should be compared to the transverse mode spacing, which is usually less than 1 GHz. Even by considering transverse modes of order +100, the change in energy is still negligible compared to the total energy in the

cavity field such that  $g_{q,j,p} \approx g_q$ . For generality, we will keep the full mode dependence in  $g_{\mathbf{p}}$ , and only after having derived the general result will we simplify  $g_{\mathbf{p}}$ .

Due to the dipole coupling, the Hamiltonian contains terms that take energy from the electric field and use it to excite the atom and vice versa, but it also contains counter-rotating terms which excite the atoms and add energy to the electric field. Simultaneously, the reverse process of deexciting an atom and removing energy from the electric field is happening. Therefore each single counter-rotating process breaks energy conservation, but on average, the process of adding and removing energy happens equally often. The expectation value of the Hamiltonian is, therefore, still conserved. However, the counter-rotating processes evolve on a much shorter time scale than the co-rotating terms, such that on the time scale of the energy-conserving processes, the counter-rotating terms can often be neglected. This approximation is known as the rotating wave approximation (RWA). Consider the unitary transformation to the frame rotating with the pump carrier frequency

$$U_c = \bigotimes_{q,j} \exp \left( -i\omega_c t (\sigma^+ \sigma^- + a_{\mathbf{p}}^\dagger a_{\mathbf{p}}) \right). \quad (3.12)$$

As the transformation is time-dependent, the Hamiltonian in the rotating frame is [121]

$$H_r = U^\dagger H U - \omega_c \left( \sigma^+ \sigma^- + \sum_{\mathbf{p}} a_{\mathbf{p}}^\dagger a_{\mathbf{p}} \right). \quad (3.13)$$

Because the transformation is diagonal in the number basis, the creation and annihilation operators can directly be written in the rotating frame [120]

$$U^\dagger \sigma^+ U = e^{i\omega_c t} \sigma^+, \quad U^\dagger \sigma^- U = e^{-i\omega_c t} \sigma^-, \quad U^\dagger a_{\mathbf{p}}^\dagger U = e^{i\omega_c t} a_{\mathbf{p}}^\dagger, \quad U^\dagger a_{\mathbf{p}} U = e^{-i\omega_c t} a_{\mathbf{p}}. \quad (3.14)$$

The full Hamiltonian in the rotating frame is

$$H_r = \Delta_a \sigma^+ \sigma^- + \sum_{\mathbf{p}} \Delta_{\mathbf{p}} a_{\mathbf{p}}^\dagger a_{\mathbf{p}} + \left( \lambda \eta_p(\mathbf{r}_0) (\sigma^+ e^{-if(t)} + \sigma^+ e^{2i\omega_c t + if(t)}) \right. \\ \left. + \sum_{\mathbf{p}} g_{\mathbf{p}} u_{\mathbf{p}}(\mathbf{r}_0) (a_{\mathbf{p}} \sigma^+ + a_{\mathbf{p}}^\dagger \sigma^+ e^{2i\omega_c t}) + H.c. \right), \quad (3.15)$$

where the detunings  $\Delta_a = \omega_e - \omega_c$  and  $\Delta_{\mathbf{p}} = \omega_{\mathbf{p}} - \omega_c$  have been introduced. As discussed, the carrier frequency is on the order of hundreds of THz, whereas the largest detunings will be on the order of hundreds of GHz, making the RWA well justified.

To extend the TLS description to a large cloud of atoms, the atomic operators are

promoted to field operators [39]

$$\sigma^+ = |e\rangle \langle g| \rightarrow \int d^3\mathbf{r} \psi_e^\dagger(\mathbf{r}) \psi_g(\mathbf{r}), \quad (3.16)$$

where the field operators satisfy the bosonic commutation relations in eq. (2.17).

If there is occupation in the excited state, then bosonization does not give a good description of the physical system as it is necessary to constrain the Hilbert space of the bosons. Constraining the Hilbert space can be done using, for example, semionic methods [124, 125], or a hardcore boson approach [126].

For the experiments of interest, it is not necessary to constrain the Hilbert space because they essentially couple the light field to the motion of the ground-state atoms. Coupling the photon to the motion of the atoms can be achieved by having the pump far detuned from the electronic transition. The regime where the detuning  $\Delta_a$  between pump and atom is the largest energy scale is called the dispersive regime. In the dispersive regime, the excited state is only virtually excited, and the trapping potential and momentum of the excited state can be ignored. By bosonizing the TLS Hamiltonian in eq. (3.15) using eq. (3.16), the resulting many-body Hamiltonian in the rotating frame of the carrier frequency is

$$H = \int d^3\mathbf{r} \left\{ \psi_g^\dagger \left( -\frac{\nabla^2}{2m} + V_g(\mathbf{r}) - \mu_g \right) \psi_g + \psi_e^\dagger \Delta_a \psi_e + \psi_e^\dagger \left( \sum_{\mathbf{p}} g_q u_{\mathbf{p}}(\mathbf{r}) a_{\mathbf{p}} + \lambda \eta_p(\mathbf{r}) e^{-if(t)} \right) \psi_g + H.c. \right\} + \sum_{\mathbf{p}} \Delta_{\mathbf{p}} a_{\mathbf{p}}^\dagger a_{\mathbf{p}}, \quad (3.17)$$

where  $V_g(\mathbf{r})$  is the trapping potential of the ground state,  $\nabla^2 = (\partial_x^2 + \partial_y^2 + \partial_z^2)$  is spatial derivative operator,  $m$  is the mass of the atom and  $\mu_g$  is the chemical potential of the ground-state atoms. As the spatial argument of all atom fields is identical, it has been suppressed.

The atomic ground-state field is not diagonal in the spatial representation due to the spatial derivatives and the trapping potential, making it advantageous to solve the trapped ground-state atom problem first. To this extent, we consider a trapping potential that is symmetric and harmonic in the transverse plane and a long box trap in the longitudinal direction. In experiments, harmonic traps are used in all three directions, but the trap in the  $z$ -direction is much shallower than in the transverse directions, Therefore, the longitudinal length of the atomic cloud is much larger than the wavelength of the pump and cavity field [81]. In this case, the mode functions of the shallow harmonic trap have a similar overlap with the longitudinal cavity field as if the longitudinal trap was a box

trap. The resulting eigenvalue problem for the ground-state wave function  $\Psi_g(r, \phi, z)$  is

$$\left(-\frac{\partial_r^2}{2m} - \frac{1}{2mr}\partial_r - \frac{\partial_\theta^2}{2mr^2} + \frac{r^2}{2mL_H^4} - \frac{\partial_z^2}{2m}\right)\Psi_g(r, \theta, z) = E\Psi_g(r, \theta, z), \quad (3.18)$$

where  $L_H$  sets the transverse diameter of the atom cloud. The eigenvalue problem can be solved by separating the variables, and for the longitudinal part, the periodic boundary conditions with a trap of length  $L_z$  give rise to an exponential oscillation. The transverse part is a two-dimensional isotropic harmonic oscillator [127], which leads to the Laguerre-Gauss modes in eq. (3.7). The normalized ground-state atom wave function takes the form

$$\Psi_{\mathbf{n}}(r, \theta, z) = \langle \mathbf{r} | \Psi_{\mathbf{n}} \rangle = \frac{2e^{ikz}}{L_H\sqrt{2\pi L_z}} \text{LG}_{j,p}(r/L_H, \theta), \quad (3.19)$$

where  $\mathbf{n} = (k, j, p)$  is a composite index similar to the composite cavity index  $\mathbf{p}$ . The energy of the state is

$$E_{\mathbf{n}} = \frac{k^2}{2m} + \frac{1}{mL_H^2}(2j + p) - \mu_g, \quad (3.20)$$

where the zero-point energy has been absorbed into the chemical potential. The ground-state field operators can be expanded in the basis spanned by eq. (3.19)  $\psi_g(\mathbf{r}) = \sum_{\mathbf{n}} \Psi_{\mathbf{n}}(\mathbf{r})\psi_{\mathbf{n}}$ . As the spatial distributions of the excited state can be ignored in the dispersive regime, any complete basis can be chosen for the excited-state field operators  $\psi_e(\mathbf{r}) = \sum_{\mathbf{n}} \Phi_{\mathbf{n}}(\mathbf{r})\phi_{\mathbf{n}}$  [39]. The representation of the Hamiltonian from eq. (3.17) in these basis states is

$$H = \sum_{\mathbf{p}} \Delta_{\mathbf{p}} a_{\mathbf{p}}^\dagger a_{\mathbf{p}} + \sum_{\mathbf{n}, \mathbf{m}} \left\{ \delta_{\mathbf{n}, \mathbf{m}} \psi_{\mathbf{n}}^\dagger E_{\mathbf{n}} \psi_{\mathbf{m}} + \delta_{\mathbf{n}, \mathbf{m}} \phi_{\mathbf{n}}^\dagger \Delta_a \phi_{\mathbf{m}} \right. \\ \left. + \phi_{\mathbf{n}}^\dagger \left( \sum_{\mathbf{p}} g_{\mathbf{p}} \langle \Phi_{\mathbf{n}} | u_{\mathbf{p}} | \Psi_{\mathbf{m}} \rangle a_{\mathbf{p}} + \lambda \langle \Phi_{\mathbf{n}} | \eta_p | \Psi_{\mathbf{m}} \rangle e^{-if(t)} \right) \psi_{\mathbf{m}} + H.c. \right\}, \quad (3.21)$$

where the overlaps are

$$\langle \Phi_{\mathbf{n}} | u_{\mathbf{p}} | \Psi_{\mathbf{m}} \rangle = \int d^3\mathbf{r} \bar{\Phi}_{\mathbf{n}}(r, \theta, z) u_{\mathbf{p}}(r, \theta, z) \Psi_{\mathbf{m}}(r, \theta, z), \quad (3.22)$$

and

$$\langle \Phi_{\mathbf{n}} | \eta_p | \Psi_{\mathbf{m}} \rangle = \int d^3\mathbf{r} \bar{\Phi}_{\mathbf{n}}(r, \theta, z) \eta_p(r, \theta, z) \Psi_{\mathbf{m}}(r, \theta, z). \quad (3.23)$$

### 3.3 Non-equilibrium action

The Hamiltonian does not include the effect of photon loss from the cavity, which is intrinsic to the experimental setups. The cavity loss occurs because the mirrors are

not perfectly reflecting and has the advantage that it allows one to do non-destructive measurements of the system. To model the cavity loss theoretically, the cavity can be coupled to an electromagnetic vacuum environment. In section 2.8 we have shown how this can be included in the action by giving a constant imaginary contribution to the self-energies.

To construct the full non-equilibrium theory, the first step is to write the action based on the Hamiltonian in eq. (3.21). As discussed in chapter 2, this is done by putting the normal-ordered Hamiltonian on the contour in fig. 2.1 and then performing the Keldysh rotation on the contour fields. The non-interacting part of the action takes the form

$$\begin{aligned} \mathcal{S}_0 = \int \frac{d\omega}{2\pi} \left\{ \sum_{\mathbf{n}} (1 - \delta_{\mathbf{n},\mathbf{0}}) \begin{pmatrix} \bar{\psi}_{\mathbf{n}}^c \\ \bar{\psi}_{\mathbf{n}}^q \end{pmatrix}^T \begin{pmatrix} 0 & (G^A)_{g0}^{-1} \\ (G^R)_{g0}^{-1} & P_{g0}^K \end{pmatrix} \begin{pmatrix} \psi_{\mathbf{n}}^c \\ \psi_{\mathbf{n}}^q \end{pmatrix} \right. \\ \left. + \begin{pmatrix} \bar{\phi}_{\mathbf{n}}^c \\ \bar{\phi}_{\mathbf{n}}^q \end{pmatrix}^T \begin{pmatrix} 0 & (G^A)_{e0}^{-1} \\ (G^R)_{e0}^{-1} & P_{e0}^K \end{pmatrix} \begin{pmatrix} \phi_{\mathbf{n}}^c \\ \phi_{\mathbf{n}}^q \end{pmatrix} + \begin{pmatrix} \bar{a}_{\mathbf{p}}^c \\ \bar{a}_{\mathbf{p}}^q \end{pmatrix}^T \begin{pmatrix} 0 & (G^A)_{a0}^{-1} \\ (G^R)_{a0}^{-1} & P_{a0}^K \end{pmatrix} \begin{pmatrix} a_{\mathbf{p}}^c \\ a_{\mathbf{p}}^q \end{pmatrix} \right\}, \end{aligned} \quad (3.24)$$

where the previous operators are now complex fields, and the inverse bare propagators are given by

$$(G^R)_{\gamma 0}^{-1}(\omega, \mathbf{k}) = \omega - \mathcal{E}_{\gamma, \mathbf{k}} + i\Gamma_{\gamma, \mathbf{k}}, \quad P_{\gamma, \mathbf{k}}^K = i2\Gamma_{\gamma, \mathbf{k}} \quad (3.25)$$

with  $\mathcal{E}_{\gamma, \mathbf{k}} = (E_{\mathbf{k}}, \Delta_a, \Delta_{\mathbf{k}})$  being the different detunings and energies for  $\gamma \in \{g, e, a\}$  and  $\Gamma_{\gamma, \mathbf{k}} = (0^+, 0^+, \kappa_{\mathbf{k}})$  for the same three values of  $\gamma$ . The retarded propagator for the ground-state atoms in eq. (3.24) can be understood as describing density and phase fluctuations in the atomic cloud. Here we have assumed that the system is at zero temperature and that the spectral density of the electromagnetic environment is flat, as discussed in section 2.8. Through this environment, the cavity can lose photons with rate  $\kappa_{\mathbf{p}} > 0$ .

At zero temperature, all ground-state atoms will condense into the lowest energy mode and form a Bose-Einstein condensate (BEC) [128]. As described in section 2.6 this makes the action for the ground-state zero-energy mode unbounded, and it has to be separated out. This is done by the  $\delta$ -function factor in first line of eq. (3.24) and is equivalent to neglecting all quantum fluctuations in this mode  $\langle \psi_{\mathbf{0}}^c(\omega) \bar{\psi}_{\mathbf{0}}^q(\omega) \rangle = 0$  with  $\mathbf{0} = (0, 0, 0)$ . However, there is a finite occupation in the constant ( $\omega = 0$ ) part of the classical field component given by

$$\int d\omega \psi_{\mathbf{0}}^c(\omega)/2\pi = \int d\omega \sqrt{2N_0} \delta(\omega) = \sqrt{2N_0}, \quad (3.26)$$

with  $N_0$  being the number of atoms in the cloud.

With the bare action defined, the next step is to include interactions. For the interactions it is necessary to Fourier transform terms like  $e^{-if(t)} \bar{\phi}_{\mathbf{n}}(t) \psi_{\mathbf{m}}(t)$ . As  $f(t)$  was chosen



to be periodic with period  $T$ , the phase modulation can be written as a discrete Fourier series

$$e^{-if(t)} = \sum_{\alpha=-\infty}^{\infty} c_{\alpha} e^{-i\alpha\Omega t}, \quad (3.27)$$

with  $\Omega = T/2\pi$  and  $c_{\alpha}$  being the complex Fourier coefficients. Experimentally this can be generated using an electro-optical modulator, which makes the sum truncate at a finite value of  $\alpha$ . In practice, the largest value of  $\alpha_{\max}\Omega$  will always be much smaller than  $\Delta_a$ , such that the dispersive approximation is unaffected by the phase modulation. Because of the form of the phase modulation, the Fourier coefficients satisfy a sum rule

$$e^{-if(t)} e^{if(t)} = 1 = \sum_{\alpha,\beta} c_{\alpha} \bar{c}_{\beta} e^{-i\Omega t(\alpha-\beta)}, \quad (3.28)$$

and because all time-dependent terms have to cancel against each other, it implies that

$$\sum_{\alpha} |c_{\alpha}|^2 = 1. \quad (3.29)$$

With this representation of the phase modulation, the terms interacting with the pump can be Fourier transformed

$$\int dt e^{-if(t)} \bar{\phi}_{\mathbf{n}}(t) \psi_{\mathbf{m}}(t) = \sum_{\alpha} c_{\alpha} \int \frac{d\omega d\epsilon}{2\pi} \bar{\phi}_{\mathbf{n}}(\omega) \psi_{\mathbf{m}}(\epsilon) \delta(\omega - \alpha\Omega - \epsilon). \quad (3.30)$$

The remaining interaction term, where the atom is excited by absorbing a cavity photon, is energy conserving and given by

$$\int dt \bar{\phi}_{\mathbf{n}}(t) a_{\mathbf{p}}(t) \psi_{\mathbf{m}}(t) = \int \frac{d\omega d\epsilon d\rho}{(2\pi)^2} \bar{\phi}_{\mathbf{n}}(\omega) a_{\mathbf{p}}(\rho) \psi_{\mathbf{m}}(\epsilon) \delta(\omega - \epsilon - \rho). \quad (3.31)$$

Putting it all together, the interacting part of the action is found to be

$$\begin{aligned}
\mathcal{S}_I = & -\lambda \sum_{\mathbf{n}, \alpha} \int \frac{d\omega d\epsilon}{2\pi} \left( \sum_{\mathbf{m} \neq 0} \langle \Phi_{\mathbf{n}} | \eta_p | \Psi_{\mathbf{m}} \rangle c_{\alpha} \begin{pmatrix} \bar{\phi}_{\mathbf{n}}^c \\ \bar{\phi}_{\mathbf{n}}^q \end{pmatrix}_{\omega}^T \sigma^x \begin{pmatrix} \psi_{\mathbf{m}}^c \\ \psi_{\mathbf{m}}^q \end{pmatrix}_{\epsilon} \delta(\omega - \alpha\Omega - \epsilon) \right. \\
& \left. + \sqrt{2N_0} \langle \Phi_{\mathbf{n}} | \eta_p | \Psi_{\mathbf{0}} \rangle c_{\alpha} \bar{\phi}_{\mathbf{n}}^q(\omega) \delta(\epsilon) \delta(\omega - \alpha\Omega) + \text{H.c.} \right) \\
& - \sum_{\mathbf{n}, \mathbf{p}} \int \frac{d\omega d\epsilon d\rho}{(2\pi)^2} \frac{g_{\mathbf{p}}}{\sqrt{2}} \left( \sum_{\mathbf{m} \neq 0} \langle \Phi_{\mathbf{n}} | u_{\mathbf{p}} | \Psi_{\mathbf{m}} \rangle \phi_{\mathbf{n}}^{\gamma}(\omega) a_{\mathbf{p}}^{\alpha}(\rho) \psi_{\mathbf{n}}^{\beta}(\epsilon) M_{\alpha, \beta, \gamma} \delta(\omega - \epsilon - \rho) \right. \\
& \left. + \langle \Phi_{\mathbf{n}} | u_{\mathbf{p}} | \Psi_{\mathbf{0}} \rangle \begin{pmatrix} \bar{\phi}_{\mathbf{n}}^c \\ \bar{\phi}_{\mathbf{n}}^q \end{pmatrix}_{\omega} \sigma^x \begin{pmatrix} a_{\mathbf{p}}^c \\ a_{\mathbf{p}}^q \end{pmatrix}_{\rho} 2\pi \sqrt{2N_0} \delta(\epsilon) \delta(\omega - \rho) + \text{H.c.} \right), \tag{3.32}
\end{aligned}$$

where the condensed field component  $\psi_{\mathbf{0}}^c(\omega) = 2\pi\sqrt{2N_0}\delta(\omega)$  introduced in eq. (3.26) has been separated out. The tensor  $M_{\alpha, \beta, \gamma}$  is equal to the real off-diagonal Pauli matrix  $\sigma^x$  when  $\alpha = c$ , and equal to  $\mathbb{1}$  when  $\alpha = q$ . The Einstein summation convention has been used to indicate contraction over the repeated contour indices. The additional factor of  $1/\sqrt{2}$  in the cavity part arises from the Keldysh rotation of a three-field product.

The phase modulation of the pump leads to a shift in frequency by  $\alpha\Omega$ , and in the considered scheme,  $\Omega$  is comparable to the cavity mode splitting, which is much large than the energy scale of the motion of the atoms. To make the separation of energy scales as explicit as possible, all the energy integrals are split such that the integral over any function  $f(\omega)$  is written as

$$\begin{aligned}
\int_{-\infty}^{\infty} \frac{d\omega}{2\pi} f(\omega) &= \sum_{\alpha=-\infty}^{\infty} \int_{-\frac{\Omega}{2} + \alpha\Omega}^{\frac{\Omega}{2} + \alpha\Omega} \frac{d\omega}{2\pi} f(\omega) = \sum_{\alpha=-\infty}^{\infty} \int_{-\frac{\Omega}{2}}^{\frac{\Omega}{2}} \frac{d\omega}{2\pi} f(\omega + \alpha\Omega) \\
&= \sum_{\alpha=-\infty}^{\infty} \int_{-\frac{\Omega}{2}}^{\frac{\Omega}{2}} \frac{d\omega}{2\pi} f_{\alpha}(\omega), \tag{3.33}
\end{aligned}$$

where  $\omega$  is now only defined in the region  $\{-\Omega/2, \Omega/2\}$ , and we will refer to this as the quasienergy. We call the region where  $\alpha = 0$  the first Floquet Brillouin zone (FBZ). This rewriting is exact and can always be done. It is useful here because the pump is periodic in time, which means that taking one pump quanta (which we refer to as a Floquet photon) connects the first FBZ to the second FBZ. Taking two Floquet photons then connects the first FBZ to the third FBZ and so forth. The bare retarded propagator for the ground-state fluctuation in the  $\alpha$ th FBZ has a form

$$G_{g0, \mathbf{m}; \alpha}^R(\omega) = \frac{1}{\omega + \alpha\Omega - E_{\mathbf{m}} + i0^+}. \tag{3.34}$$

where the index  $\alpha$  refers to which FBZ the propagator belongs to. Because we are interested in low-energy physics at the scale of the motion of the atoms, we can neglect any contribution of order  $1/\Omega$ . The retarded propagator for the ground-state fluctuation is, therefore, zero outside of the first FBZ. For the excited state, we have assumed that  $\Delta_a \gg \Omega$  which means that the retarded propagator for the excited state has the same form in all FBZs. Due to the separation of energy scales, the bare propagators take the form

$$\begin{aligned}
G_{g0,\mathbf{n};\alpha}^R(\omega) &= \delta_{\alpha,0} (\omega - E_{\mathbf{n}} + i0^+)^{-1}, \quad \mathbf{n} \neq \mathbf{0} \\
G_{g0,\mathbf{n};\alpha}^K(\omega) &= -i\delta_{\alpha,0} 2\pi\delta(\omega - E_{\mathbf{n}}), \quad \mathbf{n} \neq \mathbf{0} \\
G_{e0,\mathbf{m};\alpha}^R(\omega) &= (-\Delta_a + i0^+)^{-1}, \\
G_{e0,\mathbf{m};\alpha}^K(\omega) &= -i2\pi\delta(\omega + \alpha\Omega - \Delta_a), \\
G_{a0,\mathbf{p};\alpha}^R(\omega) &= (\omega + \alpha\Omega - \Delta_{\mathbf{p}} + i\kappa_{\mathbf{p}})^{-1}, \\
P_{a0,\mathbf{p};\alpha}^K(\omega) &= i2\kappa_{\mathbf{p}}.
\end{aligned} \tag{3.35}$$

Because there is no occupation in neither the excited state nor the ground-state fluctuations (modes with  $\mathbf{n} \neq 0$ ), the atom Keldysh propagators are given by the bare spectral functions as shown in eq. (2.82). For the cavity, the Keldysh element in the action and the imaginary part of the retarded propagator are given by the loss rate of the mode as described in eq. (3.25).

For completeness, we also give the form of the interacting part of the action in its FBZ form

$$\begin{aligned}
\mathcal{S}_I &= -\lambda \sum_{\mathbf{n},\alpha} \int \frac{d\omega}{2\pi} \left( \sum_{\mathbf{m} \neq \mathbf{0}} \langle \Phi_{\mathbf{n}} | \eta_p | \Psi_{\mathbf{m}} \rangle c_{\alpha} \begin{pmatrix} \bar{\phi}_{\mathbf{n};\alpha}^c \\ \bar{\phi}_{\mathbf{n};\alpha}^q \end{pmatrix}_{\omega}^T \sigma^x \begin{pmatrix} \psi_{\mathbf{m};0}^c \\ \psi_{\mathbf{m};0}^q \end{pmatrix}_{\omega} \right. \\
&\quad \left. + \sqrt{2N_0} \langle \Phi_{\mathbf{n}} | \eta_p | \Psi_{\mathbf{0}} \rangle c_{\alpha} \bar{\phi}_{\mathbf{n};\alpha}^q(\omega) \delta(\epsilon) \delta(\omega) + \text{H.c.} \right) \\
&\quad - \sum_{\mathbf{n},\mathbf{p},\alpha} \int \frac{d\omega d\epsilon}{(2\pi)^2} \frac{g_{\mathbf{p}}}{\sqrt{2}} \left( \sum_{\mathbf{m} \neq \mathbf{0}} \langle \Phi_{\mathbf{n}} | u_{\mathbf{p}} | \Psi_{\mathbf{m}} \rangle \phi_{\mathbf{n};\alpha}^{\tilde{\gamma}}(\omega + \epsilon) a_{\mathbf{p};\alpha}^{\tilde{\alpha}}(\omega) \psi_{\mathbf{n};0}^{\tilde{\beta}}(\epsilon) M_{\tilde{\alpha},\tilde{\beta},\tilde{\gamma}} \right. \\
&\quad \left. + \langle \Phi_{\mathbf{n}} | u_{\mathbf{p}} | \Psi_{\mathbf{0}} \rangle \begin{pmatrix} \bar{\phi}_{\mathbf{n};\alpha}^c \\ \bar{\phi}_{\mathbf{n};\alpha}^q \end{pmatrix}_{\omega} \sigma^x \begin{pmatrix} a_{\mathbf{p};\alpha}^c \\ a_{\mathbf{p};\alpha}^q \end{pmatrix}_{\omega} 2\pi\sqrt{2N_0}\delta(\epsilon) + \text{H.c.} \right),
\end{aligned} \tag{3.36}$$

where all energy integrals are finite and cover a single FBZ.

### 3.4 Self-energies

With the bare propagators in eq. (3.35) and the interactions in eq. (3.36) we can derive an approximation for the self-energies. As the excited state is far detuned, any self-energy

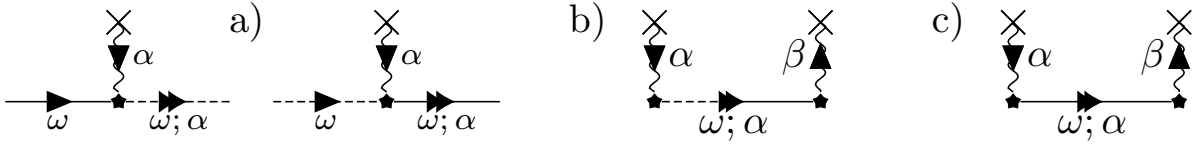


Figure 3.3: In a) the two vertices generated by the pump interaction in eq. (3.36) are shown. The Hermitian conjugate terms correspond to flipping the direction of the arrows. The ground-state atom is a line with a single arrow, while a double arrow indicates the excited state. The pump is characterized by a wavy line that ends/starts in a cross to denote its source field nature. A dashed line represents a quantum field, and a solid line a classical field. The line label denotes the energy of the propagator, and the semicolon separates the quasienergy from the Floquet index  $\alpha$  ( $\beta$ ). The star denotes the vertex, which has the value  $-i\lambda c_\alpha \langle \Phi_{\mathbf{n}} | \eta_p | \Psi_{\mathbf{m}} \rangle$ . In b) the diagram for the retarded self-energy  $\Sigma_{g;\alpha-\beta,0}^R(\omega)$  for the ground state atom is shown while c) is the diagram determining the ground state's Keldysh self-energy  $\Sigma_{g;\alpha-\beta,0}^K(\omega)$ .

correction to it can be ignored.

### 3.4.1 Stark shift

The first effect we will consider is the self-energy correction to the ground-state energy due to the pump. The vertices constructed from the interacting part of the action are shown in fig. 3.3a. As the interaction is quadratic in fields, only one self-energy type is possible, as discussed in section 2.8. A consequence of the phase modulation of the pump is that the self-energies couple different FBZs as illustrated by the retarded self-energy in fig. 3.3b. The corresponding mathematical expression for the retarded self-energy is read off from fig. 3.3b following the prescription discussed in section 2.4.2. To make the process clearer, all the factors involved in this diagram are written out, and for the retarded self-energy, we find

$$\begin{aligned} \Sigma_{g;\mathbf{m},\mathbf{n};\alpha-\beta,0}^R(\omega) &= (-1)(-i)(-i\lambda)^2 \\ &\quad \times \sum_{\mathbf{j}} c_\alpha \bar{c}_\beta \langle \Psi_{\mathbf{m}} | \bar{\eta}_p | \Phi_{\mathbf{j}} \rangle \langle \Phi_{\mathbf{j}} | \eta_p | \Psi_{\mathbf{n}} \rangle iG_{e0,\mathbf{j};\alpha}^R(\omega) \\ &= - \frac{\lambda^2 c_\alpha \bar{c}_\beta \langle \Psi_{\mathbf{m}} | \bar{\eta}_p \eta_p | \Psi_{\mathbf{n}} \rangle}{\Delta_a}. \end{aligned} \quad (3.37)$$

The self-energy, represented by fig. 3.3b, should be interpreted as a motional ground-state fluctuation in mode  $\mathbf{n}$  and at energy  $\omega$  is excited by the pump containing  $\alpha$  Floquet photons. The excitation is then transferred to the excited state, where it propagates with energy  $\omega + \alpha\Omega$  until the excited state decays by emitting  $\beta$  Floquet photons into the pump, and goes into the motional ground-state fluctuation  $\mathbf{m}$  in the  $\alpha - \beta$  FBZ with quasienergy  $\omega$ . Being in the dispersive regime makes all the excited state modes degenerate and allows

one to resum the excited-state spatial basis and write the retarded propagator as  $-1/\Delta_a$ , which has been done to get to the second line in eq. (3.37).

Using the self-energy in the Dyson equation eq. (2.53) for the retarded propagator, is equivalent to the infinite summation in eq. (2.49). The full retarded propagator for the density fluctuations in the ground-state atoms can therefore be written as the infinite series

$$G_{g,\mathbf{m},\mathbf{n};\alpha-\beta,0}(\omega, \epsilon) = \delta_{\mathbf{n},\mathbf{m}}\delta_{\alpha-\beta,0}\delta(\omega - \epsilon)G_{g0,\mathbf{n};0}(\omega) + G_{g0,\mathbf{m};\alpha-\beta}(\omega)\delta(\omega - \epsilon)\Sigma_{g,\mathbf{m},\mathbf{n};\alpha-\beta,0}^R(\omega)G_{g0,\mathbf{n};0}(\omega) + \dots \quad (3.38)$$

The first term is the bare propagator from eq. (3.35) which is only important within the first FBZ. The next term couples a bare mode with quasienergy  $\omega$  in the first FBZ with another bare mode with the same quasienergy but in the  $(\alpha - \beta)$ th FBZ. In section 3.3 it was shown that the bare propagator scales as  $1/\alpha\Omega$  in the  $\alpha$ th FBZ. This means that the value of the self-energy in eq. (3.37) has to be comparable to  $\Omega$  for the self-energy to be able to couple different FBZs. As  $\lambda^2/\Delta_a \ll \Omega$ , this is not possible. The higher-order terms in eq. (3.38) decay even faster, such that the only part of the self-energy in eq. (3.37) that has to be considered is the part that couples within the first FBZ, namely the  $\alpha = \beta$  part. The ground-state propagator then becomes independent of  $\alpha$ , and one can sum over  $\alpha$  directly at the level of the self-energy

$$\Sigma_{g,\mathbf{n},\mathbf{m}}^R(\omega) = -\sum_{\alpha} \frac{\lambda^2 |c_{\alpha}|^2 \langle \Psi_{\mathbf{m}} | \eta_p \bar{\eta}_p | \Psi_{\mathbf{n}} \rangle}{\Delta_a} = -\frac{\lambda^2 \langle \Psi_{\mathbf{m}} | \bar{\eta}_p \eta_p | \Psi_{\mathbf{n}} \rangle}{\Delta_a} = -\delta_{\mathbf{n},\mathbf{m}} \frac{\lambda^2}{\Delta_a}. \quad (3.39)$$

Here the sum rule for the coefficients in eq. (3.29) and the constant pump spatial profile have been used. The retarded self-energy correction due to the pump, therefore, simplifies to a constant Stark shift similar to the single mode case [109]. As the Stark shift is a constant, the overall shift of the energies can be absorbed in the effective chemical potential  $\mu_g$  and has no further effect on the theory.

For the Keldysh self-energy shown in fig. 3.3c, we find

$$\Sigma_{g,\mathbf{n},\mathbf{m};\alpha-\beta,0}^K(\omega) = \lambda^2 c_{\alpha} \bar{c}_{\beta} \langle \Psi_{\mathbf{m}} | \bar{\eta}_p \eta_p | \Psi_{\mathbf{n}} \rangle 2\pi\delta\left(\omega + (\alpha - \beta)\Omega - \Delta_a\right), \quad (3.40)$$

which is zero because the system is in the dispersive regime where  $\omega + (\alpha - \beta)\Omega \ll \Delta_a$ , such that the  $\delta$ -function can never be evaluated on-shell.

### 3.4.2 Cavity self-energy

Having shown that the pump modulation does not modify the ground-state atoms, we now consider the key quantity, namely the retarded self-energy for the cavity photons. The vertices corresponding to the atom-cavity interaction in eq. (3.36) are identical to the four

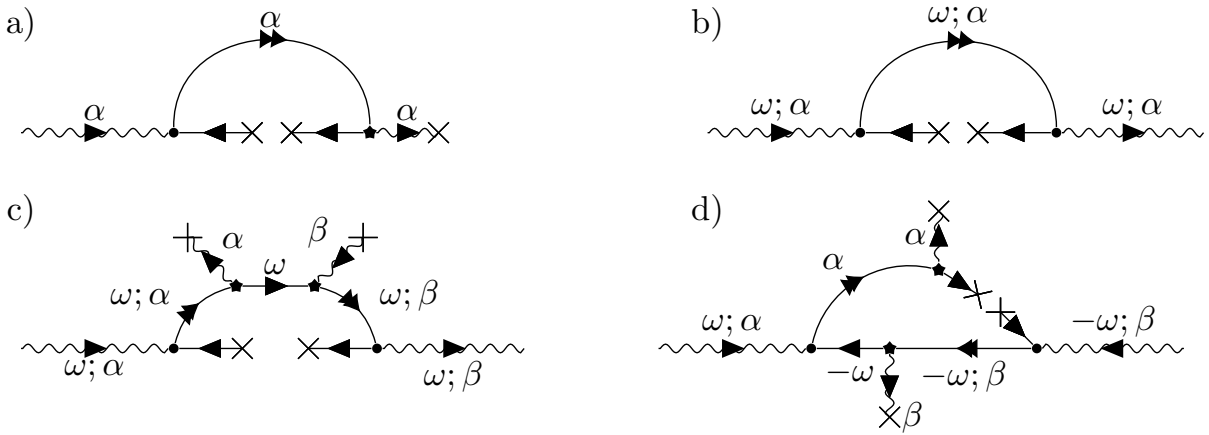


Figure 3.4: *The different retarded self-energies for the cavity, up to second order in the cavity coupling. The cavity is drawn as a wiggly line and the BEC as a ground-state line terminating/starting at a cross. The circle vertex is the cavity vertex with the value  $-ig_p \langle \Phi_n | u_p | \Psi_m \rangle / \sqrt{2}$ . The other components are drawn similarly as in fig. 3.3, and  $\alpha$  and  $\beta$  are the Floquet Brillouin zone indices. All the conjugate processes of the diagrams drawn here can be found by flipping the arrows' direction. The external cavity legs have been explicitly drawn to make the diagrams easier to interpret. a) First-order process in cavity coupling. b) The two-cavity-photon process, which is second order in the cavity coupling. c) The "normal" scattering process, which is second order in cavity coupling but includes the pump. d) An "anomalous" scattering process of the same order as c.*

vertices in fig. 2.5, with the photon being a wavy line and the atoms drawn as in fig. 3.3. Because none of the internal fields (excited state and ground-state motional fluctuations) have any occupation, many of the diagrams with different Keldysh configurations end up canceling out against each other, as discussed in section 2.7. In the remaining diagrams, all internal propagators are either advanced or retarded, and the only occupation effects come from the BEC source field in eq. (3.26) and the pump. The possible diagrams contributing to the retarded cavity self-energy up to second order in the cavity coupling are shown in fig. 3.4. None of the diagrams contains closed loops because the BEC acts as a source field.

One of the main advantages of the diagrammatic approach is that the diagrams clearly illustrate the physical processes. It shows that the full system, including the pump, is energy conserving, as the total energy going out of a diagram equals the incoming energy.

To discuss the physical processes, we will focus on the diagrams shown in fig. 3.4, as the processes in the conjugate diagrams are equivalent except for happening in the opposite order. To clarify this, consider the simplest process that affects the cavity shown in fig. 3.4a. Here the cavity excites an atom from the BEC, which goes back to the BEC by emitting into the pump. The conjugate process is where the pump excites the atom,

which then emits into the cavity. It gives the self-energy contribution

$$\begin{aligned}\Sigma_{a1,\mathbf{p};\alpha}^R(\omega) &= -\delta(\omega) \frac{2N_0\lambda g_{\mathbf{p}}\bar{c}_\alpha}{\sqrt{2}\Delta_a} \sum_{\mathbf{n}} \langle \Psi_{\mathbf{0}} | \bar{\eta}_p | \Phi_{\mathbf{n}} \rangle \langle \Phi_{\mathbf{n}} | u_{\mathbf{p}} | \Psi_{\mathbf{0}} \rangle \\ &= -\delta(\omega) \frac{2N_0\lambda g_{\mathbf{p}}\bar{c}_\alpha}{\sqrt{2}\Delta_a} \langle \Psi_{\mathbf{0}} | \bar{\eta}_p u_{\mathbf{p}} | \Psi_{\mathbf{0}} \rangle,\end{aligned}\quad (3.41)$$

which we have denoted as  $a1$  to differentiate it from the other diagrams in fig. 3.4. The value of the self-energy is determined by overlaps of the mode functions from eq. (3.6) and eq. (3.19)

$$\langle \Psi_{\mathbf{n}} | \bar{\eta}_p u_{\mathbf{p}} | \Psi_{\mathbf{n}} \rangle = \frac{2}{L_z L_H} \int_{-L_z/2}^{L_z/2} dz e^{ikz} \cos\left(\frac{qz}{L_z}\right) e^{-ikz} \int dz_{\perp} f_{\perp}, \quad (3.42)$$

The second integral is over the transverse direction, perpendicular to  $z$ . For a near-planar cavity  $V_F/\omega_T \gg 1$  such that the only longitudinal cavity mode that is energetically relevant is the one closest to the carrier frequency. The longitudinal index for the cavity is therefore set by  $q/L_z = Q$  with  $L_z Q V_F \sim \omega_c$ . Because the pump carries no longitudinal momentum, the longitudinal overlap in eq. (3.42) always vanishes, and the self-energy in eq. (3.41) will be zero.

The next diagram contributing to the cavity self-energy is the two-cavity-photon process shown in fig. 3.4b. In this process, the cavity virtually excites an excited state which then decays by emitting into the cavity again. No pump photons are involved in the process, meaning it is impossible to connect different FBZs, and the self-energy contribution is therefore diagonal in frequency and the cavity mode space

$$\Sigma_{a2,\mathbf{p},\mathbf{q};\alpha}(\omega) = \frac{N_0 g_{\mathbf{p}}^2}{\Delta_a} \langle \Psi_{\mathbf{0}} | u_{\mathbf{p}} \bar{u}_{\mathbf{p}} | \Psi_{\mathbf{0}} \rangle. \quad (3.43)$$

These mode overlaps do not vanish and the diagram is proportional to  $N_0 g_{\mathbf{p}}^2/\Delta_a$ . We assume a regime where the prefactor is small enough such that these processes are weak compared to the process in fig. 3.4c. In fig. 3.4c the cavity mode with energy  $\omega + \alpha\Omega$  excites an atom from the BEC, which then emits  $\alpha$  Floquet photons into the pump and generates a low energy density fluctuation in the BEC at energy  $\omega$ . An atom from this density fluctuation is then excited using  $\beta$  Floquet photons from the pump. The excited atom then decays back to the homogeneous BEC via emission into the cavity mode at  $\omega + \beta\Omega$ . This process dominates over the two-cavity-photon process because the pump vertex scales with the pump intensity and can therefore make up for the smallness of  $g_{\mathbf{p}}$ . For such a process to be experimentally possible, the polarization of the pump must overlap with the polarization of the cavity. This requirement can be understood from

the diagram by the fact that the diagram connects a pump vertex and a cavity vertex through an excited state. The pump vertex and the cavity vertex are, therefore, implicitly connected

$$\lambda g_{\mathbf{p}} \propto (\mathbf{t} \cdot \mathbf{d}) (\mathbf{d} \cdot \mathbf{t}_{\mathbf{p}}) = \mathbf{t} \cdot \langle g | \mathbf{r} | e \rangle \langle e | \mathbf{r} | g \rangle \cdot \mathbf{t}_{\mathbf{p}}. \quad (3.44)$$

For this to be non-zero, the pump and cavity polarizations must have non-zero overlap with the same excited state, and they must, therefore, also overlap with each other.

Because the diagram in fig. 3.4c contains the pump, it allows for coupling between different FBZs by using different Floquet photons. This coupling leads to the retarded self-energy not being diagonal in the Floquet indices  $\alpha$  and  $\beta$

$$\tilde{\Sigma}_{a,\mathbf{q},\mathbf{p};\beta,\alpha}^R(\omega) = \frac{N_0 g_{\mathbf{p}} g_{\mathbf{q}} \lambda^2 \bar{c}_{\alpha} c_{\beta}}{\Delta_a^2} \sum_{\mathbf{n}} \langle \Psi_{\mathbf{0}} | \eta_{\mathbf{p}} \bar{u}_{\mathbf{q}} | \Psi_{\mathbf{n}} \rangle G_{g_{\mathbf{0};\mathbf{n}}}^R(\omega) \langle \Psi_{\mathbf{n}} | u_{\mathbf{p}} \bar{\eta}_{\mathbf{p}} | \Psi_{\mathbf{0}} \rangle. \quad (3.45)$$

To evaluate the contribution of this process, the following overlap is required,

$$\langle \Psi_{\mathbf{n}} | u_{\mathbf{p}} \bar{\eta}_{\mathbf{p}} | \Psi_{\mathbf{0}} \rangle = \langle \Psi_{\{k,n,j\}} | u_{\{Q,m,p\}} \bar{\eta}_{\mathbf{p}} | \Psi_{\{0,0,0\}} \rangle = \mathcal{I}_{z,\{k,Q,0\}} \mathcal{I}_{\theta,\{j,p,0\}} \mathcal{I}_{r,\{j,p,0,n,m,0\}}, \quad (3.46)$$

where the composite mode number has been explicitly written out, and the integral has been split into longitudinal, angular, and radial parts. Splitting the overlap into these three parts is possible because the spatial mode functions in eq. (3.6) and eq. (3.19) are separable in their arguments. Using the mode functions, we consider each of these different integrals, the first being the longitudinal overlap

$$\mathcal{I}_{z,\{k,Q,0\}} = \frac{2}{L_z} \int_{-L_z/2}^{L_z/2} dz e^{ikz} \cos(Qz) = \begin{cases} 1 & \text{if } k = Q \\ 0 & \text{otherwise} \end{cases}, \quad (3.47)$$

which shows that the longitudinal pattern of the density fluctuation has to match the periodicity of the longitudinal cavity mode. The radial integral is given by

$$\mathcal{I}_{\theta,\{j,p,0\}} = \int_0^{2\pi} \frac{d\theta}{2\pi} e^{i\theta(p-j)} = \delta_{p,j}, \quad (3.48)$$

which is a manifestation of the conservation of angular momentum. For the diagram in fig. 3.4c, the overlap appears twice with different cavity modes but the same ground-state fluctuation. Two cavity modes can, therefore, only couple to each other if they do so through the same density fluctuation, which, due to eq. (3.48), requires them to have the same angular momentum. By choosing  $\Omega \sim 2\omega_T$  and having the carrier frequency close to the Gaussian cavity mode, the non-zero angular momentum modes will have a large energy suppression and can therefore be neglected.



The only remaining overlap is in the radial direction and given by

$$\mathcal{I}_{r,\{0,0,0,n,m,0\}} = \frac{1}{L_H^2} \int_0^\infty dr r \exp\left(-r^2(2L_H^{-2} + w_0^{-2})\right) L_n\left(2\frac{r^2}{L_H^2}\right) L_m\left(2\frac{r^2}{w_0^2}\right). \quad (3.49)$$

This integral has a closed form solution [129, 7.414.4]

$$\mathcal{I}_{r,\{0,0,0,n,m,0\}} = \frac{\Gamma(m+n+1)}{2^n n! m!} \frac{(\chi^2 - \frac{1}{2})^m}{(\chi^2 + \frac{1}{2})^{m+n+1}} {}_2F_1\left[-n, -m; -n-m; -\frac{\chi^2 + \frac{1}{2}}{\chi^2 - \frac{1}{2}}\right], \quad (3.50)$$

with  $\chi = w_0/L_H$ ,  ${}_2F_1$  is the Gauss hypergeometric function and  $\Gamma$  being the Gamma function. These overlaps are fully determined by  $\chi$  and are always real. Any further physical insight from the closed-form expression is elusive. However, in the limit where the atom cloud is significantly narrower than the cavity waist, we have  $\chi^2 \gg \frac{1}{2}$ , which leads to

$$\lim_{\chi \rightarrow \infty} \langle \Psi_{k,n,0} | u_{Q,m,0} \bar{\eta}_p | \Psi_0 \rangle = \delta_{n,0} \delta_{k,Q}. \quad (3.51)$$

The physical interpretation of this result is that for an atom cloud with a small transverse size compared to the cavity, all zero-angular momentum transverse cavity modes appear constant and equal to unity. This is intuitively seen from the plot of the radial mode functions in fig. 3.2a. In this limit, the density fluctuation is only along the longitudinal direction while the transverse envelope is Gaussian-like the BEC. As near-planar cavities have fairly large waists on the order of  $50\mu\text{m}$  [123] and experimentally, the atom cloud is usually on the order of  $3\mu\text{m}$  [81], the small atom cloud limit is experimentally relevant. Although there is no fundamental problem with going beyond this limit from a theoretical perspective, we restrict the following discussion to the small atom-cloud limit, as it considerably simplifies our expressions.

The self-energy contribution from fig. 3.4c takes the simple form

$$\tilde{\Sigma}_{a,n,m;\beta,\alpha}^R(\omega) = \frac{N_0 g^2 \lambda^2 \bar{c}_\alpha c_\beta}{\Delta_a^2} G_{g0;\{Q,0,0\}}^R(\omega), \quad (3.52)$$

where  $n, m$  are only transverse cavity mode indices for zero-angular momentum modes with longitudinal wave vector  $Q$ . Because the longitudinal cavity mode is locked to  $Q$  by the pump  $g_p$  has been simplified to be mode independent as discussed in section 3.2.

The process in fig. 3.4c is not the total contribution to the self-energy because it is also possible to switch the position of the condensate and the ground-state density fluctuation in fig. 3.4c. By drawing the diagram, one finds that the ground-state density fluctuation will propagate in the opposite direction and carry the energy  $-\omega$ . All other aspects remain the same, such that these two diagrams can be added together to give the full self-energy

contribution

$$\begin{aligned}\Sigma_{a,n,m;\alpha,\beta}^R(\omega) &= \frac{N_0 g^2 \lambda^2 \bar{c}_\alpha c_\beta}{\Delta_a^2} \left( G_{g0;\{Q,0,0\}}^R(\omega) + G_{g0;\{Q,0,0\}}^A(-\omega) \right) \\ &= \frac{2E_r N_0 g^2 \lambda^2 \bar{c}_\alpha c_\beta}{\Delta_a^2 \left( (\omega + i0^+)^2 - E_r^2 \right)} = -\Lambda^2 \bar{c}_\alpha c_\beta \Pi^R(\omega),\end{aligned}\quad (3.53)$$

where the recoil energy  $E_r = Q^2/2m$  has been introduced. All constants have been included in the prefactor  $\Lambda = \sqrt{N_0} g \lambda / \Delta_a$ , which is the effective light-matter coupling constant. The polariton in the ultracold atomic gas is, therefore, strongly interacting because of an enhancement by the number of atoms in the cloud and the power in the external laser. The  $\omega$ -dependence of the self-energy is captured in the single mode polarization function

$$\Pi^R(\omega) = \frac{-2E_r}{(\omega + i0^+)^2 - E_r^2}.\quad (3.54)$$

Beyond the limit of a small atom cloud,  $\Pi^R$  acquires a mode dependence due to the atoms coupling differently to the transverse modes.

The self-energy in eq. (3.53) has the normal structure expected from a self-energy; a cavity mode comes in, is then modified, and sent out again. As the system is driven, one can also build diagrams of the form shown in fig. 3.4d, where two cavity photons come in and are then lost into the pump. These processes are known in superconductivity as anomalous terms and are not number conserving [61]. Differently from the counter-rotating terms discussed for the rotating wave approximation in section 3.2, the anomalous processes are not linked to a different energy scale than the "normal" process in fig. 3.4c. By writing out the diagram and using the same approximation used for deriving eq. (3.53), one finds that the anomalous process has exactly the same form as the normal process in eq. (3.53). To include these processes into the action, we use an extended basis known as the Nambu basis [130] and write the retarded part of the cavity action as

$$\mathcal{S}_a^R = \frac{1}{2} \sum_{n,m,\alpha,\beta} \int_{-\Omega/2}^{\Omega/2} \frac{d\omega}{2\pi} \begin{pmatrix} \bar{a}_{n;\alpha}^q(\omega) \\ a_{n;\alpha}^q(-\omega) \end{pmatrix}^T (\mathcal{G}_{n,m;\alpha,\beta}^R)^{-1}(\omega) \begin{pmatrix} a_{m;\beta}^c(\omega) \\ \bar{a}_{m;\beta}^c(-\omega) \end{pmatrix},\quad (3.55)$$

with the inverse retarded propagator given by

$$(\mathcal{G}_{n,m;\alpha,\beta}^R)^{-1}(\omega) = \begin{pmatrix} P_{n,m;\alpha,\beta}^R(\omega) - \Sigma_{a,n,m;\alpha,\beta}^R(\omega) & -\Sigma_{a,n,m;\alpha,\beta}^R(\omega) \\ -\Sigma_{a,n,m;\alpha,\beta}^R(\omega) & P_{n,m;\alpha,\beta}^A(\omega) - \Sigma_{a,n,m;\alpha,\beta}^R(-\omega) \end{pmatrix},\quad (3.56)$$

where the diagonal elements are the inverse bare propagators in eq. (3.35)

$$P_{n,m;\alpha,\beta}^{R/A}(\omega) = \delta_{n,m}\delta_{\alpha,\beta}(\omega + \alpha\Omega - \Delta_n + / - i\kappa_n). \quad (3.57)$$

Due to the phase modulation, the action is no longer diagonal in energy but instead couples different FBZs. The coupling and extended Nambu basis leads to the action acquiring a large matrix structure of the form Floquet  $\otimes$  transverse mode  $\otimes$  Nambu, where  $\otimes$  is the Kronecker product. The Floquet structure is infinite-dimensional, while the transverse mode structure has a  $N_m$  modes and the Nambu structure is two-dimensional. The bare inverse propagators in eq. (3.57) are diagonal in the Floquet indices. The Floquet structure of the self-energy is solely determined by the Fourier coefficients  $c_\alpha$  of the phase modulation such that the Floquet matrix structure of the self-energy is

$$\Sigma_a^R \sim \begin{pmatrix} |c_N|^2 & & & & c_N \bar{c}_{-N} \\ & \ddots & & & \ddots \\ & & |c_2|^2 & c_2 \bar{c}_1 & c_2 \bar{c}_0 \\ & & c_1 \bar{c}_2 & |c_1|^2 & c_1 \bar{c}_0 \\ & & c_0 \bar{c}_2 & c_0 \bar{c}_1 & |c_0|^2 \\ & \ddots & & & \ddots \\ \bar{c}_N c_{-N} & & & & |c_{-N}|^2 \end{pmatrix}. \quad (3.58)$$

Each entry in this matrix is the coefficient from the Floquet structure that is multiplied by the matrix that describes the transverse mode  $\otimes$  Nambu structure of the action. In the small atom-cloud limit, the transverse mode  $\otimes$  Nambu of the self-energy is simply a constant matrix of size  $2N_m$  filled with ones multiplied by  $\Lambda^2 \Pi^R(\omega)$ . The decay in quasienergy,  $\omega$ , is set by the polarization function, which decays as  $1/\omega^2$  and has a magnitude on the order of  $\Lambda^2$  that is small compared to  $\Omega$ . Following an analysis similar to the treatment of the ground state, which led to eq. (3.38), shows that the only relevant cavity modes satisfy  $\alpha\Omega - \Delta_n \sim \Delta_0$ . If  $\Omega \sim 2\omega_T$ , then there will only be one relevant cavity mode in each Floquet block, which allows one to consider an effective action with a matrix structure transverse mode  $\otimes$  Nambu. To clarify the structure of the effective action, consider the normal block of the action, which is the upper left entry of eq. (3.56). The effective bare element is

$$P_{n,m}^R(\omega) = \delta_{n,m}(\omega - \tilde{\omega}_n + i\kappa_n), \quad (3.59)$$

where the effective detuning of the  $n$ th mode  $\tilde{\Delta}_n$  is its bare detuning minus the number of Floquet quantas that brings its magnitude the closest to zero. The effective self-energy

is dense in the mode space such that its components are given by

$$\Sigma_{n,m}^R(\omega) = -\Lambda^2 c_n \bar{c}_m \Pi^R(\omega). \quad (3.60)$$

As the self-energy couples the cavity mode  $n$  and  $m$ , we have generated an effective action where there is a direct coupling between all the different transverse cavity modes. The  $n, m$  component of the inverse retarded propagator for the effective model is therefore given by

$$(\mathcal{G}^R)_{n,m}^{-1}(\omega) = \begin{pmatrix} P_{n,m}^R(\omega) - \Sigma_{a,n,m}^R(\omega) & -\Sigma_{a,n,m}^R(\omega) \\ -\Sigma_{a,n,m}^R(\omega) & P_{n,m}^A(\omega) - \Sigma_{a,n,m}^R(-\omega) \end{pmatrix}. \quad (3.61)$$

Our result is based on the cavity self-energy to second order in the cavity coupling, and in the thermodynamic limit, this becomes exact [108]. That it becomes exact can be understood by going to fourth order in  $g$ , the full diagram still only contains two BEC source fields. The  $\mathcal{O}(g^4)$  diagrams, therefore, also scale linearly with the atom number. However, the cavity interaction is inversely proportional to the square of the volume. In the thermodynamic limit, the second-order process will therefore be relevant as it scales with the density, whereas the higher-order processes scale with the density over volume, which vanishes in the thermodynamic limit.

### 3.4.3 Sideband picture

So far, we have discussed the pump modulation in terms of FBZs, which is the natural language for the general theory. Having an effective model for multiple coupled transverse cavity modes, we can think of the system in a more physical picture closely related to the experimental realization.

The phase modulation in eq. (3.27) is given by a sum of exponentials rotating at  $\exp(-i\alpha\Omega t)$ . The phase modulation can therefore be understood as the pump having sidebands at  $\alpha\Omega$  with intensity in each sideband given by  $|c_\alpha|^2$ . Because of the sum rule in eq. (3.29) the pump field's total power is conserved but shared between all the sidebands. As a specific realization of this, we consider a sinusoidal phase modulation of the form

$$f(t) = B_m \sin(\Omega t), \quad (3.62)$$

where  $B_m$  is the modulation depth of the phase modulation. Using the Jacobi-Anger expansion [131, 17.1.7] the Fourier series of the phase modulation is found as

$$e^{-iB_m \sin(\Omega t)} = \sum_{\alpha=-\infty}^{\infty} J_\alpha(B_m) e^{-i\alpha\Omega t}, \quad (3.63)$$

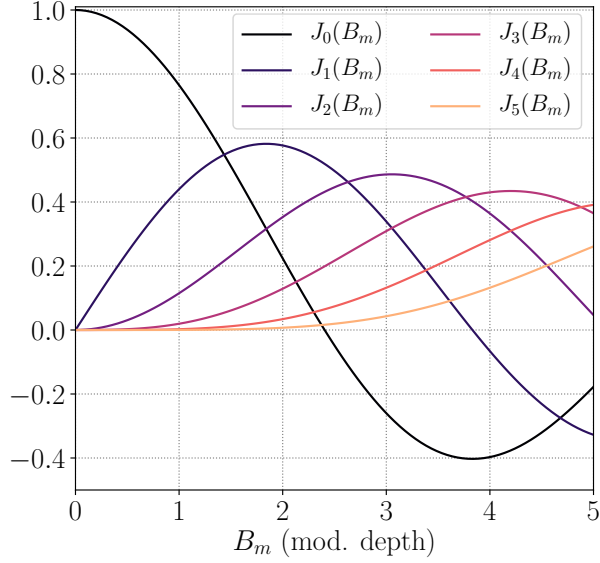


Figure 3.5: A plot of the first six Bessel functions, which corresponds to the weight in the pump sidebands when the phase modulation has a depth  $B_m$ .

where  $J_\alpha(x)$  is the Bessel function of the first kind of order  $\alpha$ . The first six of these coefficients are shown in fig. 3.5. At zero modulation depth, all weight is in the zeroth sideband, and the pump laser, therefore, has all its intensity at  $\omega = 0$  in the rotating frame. Increasing the modulation depth  $B_m$ , more weight is gradually transferred into the sidebands at higher energy. Changing  $B_m$  allows one to tune the effective couplings between the cavity modes in the self-energy as shown in eq. (3.60).

The modulation frequency is the second tuning knob in the phase modulation and allows one to tune the effective detunings of the different transverse modes. This is possible because the effective detuning of each cavity mode is set by the mode's detuning from the nearest sideband. To make this transparent, the phase modulation frequency is written as  $\Omega = 2\omega_T + \epsilon$ , with  $|\epsilon| \ll \omega_T$ . Because the transverse modes are linearly spaced in energy as shown in fig. 3.2b, the effective detuning of the  $n$ th transverse mode will be

$$\Delta_n = \Delta_0 - n\epsilon. \quad (3.64)$$

If we choose the sign of  $\epsilon > 0$ , then the higher-order modes will effectively be lower in energy than the zeroth mode. In the other case where  $\epsilon$  is chosen to be negative, the higher-order modes will be at higher energies than the zeroth mode. Using the simple phase modulation in eq. (3.62), which is easy to implement experimentally, therefore, gives a large tunability of the multimode nature of the system.

### 3.5 Multimode polaritons

The inverse retarded propagator for the effective cavity model in eq. (3.61) has a matrix structure which leads to the elements of the spectral function in eq. (2.68) being given by

$$A_{j,i}(\omega) = i (\mathcal{G}_{j,i}^R(\omega) - \bar{\mathcal{G}}_{j,i}^R(\omega)), \quad (3.65)$$

As shown in section 2.5, the diagonal components of the spectral function satisfy a sum rule which allows us to interpret them as the modification of the bare modes due to the coupling. The mode index  $j$  in the spectral function in eq. (3.65) refers to the cavity mode  $u_{Q,j,0}(z, r) = \cos(Qz) \text{LG}_{j,0}$ . In the following discussion, such a mode will be denoted as the  $\text{LG}_{j,0}$  mode. The spectral function element  $A_{0,0}$  then contains information about adding an excitation to the mode  $\text{LG}_{0,0}$ , having it propagate in the system, and then removing an excitation again from the  $\text{LG}_{0,0}$ .

#### 3.5.1 Single mode polariton

Before discussing the more complicated case, including many cavity modes, we first discuss the single mode system [108, 130, 132].

The main tuning parameter in this system is the pump intensity as it linearly affects the effective light-matter coupling strength  $\Lambda$ , which sets the magnitude of the self-energy in eq. (3.60). Furthermore, it is a good tuning parameter because there is no assumption regarding its magnitude in the derivation of self-energy. Increasing  $\Lambda$  leads to the formation of a polariton where there is a correlation between the cavity photon and a density fluctuation in the atom cloud.

When we derived the ground-state atomic mode functions in eq. (3.18), we did not include the effective optical potential that would arise from having a coherent field inside the cavity. With the choice of atomic mode functions, we are therefore neglecting any occupation of the cavity modes. The anomalous process in fig. 3.4d scatters two cavity photons into the pump meaning the cavity occupation is decreased. This process scales with the occupation in the cavity field. In the conjugate process, two cavity photons are created by scattering two pump photons into the cavity mode. This process scales with the intensity of the pump. For finite  $\Lambda$ , one would expect the cavity occupation to increase until a detailed balance between the two anomalous processes is achieved. However, this is not the case due to the homogeneous nature of the atom cloud [102]. As the atoms are uniformly distributed on the scale of the cavity wavelength, the scattered photons interfere destructively with each other, and no coherent field is created in the cavity.

At the critical value,  $\Lambda_c$ , the number of photons scattered into the cavity is so large

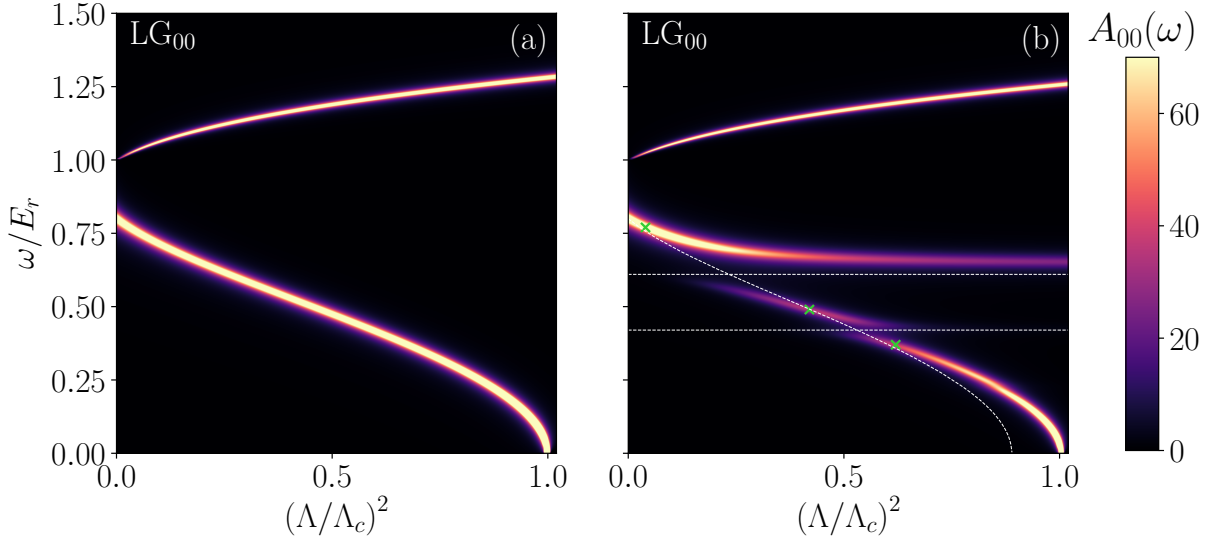


Figure 3.6: A plot of the cavity spectral function for the  $LG_{00}$  mode. The parameters are  $\Delta_0 = 0.8E_r$  and  $\kappa = 0.02E_r$ . In a) the system only has a single cavity mode as there is no phase modulation  $B_m = 0$ , and in b) the phase modulation is turned on with  $\epsilon = 0.19E_r$  and  $B_m = 0.9$ . The horizontal dashed lines represent the bare detunings of the higher-order modes, while the third dashed line is the unmodulated spectral line from a). The three crosses mark the values used in fig. 3.7.

that the atoms are starting to feel the optical potential of the cavity. At this point, the atom cloud no longer has the lowest energy when it is longitudinally homogeneous, but instead, the lowest energy mode is when the cloud has an overall density modulation set by  $Q$ . The atoms in the density modulation start scattering the pump photons constructively into the cavity. This leads to a runaway effect where the atoms in the density modulation scatter the pump field more efficiently into the cavity. The more efficient scattering into the cavity increases the depth of the optical potential for the atoms, which increases the number of atoms in the density modulation, and again more light is scattered into the cavity. Therefore, the system undergoes a phase transition. Below the critical pump power, the system is in the normal phase, where the atom is in a homogeneous cloud, and there is no coherent light field inside the cavity. At the critical pump power, it then transitions into a phase where the atomic cloud has a density modulation, and the cavity is coherently occupied. This phase is known as the superradiant or self-organized phase, depending on whether one prefers to think of the atoms' or the cavity's state. It was first experimentally observed in 2010 [133].

From the perspective of the retarded propagator of the cavity, the signature of the phase transition is that the inverse propagator becomes unbounded, as discussed in section 2.6. In the stationary state, this is seen by the vanishing of the imaginary part of the retarded propagator. When the imaginary part of the retarded propagator becomes zero,

the propagator develops a singularity on the real axis, which leads to the action diverging.

The spectral function for the  $\text{LG}_{00}$  mode for varying pump power is shown in fig. 3.6a. For  $\Lambda = 0$ , the self-energy vanishes, and the spectrum is the free Lorentzian centered at  $\Delta_0$  and with a width of  $\kappa$  from the bare propagator. As the pump is turned on, another peak appears at the recoil energy, which comes from the hybridization with the density fluctuation. Increasing  $\Lambda$  leads to increasingly strong interactions between the cavity and the density modulation, which leads to repulsion of the two peaks in the spectral function. At sufficiently high  $\Lambda$ , the lower peak is pushed to zero frequency. It still has a finite width, and only after further increasing  $\Lambda$  the width goes to zero, making the normal phase unstable through a zero-frequency polariton mode. A more detailed analysis of the phase transition is done using the classical equations in chapter 4.

### 3.5.2 Including phase modulation

To understand how the system is affected by the phase modulation, we first consider the same system but with a finite amplitude of the phase modulation  $B_m > 0$ . The case where the higher-order modes are energetically favorable over the zero mode ( $\epsilon > 0$ ) is shown for the modulation depth  $B_m = 0.9$  in fig. 3.6b. The value of  $B_m$  is chosen such that the central band of the pump has the largest weight, see fig. 3.5. The effect of the large central band weight can directly be observed in the spectral function, which is similar to its unmodulated counterpart in fig. 3.6a for small  $\Lambda$ . As  $\Lambda$  is increased, the mode is pushed down in energy and then intersects with the  $\text{LG}_{10}$  mode, which is  $\epsilon$  lower in energy. Because the two modes interact with each other, they cannot cross, but instead, an avoided crossing appears [100]. Further increasing  $\Lambda$  then forces another crossing with the  $\text{LG}_{20}$  mode. The nature of the mode changes drastically at an avoided crossing because it leads to a hybridization of the two modes. This is illustrated in fig. 3.7. Here it is shown that the fluctuation in the cavity field at low light-matter coupling, corresponding to  $p_1$  in the figure, is mainly in the  $\text{LG}_{00}$  mode because it couples stronger to the atoms. After the first avoided crossing, at  $p_2$ , the cavity fluctuation has a large contribution from  $\text{LG}_{10}$ . The interaction between the modes, through the phase modulation, leads to a superposition of several modes in the cavity field, making the polariton in the system a multimode polariton. After the second avoided crossing at  $p_3$ , the  $\text{LG}_{20}$  becomes important and also has a large weight in the cavity field fluctuation. Additionally, we note that even though the  $\text{LG}_{30}$  is lower in energy than the  $\text{LG}_{20}$  mode, it has a negligible contribution to the field superposition. This is understood by the fact that the weight in the third sideband in fig. 3.5 at  $B_m = 0.9$  is also negligible. The cavity field's superposition thus depends on both  $B_m$  and  $\epsilon$ .

For it to be possible to see these hybridization effects, the cavity linewidth must be



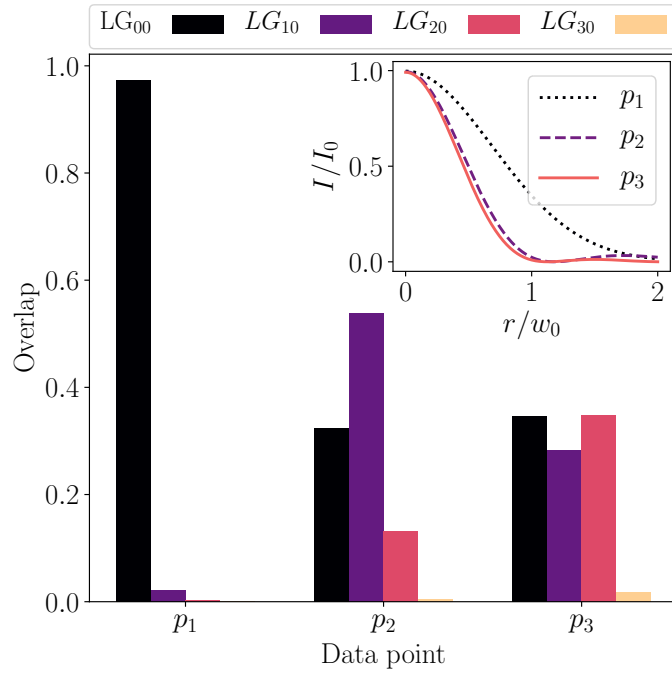


Figure 3.7: This plot shows the composition of the fluctuations in the cavity field at the three different crosses in fig. 3.6b. Each of the crosses are described as a point in the  $(\omega, (\Lambda/\Lambda_c)^2)$  plane. At the first cross  $p_1 = (0.04, 0.77)$  the  $LG_{00}$  mode dominates the the field, while after the first avoid crossing at  $p_2 = (0.42, 0.49)$  the field is mainly composed of  $LG_{10}$  and  $LG_{00}$ . At the last point  $p_3 = (0.62, 0.37)$ , the field is in a superposition with almost similar weight in all of the three lowest transverse modes. The inset shows the effective spatial potential felt by the atoms at these three different points.

below the recoil energy, as a larger linewidth will wash out any hybridization signatures in the spectrums. Current state-of-the-art experimental setups with resolution below the recoil energy exist [81], such that the observation of the described hybridization effects is within reach. For the experiment in [81], Rubidium was used, and choosing a lighter atom, such as Lithium, would increase the recoil energy by around a factor of 10. The recoil energy would then be  $\sim 0.2$  MHz and would still be significantly smaller than the transverse energy spacing of the cavity modes  $\omega_T \sim 0.1$ GHz such that the effective model would be well-justified. In this case the linewidth would be about an order magnitude less than the recoil energy making the anti-crossings clearly visible.

The hybridization is not directly visible if one considers a system without sub-recoil resolution. However, one would still be able to observe that the cavity field will be in a superposition of different modes as this does not rely on visible avoided crossings.

Besides the avoided crossing and multimode nature of the polariton, it is also worth mentioning that by including more modes into the cavity field, the waist of the cavity is effectively decreased. The transverse intensity profile of the cavity field is plotted in the inset of fig. 3.7 and in the dispersive regime, the width of the intensity profile directly relates to the range for the cavity mediated atom-atom interactions [110]. If the effective interaction range can be tuned, it will open up a range of new physical models that can be investigated using the ultracold atom gas systems. Current experimental setups are limited because there is a large discrepancy between the cavity waist and the size of the transverse atom cloud. In this regime one would need a high-order transverse mode to realize short-ranged atom-atom interactions using a phase modulation of the pump. A high-order transverse mode decreases the waist as the mode's center peaks decrease in size with the mode number, as shown in fig. 3.2a. This is experimentally challenging as these modes also extend far in the transverse direction, making them harder to stabilize in the cavity. To use the phase modulation to create short-range atom-atom interactions, one should instead consider moving the atom cloud away from the center of the cavity, where nodes of the different modes can potentially be used to generate smaller effective interactions between the atoms.

So far, we have discussed how the system behaves when the higher-order modes are energetically preferable to the  $LG_{00}$  mode. One can also consider the opposite scenario, where the higher-order modes are energetically unfavorable by choosing  $\epsilon < 0$ . For a negative  $\epsilon$ , the spectral functions for the first four transverse modes are plotted in fig. 3.8 as a function of the detuning. The spectral functions are plotted at constant ratio  $(\Lambda/\Lambda_c)^2 = 0.7$  but it is important to note that  $\Lambda_c$  is a function of  $B_m$ . Keeping  $\Lambda/\Lambda_c$  constant allows us to compare the spectral functions when the system is in the vicinity of the phase transition. For comparison, we plot the quasiparticle energy for each mode, given by

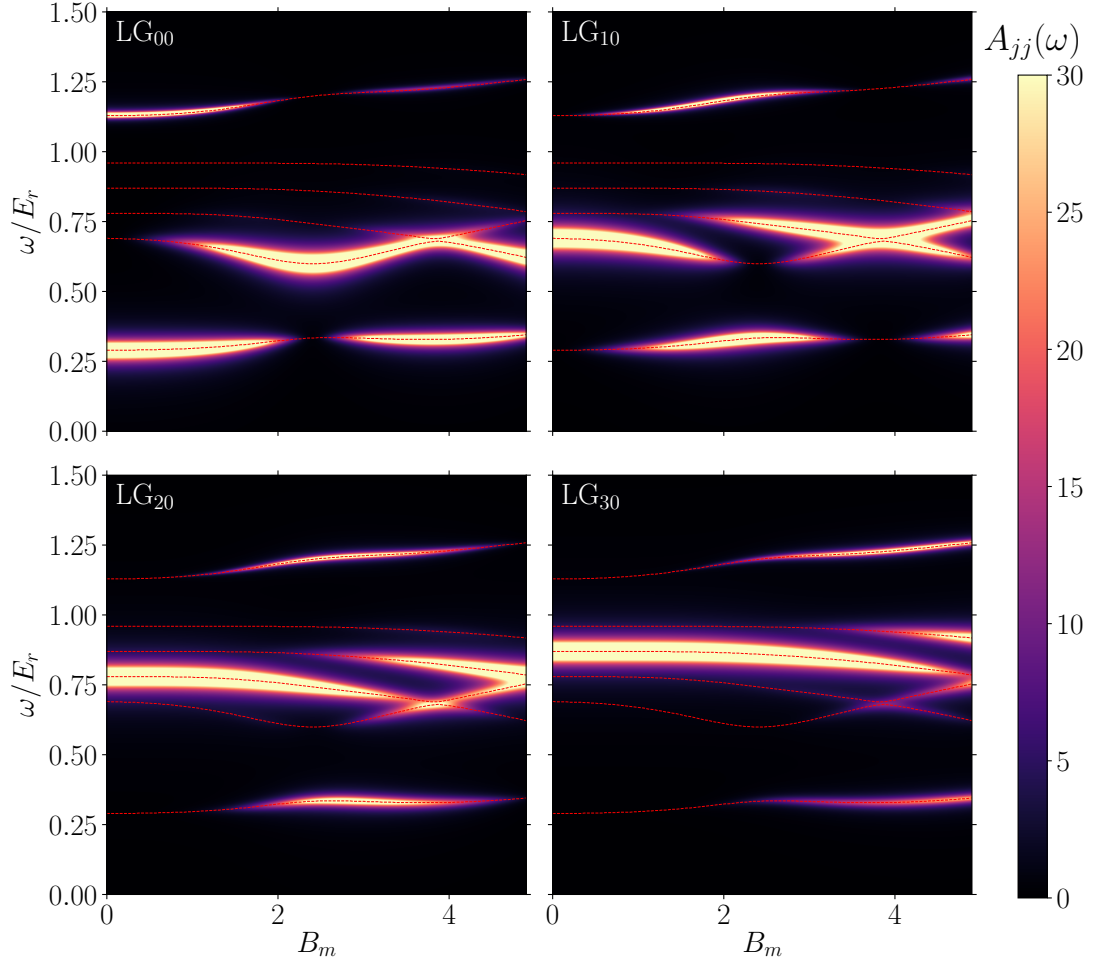


Figure 3.8: Plots of the spectral functions for the first 4 transverse modes as a function of the modulation depth  $B_m$ . The higher order modes are higher in energy than the LG<sub>00</sub> mode as  $\epsilon = -0.09E_r$ . the effective light-matter coupling strength is kept at a fixed ratio  $(\Lambda/\Lambda_c)^2 = 0.7$ . Notice that  $|\lambda_c$  is a function of  $B_m$  see eq. (3.67). The red lines are the quasiparticle energies of each mode described by eq. (2.71). The cavity parameters are  $\kappa = 0.02E_r$  and  $\Delta_0 = 0.6E_r$ .

eq. (2.71). At  $B_m = 0$  the  $\text{LG}_{00}$  mode is pushed down to a frequency around  $0.3E_r$  and couples significantly to the atom, which is seen by a clear feature from the atomic part of the polariton in the  $\text{LG}_{00}$  spectral function. This can be qualitatively compared to a line scan at  $0.7(\Lambda/\Lambda_c)^2$  in fig. 3.6a. At this modulation depth, none of the higher-order cavity modes are part of the polariton, and their spectral functions are purely Lorentzian at their respective bare detunings given by eq. (3.64). As  $B_m$  is increased, the height of the pump sideband for the  $\text{LG}_{10}$  mode increases according to fig. 3.5, which leads to this mode being mixed into the polariton. This can be seen in fig. 3.8 by the atomic mode starting to appear in  $A_{11}$ , and the spectral functions  $A_{00}$  and  $A_{11}$  have features emerging at the same frequencies. The admixture of the  $\text{LG}_{00}$  mode is decreasing due to the decreasing height in carrier peak of the pump see fig. 3.5, until  $B_m \sim 2.4$  where  $J_0(B_m) \approx 0$ . Then  $\text{LG}_{00}$  is completely removed from the polariton, the atom admixture vanishes in  $A_{00}$ , and the unperturbed Lorentzian is the only feature remaining. At  $B_m \sim 2.4$ , the polariton has significant weight in both  $\text{LG}_{10}$  and  $\text{LG}_{20}$  and the peaks of the spectral functions are significantly displaced from the bare values, which indicates that both modes strongly couples to the atoms. For  $B_m \approx 4$ , the polariton consists of a superposition of all four modes apart from  $\text{LG}_{10}$ , which is again understood from fig. 3.5.

The explicit example shows that even for  $\epsilon < 0$ , strongly coupled multimode polaritons can be generated using the simple sinusoidal phase modulation scheme.

### 3.6 Multimode superradiance

In this section, we discuss how the changes in the polariton spectrum due to the phase modulation carry over to the superradiant phase transition.

We have seen that the critical value of the phase transition is affected by the phase modulation. It became apparent in fig. 3.8 when the atomic peak in the spectral function was moved to higher energy as  $B_m$  increases. The atomic peak being pushed to higher energies means that the coupling strength between the cavity and the atoms has increased. As the ratio  $\Lambda/\Lambda_c$  is kept constant, both  $\Lambda$  and  $\Lambda_c$  must have increased for larger values of  $B_m$ .

A rigorous treatment of the critical coupling strength will follow in chapter 4, and for the single mode case, we find the well-known result [107]

$$\Lambda_c^2 = \frac{E_R(\Delta_0^2 + \kappa^2)}{2\Delta_0}. \quad (3.66)$$

In the regime where  $\kappa \ll \Delta_0$ , the critical coupling is seen to scale linearly with the detuning. This single-mode effect carries over qualitatively to fig. 3.8, as the higher-order

modes in fig. 3.8 have larger detunings than the zeroth order mode, and we indirectly observe an increase in  $\Lambda_c$  when these modes start coupling to the atoms.

To investigate how the phase modulation affects the critical coupling, consider first the simplest case where  $\epsilon = 0$ , such that the cavity modes are effectively degenerate. In this case, we expect that the critical coupling is unchanged by  $B_m$  because the cavity modes are effectively degenerate. The result is shown in fig. 3.9a, by the dashed black line and predicts that a non-monotonic increasing value of  $\Lambda_c$  would be observed. This behavior is explained by the symmetrically generated sidebands above and below the carrier frequency due to the sinusoidal phase modulation. Combined with the fact that the near-planar cavity only has modes at higher energy than  $\text{LG}_{00}$ , all intensity in the lower energy sidebands is effectively lost. The lost intensity can be accounted for by renormalizing  $\Lambda$

$$\Lambda \rightarrow \frac{\Lambda}{\sqrt{\sum_{0 \leq \alpha \leq \alpha_{\max}} J_\alpha(B_m)^2}} = \Lambda(B_m). \quad (3.67)$$

The renormalized critical coupling for  $\epsilon = 0$  is now independent of  $B_m$  as shown by the solid black line in fig. 3.9a.

In the case where  $\epsilon > 0$ , as considered in fig. 3.6, the higher-order modes are energetically favorable. The critical coupling as a function of  $B_m$  is plotted as the red lines in fig. 3.9a. We observe that after renormalizing  $\Lambda_c$  the critical coupling decreases with  $B_m$ , which is expected from the single mode result in eq. (3.66). However, when the modes have different detunings, the critical coupling is not a linear function of  $B_m$ , which highlights the interplay between the effective detuning and the pump sideband height.

Apart from the shifted critical coupling, we can observe an intriguing effect that hints at a qualitatively new nature of the superradiant phase itself. Instead of an unstable polariton mode at zero frequency, there is an indication that it can be pushed to finite frequency.

The superradiant phase has been described as a phase with finite occupation in a zero-frequency polariton mode. Mathematically, the instability of the system occurs when the inverse retarded matrix propagator  $(\mathcal{G}^R(0))^{-1}$  acquires an eigenvalue with a value of zero. At this point, the retarded propagator is no longer defined, and the action has become unbounded, signaling the phase transition. Computing  $\Lambda_c$  for when this zero-eigenvalue occurs, we find that there are regions in the parameter space  $(B_m, \epsilon)$  where the inverse propagator at  $\omega = 0$  cannot become unstable. The zero-frequency polariton not having an instability is not equivalent to the system having no transition into a superradiant state. Instead, what happens is that a polariton mode can become unstable at a finite frequency. Computing this instability from the retarded propagator is cumbersome, as it

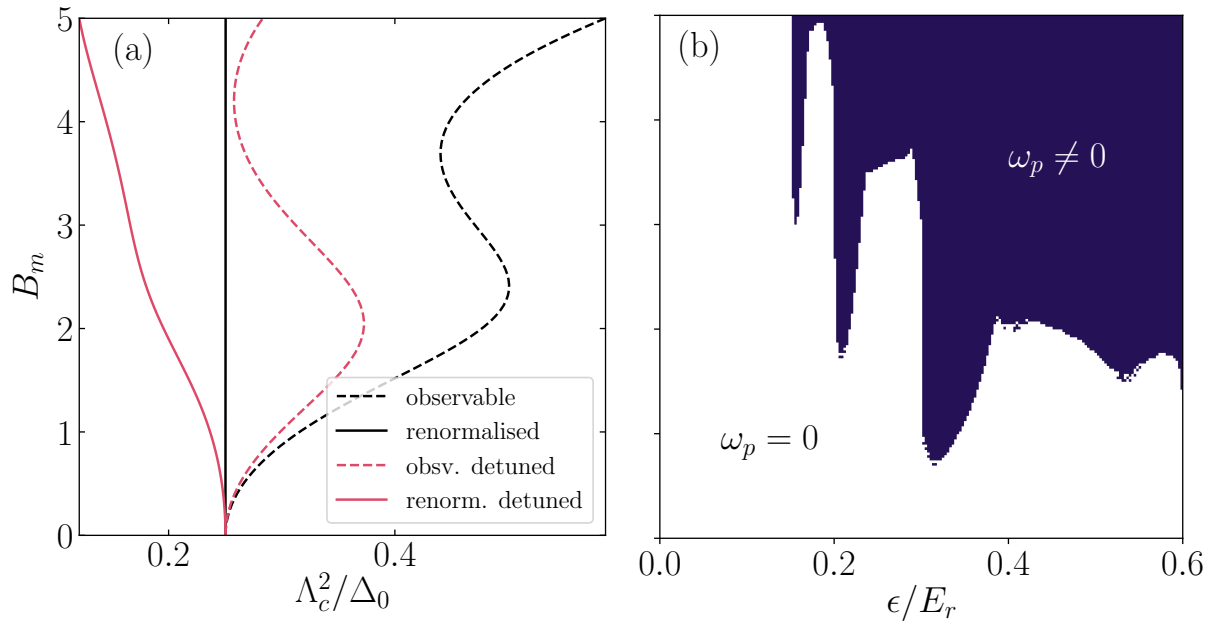


Figure 3.9: *a)* The plot shows the critical coupling strength for  $\epsilon = 0$  (black lines) and  $\epsilon = 0.1E_r$  (colored line). The dashed lines represent what would be experimentally observed, and the solid lines are the renormalized critical couplings from eq. (3.67). *b)* Phase diagram of the frequency of polariton mode,  $\omega_p$ , which becomes unstable. The cavity parameters are  $\kappa = 0.05E_r$  and  $\Delta_0 = 0.6E_r$ .

requires one to solve the equation

$$\text{Det} \left( (\mathcal{G}^R(\omega))^{-1} \right) = 0, \quad (3.68)$$

as a function of  $\Lambda$  and  $\omega$ . Performing this non-trivial numerical task leads to the result shown in fig. 3.9b. There is a sizable region of parameter space where the dominating instability is a polariton mode at finite frequency. The small disconnected regions of fig. 3.9b occur due to the two-dimensional root-finding routine not being perfectly robust. By carefully investigating the parameters, one can see that the three lobes in the phase diagram are connected to a cavity mode acquiring an effective negative detuning. This means that the cavity mode has lower energy than its sideband. The phase diagram, therefore, hints towards a qualitative change of the superradiant phase if cavity modes acquire negative detunings. Understanding the nature of the instability by numerically solving eq. (3.68) is inefficient as it requires investigating the large parameter space numerically. In chapter 4 we will use a different approach to get a deeper understanding of how the superradiant state is modified in this multimode model.

### 3.7 Summary and discussion

In this chapter, we have shown how effective interactions between different cavity modes that have a large frequency separation can be generated using a phase modulation. The effective interaction originates from the different cavity modes coupling strongly to the motion of the same atom gas. The atomic gas, therefore, acts as a mediator of interactions between the cavity modes. Due to the strong coupling between the cavity modes and the motion of the atomic gas, the system forms a polariton that contains a superposition of many cavity modes, making it a polariton with a multimode nature. In the regime where the cavity loss is below the recoil energy of the atoms, the different cavity modes interact strongly with each other, giving rise to avoided crossings in the spectrum. We have shown that the superposition of the modes in the polariton and the cavity modes' effective interactions can be tuned by the phase modulation parameters. We find signs that the multimode nature of the polariton makes it possible for the system to transition into a superradiant phase that oscillates at a finite frequency.

To illustrate the scheme, we have focused on a near-planar cavity where the transverse cavity modes are linearly spaced in frequency and the regime where the atom cloud is small compared to the cavity waist. Both of these regimes make the equations and analysis simpler, but none of them are required for the scheme to work. It only relies on the energy scale set by the frequency difference of the relevant transverse cavity modes being much larger than the recoil energy of the atom. If the atomic overlaps are different for the different transverse modes, then this effect can be directly accounted for by choosing the height of the pump sidebands accordingly. If the cavity modes are not linearly spaced, then this can be accounted for by not using a periodic phase modulation but instead a generic frequency comb.

An interesting question that has not been investigated here is how the pump envelope modifies the results. The transverse pump has a wavelength that is equal to the wavelength of the longitudinal cavity mode. This gives rise to an optical potential in the transverse direction, which changes the transverse-mode overlaps between the cavity modes and the atom cloud. One could also investigate how a pump with angular momentum affects the polariton, as this gives rise to coupling between modes of different angular momentum. Lastly, the question of how small an effective atom-atom interaction-range one can create by using a superposition of a realistic number of transverse cavity modes also requires further investigations.

# Chapter 4

## Polariton limit cycles

### 4.1 Introduction

In the previous chapter, phase modulation of the pump laser was used to couple several transverse cavity modes strongly to the motion of an ultracold gas of atoms. The cavity photon coupled to the atomic motion because the pump laser frequencies were tuned far below the electronic transition of the atoms. Our investigations showed a large parameter region, where the superradiant state did not emerge through a mode softening; instead, the system acquired a finite frequency instability. The emergence of a finite frequency instability is surprising as the system is described using an effective time-independent model. The effective model was derived by relying on the separation of energy scales inherent to the system, and it was intuitively understood as the pump having sidebands close to each cavity mode. Preliminary investigations of the phase diagram hinted at a connection between a cavity mode acquiring a negative detuning and the polariton developing a finite frequency instability.

The sign of detunings can play a vital role in the behavior of the system, exemplified by considering the ultracold gas in a single mode cavity without modulation of the pump. When the pump is detuned far below the atomic transition and slightly below the cavity mode, the optical potential for the atoms created by occupation of the cavity field is an attractive potential that favors a density wave in the atoms [13]. The dispersive regime can also be reached if the pump is detuned far above the electronic transition and the cavity frequency is slightly above the laser frequency. In this dispersive regime, the optical potential for the atoms becomes repulsive [13]. This repulsive interaction can drive the system into a limit cycle, and even chaos [134, 135]. These predictions have recently been verified experimentally [136]. While using a pump with a frequency above the electronic transition can lead to limit cycles, the phase diagram differs from what we observe in the multimode model.



Our multimode model is time-independent, but oscillating steady states have been proposed and investigated previously in similar systems using a modulation of the pump laser at frequencies comparable to the recoil energy. In this case, the modulation frequency is much smaller than the cavity spacing, and only a single cavity mode is relevant. However, because the modulation frequency is comparable to the intrinsic time scale of the atomic motion, the model can not be simplified to one that is time-independent. The parametrically driven and closed Dicke model was found to exhibit a rich phase diagram due to the driving [137]. Dissipation was included in the description by ref. [138] where they found a new oscillating phase which they interpreted as a normal phase with pulsed superradiance.

Following these ideas, the effect of a modulated pump, with a modulation frequency comparable to the recoil energy, was considered in the BEC-cavity system in [139, 140]. Here it was found that the pump modulation can suppress the density wave in the atom mode and that if the modulation frequency was comparable to the recoil energy, the system could exhibit a limit cycle. The limit cycle was found to be robust, to some level, against noise and imperfections in the modulation protocol.

A similar system was numerically investigated in [141], where collisions between the atoms were included. This system also had a limit cycle between two different symmetry-broken states, but the presence of atom collisions was numerically found to lead to heating. A recent experiment [142] done with the modulation close to the recoil energy found the atomic state of the system switching between two  $\mathcal{Z}_2$  symmetry-broken states with half the period of the modulation frequency. These oscillations survived for less than ten cycles, which was attributed to non-negligible atom-atom interactions and atom losses by numerical simulations.

In all the discussed systems, the oscillating steady states were generated either by the repulsive optical potential of the atom or by driving at a frequency close to the recoil energy. As neither of these mechanisms are present in our effective model they cannot directly explain the phase diagram from chapter 3.

In [64], it was experimentally found that for a negatively detuned cavity, the system does not soften at the transition but instead hardens. They argue that this is because the cavity phase is shifted, in relation to the emerging density wave pattern, such that a negatively detuned cavity mode leads to a suppression of the density wave towards the homogenous atom configuration. An experiment with two pump lasers, one below and one above the cavity frequency, was performed in [143], which showed that it was possible to use the pump above the cavity frequency to suppress the density wave generally favored by the lower frequency pump. This understanding of a single negatively detuned cavity mode suggests that having both negatively and positively detuned cavity modes in the

system can lead to a competition between favoring and suppressing the density wave.

To investigate the superradiant phase, we consider a generalized model of the sinusoidal phase modulation. It consists of several cavity modes with variable detunings and variable coupling strengths to the atoms.

The effective model emerging from a multi-colored laser drive was previously discussed in [144,145]. They considered all cavity modes having the same detuning or the bad cavity limit and observed no limit cycles. Even in these regimes, they show that the system can be used for several applications, such as the simulation of Hopfield networks and associative memories. Differently from those investigations, we consider the case where the cavity linewidth is below the recoil energy of the atoms, as this is where our initial calculations suggest finite frequency instabilities emerge.

By constructing the classical equations for our multimode model, we can derive analytic expressions for the frequencies and critical couplings of the unstable modes. We show that the finite frequency instability is truly an effect of having a competition between a negatively and a positively detuned cavity mode, which can be understood by considering the behavior of the eigenvalues (EVs) of the linear stability analysis. These results show that we can tune the frequency of the instability to any value on the scale of the recoil momentum by adjusting the effective parameters of the model. Going beyond the linear stability analysis, we show that the single mode superradiant transition, on the classical level, corresponds to a pitchfork bifurcation. With several modes present, this leads the system to exhibit Hopf-bifurcations. Even more striking, the effective model can accommodate several limit cycles simultaneously at different frequencies. From a normal form analysis of the Double-Hopf bifurcations, the possible steady states of the system is mapped out. Lastly, some preliminary investigations into the effect of including atom-atom interactions are discussed. These investigations allow us to predict that specific density modulations should grow due to the presence of the limit cycle, effectively heating the system. However, our investigations suggest that the heating rate can be dramatically decreased by adjusting the frequency of the limit cycle, and the limit-cycle phase can therefore be metastable.

## 4.2 Minimal model

For the minimal model, we will consider a similar system as in chapter 3 and only briefly mention the key approximations and findings discussed in detail in that chapter. The system consists of a linear cavity containing an ultracold gas of  $N_0$  bosonic atoms in the center. The gas is driven by a transverse pump laser, which we generalize to have sidebands with arbitrary frequencies and magnitudes. The cavity is assumed to support

several different transverse modes, and the atom cloud is modeled as long in the longitudinal direction (compared to the inverse recoil momentum) and small in the transverse directions compared to the cavity waist. In this regime, the atoms couple equally to all zero angular momentum cavity modes. The frequency of the pump laser and its sidebands are detuned far below the atomic transition such that the excited state can be adiabatically eliminated. In this dispersive regime, the cavity couples directly to the spatial motion of the ground state of the atoms. We assume the transverse pump carries no momentum, meaning the mode function for the pump is spatially uniform. Because all transverse cavity modes, that couple to the atoms, has approximately identical overlaps with the small atom cloud, and the pump profile is assumed constant, the model can be simplified to a one-dimensional model. A greater transverse extent of the atom cloud changes the effective coupling strength between the modes and the atom cloud. It can be accounted for by changing the power of the pump sidebands accordingly.

The Hamiltonian for this minimal model is given by

$$H = \int_{-L/2}^{L/2} dx \hat{\psi}^\dagger(x) \left( -\frac{1}{2m} \frac{d^2}{dx^2} + \frac{1}{\sqrt{L}} \cos(xQ) \sum_i \eta_i (\hat{\phi}_i + \hat{\phi}_i^\dagger) \right) \hat{\psi}(x) + g \int dx \hat{\psi}^\dagger(x) \hat{\psi}^\dagger(x) \hat{\psi}(x) \hat{\psi}(x) + \sum_i \Delta_i \hat{\phi}_i^\dagger \hat{\phi}_i, \quad (4.1)$$

where  $\hat{\psi}$  is the bosonic field operator for motion of the ground-state atoms and  $\hat{\phi}_i$  the annihilation operator for the  $i$ th cavity mode. The atom mass is  $m$  and  $\Delta_i = \omega_{c,i} - \omega_{p,i}$  is the effective detuning of the  $i$ th cavity mode with frequency  $\omega_{x,i}$  from the pumps  $i$ th sideband at frequency  $\omega_{p,i}$ . The detuning of the cavity modes can be separately tuned by individually changing the frequency of the pump sidebands. The length of the cavity is  $L$ , and  $Q = 2\pi/\lambda_p$  is the wavevector of the cavity mode the pump photons are scattered into. The cavity wavevector is set by the pump wavelength  $\lambda_p$ . The pump sidebands all effectively have the same wavelength because the frequency of the pump is  $\sim 300$ THz. The large frequency of the pump means that even if the sideband is 10 GHz higher in frequency, then the difference in wavelength is

$$\lambda_p - \lambda_{p,\text{sideband}} \approx \frac{c}{300 \times 10^{12}} - \frac{c}{300 \times 10^{12} + 10^{10}} \approx 3 \times 10^{-2} \text{nm}. \quad (4.2)$$

As the transverse size of the atom cloud is on the order of  $\mu\text{m}$  [81], the wavelength difference of the sidebands can be neglected. The effective coupling between the  $i$ th cavity mode and the atom cloud is set by  $\eta_i$ . The coupling is local in space and time due to the adiabatic elimination of the excited state. As discussed in chapter 3 and above, this coupling can be tuned individually for each mode by tuning the relative power in the

sidebands. For an ultracold and dilute gas, the contact interaction is a good approximation to the two-body scattering potential [128], and we denote the contact interaction strength by  $g$ . This interaction is repulsive ( $g > 0$ ). The processes involving two cavity photons and no pump are neglected as the single photon interaction strength is much smaller than the interaction with the pump field as discussed in chapter 3.

To effectively deal with the spatial derivative in the Hamiltonian, the atom field operators are expanded in plane waves with periodic boundary conditions

$$\hat{\psi}(x) = \sum_k \frac{1}{\sqrt{L}} \hat{\psi}_k e^{ikx}, \quad \text{with } k = \frac{2\pi n}{L} \text{ and } n = 0, \pm 1, \pm 2, \dots \quad (4.3)$$

With the discrete and continuous  $\delta$ -function being related by

$$\frac{1}{L} \int dx e^{-ikx} = \delta_{k,0}, \quad \frac{1}{L} \sum_k e^{ikx} = \delta(x), \quad (4.4)$$

the Hamiltonian takes the form

$$\begin{aligned} H = & \sum_k \hat{\psi}_k^\dagger \hat{\psi}_k \frac{k^2}{2m} + \frac{1}{2\sqrt{L}} \sum_{i,k} \eta_i \left( \hat{\psi}_k^\dagger \hat{\psi}_{k+Q} + \hat{\psi}_k^\dagger \hat{\psi}_{k-Q} \right) \left( \hat{\phi}_i + \hat{\phi}_i^\dagger \right) \\ & + \frac{g}{L} \sum_{k,q,q'} \hat{\psi}_k^\dagger \hat{\psi}_q^\dagger \hat{\psi}_{q'} \hat{\psi}_{k+q-q'} + \sum_i \Delta_i \hat{\phi}_i^\dagger \hat{\phi}_i, \end{aligned} \quad (4.5)$$

Including cavity loss and atom broadening is essential in this driven system. These effects are included by constructing a non-equilibrium action for the Hamiltonian in eq. (4.5) and adding decay/broadening through linear coupling to an empty environment, similarly as we did in chapter 3. The action for the bare system takes the form

$$S_0 = \int dt dt' \left( \sum_k \begin{pmatrix} \bar{\psi}_c \\ \bar{\psi}_q \end{pmatrix}_{k,t}^T \mathcal{G}_{0,k}^{-1}(t, t') \begin{pmatrix} \psi_c \\ \psi_q \end{pmatrix}_{k,t'} + \sum_i \begin{pmatrix} \bar{\phi}_{c,i} \\ \bar{\phi}_{q,i} \end{pmatrix}_t \mathcal{D}_{0,i}^{-1}(t, t') \begin{pmatrix} \phi_{c,i} \\ \phi_{q,i} \end{pmatrix}_{t'} \right), \quad (4.6)$$

with the Keldysh structure of the bare inverse atom propagators being

$$\mathcal{G}_0^{-1} = \begin{pmatrix} 0 & [\mathcal{G}_0^A]^{-1} \\ [\mathcal{G}_0^R]^{-1} & [\mathcal{G}_0^{-1}]^K \end{pmatrix}, \quad (4.7)$$

while the space-time dependence of the retarded/advanced inverse Greens function is

$$\left[ G_{0,k}^{R/A} \right]^{-1}(t, t') = \delta(t - t') \left( i\partial_{t'} - \frac{k^2}{2m} \pm i\kappa_{a,k} \right). \quad (4.8)$$

Here  $\kappa_{a,k}$  is a positive decay rate that will generally be considered infinitesimal. The

matrix-valued inverse propagator for the bare boson has the form

$$\mathcal{D}_{0,i}^{-1}(t, t') = \delta(t - t') \begin{pmatrix} 0 & -i\partial_{t'} - \Delta_i - i\kappa_i \\ i\partial_{t'} - \Delta_i + i\kappa_i & i2\kappa_i \end{pmatrix}, \quad (4.9)$$

where  $\kappa_i$  is the finite and positive loss rate of the  $i$ th cavity mode. Using the Keldysh rotation, the dispersive interaction in the Hamiltonian leads to a term in the action of the form

$$S_{I,C} = -\frac{1}{2\sqrt{2L}} \sum_{i,k_1,k_2} \int dt \left( \eta_i \delta_{k_1 \pm Q, k_2} \bar{\psi}_{k_1, \rho} \psi_{k_2, \beta} \phi_{i, \alpha} M^{\alpha\beta\rho} + c.c. \right), \quad (4.10)$$

where the time dependence of the complex fields has been suppressed.  $M^{\alpha\beta\rho} = \left( \sigma_1^{\alpha\beta}, \delta^{\alpha\beta} \right)^\rho$  describes the vertex's Keldysh structure such that  $\alpha, \beta, \rho \in \{c, q\}$ .

Lastly, the contact interaction gives rise to the term

$$S_{I,g} = -\frac{g}{2L} \sum_{k_1, k_2, k_3} \bar{\psi}_{k_1, q} \bar{\psi}_{k_2, c} \psi_{k_3, c} \psi_{k_1+k_2-k_3, c} + \bar{\psi}_{k_1, c} \bar{\psi}_{k_2, q} \psi_{k_3, q} \psi_{k_1+k_2-k_3, q} + c.c. \quad (4.11)$$

### 4.3 Classical equations of motion

Both the atomic ground state's motion and the cavity photons are bosonic excitations, and we want to understand the behavior both at and after the transition into the superradiant state. Going past the critical point, we expect a similar situation to the time-invariant superradiant transition, where the cavity acquires a macroscopic occupation. When this happens, the coherent part has to be separated from the fluctuations as discussed in section 2.6. Due to the coherent occupation, the occupied fields dominate over quantum fluctuations, and the dynamics of the fields are well approximated by solving the classical equations. To derive these from the action, we follow the procedure described in section 2.4.1.

Due to the complex conjugate relation between the fields, it is sufficient to derive the equations for either the field or its conjugate. The saddle-point equations are then given as

$$\begin{aligned} \frac{\delta S}{\delta \bar{\phi}_{q,i}(t)} \Big|_{\phi_{q,i}=\psi_{q,k}=0} &= 0, \\ \frac{\delta S}{\delta \bar{\psi}_{q,k}(t)} \Big|_{\phi_{q,i}=\psi_{q,k}=0} &= 0. \end{aligned} \quad (4.12)$$

As the photon is lossy, it leads to fluctuations in the field, which are neglected when using the classical approximation. The two features that account for the out-of-equilibrium nature of the photon are the pole of the retarded propagator being a finite distance from

the real axis and  $P_i^K$  having a finite value of  $i2\kappa_i$ . In the classical equations, we include the complex pole of the retarded propagator. Still, we are neglecting the finite value of  $P_i^K$  as this is quadratic in the quantum field and will therefore vanish when taking the quantum fields to zero. To improve upon this, the q-q block of the cavity can be rewritten using a Hubbard-Stratonovich transformation [146, 147]

$$\begin{aligned} & \int \mathcal{D}[\bar{\phi}_{q,i}, \phi_{q,i}] e^{i \int dt \bar{\phi}_{q,i}(t) i2\kappa \phi_{q,i}(t)} \\ &= \int \mathcal{D}[\bar{\phi}_{q,i}, \phi_{q,i}] \int \mathcal{D}[\bar{\xi}, \xi] e^{i \int dt \bar{\xi}_i(t) \frac{i}{2\kappa} \xi(t) - i \bar{\xi}_i(t) \phi_{q,i}(t) - i \bar{\phi}_{q,i}(t) \xi_i(t)}, \end{aligned} \quad (4.13)$$

where  $\xi$  is normalized according to  $\int \mathcal{D}[\bar{\xi}_i, \xi_i] e^{-1 \int dt \bar{\xi}_i \frac{1}{2\kappa} \xi} = 1$ . Using the Hubbard-Stratonovich transformation to rewrite the quadratic q-q component of the cavity, the equations become semiclassical.

Lastly, we are interested in the thermodynamic limit where  $N_0, L \rightarrow \infty$  in a way such that the density of atoms  $N_0/L = n_\psi$  is kept constant. To this extent, a factor of  $\sqrt{N_0}$  is extracted from both cavity and atom fields. The effect of the thermodynamic limit can be accounted for by rescaling the two interaction parameters:  $\eta_i \rightarrow \sqrt{N_0} \eta_i / \sqrt{2}$  and  $g \rightarrow N_0 g / 2$ , where the factors of 2 and  $\sqrt{2}$  are merely for convenience. Another consequence of taking the thermodynamic limit is that the momentum states become dense such that the atom momentum can take any value. Integrals can therefore replace the momentum sums. However, one always has to discretize on a grid for numerical computations, so the sum notation is kept. Notice that the normalization condition on the atoms means that all converged calculations are independent of grid choices.

The semiclassical equations for the cavity modes, with the renormalized parameters, take the form

$$i\dot{\phi}_i(t) = (\Delta_i - i\kappa_i) \phi_i(t) + i \frac{\xi_i(t)}{\sqrt{N_0}} + \frac{\eta_i}{2} \sum_k \bar{\psi}_k(t) (\psi_{k+Q}(t) + \psi_{k-Q}(t)). \quad (4.14)$$

As the noise  $\xi_i$  is randomly chosen from a Gaussian distribution, the lossy nature of the cavity has translated into the equations having a stochastic nature. By including the cavity noise through the Hubbard-Stratonovich field, the semiclassical equations are of the Langevin type. As the different atomic momentum states are assumed to be almost infinitely long-lived, their equations of motion is only stochastic indirectly through the cavity. Furthermore, we see that in the thermodynamic limit, the noise scales inversely with the root of the atom number. Noise is, therefore, a small perturbation to the system, and we neglect it and consider the classical equations.

The classical equations for the atoms are given by

$$i\dot{\psi}_k(t) = \left( \frac{k^2}{2m} - i\kappa_{a,k} \right) \psi_k(t) + \sum_i \eta_i \operatorname{Re} \phi_i(t) \left( \psi_{k+Q}(t) + \psi_{k-Q}(t) \right) + g \sum_{k',q} \bar{\psi}_{k'} \psi_q \psi_{k+k'-q}. \quad (4.15)$$

eqs. (4.14) and (4.15) constitute the classical equations that describe the coherent occupation of the fields.

## 4.4 Linear stability of the normal phase

For the phase diagram in chapter 3 the atoms were assumed non-interacting, and we will make the same assumption here. Starting from a homogeneous cloud, the only relevant atom modes are those at a multiple of the recoil momentum. The necessary atom basis is therefore composed of  $\psi_{nQ}$  with  $n \in \{0, \pm 1, \pm 2, \dots\}$ . As the atoms are assumed non-interacting, the atomic states are symmetric around zero momentum leading to the symmetry  $\psi_n(t) = \psi_{-n}(t)$ . The symmetry allows us to write the equations exclusively for the positive momentum states. In the limit where the atoms are assumed completely lossless, the atom number must be conserved. Using the symmetry to reduce the dimension is done by renormalizing the atom fields in such a way that the atom number conservation is maintained

$$\begin{aligned} 1 &= \sum_{n=-\infty}^{\infty} |\psi_n(t)|^2 = |\psi_0(t)|^2 + \sum_{n=-\infty}^{-1} |\psi_n(t)|^2 + \sum_{n=1}^{\infty} |\psi_n(t)|^2 \\ &= |\psi_0(t)|^2 + \sum_{n=1}^{\infty} 2|\psi_n(t)|^2 = \sum_{n=0}^{\infty} |\psi_n(t) \sqrt{\delta_{n>0} + 1}|^2. \end{aligned} \quad (4.16)$$

Renormalizing the atom fields, the classical equations, in the thermodynamic limit, take their final form

$$\begin{aligned} i\dot{\phi}_i(t) &= (\Delta_i - i\kappa_i) \phi_i(t) \\ &\quad + \frac{\eta_i}{2} \sum_{n=0}^{\infty} \Gamma_n \bar{\psi}_n(t) \left( \psi_{n+1}(t) + \delta_{n>0} \Gamma_{|n-1|} |\psi_{|n-1|}(t) \right), \\ i\dot{\psi}_n(t) &= (E_R n^2 - i\kappa_{a,n}) \psi_n(t) \\ &\quad + \frac{1}{\Gamma_n} \sum_i \eta_i \operatorname{Re} \phi_i(t) \left( \psi_{n+1}(t) + \Gamma_{|n-1|} |\psi_{|n-1|}(t) \right), \end{aligned} \quad (4.17)$$

where  $E_R = \frac{Q^2}{2m}$  is the recoil energy and  $\Gamma_n = \sqrt{1 + \delta_{n,0}}$ . In the limit  $\kappa_{a,n} = 0$  the change in the atom number is  $\partial_t \sum_{n=0}^{N_a} |\psi_n(t)|^2 = \mathcal{O}(\psi_{N_a}(t) \bar{\psi}_{N_a+1}(t))$ . By truncating at a sufficiently high recoil momentum state  $N_a$ , the atom number can be conserved to

arbitrary accuracy. To make our model more realistic, we will choose  $\kappa_{a,0} = 0$  and only let the finite momentum modes have non-zero linewidth. We will discuss this further in section 4.5.1.

#### 4.4.1 Normal-phase fixed point

The classical equations constitutes a system of non-linear first-order differential equations which is conveniently written as

$$\dot{\mathbf{X}} = F(\mathbf{X}), \text{ with } \mathbf{X} = (\phi_1, \bar{\phi}_1, \dots, \phi_{N_c}, \bar{\phi}_{N_c}, \psi_0, \bar{\psi}_0, \dots, \psi_{N_a}, \bar{\psi}_{N_a})^T, \quad (4.18)$$

where  $F$  is defined by eq. (4.17). Even after using the symmetry to remove redundant information, the dimension of the set of non-linear equations is  $2N_c + 2(N_a + 1)$ . The combination of a large dimensionality and the non-linearity makes an analytical solution to the full problem impossible. Even the steady-state solution is challenging to find because Fourier transforming from time to energy introduces convolutions, turning the differential equations into integral equations that are not easier to solve. However, a perturbative analytic approach is possible if one knows a solution that is a fixed point  $\mathbf{X}_0$  of the evolution such that  $F(\mathbf{X})|_{\mathbf{X}=\mathbf{X}_0} = 0$ . The system has one well-known fixed point, namely the one describing the normal phase (NP). In the NP the atoms are all in the motional ground state, and the cavity has no coherent field. The fixed point is easily verified by substituting  $\phi_i = \psi_{n>0} = 0$  and  $\psi_0 = 1$  into eq. (4.17). Around a fixed point, the behavior of the complicated system can be simplified by considering the fluctuations around the fixed point described by  $\mathbf{u} = \mathbf{X}_0 - \mathbf{X}$ . Close to  $\mathbf{X}_0$ , the dynamics of the system are well approximated by the linearized dynamics described by the Jacobian  $\nabla F(\mathbf{X})$  evaluated at the fixed point. The behavior of the linearized dynamics can then be understood by finding the EVs of  $\nabla F(\mathbf{X})|_{\mathbf{X}=\mathbf{X}_0}$ . The EVs are related to the linear response of the system, which is described by the retarded propagator [13]. In the thermodynamic limit the poles of the retarded propagator, we discussed in chapter 3, are equivalent to the EVs from our linear stability analysis [108]. Note that in our linear stability analysis, the real and imaginary part of the EVs have the opposite physical interpretation of the poles.

#### Jacobian at fixed point

To find the Jacobian, one takes derivatives of  $F(\mathbf{X})$  with respect to the different fields (and the conjugate fields). As we will evaluate this at the NP fixed point, many elements in  $F(\mathbf{X})$  can be neglected. The fluctuations that will interact with the rest of the system have a quadratic term with one of the factors being  $\psi_0$  ( $\bar{\psi}_0$ ) as this is the only field that has a non-zero value in the NP. All the fields which equation of motion (EOM) do not



contain such a term are uncoupled around  $\mathbf{X}_0$  and do not affect the dynamics. The only fields obeying this constraint are the cavity fields and the recoil momentum mode such that the relevant part of  $F(\mathbf{X})$  is

$$\begin{aligned} F(\phi_j) &= (-i\Delta_j - \kappa_j)\phi_j - i\frac{\eta_j}{\sqrt{2}}(\bar{\psi}_0\psi_1 + \bar{\psi}_1\psi_0), \\ F(\psi_1) &= (-iE_R - \kappa_{a,1})\psi_1 - i\sum_j \frac{\eta_j}{\sqrt{2}}(\bar{\phi}_{j_i} + \phi_j)\psi_0. \end{aligned} \quad (4.19)$$

Because the cavity fields do not couple directly to each other we can write the Jacobian, evaluated at the fixed point, in a block form

$$L_0 = \nabla F(\mathbf{X})|_{\mathbf{X}=\mathbf{x}_0} = \begin{pmatrix} \mathbf{A}_0 & 0 & \cdots & 0 & \mathbf{B}_0 \\ 0 & \mathbf{A}_1 & 0 & \cdots & \mathbf{B}_1 \\ \vdots & & \ddots & \vdots & \vdots \\ 0 & \cdots & \cdots & \mathbf{A}_{N_c} & \mathbf{B}_{N_c} \\ \mathbf{C}_0 & \mathbf{C}_1 & \cdots & \mathbf{C}_{N_c} & \mathbf{D} \end{pmatrix} = \begin{pmatrix} \mathbf{A} & \mathbf{B} \\ \mathbf{C} & \mathbf{D} \end{pmatrix}. \quad (4.20)$$

The  $\mathbf{A}$  block is of size  $2N_c \times 2N_c$  and is diagonal. One can split  $\mathbf{A}$  into  $N_c$  blocks of dimension  $2 \times 2$  describing the different cavity modes. The  $\mathbf{B}$  ( $\mathbf{C}$ ) block is rectangular with the shape  $2N_c \times 2$  ( $2 \times 2N_c$ ) and can again be split into  $2 \times 2$  blocks for each cavity mode. The three different types of  $2 \times 2$  matrices are

$$\begin{aligned} \mathbf{A}_j &= \text{diag}(\{-i\Delta_j - \kappa_j, i\Delta_j - \kappa_j\}), \\ \mathbf{B}_j = \mathbf{C}_j &= -i\frac{\eta_j}{\sqrt{2}}(\sigma_z + i\sigma_y), \\ \mathbf{D} &= \text{diag}(\{-iE_R - \kappa_{a,1}, iE_R - \kappa_{a,1}\}). \end{aligned} \quad (4.21)$$

The Jacobian obeys the symmetry

$$\Pi^x L_0 \Pi^x = \bar{L}_0, \quad (4.22)$$

with  $\Pi^x = \mathbf{1}_{N_c+1} \otimes \sigma^x$ , where  $\mathbf{1}_{N_c+1}$  is the  $(N_c + 1)$ -dimensional identity matrix and  $\sigma^x$  is the first Pauli matrix. The transformation is involutory ( $\Pi^x \Pi^x = \mathbf{1}_{2N_c+2}$ ) meaning that the eigenvalues of  $L_0$  must either be purely real or come in complex conjugate pairs.

### Eigenvalues of Jacobian

To compute the EVs  $\lambda$  of  $L_0$  one has to solve the characteristic equation which is given by  $\text{Det}(L_0 - \mathbf{1}\lambda) = 0$ . Using the Schur complement, the determinant can be written as

$$\text{Det}(L_0 - \mathbf{1}\lambda) = \text{Det}(\mathbb{A} - \mathbf{1}\lambda) \text{Det}(\mathbf{D} - \mathbf{1}\lambda - \mathbf{B}^T (\mathbb{A} - \mathbf{1}\lambda)^{-1} \mathbf{B}) = 0. \quad (4.23)$$

This rewriting is valid as long as  $\lambda$  is not an EV of  $\mathbb{A}$  and the EV equation further simplifies to only finding the root of the Schur complement, which is the second determinant factor in eq. (4.23). As all cavity interactions are mediated by the atoms, the third term in the Schur complements can be written as a sum over cavity modes such that the EV problem takes the form

$$\text{Det} \left( \mathbf{D} - \mathbf{1}\lambda - \sum_{j=0}^{N_c} \mathbf{B}_j (\mathbf{A}_j - \mathbf{1}\lambda)^{-1} \mathbf{B}_j \right) = 0. \quad (4.24)$$

In the linear stability analysis, the phase transition to the superradiant state (SR) is signaled by a mode becoming unstable. With our chosen definitions, the real part of the EVs determines the stability of the modes. If the real part is negative then the mode decays exponentially and is, therefore, stable. If the real part of the EV is positive, then the mode grows exponentially, and the system will move away from the fixed point exponentially as a function of time. A marginally stable mode is one in which the real part of its EV vanishes. Without coupling ( $\eta_i = 0 \forall i$ ) the EVs are given by the elements of  $\mathbf{A}_j$  and  $\mathbf{D}$ . They all have a negative real part, meaning that in the NP, all modes are stable and relax exponentially quickly to the NP fixed point. As the coupling is switched on, the cavity modes and atom clouds start interacting, leading to the frequency (imaginary part of the EV) and the real part changing from the bare values.

Within the field of classical dynamics, the change of the fixed point's stability is known as a bifurcation, and the point at which the real part of the EV becomes zero is the critical point. The distinction between a phase transition and a bifurcation is that a phase transition can only exhibit singular features in the thermodynamic limit [148]. Bifurcations are sharp features even for finite dimensional systems but only exhibit singular features in the infinite time limit. For mean-field phase transitions, the thermodynamic limit becomes analogous to the infinite time limit of bifurcations [148, 149]. Our classical equations are equivalent to mean-field equations such that the bifurcation is analogous to a phase transition.

To identify the critical point, the EV problem for the Jacobian must be solved under the constraint that the real part of the EV is zero, namely  $\lambda \rightarrow i\omega$  with  $\omega$  being a real number. This direct substitution simplifies the EV problem in eq. (4.24), and the form

for the  $j$ th cavity-mode sector is found to be

$$\mathbf{B}_j (\mathbf{A}_j - i\mathbf{1}\omega) \mathbf{B}_j = i (\beta_{r,j}(\omega) + i\beta_{i,j}(\omega)) \begin{pmatrix} -1 & -1 \\ 1 & 1 \end{pmatrix}, \quad (4.25)$$

where the  $\beta$ 's are given by

$$\begin{aligned} \beta_{r,j}(\omega) &= \Delta_j \eta_j^2 \frac{\kappa_j^2 + \Delta_j^2 - \omega^2}{\omega^4 + 2\omega^2 (\kappa_j^2 - \Delta_j^2) + (\kappa_j^2 + \Delta_j^2)^2}, \\ \beta_{i,j}(\omega) &= \frac{-2\Delta_j \kappa_j \eta_j^2 \omega}{\omega^4 + 2\omega^2 (\kappa_j^2 - \Delta_j^2) + (\kappa_j^2 + \Delta_j^2)^2}. \end{aligned} \quad (4.26)$$

From these mode-dependent quantities, one can define the total quantities that are just the sum over all cavity modes  $\beta_{r/i} = \sum_j \beta_{r/i,j}$  and the characteristic equation for the EV problem is simplified to computing the determinant of a  $2 \times 2$  matrix

$$\begin{aligned} \text{Det} \begin{pmatrix} -iE_R - \kappa_{a,1} - i\omega + i\beta(\omega) & i\beta(\omega) \\ -i\beta(\omega) & iE_R - \kappa_{a,1} - i\omega - i\beta(\omega) \end{pmatrix} \\ = E_R^2 - 2E_R\beta(\omega) + \kappa_{a,1}^2 + 2i\kappa_{a,1}\omega - \omega^2 = 0, \end{aligned} \quad (4.27)$$

with  $\beta = \beta_r + i\beta_i$ . Separating into real and imaginary parts, we finally arrive at two coupled equations

$$\begin{aligned} E_R^2 - 2E_R \sum_j \beta_{r,j}(\omega) + \kappa_{a,1}^2 - \omega^2 &= 0, \\ \kappa_{a,1}\omega - E_R \sum_j \beta_{i,j}(\omega) &= 0. \end{aligned} \quad (4.28)$$

The critical parameter for these equations is the total coupling strength  $\Lambda$  which can be made more explicit by writing  $\eta_j^2 = \Lambda c_j^2$  where

$$\sum_j c_j^2 = 1. \quad (4.29)$$

The coefficient  $c_j^2$  represents the relative amount of pump power/coupling strength in the  $j$ th sideband. For the sinusoidal phase modulation in chapter 3 the  $c_j$ 's were Bessel functions set by the modulation depth. In this generalized model, we chose the  $c_j$ 's freely, assuming that the pump sideband can be freely designed. Notice that compared to the chapter 3,  $\Lambda$  here is defined as the square of its counterpart.

The total coupling strength is determined by  $\Lambda$ , meaning that the two equations in (4.28) are used to determine the two unknowns  $\omega$ , and  $\Lambda_c$  were, to iterate,  $\Lambda_c$  is related to the total critical coupling strength at which the mode with frequency  $\omega$  becomes

undamped. To solve the coupled equations in eq. (4.28),  $\Lambda_c$  is isolated in the first equation and then substituted into the second. The result is an equation for  $\omega$  of the form

$$\omega \sum_{j=0}^{N_c-1} c_j^2 \Delta_j \frac{\kappa_j (E_r^2 + \kappa_{a,1}^2 - \omega^2) + \kappa_{a,1} (\Delta_j^2 + \kappa_j^2 - \omega^2)}{\omega^4 + 2\omega^2 (\kappa_j^2 - \Delta_j^2) + (\Delta_j^2 + \kappa_j^2)^2} = 0. \quad (4.30)$$

By writing all terms with a common denominator, the structure of the equation becomes more transparent

$$\begin{aligned} \omega \sum_{j=0}^{N_c-1} c_j^2 \Delta_j (\kappa_j (E_R^2 + \kappa_{a,1}^2) + \kappa_{a,1} (\Delta_j^2 + \kappa_j^2) - \omega^2 (\kappa_{a,1} + \kappa_j)) \\ \times \prod_{i \neq j} (\omega^4 + 2\omega^2 (\kappa_i^2 - \Delta_i^2) + (\Delta_i^2 + \kappa_i^2)^2) = 0. \end{aligned} \quad (4.31)$$

As this equation contains high powers of  $\omega$ , there will be several solutions. Only solutions with a real  $\omega$  are valid, and further, the only physical solutions are the ones with real values for the critical coupling

$$\Lambda_c = \frac{E_R^2 + \kappa_{a,1}^2 - \omega^2}{2E_R \sum_{j=0}^{N_c-1} c_j^2 \frac{(\Delta_j^2 + \kappa_j^2 - \omega^2) \Delta_j}{\omega^4 + 2\omega^2 (\kappa_j^2 - \Delta_j^2) + (\Delta_j^2 + \kappa_j^2)^2}}. \quad (4.32)$$

#### 4.4.2 One-mode cavity

The simplest case is when only a single cavity mode is relevant such that  $c_0^2 = 1$  and the critical frequency equation (4.31) simplifies to

$$\begin{aligned} \omega (\kappa_{a,1} (\kappa_0^2 + \Delta_0^2 - \omega^2) + \kappa_0 (\kappa_{a,1}^2 + E_R^2 - \omega^2)) = 0, \\ \rightarrow \omega = 0 \text{ or } \omega^2 = \frac{(\kappa_0^2 + \Delta_0^2) \kappa_{a,1} + (\kappa_{a,1}^2 + E_R^2) \kappa_0}{\kappa_{a,1} + \kappa_0}. \end{aligned} \quad (4.33)$$

Experimentally the atom loss is the smallest loss rate and the non-trivial solution can be linearized around  $\kappa_{a,1} = 0$

$$\omega^2 = E_R^2 + \frac{\kappa_{a,1}}{\kappa_0} (\kappa_0^2 + \Delta_0^2 - E_R^2) + \mathcal{O}(\kappa_{a,1}^2). \quad (4.34)$$

In the limit of small  $\kappa_{a,1}/\kappa_0$ , we get

$$\omega \approx \pm \left( E_R + \frac{\kappa_{a,1}}{\kappa_0} (\kappa_0^2 + \Delta_0^2 - E_R^2) \right). \quad (4.35)$$

The instability has an energy equal to the recoil energy but with a shift proportional to  $\kappa_{a,1}/\kappa_0$ . The direction of the shift is set by  $\text{sign}(\Delta_0^2 + \kappa_0^2 - E_R^2)$ . For ultracold atomic systems  $\kappa_{1,a} \ll \kappa_0$ , so when  $\Delta_0^2 + \kappa_0^2 - E_R^2 < 0$ , then the frequency of the instability is slightly below the recoil energy and slightly above recoil when the amplitude of the cavity detuning is above the recoil energy.

For physical solutions, the corresponding coupling strengths have to be real, meaning that  $\Lambda_c \geq 0$ . For the zero-frequency solution, the critical coupling is

$$\Lambda_c|_{\omega=0} = \frac{(E_R^2 + \kappa_{a,1}^2)(\Delta_0^2 + \kappa_0^2)}{2E_R\Delta_0}, \quad (4.36)$$

which is equivalent to the well-known single mode result [107]. As long as  $\Delta_0 > 0$ , the critical value will be real, and the zero-frequency solution is physical. For the solution with a frequency around the recoil energy, we can expand to linear order in  $\omega^2$  around the recoil energy and neglect all terms proportional to  $\kappa_{a,1}^2$ . To keep the structure clear, we have expressed everything in units of the recoil energy

$$\Lambda_c|_{\omega \approx 1} = -\frac{1 + 2(\kappa_0^2 - \Delta_0^2) + (\kappa_0^2 + \Delta_0^2)^2}{2\Delta_0(\kappa_0^2 + \Delta_0^2 - 1)}(\omega^2 - 1) + \mathcal{O}(\omega^2 - 1)^2, \quad (4.37)$$

The sign of  $\Lambda_c$  determines if a mode at  $\omega$  can become unstable in a physical system. To that extent, we first consider the structure of the numerator. It is of the form  $\Delta_0^4 - 2b\Delta_0^2 + c$  with  $b = 1 - \kappa_0^2$  and  $c = 1 + 2\kappa_0^2 + \kappa_0^4$ . For this numerator to have node for some value of  $|\Delta_0|$ , there must be real solutions to

$$\Delta_0^2 = b \pm \sqrt{b^2 - c}. \quad (4.38)$$

This requires that

$$\begin{aligned} b^2 &\geq c \\ 1 - 2\kappa_0^2 + \kappa_0^4 &\geq 1 + 2\kappa_0^2 + \kappa_0^4 \\ -\kappa_0 &\geq \kappa_0, \end{aligned} \quad (4.39)$$

which is only possible when the cavity mode has no loss. At  $\Delta_0 = 0$  the numerator in eq. (4.37) is positive and as it has no nodes, the numerator must stay positive for all values of  $|\Delta_0|$  and  $\kappa_0 > 0$ . With the sign of the numerator known, we look at the factor in parenthesis in the denominator of eq. (4.37). This term has a negative sign when the magnitude of the cavity detuning is below the recoil energy by more than  $\kappa_0$ . In this regime, it was found in eq. (4.35) that the frequency will be below the recoil, and the sign from the parenthesis, therefore, cancels against the sign from  $\omega^2 - 1$ . When  $\kappa_0^2 + \Delta_0^2 - 1 > 1$ , then the parenthesis and  $\omega^2 - 1$  are both positive. This means that the

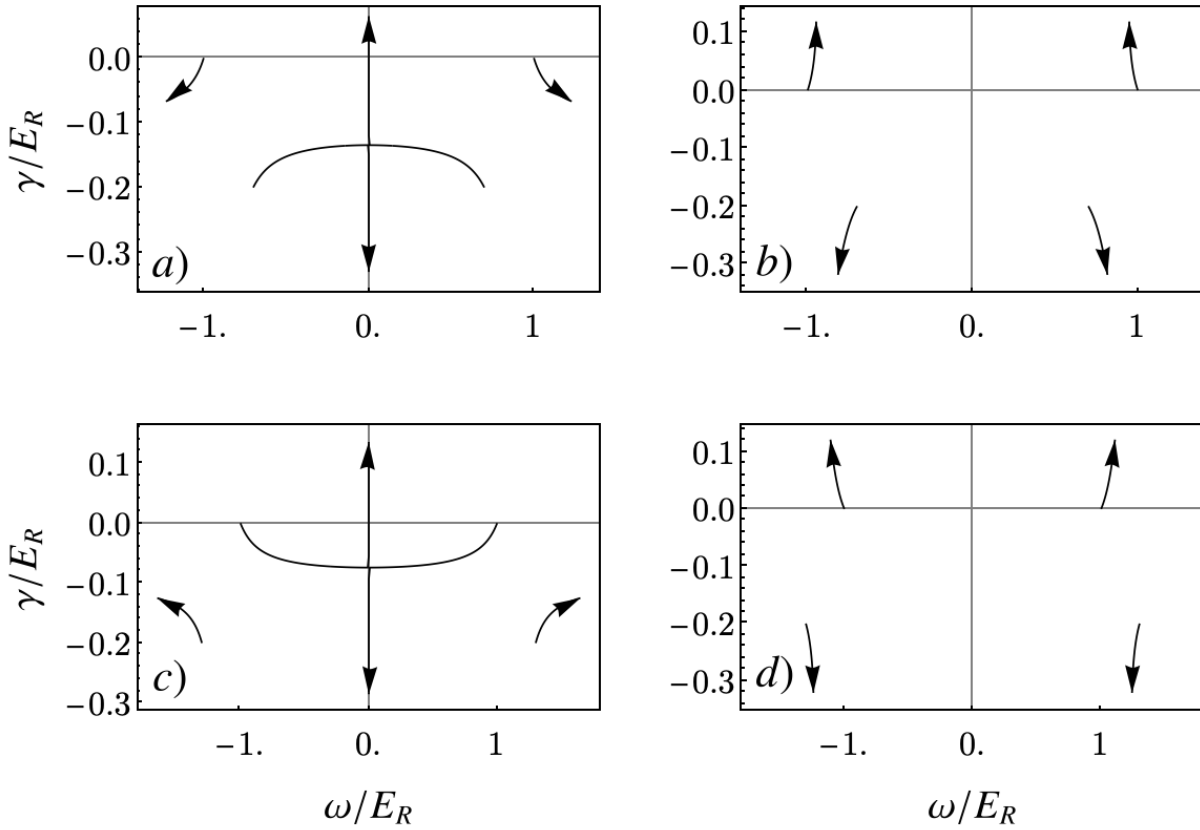


Figure 4.1: Frequency and damping of the fluctuations for a non-interacting BEC in a single cavity mode, as the coupling strength is increased. The fluctuations are described by the EVs of the linearized dynamics. The x-axis represents the EV's imaginary part (frequency), and the y-axis represents the EV's real part (loss/drive). Each line represents the path an EV takes as the coupling increases, and the arrows indicate the direction of increasing coupling strength. When a EV pair hits  $\gamma = 0$ , the mode changes from decaying to growing. The four different plots shows different detunings for the cavity mode: a)  $0.7E_R$ , b)  $-0.7E_R$ , c)  $1.3E_R$ , d)  $-1.3E_R$ . The cavity has a loss rate of  $\kappa = 1/5E_R$  while for the recoil momentum state, the loss has been chosen as  $10^{-8}E_R$ .

only sign we can use to make this instability physical is to change the sign of the detuning such that  $\Delta_0 < 0$ . Therefore, the cavity has to sit below the pump frequency. As this happens, one observes that  $\Lambda_c$  is proportional to  $\omega^2 - 1$ , which was shown in eq. (4.34) to be of order  $\kappa_{a,1}/\kappa_0$ . The critical coupling in the relevant experimental limit will therefore be very small. The smallness of the coupling means that no polariton will have formed, and the unstable mode will be energetically purely atomic. For this reason, we denote this instability as the atomic instability. It is experimentally unwanted as it does not lead to a coherent field in the cavity. Because there is no cavity field to stabilize atoms, the cloud is broken apart in a process that can be thought of as heating of the atom cloud. This should be compared to the zero-frequency instability, which is a polaritonic instability due to the finite coupling strength. The cavity part of the polariton is lossy and can dissipate the energy from the pump, thereby mitigating the heating.

While the linear stability analysis does not give us all the information about the SR phase, it does describe the excitations of the system in the NP that becomes unstable. To understand how the system becomes unstable, we investigate the EVs of the system as the coupling strength increases. For  $\Lambda = 0$ , the cavity mode leads to two EVs with imaginary values equal to  $\pm\Delta_0$  and a negative real part equal to  $\kappa_0$ . The atom recoil mode gives rise to two EVs at  $\pm E_R$  and a small negative real part due to  $\kappa_{a,1}$ . As  $\Lambda$  increases, the EVs start coupling, and consequently move in the complex plane. Due to the symmetry of the Jacobian in eq. (4.22), the EVs always come in complex conjugate pairs.

The movement of the EVs is shown for four different cavity detunings in fig. 4.1. Here each EV is written as  $\lambda = \gamma + i\omega$  with  $\gamma, \omega$  being real. The horizontal axis at  $\gamma = 0$  is denoted as the  $\omega$ -axis, and the vertical axis at  $\omega = 0$  is referred to as the  $\gamma$ -axis. For a positive detuned cavity with a detuning less than the recoil, we observe, in fig. 4.1a, that the frequency of the EVs that start out being purely photon-like moves symmetrically towards the  $\gamma$ -axis. Once their frequency hit zero, one becomes unstable by crossing the  $\omega$ -axis into the  $\gamma > 0$  plane. We denote this as a zero-frequency instability. Similarly, in fig. 4.1c, the system also develops a zero-frequency instability, but because  $\Delta_0 > E_R$ , the EV that initially belonged to the atomic mode is the EV being pushed towards zero frequency. For both positively detuned cases in fig. 4.1(a,c), the cavity and atom EVs are attracted towards each other along the  $\gamma$ -direction and subsequently repel along the  $\omega$ -direction until the frequency of an EV pair becomes zero.

Consider now the negatively detuned case in fig. 4.1(b, d). In both these cases, the atomic instability is observed as the atomic EV is immediately pushed into the  $\gamma > 0$  plane. Figure 4.1(b, d) shows the atom mode shifts its frequency depending on the magnitude of the cavity detuning as predicted in eq. (4.35). Notice that for the negative

detuning case, we have gone far beyond the threshold value to exaggerate the minute effects discussed for this situation. The negatively detuned cavity mode behaves opposite to its positively detuned counterpart as it has a repulsive interaction with the atom mode along the  $\gamma$ -axis but an attractive interaction along the  $\omega$ -axis.

### 4.4.3 Two-mode cavity

For the single mode case, we see either an unstable polariton at zero frequency and finite coupling strength or an unstable atom mode with a frequency close to the recoil energy at infinitesimal coupling. We now investigate how the situation changes by including a second cavity mode. First, we note that  $\omega = 0$  always solves eq. (4.31), but the additional mode changes the critical coupling as was seen in chapter 3. The critical coupling of the zero-frequency instability is found from eq. (4.32)

$$\begin{aligned} \Lambda_c|_{\omega=0} &= \frac{1 + \kappa_{a,1}^2}{2 \left( c_0^2 \frac{\Delta_0}{\Delta_0^2 + \kappa_0^2} + c_1^2 \frac{\Delta_1}{\Delta_1^2 + \kappa_1^2} \right)} \\ &= \frac{(1 + \kappa_{a,1}^2) (\Delta_0^2 + \kappa_0^2) (\Delta_1^2 + \kappa_1^2)}{2 \left[ c_0^2 \left( \Delta_0 (\Delta_1^2 + \kappa_1^2) - \Delta_1 (\Delta_0^2 + \kappa_0^2) \right) + \Delta_1 (\Delta_0^2 + \kappa_0^2) \right]}, \end{aligned} \quad (4.40)$$

where the normalization of the  $c_j$ 's, from eq. (4.29), has been used to eliminate  $c_1$  and everything has been written in units of recoil energy. As a consistency check one sees that  $c_0 = 1$ , leads to the the single mode result in eq. (4.36). The zero-frequency solution is only physical if the critical coupling is positive. The numerator only contains squared terms, such that the sign is set by the denominator

$$c_0^2 \left( \Delta_0 (\Delta_1^2 + \kappa_1^2) - \Delta_1 (\Delta_0^2 + \kappa_0^2) \right) + \Delta_1 (\Delta_0^2 + \kappa_0^2). \quad (4.41)$$

As  $c_0^2$  is always less than one in the two-mode case, this solution is always physical when both  $\Delta_i > 0$ . If one of the detunings (here we chose  $\Delta_1$ ) is negative, then the zero-frequency solution is only physical if the couplings of the two modes are distributed such that

$$c_0^2 > \frac{|\Delta_1|}{\Delta_0 (\Delta_1^2 + \kappa_1^2) (\Delta_0^2 + \kappa_0^2)^{-1} + |\Delta_1|}. \quad (4.42)$$

As long as the positively detuned mode couples strongly enough to compensate the atomic instability, the system can exhibit a zero-frequency instability even when one mode acquires a negative detuning.

Consider now the finite frequency instabilities with  $\Delta_1 < 0$  and  $|\Delta_1| \neq \Delta_0$ . Already for two modes, eq. (4.31) have six free parameters. We consider only part of this



high-dimensional parameter space to make the expressions less unwieldy. Guided by the experimentally relevant regime, the atom loss is kept infinitesimally small ( $\kappa_{a,1} \rightarrow 0$ ). It is also assumed that the two cavity modes have the same linewidth ( $\kappa_0 = \kappa_1 = \kappa$ ), which for two similar modes in a high-quality cavity is a good approximation. The unstable polariton frequencies (up to linear order in  $\kappa_{a,1}$ ) are then given as the solutions of

$$c_0^2 \Delta_0 \left( 1 - \omega^2 + \frac{\kappa_{a,1}}{\kappa} (\Delta_0^2 + \kappa^2 - \omega^2) \right) \left( \omega^4 + 2\omega^2(\kappa^2 - \Delta_1^2) + (\kappa^2 + \Delta_1^2)^2 \right) + c_1^2 \Delta_1 \left( 1 - \omega^2 + \frac{\kappa_{a,1}}{\kappa} (\Delta_1^2 + \kappa^2 - \omega^2) \right) \left( \omega^4 + 2\omega^2(\kappa^2 - \Delta_0^2) + (\kappa^2 + \Delta_0^2)^2 \right) = 0, \quad (4.43)$$

The first parenthesis of each term is similar to the atomic instability observed in the single mode case. For the atomic instability, it was found that a slight perturbation of the frequency away from the recoil energy was necessary to predict the physicality of the instability. The sign of the frequency shift in eq. (4.35) was given by the sign of  $\Delta_i^2 + \kappa^2 - 1$ . When the factors of  $\Delta_i^2 + \kappa^2 - 1$  have the same sign in both terms, we can make both terms arbitrarily small simultaneously by inserting the same atom-instability frequency for  $\omega$ . We, therefore, expand the two-mode version of eq. (4.32) in  $\omega^2$  to linear order around the recoil energy

$$\Lambda_c|_{\omega=\pm 1} = -\frac{\omega^2 - 1}{2 \left( \frac{c_0^2 \Delta_0 (\Delta_0^2 + \kappa^2 - 1)}{1 + 2(\kappa^2 - \Delta_0^2) + (\kappa^2 + \Delta_0^2)^2} - \frac{c_1^2 |\Delta_1| (\Delta_1^2 + \kappa^2 - 1)}{1 + 2(\kappa^2 - \Delta_1^2) + (\kappa^2 + \Delta_1^2)^2} \right)} + \mathcal{O}(\omega^2 - 1)^2. \quad (4.44)$$

The denominators of each of the two sub-fractions have the same form as the numerator discussed in eq. (4.38), and it was always found to be positive. The only sign-change possible is changing the magnitudes of the detunings (as we have chosen their signs). When both detunings satisfy  $\Delta_i^2 + \kappa^2 - 1 < 0$ , both denominators have a sign change. The sign change is canceled out by  $\omega^2$  being slightly below recoil. The same thing happens in the opposite case where  $\Delta_i^2 + \kappa^2 - 1 > 0$ . The system is therefore "protected" against the atomic instability as long as

$$\frac{c_0^2 \Delta_0 (\Delta_0^2 + \kappa^2 - 1)}{1 + 2(\kappa^2 - \Delta_0^2) + (\kappa^2 + \Delta_0^2)^2} > \frac{c_1^2 |\Delta_1| (\Delta_1^2 + \kappa^2 - 1)}{1 + 2(\kappa^2 - \Delta_1^2) + (\kappa^2 + \Delta_1^2)^2}. \quad (4.45)$$

To extract some physical insight from this, consider the case with equal atom coupling  $c_0^2 = 1/2 = c_1^2$  and small  $\kappa$ . If both magnitudes are much larger than the recoil energy, then both sides scale inversely with the magnitude of the detuning

$$\frac{1}{\Delta_0} > \frac{1}{|\Delta_1|}. \quad (4.46)$$

The system is therefore protected against the atomic instability when  $\Delta_0 < |\Delta_1|$ . When both magnitudes of the detunings are significantly below the recoil, then the two sides scale linearly with the magnitude of the detuning

$$\Delta_0 > |\Delta_1|, \quad (4.47)$$

and one arrives at the opposite condition for having the system protected against the atomic instability. Interpolating between these two cases shows that the equally coupled system is protected against the atomic instability as long as the magnitude of the positive detuning is between the magnitude of the negative detuning and the recoil energy. This prediction is consistent with the observations in fig. 4.1, as it states that a positive detuning pulls the atom EV deeper into the  $\gamma < 0$  plane, making it more stable. In contrast, the negatively detuned mode has a repulsive interaction with the atom EV and therefore tries to push the atom EV into the  $\gamma > 0$  plane. To avoid the atomic instability, the positive detuning must therefore be in between the negative detuning and the recoil energy.

The two-mode critical frequency equation in eq. (4.43) has solutions which are neither at  $\omega = 0$  nor  $\omega \approx 1$  and these can be found by solving

$$\omega^4 (c_0^2 \Delta_0 + c_1^2 \Delta_1) + 2\omega^2 (2\kappa^2 - \Delta_1^2 - \Delta_0^2) + \Delta_0^4 + \Delta_1^4 + 2\kappa^2 (\Delta_0^2 + \Delta_1^2) + \kappa^4 = 0, \quad (4.48)$$

which is a quadratic equation for  $\omega^2$  with the solution

$$\omega^2 = \frac{(\Delta_1^2 + \Delta_0^2 - 2\kappa^2)}{(c_0^2 \Delta_0 + c_1^2 \Delta_1)} \pm \sqrt{\left( \frac{2\kappa^2 - \Delta_1^2 - \Delta_0^2}{c_0^2 \Delta_0 + c_1^2 \Delta_1} \right)^2 - \frac{\Delta_0^4 + \Delta_1^4 + 2\kappa^2 (\Delta_0^2 + \Delta_1^2) + \kappa^4}{c_0^2 \Delta_0 + c_1^2 \Delta_1}}. \quad (4.49)$$

Whenever this is positive and real, the frequency can potentially lead to a physical instability. We consider a few different cases to extract insight from the solution, which are shown in fig. (4.2). For simplicity, we let the two cavity modes couple equally strongly to the atoms. In fig. 4.2a, the negatively detuned mode has an initial detuning with a magnitude between the positively detuned mode and the recoil energy. Here the atomic instability happens immediately due to the repulsive interaction between the negatively detuned cavity mode and the atom mode. When the magnitudes of the two cavity detunings are exchanged in fig. 4.2b, it is instead observed that the atom EV is pulled down and pushes the closest cavity EV towards zero frequency. However, its path is obstructed by the negatively detuned cavity mode, which moves towards the atom mode. As seen in chapter 3 two interacting modes cannot cross each other, and the system instead has an avoided crossing. One of the EVs is then pushed into the  $\gamma > 0$  plane such that a

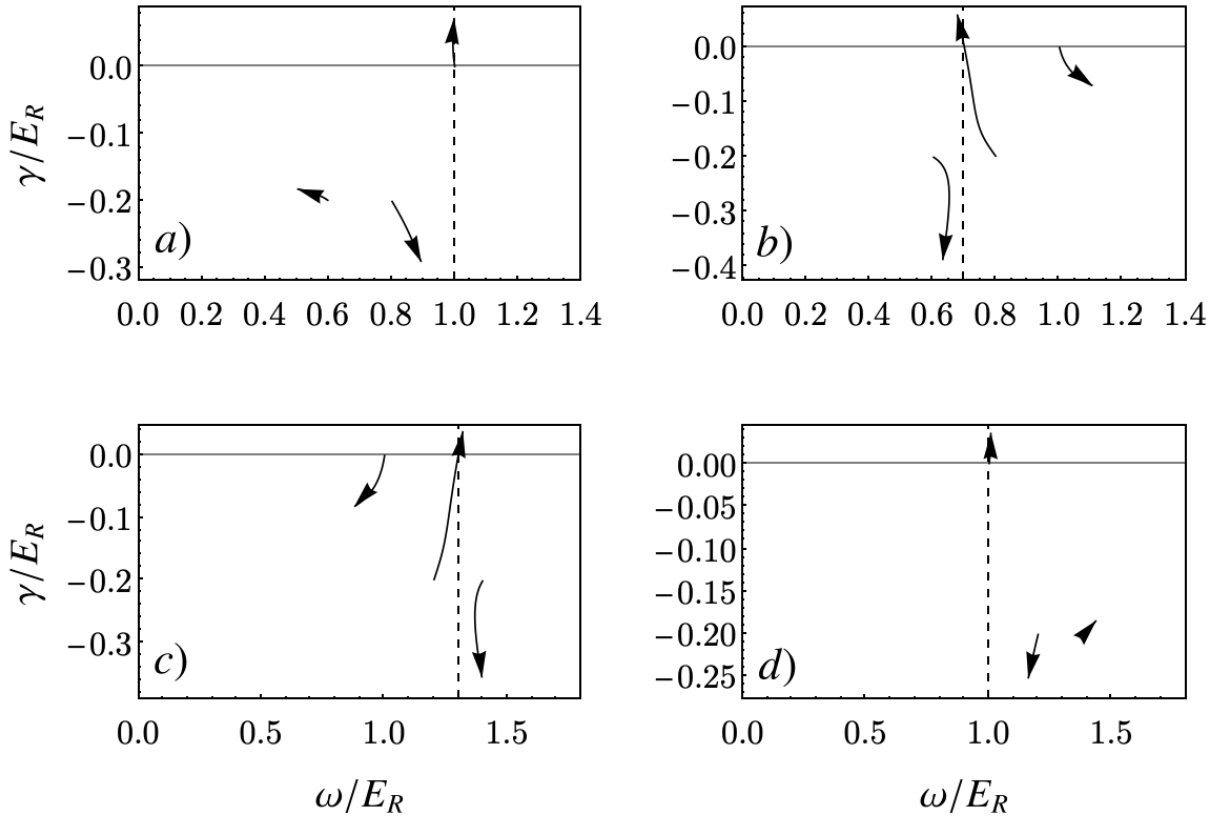


Figure 4.2: A similar plot as fig. 4.1 but for a system with two cavity modes. Due to the symmetry, only the positive frequency axis is shown. For all the plots shown here, the two modes couple equally to the atom:  $c_0 = c_1$  and have identical loss rates:  $\kappa_0 = \kappa_1 = \kappa = 0.2E_R$ . The recoil momentum mode has been given a linewidth of  $\kappa_{a,1} = 10^{-8}E_R$ . The four different plots shows four different detuning cases  $(\Delta_0, \Delta_1)$ : a)  $(0.6, -0.8)$ , b)  $(-0.6, 0.8)$ , c)  $(1.2, -1.4)$ , d)  $(-1.2, 1.4)$ . The dashed line indicates the frequency of the mode that becomes unstable.

polaritonic instability at a finite frequency develops.

The avoided crossing of the EVs is only possible due to the interaction between the modes discussed in chapter 3 and therefore requires a finite coupling strength. The avoided crossing also signifies that the unstable polariton mode is a superposition of both the positively and negatively detuned cavity mode. The comparison to the avoided crossing in chapter 3 is instructive, but the avoided crossing observed does have a fundamental difference. Namely, the two modes interacting are from different Nambu sectors, whereas in chapter 3 the avoided crossing happens between modes in the same Nambu sector. Because the self-energy is constant in Nambu space, two different cavity modes from different Nambu sectors interact as strongly as the same cavity modes within the same Nambu sector. It is because the modes are from different Nambu sectors that the avoided crossing leads to a splitting in the line widths instead of the frequencies as seen in chapter 3.

Using the understanding of repulsion and attraction of the EVs, we expect that if both cavity modes have a magnitude that is large than the recoil energy, then the finite-frequency polaritonic instability can only emerge when the positive mode is closer to the atom mode. This is shown in fig. 4.2c. In this case, the positive mode will move towards a higher frequency, and the atom EV will move toward zero. Due to the mediated interactions between the cavity modes, the positively and negatively detuned modes repel each other along the  $\gamma$  direction, and a finite frequency instability at  $\omega > E_R$  is realized. The finite frequency instability can only be realized by an avoided crossing, and it is, therefore, essential that the two cavity EVs are moving toward each other. If that is not the case, as in fig. 4.2d, then the atomic instability arises at infinitesimal couplings strength.

#### 4.4.4 Four-mode cavity

Introducing a second mode added a qualitatively new feature to polaritonic instability, namely that it acquired a finite and tuneable frequency. How does the situation then change if more cavity modes are included? To answer this question, we consider the case with four cavity modes. With four modes, there are no apparent simplifications of the characteristic equations for the critical parameters. However, with the understanding of EVs movement we have acquired from the one- and two-mode cases, we have a qualitative picture that can be used as a guide. An exciting question one can ask with four modes is if we can generate several polaritonic instabilities at finite frequency. The two instabilities must occur at similar coupling strengths for our linear stability to be valid. From the scenarios seen in fig. 4.2 the simplest solution is to combine fig. 4.2b and fig. 4.2c. In this parameter regime, there are two independent groups of cavity modes. Both groups consist of a positively and a negatively detuned cavity mode. One group has the magnitudes of

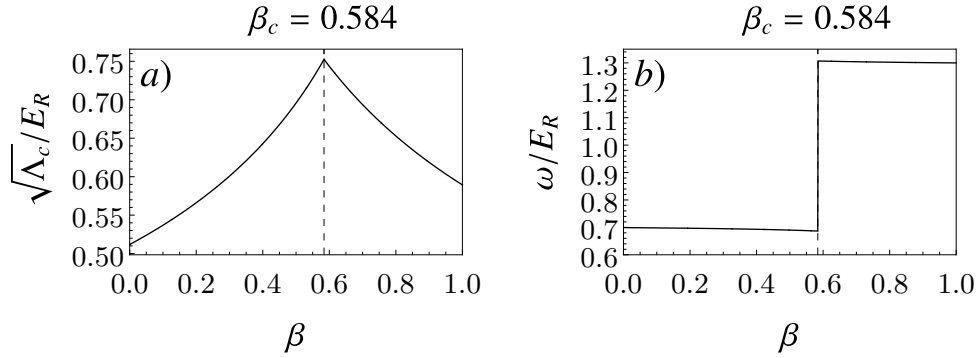


Figure 4.3: *Critical values for a system with four cavity modes that are the combination of the two scenarios in fig. 4.2(b,c) such that the detunings are given by  $\Delta_4 = (-0.6, 0.8, 1.2, -1.4)^T E_R$  and the loss rate for all modes is  $\kappa = 0.2E_R$  while  $\kappa_{a,1} = 10^{-8}E_R$ . The sideband heights are described by eq. (4.50). a) The critical coupling for which the first EV of the linearized equations becomes unstable. b) The corresponding frequency of the critical EV.*

their detunings below the recoil energy as in fig. 4.2b, which we refer to as the below recoil group, and the detunings of the modes in the other groups both have a larger magnitude than the recoil energy as in fig. 4.2c. The second group is therefore referred to as the above recoil group. The modes within each group couple equally strongly to the atomic mode, but the two groups have different coupling strengths to the atoms. Splitting into these two groups has the advantage that non-trivial effects can be investigated while understanding each group individually. To tune between the above recoil versus the below recoil group, we can use a single parameter  $\beta \in \{0, 1\}$  and write the  $c_j$  coefficients as a vector

$$\mathbf{c}_4(\beta) = \frac{1}{\sqrt{2}} \left( \sqrt{1-\beta}, \sqrt{1-\beta}, \sqrt{\beta}, \sqrt{\beta} \right)^T, \quad (4.50)$$

which satisfies the normalization conditions on the coefficients. The corresponding vector containing the detunings of the cavity modes is sorted by the magnitudes and written as

$$\Delta_4 = ( -|\Delta_0|, \Delta_1, \Delta_2, -|\Delta_3| )^T, \quad (4.51)$$

where  $\Delta_{1,2} > 0$  and  $\Delta_{0,3} < 0$ . For simplicity, it is assumed that all the cavity modes have the same loss rate,  $\kappa_i = \kappa < E_R$ .

In fig. 4.3a we plot  $\sqrt{\Lambda_C}$  as a function of  $\beta$  and observe a clear cusp at a critical value  $\beta_c$ . The value of  $\sqrt{\Lambda_C}$  is minimal at the two maximal values of  $\beta$  because, in those cases, one group has all the atom coupling. One group having all the weight at the endpoints is directly reflected in the critical frequency shown in fig. 4.3b, where  $\omega$  has the same frequencies as in fig. 4.2(b,c). As  $\beta$  moves away from either endpoint, the critical coupling

increases in fig. 4.3a because the mode that becomes critical couples less to the atoms, and a larger critical coupling is therefore required to make the mode unstable. At the critical point, the two groups become unstable at the same critical coupling, which generates the cusp. Because the frequency separation between the two groups is large compared to  $\kappa$ , we observe that the unstable frequencies are hardly perturbed when moving away from the endpoints. This scale separation leads to a sharp discrete jump in the critical frequency at the critical point.

In this narrow linewidth regime, we can tune the ratio of the two critical frequencies by simply shifting one of the group's detunings by a constant. Such a shift brings one group closer to  $E_R$ , which will be reflected in the value of  $\beta_c$  by changing such that the group closest to  $E_R$  gets a smaller coupling strength.

The linear analysis shows that we can generate multiple simultaneous instabilities of a polaritonic character. In the recoil resolved regime we see that it is possible to have independent groups of cavity modes becoming unstable and this leads to features in both the critical coupling and the critical frequency that are not smooth.

#### 4.4.5 Phase diagram

The understanding of the interaction between the EVs of the linearized dynamics, can now be used to explain the phase diagram from chapter 3. Using the linear analysis, we have computed the same phase diagram and carefully mapped the frequency of the instability, which is shown in fig. 4.4. We have used the same definition of  $B_m$  and  $\epsilon$  such that the detunings of the cavity modes are given by

$$\Delta_n = \Delta_0 - n\epsilon, \quad (4.52)$$

and the coupling coefficients are determined by  $B_m$  through

$$c_n = J_n(B_m). \quad (4.53)$$

The result in fig. 4.4 highlights that the phase diagram in fig. 3.9, actually contains many different phases. There are two large regions: the zero-frequency region discussed in chapter 3 and the atomic-instability region at a frequency close to the recoil energy. As these two phases are well understood, the focus will be on the other parts of the phase diagram. Consider first the three low-frequency lobes with lighter blue shading. The first thing to notice is that the lower-energy edge of these lobes is almost straight, which signals an abrupt change. The  $\epsilon$  value where the edges occur can be understood by considering the ratios  $\Delta_0/\epsilon$ :  $0.6/0.15 = 4$ ,  $0.6/0.2 = 3$ ,  $0.6/0.3 = 2$ . The ratios are integers,

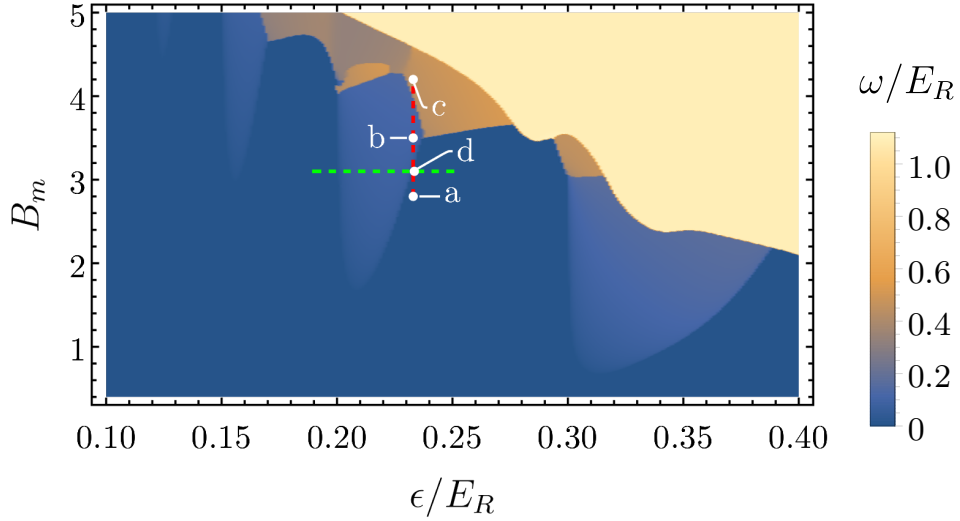


Figure 4.4: Part of the phase diagram computed in fig. 3.9 with the frequency of the first unstable mode indicated by the color code. The detuning of the cavity modes is set by  $\epsilon$  through eq. (4.53) while  $B_m$  determines the modes' coupling to the atoms through eq. (4.52). The two dashed lines represent the scans in fig. 4.6. The white dots indicate different phases, which EV dynamics are shown in fig. 4.5. The parameters are equal to those in fig. 3.9 such that  $\Delta_0 = 0.6E_R$  and  $\kappa = 0.05E_R$ . The atom broadening is  $\kappa_{a,1} = 10^{-8}E_R$  and seven cavity modes have been included. The results are converged with respect to both atom broadening and the number of cavity modes.

meaning that if one, for example, considers the  $\epsilon = 0.3E_R$  lobe, then by absorbing two Floquet photons, the corresponding effective detuning will be zero or in the sideband picture of the effective model: the detuning of the  $n = 2$  cavity mode becomes zero. The lobes, therefore, arise because a mode gets a slightly negative detuning. The fact that the detuning is only slightly negative explains why the critical mode's frequency is small within these lobes. To illustrate this, we consider the EVs' movement as a function of coupling strength.

As cavity modes interact, the EVs cannot be associated with one specific mode. To this extent, we will refer to the EVs that have their frequencies pushed away from the recoil energy as the positive EVs to connect with a positively detuned cavity mode. For the same reason, we will refer to the EVs that move towards the recoil energy in the  $\omega$ -direction as negative EVs.

The EVs' movement at the point  $b$  in fig. 4.4 has been plotted in fig. 4.5b. The negative EV is close to  $\omega = 0$  and interacts with the positive EV at a small frequency. Because the interaction happens at a small frequency, so does the instability.

For larger  $\epsilon$ , the mode that becomes negatively detuned is a lower-order cavity mode, which means that the coupling coefficient  $c_n$  in eq. (4.52), acquires an appreciable value for smaller modulation depth  $B_m$ . The lobes at larger  $\epsilon$  therefore also appear at smaller

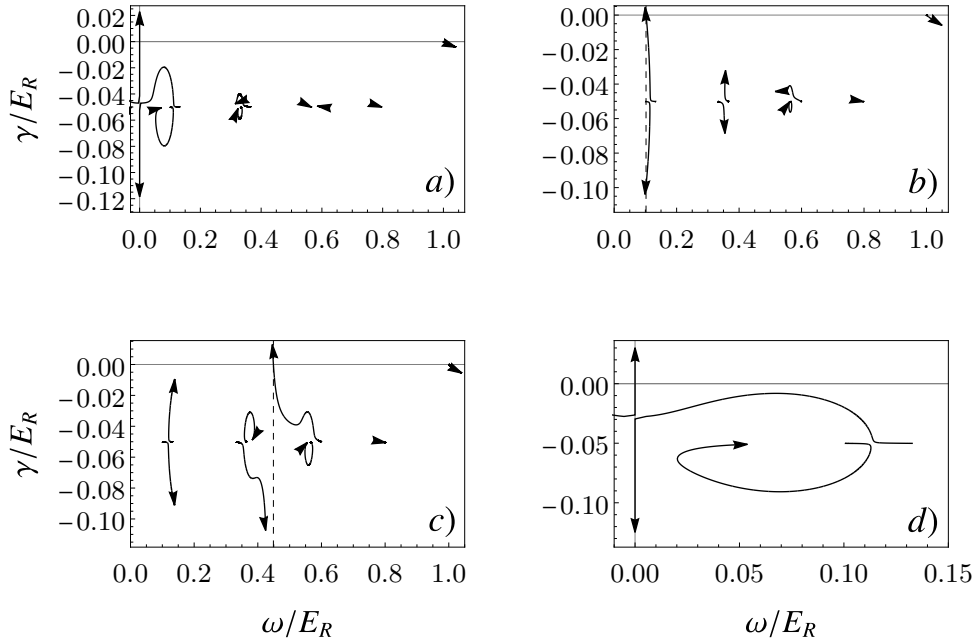


Figure 4.5: *The EVs dynamics in the four different phases indicated by the dots in fig. 4.4. The number of cavity modes is equal to the number of modes used to compute the phase diagram in fig. 4.4.*

values of  $B_m$ .

Looking closely at fig. 4.4 we observe a very faint lobe emerging at  $\epsilon_c \approx 0.12E_R$  and for large values of  $B_m$ . This lobe corresponds to the cavity mode  $n = 5$  acquiring negative detuning and therefore require a large  $B_m$  to generate any weight in sideband  $c_5 = J_5(B_m)$ .

To further confirm our interpretation of the lobes, we can scan through one of these lobes horizontally. The scan along the horizontal green dashed line in fig. 4.4 is shown in fig. 4.6a. Considering the critical frequency, represented as the blue line in fig. 4.6a, a sudden onset at  $0.2E_R$  is observed. The sudden onset corresponds to the point where the cavity mode  $n = 3$  acquires a negative detuning. The onset is sudden because the positively detuned mode is at a finite frequency. The two EVs will move towards each other and give rise to an instability that is around half the frequency of the positively detuned mode. The specific finite value for the onset also depends on the coupling coefficients of the two modes, as this will determine how quickly the two EVs move. This sudden onset means that the transition from zero frequency to finite frequency is discrete.

As  $\epsilon$  is increased, the magnitude of the negative detuning is pushed to higher energy, see eq. (4.53), while the positive detuning decreases. The opposite shift of the two detunings leads to a shift of the "midpoint" between the two detunings. This "midpoint" shift explains the increasing frequency seen in fig. 4.6a for  $0.2 < \epsilon/E_R < 0.22$ .

The two detunings being shifted closer towards each other results in needing a smaller



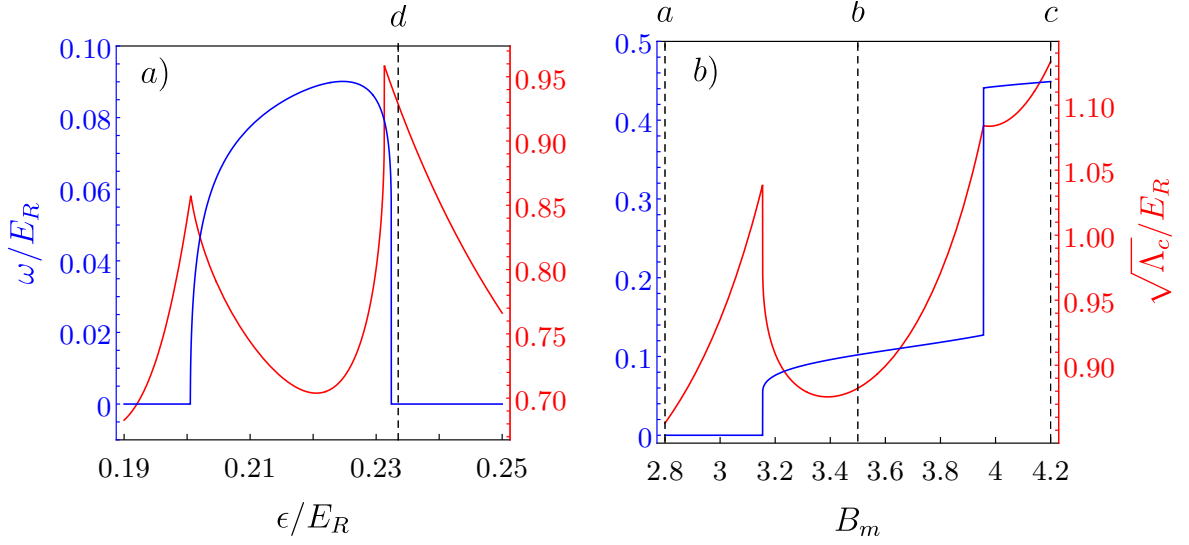


Figure 4.6: *Line scans along the phase diagram in fig. 4.4. The dashed lines and corresponding letters indicate the values for the EV movements in fig. 4.5. The blue lines represent the critical frequency, and the red lines represent the critical coupling strength. a) A scan along the dashed green horizontal line, and b) a scan along the dashed red vertical line in fig. 4.4.*

$\Lambda$  before the EVS starts interacting. At some point, the two detunings are close enough that the EV deflected towards  $\gamma = 0$  does not get critical but instead bends back down towards larger linewidth. This phenomenon is highlighted in fig. 4.5d, where we have crossed the higher-frequency edge of the lobe and consider point d in fig. 4.4. Here the positive EV can move around the negative EV without becoming critical. It can intuitively be thought of as the EVs having a finite range of interaction in the complex plane with the range depending linearly on  $\Lambda$ . The maximum of the frequency in fig. 4.6a is a consequence of the EV being pushed towards  $\gamma = 0$  slowly starting to turn back towards  $\omega = 0$  as the effective range of the interaction between the EVs decreases. The effective interaction decreases until it is small enough for the EVs to pass around each other without generating an instability, and the zero-frequency instability reappears as in fig. 4.5d. From this analysis we understand that the lobes can be thought of as a single group consisting of oppositely detuned cavity modes leading to the instability. The unstable polariton mode will therefore only be a superposition of these two cavity modes. As the bare detunings are changed by  $\epsilon$ , the finite frequency resulting from this polariton is not equivalent over the entire phase but changes based on the bare detunings.

The same line of reasoning used for the for critical frequency can also explain the behavior of the critical coupling shown with the solid red line in fig. 4.6a. Investigating the critical coupling for a single mode and the zero-frequency instability in eq. (4.36), it is seen that when the detuning is smaller than the cavity loss rate, then the critical coupling

diverges as

$$\Lambda_c \propto \frac{\kappa^2}{\Delta_0}. \quad (4.54)$$

This divergence gives rise to the increasing critical coupling for  $\epsilon < 0.2E_R$  in fig. 4.6a. It does so because the mode being made unstable is the mode with a positive detuning at  $\epsilon < 0.2E_R$  that is pushed to zero at  $\epsilon = 0.2E_R$ . As the mode acquires a negative detuning, the negative EV leads to a finite frequency instability. The critical coupling decreases because the EVs have to move less before the instability is generated, which leads to a minimum in the critical coupling at the point where there is the largest frequency. Increasing  $\epsilon$  beyond this optimum leads to the positive EV starting to bend back, and the slope with which it approaches  $\gamma = 0$  is, therefore, shallower. The shallower slope requires the EV to move further before reaching  $\gamma = 0$ , and consequently the critical coupling is increased. At the transition point to the zero-frequency instability at  $\epsilon = 0.233E_R$ , the EV deflection is maximal and therefore requires a large coupling strength for the two EVs to move around each other.

Having understood the lobes in the phase diagram, we now turn our attention to one of the other striking features in the fig. 4.4, namely the additional higher-frequency phases present inside the finite-frequency instability region. To understand these phases, a line scan of the critical frequency and coupling along the red vertical line in fig. 4.4 is shown in fig. 4.6b. The scan starts in a zero-frequency phase shown in fig. 4.5a, where the positive EV is observed moving around the negative EV. At the modulation considered in fig. 4.5a, the negatively detuned mode's sideband has a small amplitude resulting in only a weak interaction between the two EVs. As the modulation depth is increased, the negative EV with a small frequency starts coupling stronger to the atoms. The stronger atom coupling increases the effective interaction between the two EVs, which in turn causes a greater deflection of the positive EV. The increased deflection makes it harder for the positive EV to reach  $\omega = 0$ , and the critical coupling, seen in fig. 4.6b has to increase. Once the negative mode couples strongly enough to the atom, the positive EV will be pushed to criticality with a finite frequency. Again a discontinuous transition in the frequency is observed. Because the negative detuning already has a finite value, the discrete jump in frequency is significantly larger than the jump observed in fig. 4.6a.

After entering the first finite-frequency phase, the frequency again increases. In this case, the frequency increase is explained by the negative EV acquiring stronger atom coupling as  $B_m$  increases, which leads to an increasing deflection of the positive EV. As  $B_m$  is continuously increased, the modulation transfers weight to different sets of modes, and a new jump in the frequency is observed. As observed in fig. 4.5c, the new frequency is an effect of having a different set of positive and negative EVs, causing the instability, and resulting in another discontinuous transition. In the phases *a* and *b*, the instability is

mainly due to interactions between two cavity modes, similarly to the scenarios explored in the previous two- and four-mode cases. For phase  $c$ , this is not the case as the critical mode arises due to interaction with three other cavity modes. The unstable polariton will therefore have significant weight in all these four modes. The different finite-frequency regions of the phase diagram in fig. 4.4 are therefore distinguishable both by the frequencies and by the cavity mode composition of the unstable polariton mode. Consequently, as the transition from  $b$  to  $c$  happens, the occupation of the cavity modes will switch discontinuously as the frequency does. If the experiment is performed, then the discontinuous behavior is in the infinite-time limit, analogous to a phase transition requiring the thermodynamic limit as discussed in section 4.4.1. These statements are only based on linear stability, so to validate these statements, we have to investigate the system's behavior once the NP fixed point has become unstable.

Having analyzed the phase diagram thoroughly, we have seen that the lobes are explained by modes acquiring negative detunings. The full phase diagram exhibits a complex structure where each phase is well-understood by our understanding of the EV movement. It is also understood that the complexity of the phase diagram is a consequence of the non-linear nature of the modulation and the fact that many modes are present in the system. This means that the phase diagram will look different if the phase modulation is changed to differ from the sinusoidal type. The choice of modulation therefore allows one to engineer the phase diagram.

## 4.5 Beyond the normal phase

We now seek to go slightly past the CP to understand how the system behaves outside the normal phase. According to linear stability, the polaritonic instabilities grow exponentially, which makes it necessary to include the non-linear effects to stabilize these modes. Moving only slightly past the CP, one could expand eq. (4.18) to higher order in derivatives. However, this does not take advantage of the fact that the linear part has already been solved. Instead, it leads to a high-dimensional non-linear system of differential equations. To avoid this, we take advantage of the insight gained from the linearization around the CP. The center manifold theorem [150] states that sufficiently close to the CP, the system can be described by the modes predicted critical by the linear stability analysis. The critical modes are the ones that acquire a zero linewidth, and the linear stability analysis showed that the critical modes consist of the cavity modes and the recoil momentum mode of the atoms. These modes constitute the center manifold.

Our approach will be to go slightly beyond the CP by including non-linear effects on the center manifold. Once the recoil momentum mode acquires any occupation, our

straightforward approach will fail because the number conservation of the atoms will be broken. The atom conservation is broken because the homogeneous atom mode is orthogonal to the center manifold. It is therefore important to rewrite the equations in eq. (4.17) in a form where occupation of the center manifold does not break atom number conservation.

### 4.5.1 Conserving system of real equations for the center manifold

The center manifold is not conserving because it is orthogonal to the homogeneous atom mode. To solve this problem, we can use number conservation to eliminate  $\psi_0$  from the full set of equations, but because  $\psi_0$  is a complex field, it has two degrees of freedom. Therefore, number conservation is not enough to eliminate  $\psi_0$ . By inspecting the equations of motion in eq. (4.17) one observes that the cavity only couples to products involving both an atom field and a conjugate atom field. Due to the nature of the coupling, the cavity modes are unaffected by applying the same rotation to all-atom fields. We define these rotated fields as

$$\psi'_n(t) = e^{i\Theta(t)}\psi_n(t), \quad (4.55)$$

where  $\Theta(t)$  is a real function of  $t$ . Using eq. (4.17) the EOM for the primed fields takes the form

$$\begin{aligned} i\dot{\phi}_i(t) &= (\Delta_i - i\kappa_i)\phi_i(t) + \frac{\eta_i}{2} \sum_{n=0}^{\infty} \Gamma_n \bar{\psi}'_n(t) (\psi'_{n+1}(t) + \delta_{n>0} \Gamma_{|n-1|} \psi'_{|n-1|}(t)), \\ i\dot{\psi}'_n(t) &= (E_R n^2 - i\kappa_{a,n} - \partial_t \Theta(t)) \psi'_n(t) + \frac{1}{\Gamma_n} \sum_i \eta_i \text{Re } \phi_i(t) (\psi'_{n+1}(t) + \Gamma_{|n-1|} \psi'_{|n-1|}(t)), \end{aligned} \quad (4.56)$$

such that the only difference is a time-dependent energy shift of all atomic states. This shift can be exploited to eliminate one degree of freedom, and in our case, the obvious choice is to choose  $\Theta(t)$  such that  $\text{Im } \psi'_0(t) = 0 \forall t$ . For an initial condition such that  $\text{Im } \psi'_0(0) = 0$ , one can write the equation for  $\Theta$  by requiring that the imaginary part of  $\psi_0$  is constant

$$\begin{aligned} \partial_t \text{Im } \psi'_0(t) &= \text{Im } \partial_t \psi'_0(t) = \frac{1}{2i} (\partial_t \psi'_0(t) - \partial_t \bar{\psi}'_0(t)) \\ &= \dot{\Theta}(t) \text{Re } \psi'_0(t) - \sqrt{2} \text{Re } \psi'_1(t) \sum_i \eta_i \text{Re } \phi_i(t) = 0, \end{aligned} \quad (4.57)$$

which leads to the derivative of  $\Theta$  being

$$\dot{\Theta}(t) = \sqrt{2} \frac{\text{Re} \psi'_1(t)}{\text{Re} \psi'_0(t)} \sum_i \eta_i \text{Re} \phi_i(t). \quad (4.58)$$

Note that at the NP fixed point  $\dot{\Theta}$  is zero, such that  $\dot{\Theta}$  does not change the fixed point. The complex equations are now rewritten in equations for the real and imaginary parts using the  $X$  and  $P$  quadratures defined as

$$\begin{aligned} \phi_i(t) &= \frac{1}{\sqrt{2}} \left( X_i(t) + iP_i(t) \right), \\ \psi'_n(t) &= \frac{1}{\sqrt{2}} \left( X_{a,n}(t) + iP_{a,n}(t) \right). \end{aligned} \quad (4.59)$$

The EOM for the quadratures fields takes the form

$$\begin{aligned} \dot{X}_i &= \Delta_i P_i - \kappa_i X_i, \\ \dot{P}_i &= -\Delta_i X_i - \kappa_i P_i - \frac{\eta_i}{2\sqrt{2}} \sum_{n=0}^{\infty} \Gamma_n \left( X_{a,n} (X_{a,n+1} + \delta_{n>0} \Gamma_{|n-1|} X_{a,|n-1|}) \right. \\ &\quad \left. + P_{a,n} (P_{a,n+1} + \delta_{n>0} \Gamma_{|n-1|} P_{a,|n-1|}) \right), \\ \dot{X}_{a,n} &= \left( E_R n^2 - \frac{X_{a,1}}{X_{a,0}} \sum_i \eta_i X_i \right) P_{a,n} - \kappa_{a,n} X_{a,n} \\ &\quad + \frac{1}{\sqrt{2} \Gamma_n} \sum_i \eta_i X_i(t) (P_{a,n+1} + \Gamma_{|n-1|} P_{a,|n-1|}), \\ \dot{P}_{a,n} &= - \left( E_R n^2 - \frac{X_{a,1}}{X_{a,0}} \sum_i \eta_i X_i \right) X_{a,n} - \kappa_{a,n} P_{a,n} \\ &\quad - \frac{1}{\sqrt{2} \Gamma_n} \sum_i \eta_i X_i (X_{a,n+1} + \Gamma_{|n-1|} X_{a,|n-1|}), \end{aligned} \quad (4.60)$$

where the solution in eq. (4.58) have been inserted and the time-dependence of the quadratures have been suppressed. The normalization condition in eq. (4.16) then takes the form

$$1 = \frac{1}{2} \sum_n (X_{a,n}^2 + P_{a,n}^2). \quad (4.61)$$

As the rotation  $\Theta$  guarantees that  $P_{a,0}$  will stay zero throughout the evolution, we can use the normalization to eliminate  $X_{a,0}$

$$X_{a,0} = \sqrt{2n_0}, \quad \text{with } n_0 = 1 - \frac{1}{2} \sum_{n=1} (X_{a,n}^2 + P_{a,n}^2). \quad (4.62)$$

The resulting real system that explicitly conserves the atom number within the center manifold is

$$\begin{aligned}
\dot{X}_i &= \Delta_i P_i - \kappa_i X_i, \\
\dot{P}_i &= -\Delta_i X_i - \kappa_i P_i - \eta_i X_a \sqrt{2 - X_a^2 - P_a^2}, \\
\dot{X}_a &= E_R P_a - \kappa_a X_a - \frac{X_a P_a}{\sqrt{2 - X_a^2 - P_a^2}} \sum_i \eta_i X_i \\
\dot{P}_a &= -E_R X_a - \kappa_a P_a + \left( \frac{X_a^2}{\sqrt{2 - X_a^2 - P_a^2}} - \sqrt{2 - X_a^2 - P_a^2} \right) \sum_i \eta_i X_i,
\end{aligned} \tag{4.63}$$

where we have dropped the label of the atom field as only the recoil ( $n = 1$ ) mode remains. With these EOMs, it is worth mentioning that the atom loss has been modeled in a manner that conserves the number of atoms. The evolution is explicitly number conserving but the non-homogeneous atomic modes have a non-zero linewidth. The process described through eq. (4.63) is, therefore, not a loss of atoms out of the trap but instead decay from the finite momentum states into the homogeneous state [151]. Our modeling of the loss is still not ideal as it does not conserve energy. As we consider the limit of  $\kappa_a \rightarrow 0$ , the breaking of energy conservation can be neglected.

To verify the equations in eq. (4.63) one can repeat the linear analysis with the real equations in eq. (4.63), and one correctly finds that these equations lead, apart from a unitary rotation, to precisely the same Jacobian matrix as eq. (4.20), such that the equations describe the correct center manifold. This is explicitly shown in appendix E. The fact that the Jacobian can be written on a form where all entries are real is a direct consequence of the symmetry in eq. (4.22).

### 4.5.2 Double Hopf bifurcation and Stuart-Landau equations

The system of equations in eq. (4.63) provides an ideal starting point for exploring the behavior once the system has crossed the CP. To find the right approach for dealing with the non-linearities of the equations, we first consider the qualitative features found for the system so far. It has been found that the NP fixed point becomes unstable at a critical value of the coupling strength. We have discussed different cases: the zero-frequency polariton instability from chapter 3 and the atomic instability, which destroys the atom cloud without any emergence of polaritons. The main new feature generated by the interacting multimode polaritons is that when some modes acquire a negative detuning, the critical mode can have a finite frequency. These tuneable finite-frequency instabilities always come in complex conjugate pairs. When the critical modes come in complex conjugate pairs, the system can give rise to a Hopf bifurcation [152]. If a system has a

(supercritical) Hopf bifurcation, then it does not just exponentially diverge as predicted by linear stability but instead has steady-state solutions that are periodic in time. These solutions are known as limit cycles. For limit cycle solutions to be stable, the system has to satisfy specific generic properties known as the Hopf theorem. We will do a perturbative expansion of our dynamics, which will be a good approximation to the new stable fixed point beyond the CP. This perturbative approach will show under which conditions the limit cycle can be stable. Specifically, we will focus on the non-trivial case discovered for the four-mode scenario, where two complex conjugate pairs with different frequencies become critical at the same coupling strength. Under general conditions, this scenario can lead to a bifurcation known as the double Hopf or Hopf-Hopf bifurcation [150]. It is a codimension-two bifurcation, meaning that the effective description must consist of two complex coupled non-linear equations. From the perturbative derivation, we will find a form that can be directly compared to the generic form of the double Hopf bifurcation, which allows us to investigate the system's possible steady-state solutions. The key feature we will rely on to derive the perturbative equations is that the growth rates of the critical modes, once we have gone slightly past the CP, are small. This allows us to separate two timescales: a fast time scale due to the finite frequency of the critical modes and a slow time scale due to the growth rate of the EVs. We will extend the approach for the Hopf bifurcation from [153] to the double Hopf bifurcation, which leads to a set of coupled Stuart-Landau equations that describes the system in a region close to the CP.

### Coupled Landau-Stuart equations

The goal of the perturbative approach is to capture non-linear effects on the modes that become critical at the CP. The starting point is the generic form of the EOMs from eq. (4.18)

$$\dot{\mathbf{X}} = F(\mathbf{X}, \mu), \quad (4.64)$$

where boldface will be used to indicate a vector. The vector of independent variables ( $X_{a/i}$  and  $P_{a/i}$ ) is  $\mathbf{X}$  and  $\mu = \Lambda - \Lambda_c$  is the distance from the CP. Our definition of  $\mu$  means that for  $\mu > 0$ , the linear analysis predicts the system to be unstable. By eliminating the state  $\psi_{a,0}$ , the NP fixed point is  $\mathbf{X}_0 = \mathbf{0}$  meaning that the distance to the fixed point is  $\mathbf{u} = \mathbf{X} - \mathbf{X}_0 = \mathbf{X}$ . As long as we are close to the fixed point, we can write the evolution

of the  $i$ th component of  $\mathbf{u}$  as an expansion around  $\mathbf{0}$

$$\begin{aligned}
\dot{u}_i &= \dot{X}_i = F_i(\mathbf{X}, \mu) \\
&= F_i(\mathbf{0}, \mu) + \left. \frac{\partial F_i}{\partial X^j} \right|_{\mathbf{x}=\mathbf{0}} u_j + \frac{1}{2} \left. \frac{\partial^2 F_i}{\partial X^j \partial X^k} \right|_{\mathbf{x}=\mathbf{0}} u_j u_k + \frac{1}{3!} \left. \frac{\partial^3 F_i}{\partial X^j \partial X^k \partial X^q} \right|_{\mathbf{x}=\mathbf{0}} u_j u_k u_q + \dots \\
&= L_i^j u_j + M_i^{j,k} u_j u_k + N_i^{j,k,q} u_j u_k u_q + \dots,
\end{aligned} \tag{4.65}$$

where Einstein summation notation has been used. Because the derivatives can be done in any order (a simplification arising from working with real fields), the tensors  $M$  and  $N$  are symmetric with respect to the order of the superscript. Our approach is now to expand all elements in eq. (4.65) around small  $\mu$ . Expanding  $L$  gives

$$L = L_0 + \mu L_1 + \mu^2 L_2 + \dots \tag{4.66}$$

where  $L_0$  is the Jacobian for which we have two critical solutions

$$L_0 \mathbf{v}_R^{(1/2)} = \lambda_0^{(1/2)} \mathbf{v}_R^{(1/2)}, \quad \text{with } \lambda_0^{(1/2)} = i\omega_0^{(1/2)}, \tag{4.67}$$

where  $\mathbf{v}_R^\alpha$  is the right eigenvector for the  $\alpha \in \{1, 2\}$  eigenvalue  $\lambda_0^\alpha$ , which is purely imaginary at the CP. Because the solutions are complex, there are also the associated left eigenvectors

$$\mathbf{v}_L^{(1/2)} L_0 = \lambda_0^{(1/2)} \mathbf{v}_L^{(1/2)}. \tag{4.68}$$

The normalisation used is  $\mathbf{v}_L^{(\alpha)} \mathbf{v}_R^{(\beta)} = \bar{\mathbf{v}}_L^{(\alpha)} \bar{\mathbf{v}}_R^{(\beta)} = \delta_{\alpha,\beta}$  and  $\mathbf{v}_L^{(\alpha)} \bar{\mathbf{v}}_R^{(\beta)} = \bar{\mathbf{v}}_L^{(\alpha)} \mathbf{v}_R^{(\beta)} = 0$ , with the bar denoting conjugation. With these eigenvectors, we can define an expansion of the EVs

$$\lambda^{(\alpha)} = \lambda_0^{(\alpha)} + \mu \lambda_1^{(\alpha)} + \mu^2 \lambda_2^{(\alpha)} + \dots, \tag{4.69}$$

with  $\lambda_n^{(\alpha)} = \mathbf{v}_L^{(\alpha)} L_n \mathbf{v}_R^{(\alpha)}$ . Beyond the CP, the system becomes unstable which means that  $\text{Re } \lambda_1^\alpha = \gamma_1^\alpha > 0$ , while the frequency shift  $\text{Im } \lambda_1^\alpha = \omega_1^\alpha$  can take any sign.

Just like the linear part was expanded, the higher order tensors can also be expanded

$$M = M_0 + \mu M_1 + \dots, \quad \text{and } N = N_0 + \mu N_1 + \dots \tag{4.70}$$

Having expanded all the tensors, we seek to write the new stable fixed point as an expansion around the linear analysis. As the bifurcation is of the Hopf type, the distance  $\mathbf{u}$  to the new stable fixed point scales as the square root of  $\mu$  [154]. It is advantageous to write  $\mu = \chi \epsilon^2$ , where  $\chi = \text{sgn } \mu$  keeps track of which side of the bifurcation the system is on.



With this, we can write the expansion of the new solution as

$$\mathbf{u} = \epsilon \mathbf{u}_1 + \epsilon^2 \mathbf{u}_2 + \dots \quad (4.71)$$

As mentioned previously, the system has two separate time scales close to the bifurcation. The time scales can be made apparent in the expansion by splitting the time into two parts  $t \rightarrow t + \epsilon^2 \tau$ , which also means that  $dt \rightarrow dt + \epsilon^2 d\tau$ . As  $\epsilon^2$  is small we treat  $t$  and  $\tau$  as independent variables. Now all the different parts can be inserted into eq. (4.65), and everything can be ordered according to the powers in  $\epsilon$

$$\begin{aligned} & (\partial_t + \epsilon^2 \partial_\tau - L_0 - \chi \epsilon^2 L_1 - \dots) (\epsilon \mathbf{u}_1 + \epsilon^2 \mathbf{u}_2 + \dots) \\ & = \epsilon^2 M_0 \mathbf{u}_1 \mathbf{u}_1 + 2\epsilon^3 M_0 \mathbf{u}_1 \mathbf{u}_2 + \epsilon^3 N_0 \mathbf{u}_1 \mathbf{u}_1 \mathbf{u}_1 + \dots \end{aligned} \quad (4.72)$$

As different powers are orthogonal to each other [155], we can write equations for each power of  $\epsilon$ . For the  $n$ th power it can be written as  $(\partial_t - L_0) \mathbf{u}_n = B_n$  where the  $B_n$ 's for the first three powers are found to be

$$\begin{aligned} B_1 &= 0, \\ B_2 &= M_0 \mathbf{u}_1 \mathbf{u}_1, \\ B_3 &= (-\partial_\tau + \chi L_1) \mathbf{u}_1 + 2M_0 \mathbf{u}_1 \mathbf{u}_2 + N_0 \mathbf{u}_1 \mathbf{u}_1 \mathbf{u}_1, \end{aligned} \quad (4.73)$$

where it is observed that  $B_n$  only depends on  $\mathbf{u}_{m < n}$ . For an equation of the form  $Ly = f$ , where  $L$  is a bounded linear operator, to have a solution, the force  $f$  has to be orthogonal to the solutions of the adjoint homogeneous problem

$$\langle v, f \rangle = 0, \quad (4.74)$$

for every  $v$  that solves  $vL^\dagger = 0$ . This condition is known as the Fredholm alternative [155] or the solvability condition [156]. For our problem, the adjoint operator is  $L^\dagger = -\overleftarrow{\partial}_t - L_0$ , for which we have two linearly independent solutions (and the conjugate of these)

$$\mathbf{v}_L^{(\alpha)} e^{-i\omega_0^{(\alpha)} t} \left( -\overleftarrow{\partial}_t - L_0 \right) = 0, \quad (4.75)$$

where the arrow indicates that the derivative is acting to the left. The Fredholm alternative then states that the system only has solutions if

$$\int_0^{2\pi/\omega_0^{(\alpha)}} \mathbf{v}_L^{(\alpha)} e^{-i\omega_0^{(\alpha)} t} B_n dt = 0 \quad \forall \alpha \in \{1, 2\}. \quad (4.76)$$

From the  $\mathcal{O}(\epsilon)$  equation ( $n = 1$ ) we find that  $\mathbf{u}_1$  has a form

$$\mathbf{u}_1 = W_1(\tau)\mathbf{v}_R^{(1)}e^{i\omega_0^{(1)}t} + W_2(\tau)\mathbf{v}_R^{(2)}e^{i\omega_0^{(2)}t} + c.c., \quad (4.77)$$

where  $W_\alpha(\tau)$  is a complex function that only depends on the slow time. As  $B_2$  is written in terms of  $\mathbf{u}_1$  this will also be a periodic function in  $t$  and this extends to all  $B_n$ s. The periodicity makes it possible to write  $B_n$  as a double Fourier series in  $t$

$$B_n(t, \tau) = \sum_{k,q} B_n^{(k,q)}(\tau) \exp\left(it\left(k\omega_0^{(1)} + q\omega_0^{(2)}\right)\right). \quad (4.78)$$

For there to be solutions, the Fredholm alternative then gives a condition on two of the Fourier components

$$\mathbf{v}_L^{(1)}B_n^{(1,0)}(\tau) = 0 \text{ and } \mathbf{v}_L^{(2)}B_n^{(0,1)}(\tau) = 0. \quad (4.79)$$

$B_1$  has no oscillations and therefore trivially satisfies the solvability condition. Inserting the solution for  $\mathbf{u}_1$  into  $B_2$  we find

$$\begin{aligned} B_2(t, \tau) = & M_0 \sum_{\alpha=1,2} \left( W_\alpha^2 \mathbf{v}_R^\alpha \mathbf{v}_R^\alpha e^{i2\omega_0^{(\alpha)}t} + 2|W_\alpha|^2 \bar{\mathbf{v}}_R^\alpha \mathbf{v}_R^\alpha + \bar{W}_\alpha^2 \bar{\mathbf{v}}_R^\alpha \bar{\mathbf{v}}_R^\alpha e^{-i2\omega_0^{(\alpha)}t} \right) \\ & + 2M_0 \left( W_1 W_2 \mathbf{v}_R^{(1)} \mathbf{v}_R^{(2)} e^{it\omega_0^{(1)} + it\omega_0^{(2)}} + \bar{W}_1 \bar{W}_2 \bar{\mathbf{v}}_R^{(1)} \bar{\mathbf{v}}_R^{(2)} e^{-it\omega_0^{(1)} - it\omega_0^{(2)}} \right) \\ & + \bar{W}_1 W_2 \bar{\mathbf{v}}_R^{(1)} \mathbf{v}_R^{(2)} e^{-it\omega_0^{(1)} + it\omega_0^{(2)}} + \bar{W}_2 W_1 \bar{\mathbf{v}}_R^{(2)} \mathbf{v}_R^{(1)} e^{it\omega_0^{(1)} - it\omega_0^{(2)}}, \end{aligned} \quad (4.80)$$

where we used the tensors' symmetry properties to collect similar terms. By inspection, it is seen that  $B_2$  also has no component, which gives rise to just one of the oscillations such that  $B_2$  also trivially satisfies the solvability condition. This means one has to consider  $B_3$  to get a condition on  $W_1$  and  $W_2$ . To compute  $B_3$ , one needs  $\mathbf{u}_2$ , and as this is determined from the  $\mathcal{O}(\epsilon^2)$  equation, we can try a convenient ansatz with the same frequencies as seen in eq. (4.80)

$$\begin{aligned} \mathbf{u}_2 = & \sum_{\alpha=1,2} \mathbf{V}_+^{(\alpha)} W_\alpha^2 e^{i2\omega_0^{(\alpha)}t} + \mathbf{V}_- \bar{W}_\alpha^2 e^{-i2\omega_0^{(\alpha)}t} + \mathbf{V}_0 |W_\alpha|^2 \\ & + \mathbf{A}_{++} W_1 W_2 e^{it\omega_0^{(1)} + it\omega_0^{(2)}} + \mathbf{A}_{--} \bar{W}_1 \bar{W}_2 e^{-it\omega_0^{(1)} - it\omega_0^{(2)}} \\ & + \mathbf{A}_{+-} W_1 \bar{W}_2 e^{it\omega_0^{(1)} - it\omega_0^{(2)}} + \mathbf{A}_{-+} \bar{W}_1 W_2 e^{-it\omega_0^{(1)} + it\omega_0^{(2)}} + c_0 \mathbf{u}_1. \end{aligned} \quad (4.81)$$

To determine the vectors in this solution we insert the ansatz into the  $\mathcal{O}(\epsilon^2)$  equation in

eq. (4.73) which gives the form of the vectors

$$\begin{aligned}
\mathbf{V}_+^{(\alpha)} = \bar{\mathbf{V}}_-^{(\alpha)} &= - \left( L_0 - i2\omega_0^{(\alpha)} \mathbf{1} \right)^{-1} M_0 \mathbf{v}_R^{(\alpha)} \mathbf{v}_R^{(\alpha)}, \\
\mathbf{V}_0^{(\alpha)} &= - L_0^{-1} 2M_0 \bar{\mathbf{v}}_R^{(\alpha)} \mathbf{v}_R^{(\alpha)}, \\
\mathbf{A}_{++} = \bar{\mathbf{A}}_{--} &= - \left( L_0 - i\omega_0^{(1)} \mathbf{1} - i\omega_0^{(2)} \mathbf{1} \right)^{-1} 2M_0 \mathbf{v}_R^{(1)} \mathbf{v}_R^{(2)}, \\
\mathbf{A}_{+-} = \mathbf{A}_{-+} &= - \left( L_0 - i\omega_0^{(1)} \mathbf{1} + i\omega_0^{(2)} \mathbf{1} \right)^{-1} 2M_0 \mathbf{v}_R^{(1)} \bar{\mathbf{v}}_R^{(2)}.
\end{aligned} \tag{4.82}$$

Notice that we have no equation for  $c_0$ , but at  $\mathcal{O}(\epsilon^3)$ , this term does not contribute. It does not contribute because the only terms that contribute to the solvability condition are those in  $B_3$ , which has a  $t$ -dependence of the form  $e^{-i\omega_0^{(\alpha)}t}$ . The  $(1, 0)$  Fourier component of  $B_3$  from eq. (4.78) is found by inserting eq. (4.77) and eq. (4.81) into the  $\mathcal{O}(\epsilon^3)$  equation in eq. (4.73)

$$\begin{aligned}
B_3^{(1,0)}(t) &= (-\partial_\tau + \chi L_1) W_1 \mathbf{v}_R^{(1)} + 2M_0 \left( \mathbf{V}_+^{(1)} \bar{\mathbf{v}}_R^{(1)} |W_1|^2 W_1 \right. \\
&\quad + \mathbf{V}_0^{(1)} \mathbf{v}_R^{(1)} |W_1|^2 W_1 + \mathbf{A}_{++} \bar{\mathbf{v}}_R^{(2)} W_1 |W_2|^2 \\
&\quad + \left. \mathbf{A}_{+-} \mathbf{v}_R^{(2)} W_1 |W_2|^2 \right) \\
&\quad + 3N_0 \left( |W_1|^2 |W_1|^2 \mathbf{v}_R^{(1)} \mathbf{v}_R^{(1)} \bar{\mathbf{v}}_R^{(1)} + 2W_1 |W_2|^2 \mathbf{v}_R^{(1)} \mathbf{v}_R^{(2)} \bar{\mathbf{v}}_R^{(2)} \right).
\end{aligned} \tag{4.83}$$

The equation for  $B_3^{(0,1)}$  is found by swapping  $1 \leftrightarrow 2$  and  $\mathbf{A}_{+-} \leftrightarrow \mathbf{A}_{-+}$ . With these two components, the equations derived from the Fredholm alternative in eq. (4.79) lead to two coupled equations for  $W_1$  and  $W_2$

$$\begin{aligned}
\partial_\tau W_1 &= \chi \lambda_1^{(1)} W_1 - g_{1,1} |W_1|^2 W_1 - g_{1,2} |W_2|^2 W_1, \\
\partial_\tau W_2 &= \chi \lambda_1^{(2)} W_2 - g_{2,2} |W_2|^2 W_2 - g_{2,1} |W_1|^2 W_2,
\end{aligned} \tag{4.84}$$

where the non-linear coefficients in the  $W_1$  equation are given by

$$\begin{aligned}
g_{1,1} &= 2\mathbf{v}_L^{(1)} M_0 \left( \mathbf{V}_+^{(1)} \bar{\mathbf{v}}_R^{(1)} + \mathbf{V}_0^{(1)} \mathbf{v}_R^{(1)} \right) \\
&\quad + 3\mathbf{v}_L^{(1)} N_0 \mathbf{v}_R^{(1)} \mathbf{v}_R^{(1)} \bar{\mathbf{v}}_R^{(1)}, \\
g_{1,2} &= 2\mathbf{v}_L^{(1)} M_0 \left( \mathbf{A}_{++} \bar{\mathbf{v}}_R^{(2)} + \mathbf{A}_{+-} \mathbf{v}_R^{(2)} \right) \\
&\quad + 6\mathbf{v}_L^{(1)} N_0 \mathbf{v}_R^{(1)} \mathbf{v}_R^{(1)} \bar{\mathbf{v}}_R^{(2)}.
\end{aligned} \tag{4.85}$$

The non-linear elements for  $W_2$  are found from eq. (4.85) by the same swapping used to get  $B_3^{(0,1)}$ . The equations in eq. (4.84) are of the form of two coupled Stuart-Landau equations [153].

To solve these coupled equations the complex numbers  $W$  are written in their polar form  $W_\alpha = R_\alpha e^{i\theta_\alpha}$  where  $R_\alpha \geq 0$  and  $\theta$  is real. To simplify the resulting real equations the coupling elements are split into a real and imaginary part:  $g_{\alpha,\beta} = g_{\alpha,\beta}^r + ig_{\alpha,\beta}^i$ . The four real equations take the form

$$\begin{aligned}\dot{R}_1 &= \chi\gamma_1^{(1)}R_1 - g_{1,1}^rR_1^3 - g_{1,2}^rR_1R_2^2, \\ \dot{R}_2 &= \chi\gamma_2^{(1)}R_2 - g_{2,2}^rR_2^3 - g_{2,1}^rR_2R_1^2, \\ \dot{\theta}_1 &= \chi\omega_1^{(1)} - R_1^2g_{1,1}^i - R_2^2g_{1,2}^i, \\ \dot{\theta}_2 &= \chi\omega_1^{(2)} - R_2^2g_{2,2}^i - R_1^2g_{2,1}^i.\end{aligned}\tag{4.86}$$

The simplest non-trivial solution is to set the amplitudes to be constants such that  $\dot{R}_\alpha = 0$  and  $R_\alpha = R_{\alpha,c}$

$$\begin{aligned}R_{\alpha,c}^2 &= \chi \frac{\gamma_1^{(\alpha)}g_{\beta,\beta}^r - \gamma_1^{(\beta)}g_{\alpha,\beta}^r}{g_{\alpha,\alpha}^r g_{\beta,\beta}^r - \chi g_{\alpha,\beta}^r g_{\beta,\alpha}^r}, \\ \theta_{\alpha,c} &= \tilde{\omega}_\alpha \tau = \left( \chi\omega_1^{(\alpha)} - R_{\alpha,c}^2 g_{\alpha,\alpha}^i - R_{\beta,c}^2 g_{\alpha,\beta}^i \right) \tau,\end{aligned}\tag{4.87}$$

with  $\alpha \neq \beta$ . This solution represents the critical mode  $\alpha$  performing perfect circular rotations with the frequency set by  $\tilde{\omega}_\alpha$  such that the new steady-state is given by

$$\mathbf{X} = \sqrt{\mu} \sum_{\alpha} \left( R_{\alpha} \mathbf{v}_R^{(\alpha)} e^{i(\omega_0^{(\alpha)} + \mu\tilde{\omega}_\alpha)t} + c.c. \right),\tag{4.88}$$

where the slow time  $\tau$  has been expressed through the fast time  $t$  as  $\tau = \epsilon^2 t = \mu t$ . If only a single unstable mode is occupied ( $R_2 = 0$ ), such a periodic solution is known as a limit cycle [152]. For this solution to exist it is necessary that  $R_{\alpha,c}^2 > 0$ . In the case of two uncoupled Stuart-Landau equations ( $g_{1,2} = g_{2,1} = 0$ ), the two equations both take the form of a Hopf bifurcation. For the uncoupled limit cycle solution to exist, we see from eq. (4.87) that  $\gamma_1 \neq 0$ , which means that the EVs from linear stability have to cross the  $\gamma = 0$  axis with a finite velocity as a function of  $\mu$ . Furthermore, the evolution  $F$  must have non-zero higher-order derivatives around the NP such that  $g^r \neq 0$ . These two conditions, together with the requirement of the system to have a conjugate pair of critical finite-frequency EVs, are equivalent to the conditions in the Hopf bifurcation theorem [150].

For the codimension-two case, i.e., double Hopf, these conditions can only confirm a perfect circular limit cycle, which means that the only state we can determine is when  $R_{\alpha,c} > 0$  for both  $\alpha$ . To understand what happens when one of the  $R_{\alpha,c}$ 's does not satisfy this condition, it is necessary to consider the normal form of the double Hopf bifurcation. Before doing this, we will first discuss the result of applying our analysis to the multimode cavity model.

### 4.5.3 Stuart-Landau equations the for multimode polaritons

For constructing the Stuart-Landau equations for the multimode polaritons, it is essential to consider the symmetries. The first symmetry is the  $U(1)$  responsible for the conservation of atom number, which we already discussed. On the mathematical level, this symmetry is important because the elements in eq. (4.82) contain the inverse of the Jacobian  $L_0$  and the eigenvalue of the  $\psi_0$  mode is zero. Consequently, if  $\psi_0$  is not eliminated from the equations but directly included in the center manifold, then not only will we break number conservation, but the inverse Jacobian becomes singular due to the zero eigenvalue of  $\psi_0$ . If one tries to circumvent this by adding a small linewidth to the homogeneous mode, then the specific value of the linewidth will more or less exclusively determine the value of the inverse Jacobian, thus leading to non-physical results.

The second symmetry is a  $\mathcal{Z}_2$  symmetry. Considering the equations of motion in eq. (4.17) one sees that a  $\pi$  phase shift of the cavity modes  $\phi_i \rightarrow -\phi_i$  and a momentum-dependent rotation of the atom states  $\psi_n \rightarrow e^{in\pi}\psi_n$ , leaves the equations invariant. We denote this symmetry operation  $\mathbb{R}$ . In the NP the solution is  $\phi_i = 0 = \psi_{n>0}$  and  $\psi_0 = 1$  which is invariant under  $\mathbb{R}$ . As the EOMs are invariant, we expect the same for the solutions. Within the center manifold, the only relevant modes are the cavity modes  $\phi_i$  and the recoil momentum atom mode  $\psi_1$ . Applying  $\mathbb{R}$  to a vector within the center manifold  $\mathbf{v}_{cm}$  amounts to a  $\pi$  phase shift  $\mathbb{R}(\phi_i, \psi_1) = (-\phi_i, -\psi_1)\forall i$ . The equations for the center manifold, therefore, have to obey

$$\mathbb{R}F(v_{cm}) = F(\mathbb{R}v_{cm}) \rightarrow -F(v_{cm}) = F(-v_{cm}). \quad (4.89)$$

Considering the generic derivation in the previous section, this can only be true if  $M = 0$ . In appendix E we derive  $L_0$ ,  $L_1$ ,  $M_0$  and  $N_0$  directly. As mentioned earlier, we find that  $L_0$  is equivalent to the result found for the complex system in eq. (4.20). Furthermore,  $L$  only linearly depends on  $\mu$ , meaning that  $L_2 = 0$ . It is also explicitly shown that  $M_0$  indeed is zero on the center manifold but is non-zero beyond the center manifold.  $M_0$  being non-zero beyond the center manifold is allowed because  $\mathbb{R}$  leaves all the even atom modes invariant. For  $N_0$ , we find the five distinct elements given by eq. (E.16). Due to the  $\mathcal{Z}_2$  symmetry, the coupling coefficients are entirely determined by  $N_0$  and the eigenvectors of the Jacobian. The solution to the Stuart-Landau for the two-mode case discussed in fig. 4.2b is shown in fig. 4.7a. Here the absolute value of the first cavity field (gray line) and the recoil field (black dashed line) have been plotted. The frequency predicted by linear stability is close to  $0.7E_R$ , but because the absolute value is considered, the fields should be oscillating at twice the frequency  $1.4E_R$ , which corresponds to the period  $\sim 0.45E_R^{-1}$  observed in fig. 4.7a. As expected from the Stuart-Landau solution in eq. (4.88), the cavity

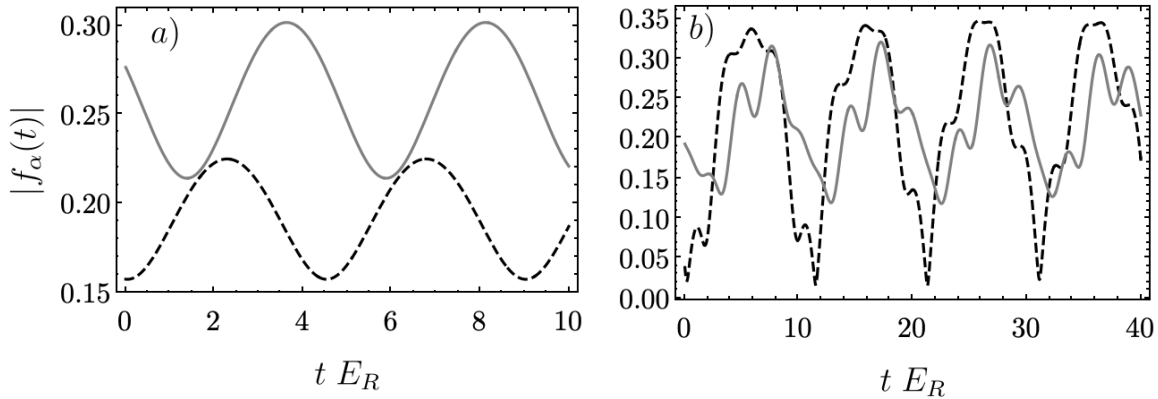


Figure 4.7: Plots of the occupation of the recoil field (black dashed) and the first cavity field (gray) of two different limit cycle phases. In both cases the distance to the CP is  $\mu = 0.03\sqrt{\Lambda_c}$ . a) The two-mode case discussed in fig. 4.2b where the limit cycle has a period of  $2\pi/0.7E_R \approx 0.45E_R^{-1}$ . b) The four-mode case from fig. 4.3 at the double Hopf bifurcation point. As the frequencies are incommensurate, the fields are not periodic.

and the atom oscillate at the same frequency. The steady state is dramatically different for the double-Hopf bifurcation point predicted by linear stability in fig. 4.3. The steady state of the four-mode double-Hopf bifurcation is plotted in fig. 4.7b. The frequencies of the two unstable modes are  $\sim 0.7E_R$  and  $\sim 1.3E_R$ . The incommensurability of the two frequencies, leads to the occupations of both the atom field and the first cavity field not being periodic. As the atom field couples to two different frequency limit cycles, it is observed that the atom field and first cavity field do not oscillate in the same manner.

#### 4.5.4 Double Hopf normal form

Having seen the single limit-cycle and the two limit-cycle steady states, we now investigate the possible steady states the four-mode system can exhibit. To this extent, we consider the generic double Hopf bifurcation. It can be shown that if the two different frequencies are not commensurate, such that  $k\omega_0^{(1)} \neq l\omega_0^{(2)}$  for  $k, l > 0, k + l \leq 5$ , and all  $g_{\alpha,\beta}^r \neq 0$  then a system with a double Hopf bifurcation can, sufficiently close to the bifurcation, be mapped to a form like eq. (4.86) [150]. This form is known as the truncated normal form. If one further neglects the correction to the frequencies, one arrives at two equations commonly referred to as the amplitude equations

$$\begin{aligned}\dot{R}_1 &= \gamma_1^{(1)} R_1 - g_{1,1}^r R_1^3 - g_{1,2}^r R_1 R_2^2, \\ \dot{R}_2 &= \gamma_1^{(2)} R_2 - g_{2,2}^r R_2^3 - g_{2,1}^r R_2 R_1^2.\end{aligned}\tag{4.90}$$

The topology of the bifurcation diagram for these equations is rich and contains 36 different kinds of bifurcations; however, these are separated into two main groups. If  $g_{1,1}^r g_{2,2}^r > 0$  then the system falls into what is known as the "simple" case which has 15 different phases, whereas if  $g_{1,1}^r g_{2,2}^r < 0$  then the system belongs to the "difficult" case [150] which has 21 different phases. One difference between the two cases is that the "difficult" case can have an emerging limit cycle in the amplitude equations, which is impossible in the "simple" case. Such an amplitude limit cycle is an additional limit cycle in the system that is not directly related to the frequencies of the critical modes. Another difference is that the "simple" case phases are not topologically changed by the inclusion of higher-order terms in eq. (4.90), whereas the topology of the "difficult" case phases can be qualitatively changed when higher-order terms beyond those derived from our Stuart-Landau approach are included in the amplitude equations in eq. (4.90).

The first task is to identify if our multimode model falls into the "difficult" or the "simple" case. To solve this task, it is necessary to explore the parameter space in some fashion. For the four-mode case, we have four detunings, three coupling coefficients, and four cavity losses, which lead to an eleven-dimensional parameter space. A complete mapping of this parameter space is intractable. We are only interested in the part of this phase space that contains a double Hopf bifurcation but finding all regions of phase space that contains a double Hopf bifurcation is a challenging problem.

To make the problem tractable, we constrain the parameter space to the four-mode case already considered, where the system can be split into two groups: two detunings with a magnitude smaller than the recoil energy and two with a magnitude larger than the recoil energy. For the below-recoil group, the mode with the smallest magnitude has a negative detuning, while the one close to recoil energy has to have a positive detuning. For the above-recoil group, the mode with the larger magnitude has to be negatively detuned from its sideband, while the mode closest to the recoil energy has to be positively detuned. Furthermore, we do not let any coupling coefficients be zero and choose all cavity losses to be in the range  $\{E_R/100, E_R/10\}$ . Within these constraints, we perform a uniform random sampling of all the allowed parameters. A weighting between the below- and above-recoil momentum groups is then introduced so that the modes in the below-recoil group have their coupling coefficients scaled by  $\sqrt{\beta/2}$  and the modes in the above-recoil group have their coupling coefficients scaled by  $\sqrt{1-\beta/2}$ . Using the parameter  $\beta \in \{0, 1\}$ , we can find the point where both groups become critical simultaneously, such that the system has a double Hopf bifurcation.

The result of this sampling is shown in fig. 4.8 and from fig. 4.8a, it is observed that  $g_{1,1}^r g_{2,2}^r > 0$ , meaning that the system always falls in the "simple" case. The next step is to identify which of the 15 possible steady states in the "simple" case the system can

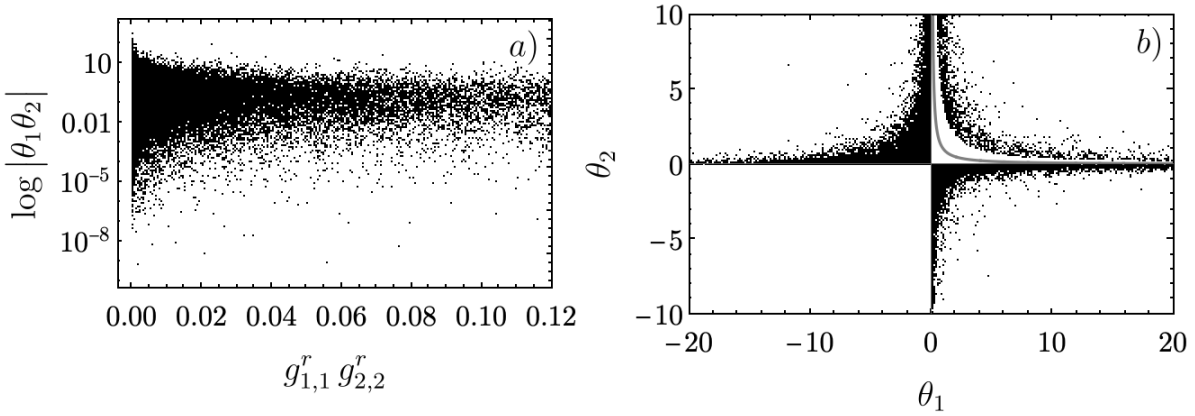


Figure 4.8: *Random sampling of the restricted parameter space, consisting of  $6.7 \times 10^4$  points, for the double Hopf bifurcation according to the constraints discussed in section 4.5.4.  $\theta_\alpha$  are the effective off-diagonal couplings from eq. (4.91). In a) it is shown that the system always falls in the "simple" case as no points have a negative value along the x-axis. It also shows that the off-diagonal couplings can have very different amplitudes. b) The relation between the off-diagonal couplings for each data point. The majority of the points fall in the second and fourth quadrants. The third quadrant has no points, and the points in the first quadrant always fall above the gray line, which is a plot of  $1/\theta_1$ .*

exhibit. The first feature of our system is that  $\gamma_1^{(\alpha)} > 0$  for all points in the considered parameter space. Consequently, the linear solution always leads to the growth of the two limit cycles. The steady-state can, however, change due to the off-diagonal couplings  $g_{\alpha,\beta}^r$ . By mapping to a normal form [150], one finds that the relevant values for distinguishing the different phases are the off-diagonal couplings divided by the opposite diagonal terms

$$\theta_\alpha = \frac{g_{\alpha,\beta}^r}{g_{\beta,\beta}^r}, \text{ with } \beta \neq \alpha. \quad (4.91)$$

In fig. 4.8b, it is observed that either the two off-diagonal couplings have different signs or they are both positive with a product  $\theta_1 \theta_2 > 1$ . That  $\theta_1 \theta_2 > 1$  can be seen by the fact that all points lie above the gray line in fig. 4.8b which shows  $1/\theta_1$ . These features mean that only 6 of the 15 "simple" case phase portraits are possible in the parameter space we have investigated.

The six different phase portraits are sketched in fig. 4.9. The phases fig. 4.9a and fig. 4.9b are phases with only one fixed point, and only one limit cycle survives such that the steady state is similar to fig. 4.7a. These phases are reached when the data point falls in the first quadrant of fig. 4.8b, and one of the growth rates dominates such that

$$\gamma_1^{(\alpha)} > \theta_1 \gamma_1^{(\beta)}. \quad (4.92)$$



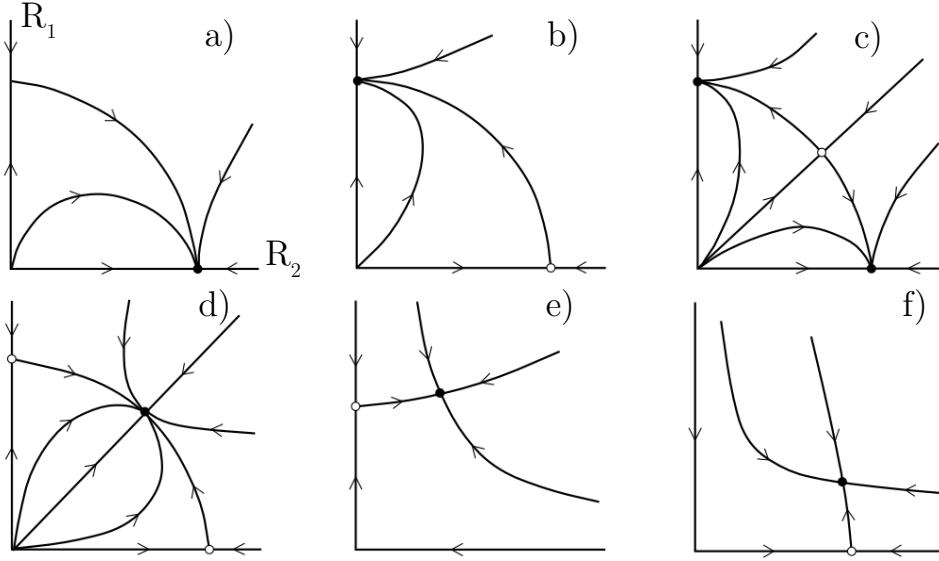


Figure 4.9: The different phase portraits possible based on the parameter sweep in fig. 4.8. The individual sketches are borrowed from figure 8.26 in [150]. A black(open) dot indicates a (un)stable fixed point.

In fig. 4.9c, the system has two fixed points, with only one of the limit cycles being stable. In this case, the oscillation of the system would depend on the initial state of the system. The system falls into this state when the off-diagonal coupling  $g_{\alpha,\beta}^r$  are both positive, and their growth rates are close to each other such that

$$\theta_\alpha^{-1} < \frac{\gamma_1^{(\alpha)}}{\gamma_1^{(\beta)}} < \theta_\beta, \quad (4.93)$$

where  $\theta_\alpha > \theta_\beta$ . From the discussed data, 166 data points fall into this phase. By investigating the EVs movement for a random configuration of the 166 data points, it is seen, in fig. 4.10a, that these configurations possess a specific feature. Namely one of the unstable modes is the EV which was initially purely atomic. These phases are straightforward to quantify as they are the only ones in our restricted phase space, where both frequencies of the instabilities in the double Hopf bifurcation are above or below the recoil frequency. By checking the other 166 points, it is observed that they all are of this nature, with frequencies either below or above the recoil. To check that the system has a bistability at such a point, we numerically integrate the original equations in eq. (4.17) slightly into the critical region with different initial conditions. If the initial condition has a significant imbalance between the two cavity groups, the system ends in the limit cycle with the largest overlap of the initial condition. In fig. 4.10b, we have initialized the system with random but small fluctuations in the cavity but with different amplitudes of the recoil

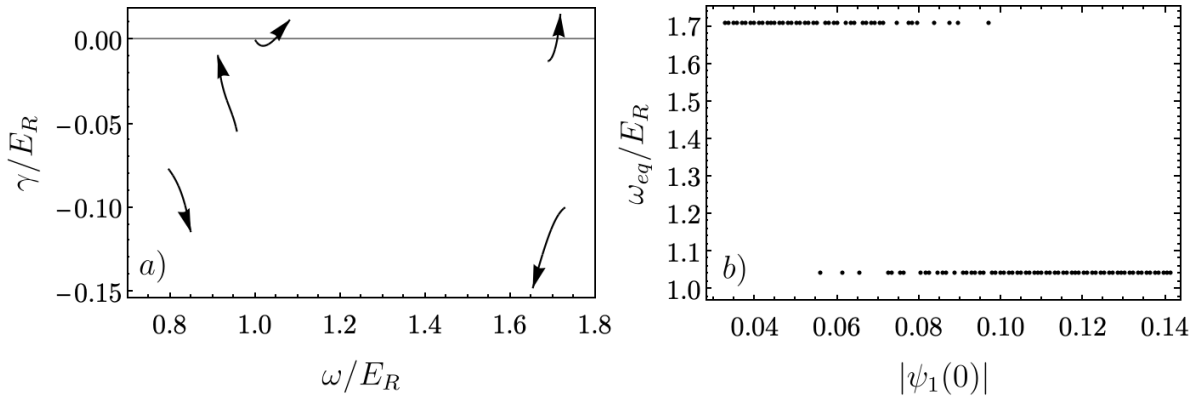


Figure 4.10: A random datapoint from the sweep in fig. 4.8, that falls within the class topologically equivalent to fig. 4.9c. The approximate parameters (in units of the recoil energy) are  $\Delta = (-0.80, 0.96, 1.69, -1.73)^T$ ,  $\kappa = (0.08, 0.05, 0.01, 0.10)^T$ ,  $\mathbf{c} = (0.29, 0.20, 0.54, 0.76)$  and the critical coupling is  $\sqrt{\Lambda_c} = 0.42$ . a) The EV movement from the linear stability of the system around the critical point. Each point in b) represents the resulting frequency of the limit cycle after long numerical integration of the center manifold with a different initial condition. The system is chosen to be slightly inside the critical region with  $\sqrt{\Lambda} = 1.03\sqrt{\Lambda_c}$ . Each initial condition has a fixed amplitude of the recoil momentum mode but a random phase. The cavity part of the initial condition is random but only of a small magnitude such  $|\phi_i(0)| < 10^{-3}$ .

momentum mode. The phase of the recoil mode was chosen randomly. In this figure, one sees that for small magnitude  $|\psi_1(0)| < 0.05$ , this particular configuration always ends up at the high-frequency (more photonic) fixed point, while for larger magnitude, the system ends up at the low-frequency fixed point which has more atomic admixture. There is a region in the middle where the separatrix is sensitive to the phase of the initial atomic state, or the small random seed in the cavity field. By choosing different parameters, one can still have a bistability (for example, any of the other 165 found configurations), but the dependence of the initial conditions will be very different. Because of the large parameter space of the system, one could look for parameters where the bistability is sensitive to specifically chosen quantities. The large difference between the steady states due to a small change in initial conditions could make the bistable parameter region of the system useful for sensing applications.

The three phases in fig. 4.9(d-f) constitute cases where both limit cycles acquire a finite value and the steady states will be similar to fig. 4.7. These phases emerge when the couplings  $g_{\alpha,\beta}^r$  have different signs, corresponding to the data points in the second and fourth quadrant in fig. 4.8b. In these phases, the system has two different limit cycles happening simultaneously, which leads to the system evolving on a two-dimensional torus in its steady-state configuration. Of all the approximately 7000 data points, half of them

possess this steady state, which means that both modes have physical solutions to the amplitude equations eq. (4.87).

### 4.5.5 Symmetry breaking of the steady states

So far we have seen that the multimode polariton can show a wide variety of steady states, and we will now connect these to the trajectories in the physical phase space. For a single limit cycle, the trajectory can be understood by considering the symmetry in eq. (4.89). To this extent, consider first the zero-frequency instability. The reflection symmetry on the center manifold means  $M_0 = 0$ , and we can therefore redo the Stuart-Landau derivation for an instability at zero frequency. If the critical mode is at zero frequency, then there are a few changes in the derivation. First, the left and right eigenvectors have to be identical and real because the critical EV is real (it is zero). Secondly, there is no fast time dependence but only the slow time dependence due to the growth of the unstable mode, so we have  $dt \rightarrow \epsilon^2 \partial \tau$ . The different  $\mathbf{u}_n$  therefore instead obey the equation

$$-L_0 \mathbf{u}_n = B_n, \quad (4.94)$$

where the  $B_n$ 's are identical to the ones in eq. (4.73). The solution  $\mathbf{u}_1$  simplifies to  $\mathbf{u}_1 = R(\tau) \mathbf{v}$  where  $R(\tau)$  is a real function and  $\mathbf{v}$  is the critical eigenvector. Lastly, the inner product in the Fredholm alternative no longer contains an integral over the period but is simply a dot product between the vectors. The result is that for a zero-frequency instability, one arrives at an equation equivalent to the single mode version of the  $R_\alpha$  equation in eq. (4.86)

$$\dot{R} = \gamma_1 R - g R^3. \quad (4.95)$$

This describes a pitchfork bifurcation and has two time-independent solutions  $R_{eq} = \pm \sqrt{\gamma_1/g}$  if  $g > 0$  (again restricting the discussion to the relevant case of the supercritical bifurcations). The new fixed points after crossing the CP is then a constant version of eq. (4.88) and given by  $\mathbf{X} = \pm \sqrt{\mu \gamma_1/g} \mathbf{v}$ . By applying the symmetry operation  $\mathbb{R}$  to one of the solutions  $\mathbf{v}$  acquires a sign change, and  $\mathbb{R}$ , therefore, leads to the other possible solution. This is the same as in the Dicke model [132]. Transforming the atoms with  $\mathbb{R}$  leads to  $\psi_n \rightarrow e^{i\pi n} \psi_n$  which is equivalent to a displacement by  $\pm \pi/Q$  in space. The two solutions, therefore, correspond to the density wave with an amplitude that scales with  $\sqrt{\mu}$  and has either a maximum or a minimum at  $x = 0$ . Dual to the displacement of the atomic density wave, the coherent field of the cavity has a phase of  $\pm \pi$  depending on which of the two solutions the system is in. Going beyond the CP leads to the spontaneous breaking of this symmetry as the system chooses one of the two solutions.

For the limit-cycle solution, the symmetry can lead to a similar case where two different

solutions are connected through  $\mathbb{R}$ . If the periodic solution is always invariant under the symmetry transformation, then solutions are known as F-cycles [150]. Conversely, if the symmetry transformation on the center manifold is a reflection, then it is known that the periodic solution  $x(t)$  is invariant under the symmetry transformation if time is simultaneously shifted by half of the minimal period ( $T$ )

$$\mathbf{R}\mathbf{x}(t) = \mathbf{x}(t + T/2). \quad (4.96)$$

Such periodic solutions are known as S-cycles. Because of the reflection symmetry in our center manifold, we know that the limit cycle is one where the system oscillates between the atoms having a maximum at  $x = 0$  and a maximum at  $x = \pi/Q$ . Simultaneously the cavity field phases are rotating between  $\pm\pi$ . With this discussion we have shown how  $\mathcal{Z}_\epsilon$ -symmetry impacts a time-periodic system.

For the single limit cycle, the atoms oscillating between the two symmetry broken states, as observed both experimentally [142] and numerically [135, 138, 141], is, therefore, a direct consequence of the reflection symmetry of the center manifold and is independent of the specific realization considered (as long as its normal form is that of the Hopf bifurcation). For the case of two simultaneous limit cycles, the system evolves on a two-torus. The two frequencies have to be commensurate for this system to be periodic. If they are not, then the dynamics of both atoms and cavity will still oscillate, but the signal will not be periodic in time as seen in fig. 4.7b.

## 4.6 Atom collisions

Having thoroughly investigated the system for non-interacting atoms, we now seek to understand if the features are robust when collisions between the atoms are included. For the previously investigated single cavity mode systems in the literature, a limit cycle emerged when the pump was modulated at a frequency comparable to the recoil energy. Including the contact interaction between atoms was numerically found to lead to heating [141] and was argued to be the leading cause of the short lifetime of the experimentally observed time crystal in [142]. It is, therefore, necessary to understand the effect of weak contact interactions in the considered multimode setup.

### 4.6.1 Linear stability with a weakly interacting BEC

The main features derived for the non-interacting system are based on the linear stability analysis. We thus first need to study how this is affected by weak contact interactions. To this extent, we consider the classical atom equation eq. (4.15) in the small  $g$  regime.

The first step is understanding how the contact interaction affects the NP fixed point. In this case, the only mode with any occupation is the zero-momentum atom mode, which in this phase is described by the equation

$$i\dot{\psi}_0 = g|\psi_0|^2\psi_0. \quad (4.97)$$

A phase shift can be used to eliminate this energy shift and effectively change the atoms' chemical potential. The shifted atom equations take the form

$$\begin{aligned} i\dot{\psi}_k(t) = & \left( \frac{k^2}{2M} - i\kappa_{a,k} - g|\psi_0|^2 \right) \psi_k(t) + \sum_i \eta_i \operatorname{Re} \phi_i(t) (\psi_{k+Q}(t) + \psi_{k-Q}(t)) \\ & + g \sum_{k',q} \bar{\psi}_{k'} \psi_q \psi_{k+k'-q}. \end{aligned} \quad (4.98)$$

Having changed the chemical potential for the atoms, one observes that  $\psi_0 = 1$  and  $\psi_{k \neq 0} = \phi_i = 0$  is again a fixed point of the full evolution.

As the cavity equations are unaffected by the shift of the chemical potential, they still only couple to recoil momentum modes, and their Jacobian is unchanged. The only part of the Jacobian that changes are the atomic one. Due to the momentum-conserving nature of the contact interaction, the equations of motion are still invariant under the transformation  $\psi_k \rightarrow e^{i\pi k} \psi_k$  and a  $\pi$  phase shift of the cavity modes.

The Jacobian is the gradient of the EOMs evaluated at the fixed point, such that the only relevant terms are linear in the deviations around the NP fixed point. For the linear stability analysis, the only relevant collision terms are therefore

$$g (|\psi_0|^2 \psi_k + \bar{\psi}_{-k} \psi_0^2). \quad (4.99)$$

They have the feature that the  $k$ 'th mode couples to itself and  $-k$ . Momentum is, therefore, still a good quantum number. Mixing the  $k$  and  $-k$  modes lead to the known Bogoliubov collective modes of a BEC [157]. The cavity coupling still only couples to modes at the recoil momentum, which makes it sensible to differentiate between atom modes that are part of the polariton and those that are not. The atom modes that do not couple directly to the cavity ( $k \neq \pm Q$ ) are then the usual phonon modes [151, 158]. For the polariton instability, we thus only have to consider the recoil momentum as in the non-interacting case. Since the  $Q$  and  $-Q$  modes are coupled, the part of the system

that contributes to the Jacobian is

$$\begin{aligned}
F(\phi_i) &= (-i\Delta_i - \kappa_i)\phi_i - i\frac{\eta_i}{2}(\bar{\psi}_0\psi_1 + \bar{\psi}_1\psi_0 + \bar{\psi}_0\psi_{-1} + \bar{\psi}_{-1}\psi_0), \\
F(\psi_1) &= (-i(E_R + g) - \kappa_a)\psi_1 - i\sum_i \frac{\eta_i}{\sqrt{2}}(\bar{\phi}_i + \phi_i)\psi_0 - ig\bar{\psi}_{-1}, \\
F(\psi_{-1}) &= (-i(E_R + g) - \kappa_a)\psi_{-1} - i\sum_i \frac{\eta_i}{\sqrt{2}}(\bar{\phi}_i + \phi_i)\psi_0 - ig\bar{\psi}_1,
\end{aligned} \tag{4.100}$$

which should be compared to eq. (4.19). Like in the non-interacting case, an infinitesimal broadening of the atom modes identical for  $Q$  and  $-Q$  is assumed. Once again, the Jacobian can be written in a block form similar to eq. (4.20) with the cavity blocks ( $\mathbf{A}_j$ ) being unchanged but the off-diagonal blocks acquiring a slightly different form

$$\begin{aligned}
\mathbf{B}_j &= -i\frac{\eta_j}{2}(\mathbb{1}, \mathbb{1}) \otimes (\sigma_z + i\sigma_y), \\
\mathbf{C}_j &= -i\frac{\eta_j}{2} \begin{pmatrix} \mathbb{1} \\ \mathbb{1} \end{pmatrix} \otimes (\sigma_z + i\sigma_y),
\end{aligned} \tag{4.101}$$

where  $\mathbb{1}$  is the  $2 \times 2$  identity matrix. The atomic block changes due to the coupling between positive and negative momentum and are given by

$$\mathbf{D} = \begin{pmatrix} -i\tilde{E}_R - \kappa_a & 0 & 0 & -ig \\ 0 & i\tilde{E}_R - \kappa_a & ig & 0 \\ 0 & -ig & -i\tilde{E}_R - \kappa_a & 0 \\ ig & 0 & 0 & i\tilde{E}_R - \kappa_a \end{pmatrix}, \tag{4.102}$$

where  $\tilde{E}_R = E_R + g$ . The determinant can now be computed using the same technique as in section 4.4.1. The equation determining the possible frequencies of the unstable modes is

$$\begin{aligned}
\omega \sum_{j=0}^{N_c-1} c_j^2 \Delta_j (\kappa_j (E_R (E_R + 2g) + \kappa_{a,1}^2) + \kappa_{a,1} (\Delta_j^2 + \kappa_j^2) - \omega^2 (\kappa_{a,1} + \kappa_j)) \\
\times \prod_{i \neq j} \left( \omega^4 + 2\omega^2 (\kappa_i^2 - \Delta_i^2) + (\Delta_i^2 + \kappa_i^2)^2 \right) = 0.
\end{aligned} \tag{4.103}$$

The physically allowed solutions are those that lead to real values for the critical coupling strength

$$\Lambda_c = \frac{E_R(E_R + 2g) + \kappa_{a,1}^2 - \omega^2}{2E_R \sum_{j=0}^{N_c-1} c_j^2 \frac{(\Delta_j^2 + \kappa_j^2 - \omega^2)\Delta_j}{\omega^4 + 2\omega^2(\kappa_j^2 - \Delta_j^2) + (\Delta_j^2 + \kappa_j^2)^2}}. \tag{4.104}$$

It is seen that these equations are equivalent to their non-interacting counterparts in eqs. (4.31) and (4.32) apart from  $E_R^2$  being modified to the Bogoliubov dispersion  $E_R(E_R +$

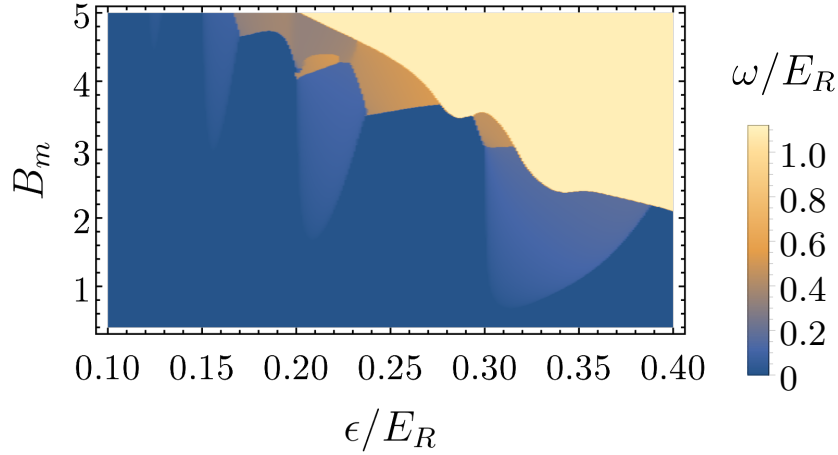


Figure 4.11: The same phase diagram as fig. 4.4 but with a contact interaction of  $g = 0.1E_R$  included.

2g). For small values of  $g$ , the linear stability results' qualitative features are unchanged. That a small  $g$  does not have a big impact on the linear stability is exemplified by the computation of the phase diagram in fig. 4.4 but with significant interactions included. Comparing the phase diagram in fig. 4.11 with fig. 4.4, which has no collisions, one sees that they are qualitatively equivalent. The only main change is that the separatrix in the atomic instability has shifted to larger  $\epsilon$ . This shows that the features discussed for the phase modulation setup in chapter 3 are not sensitive to small changes in the atom energy or interactions. For the generic two- and four-mode systems considered, the main effect is a non-trivial renormalization of the parameters. All the scenarios discussed in the non-interacting case are also present with interactions but for slightly different parameters.

One new feature different from the standard result [107] is that at a finite frequency, the critical coupling is potentially more sensitive to the specific atomic dispersion. To see this consider the critical coupling when only a single cavity mode is relevant to the system (while assuming that the system through some other mechanism has a finite frequency instability)

$$\Lambda_c = \frac{E_R(E_R + 2g) + \kappa_a^2 - \omega^2}{2E_R(\Delta_j^2 + \kappa_j^2 - \omega^2)\Delta_j} \left( \omega^4 + 2\omega^2(\kappa_j^2 - \Delta_j^2) + (\Delta_j^2 + \kappa_j^2)^2 \right). \quad (4.105)$$

For a zero-frequency instability, the two  $E_R$ 's in the denominator and numerator cancel each other such that the interactions only leads to a renormalization of the energy  $E_R \rightarrow E_R + 2g$ . The cancellation of  $E_R$  in the fraction is not possible at finite frequency. Therefore, the lowest order effect of including interactions in the limit cycle is not a simple renormalization of the recoil energy. If instead of interacting atoms, one considers

atoms at a finite, but either very low or very high temperature then it is found that the critical-coupling equation at  $\omega = 0$  is again only changed by  $E_R \rightarrow k_B T$  [105,108]. As the only change is a renormalization of the recoil energy, it means that for a zero-frequency instability, one can not see a qualitative difference between a finite temperature cloud and an interacting cloud by investigating the critical coupling. It would be interesting to investigate how the parameters for the finite-frequency instability change when the atoms have a finite temperature to see if one can observe a qualitative difference between the atomic states.

### 4.6.2 Beyond linear stability

Having seen that the linear stability is qualitatively the same as the non-interacting case, we now discuss what happens beyond the CP. The linear stability analysis has shown that interactions do not drastically change the center manifold, meaning that for small values of  $g$ , the structure of the different bifurcations remains unchanged. However, previous studies [141], and experiments [142] found that the atoms heat up due to the contact interactions. Heating is not captured within the center manifold, so one must go beyond it to capture these effects fully, and we leave this for future investigations. Instead, we consider the situation where the contact interaction is weak ( $g \sim 10^{-2} E_R$ ), such that the perturbations to the non-interacting Stuart-Landau results are negligible. First, we consider the case where the system exhibits a single-limit cycle. Following our previous approach, we assume the system crosses the critical point from the normal phase. As the limit cycle emerges and stabilizes, a finite occupation in the center manifold is generated. Using the solution for the center manifold in eq. (4.88), when only one limit-cycle mode is occupied, the recoil momentum  $X$  and  $P$  quadratures are

$$\begin{aligned} X_{a,Q} &= \sqrt{\mu} R (c_x e^{i\omega_c t} + c.c.), \\ P_{a,Q} &= \sqrt{\mu} R (c_p e^{i\omega_c t} + c.c.), \end{aligned} \quad (4.106)$$

where  $c_x$  and  $c_p$  are the complex coefficients from the right eigenvector of the center manifold and  $\omega_c$  is the frequency of the limit cycle. From the quadratures, we can reconstruct the  $\psi_Q$  field using the inverse transformation of eq. (4.59)

$$\psi_Q = c_+ e^{i\omega_c t} + c_- e^{-i\omega_c t}, \quad (4.107)$$

with  $c_+ = \sqrt{\mu/2} R (c_x + i c_p)$  and  $c_- = \sqrt{\mu/2} R (\bar{c}_x + i \bar{c}_p)$ . Notice that generally  $|c_+| \neq |c_-|$ .

In section 4.5.1, we discussed how enforcing normalization was essential for the center manifold calculation. Because of this construction, we can find the homogeneous atom



Frequency	Magnitude	Momentum
0	$b_0 \sim 1 - \mu$	0
$\omega_c$	$ c_{\pm}  \sim \sqrt{\mu}$	$Q$
$2\omega_c$	$ b_{\pm}  \sim \mu$	0

Table 4.1: A table of the occupied atomic modes when the system is in a single limit cycle. The modes and their properties are derived from the Stuart-Landau equation.

component in the limit cycle from the center manifold

$$\begin{aligned}
\psi_0 &= \sqrt{1 - 2|\psi_Q|^2} \\
&= \sqrt{1 - 2(c_+\bar{c}_- + c_-\bar{c}_+ + |c_+|^2 e^{i2\omega_c t} + |c_-|^2 e^{-i2\omega_c t})} \\
&\approx 1 - c_+\bar{c}_- - c_-\bar{c}_+ - |c_+|^2 e^{i2\omega_c t} - |c_-|^2 e^{-i2\omega_c t} \\
&= b_0 + b_+ e^{i2\omega_c t} + b_- e^{-i2\omega_c t}.
\end{aligned} \tag{4.108}$$

Here the square root was expanded around  $\mu = 0$ , similar to the approximation underlying the Stuart-Landau equation. In the last line, the Fourier coefficients of the homogeneous field have been defined as

$$b_0 = 1 - 2 \operatorname{Re}(c_+\bar{c}_-) \quad \text{and} \quad b_{\pm} = -|c_{\pm}|^2. \tag{4.109}$$

The occupied atom fields and their characteristic scalings from the Stuart-Landau results are shown in table 4.1.

The limit-cycle can be destroyed through two different mechanisms. The first to go deeper into the superradiant state. By increasing  $\mu$  it is necessary to include the next correction to the fixed point in eq. (4.81) which adds higher harmonics to steady state. Another effect of going deeper into the superradiant state is scattering from  $\psi_Q$  into  $\psi_{2Q}$ , which does not obey a reflection symmetry. When these modes become important, our center manifold analysis is insufficient, and we numerically find the limit cycle to be destroyed. The sensitivity to going beyond the center manifold is not unexpected considering that  $M_0$  is now non-zero in the Stuart-Landau equation. The scattering from  $\psi_Q$  to  $\psi_{2Q}$  happens through scattering of a pump photon into the cavity. For the occupation of the  $\psi_{2Q}$  to be significant, it is, therefore, necessary that the occupation of  $\psi_Q$  is large. By staying close to the CP our Stuart-Landau equation within the center manifold is valid. However, there is a second mechanism that can destroy the limit cycle even close to the CP. This second mechanism is for the atoms to scatter into phonon modes that are not commensurate with the cavity. Scattering into phonon modes is only possible with finite contact interactions between the atoms and we now seek to understand how the phonon scattering is affected by the limit cycle in the polariton.

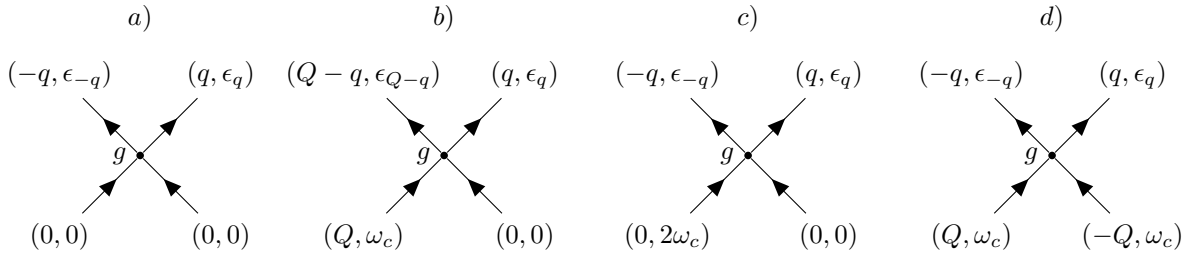


Figure 4.12: *Four different scattering events between the atomic parts of the limit cycle described by table 4.1. All four scattering events are momentum conserving and involve the scattering off a  $\psi_0(0)$  state. In a) two atoms from the homogeneous and stationary part of the system collide. This process is of  $\mathcal{O}(g)$ . In b), the homogeneous atom collides with an atom with recoil momentum and a frequency equal to the limit cycle frequency, which makes this process of  $\mathcal{O}(g\sqrt{\mu})$ . In c), the homogeneous atom collides with a homogeneous atom oscillating at twice the limit cycle frequency. This process is like the one in d) of  $\mathcal{O}(g\mu)$ . In d), two atoms with opposite recoil momentum collide, generating a phonon at a small  $q$  value. Notice that this process can also be done if the atoms have the same direction of their momenta. In that case, the two final momenta will have  $Q$  added to them.*

In the limit cycle, the atoms can be in three different states as shown in eqs. (4.107) and (4.108): a homogeneous spatial configuration that is constant in time, namely with magnitude  $b_0$ , a spatial density modulation with oscillates with frequency  $\omega_c$  and has magnitude  $|c_{\pm}|$  and a homogeneous spatial configuration that oscillates at  $2\omega_c$  with magnitude  $|b_{\pm}|$ . Due to the interactions between the atoms, these states can scatter off each other, which gives rise to new phonon modes. The four scattering processes that are lowest order in  $g$  and involve the most occupied atomic modes according to table 4.1 are shown in fig. 4.12. In the regime of small  $\mu$ , the fastest processes are those involving the homogeneous stationary atom mode because this mode has a magnitude of  $\mathcal{O}(1)$  as shown in table 4.1. The dominating process is, therefore, fig. 4.12a where two stationary atoms scatter off each other. They can scatter into two atoms with momentum  $\pm q$  such that momentum is conserved. Energy also has to be conserved, requiring  $\epsilon_q + \epsilon_{-q} = 0$ . In the regime of small  $\mu$ , the amplitude of the density modulation is tiny. The dispersion of the phonon modes is therefore well approximated as that of the bare phonons  $\epsilon_q = q^2$ , which is here written in units of the recoil energy. Since the dispersion is quadratic, energy conservation can only be satisfied if  $q = 0$ , which means that the scattering process in fig. 4.12a can not generate occupation in any phonon modes.

The next scattering channel is that of fig. 4.12b. Here an atom mode carrying recoil momentum and with the frequency of the limit cycle scatter against the state  $\psi_0(0)$ , which makes this process of order  $\mathcal{O}(g\sqrt{\mu})$ . For this process to be energy conserving, it

is necessary that

$$\begin{aligned}
\epsilon_{Q-q} + \epsilon_q - \omega_c &= 0, \\
(1 - q)^2 + q^2 - \omega_c &= 0, \\
\rightarrow q &= \frac{1}{2} \pm \frac{1}{\sqrt{2}} \sqrt{\omega_c - \frac{1}{2}}.
\end{aligned} \tag{4.110}$$

This scattering process thus acts as a source for two phonon modes at  $q$  and  $Q - q$ , such that they will grow with a rate related to  $g\sqrt{\mu}$ . This scattering channel is closed when  $\omega > 1/2$ . The dominating scattering channels then become of  $\mathcal{O}(g\mu)$  and correspond to fig. 4.12c and fig. 4.12d. Here energy conservation leads to an outgoing momentum given by  $q = \sqrt{\omega_c}$ . At the same order, there is also the process of fig. 4.12d but with both incoming momenta in the same direction. This scattering channel is only open if the limit-cycle frequency is above the recoil energy, as the momentum must satisfy  $q = \sqrt{\omega_c - 1}$ . For  $\omega_c < 1/2$ , the fastest growing phonon mode will therefore grow at a rate proportional to  $g\mu$ . We, therefore, predict that by changing  $\omega_c$  from above  $E_R/2$  to below  $E_R/2$ , the growth rate of the phonon modes should drop significantly.

Deeper inside the limit cycle phase, due to the large density modulation, one can no longer use the crude approximation of a quadratic phonon dispersion. An interesting aspect of this is that in the static case, this leads to the opening of band gaps [159]. Opening of band gaps could close off specific scattering channels as a function of the limit-cycle frequency.

Our preliminary studies have shown that the dominating growth rates of the phonon modes are linear in  $g$  and either proportional to  $\mu$  or  $\sqrt{\mu}$ . Since  $\mu$  can be tuned straightforwardly, we expect that there is an experimentally relevant regime where the limit cycle will persist for many oscillations before being destroyed by the growing phonon modes. An intriguing aspect is that the lifetime of the limit cycle should be significantly affected by changing the frequency of the limit cycle. As the frequency is tuneable in the multimode polariton system, it provides an ideal platform for these investigations experimentally and theoretically.

Lastly, we will consider what happens when the system has two limit cycles. In this case, the coupled Stuart-Landau equations lead to the recoil momentum mode moving on a two-torus

$$\psi_Q = a_+ e^{i\omega_a t} + a_- e^{-i\omega_a t} + c_+ e^{i\omega_c t} + c_- e^{-i\omega_c t}, \tag{4.111}$$

where  $\omega_a$  and  $\omega_c$  are the frequencies of the two different limit cycles. In the investigated cases, we always considered one of the limit cycles to have a frequency greater than the recoil energy. Consequently, the fastest growing phonon mode is predicted to grow with a rate of  $g\sqrt{\mu}$ . The two-torus system will not have modes that grow faster than the single mode case, but it will have more of them, as the number of possible scattering

channels increases due to the two different frequencies. Similarly to the single mode case, the momentum of the dominant growing phonon modes can be found using energy conservation. In conclusion, we can state that for experiments where the single limit cycle is observable at  $\omega_c > E_r/2$ , the two-torus solution should have a comparable lifetime.

## 4.7 Summary and discussion

In this chapter, we first performed a linear stability analysis of the classical equations for the multimode cavity model in the regime where the cavity had a sub-recoil linewidth. The analytical equations for the critical coupling and frequency have been derived for an arbitrary number of cavity modes. A careful investigation of these equations for the one-, two- and the four-mode system has shown that a negatively detuned cavity mode can greatly impact how the polariton became unstable. For the one-mode case, a negatively detuned cavity mode made the atom cloud directly unstable at infinitesimal pump power, and no polariton emerges. The situation was qualitatively changed when a second positively detuned cavity mode was included. The positively detuned cavity mode could stabilize the system, which allowed a polariton to form that became unstable at a finite frequency. By controlling the detuning of the bare cavity modes, the frequency of the polariton instability could be directly tuned. We found that the four-mode cavity mode system could have two different finite-frequency instabilities at the same critical pump power.

To investigate the fate of the unstable polariton mode beyond the critical point, we have generalized the Stuart-Landau equation to describe the case of two simultaneous finite-frequency instabilities. We found that these took the form of a double Hopf bifurcation, and through a normal form analysis, it was shown that the four-mode system could exhibit a single limit-cycle steady state, a bistable region where the initial conditions determined the steady state, and a two-torus solution where two limit cycles were simultaneously present in the system. We used the symmetry of the equations of motion to explain why a single limit-cycle steady state will be a state where the systems periodically oscillate between two states connected by a  $\mathcal{Z}_2$  symmetry. For the four-mode case, the periodicity of the system could be broken if the two different limit cycles were not commensurate. Finally, we have discussed some preliminary results of the effect of including contact interactions between the atoms. Here it was explained how that the presence of the limit cycle opened up new scattering channels. Which scattering channel were dominant could be changed by adjusting the limit-cycle frequency.

Our results gives rise to several questions that are worth further investigation. The first is finishing the analysis of the effect of atom interactions. Here the precise form of

the rate still has to be calculated. With this result, it is then possible to investigate if there are regimes where cavity cooling is efficient enough to prevent the growth of the phonon modes. Another exciting aspect is further exploring the bistability observed for the double Hopf bifurcation. If the sensitivity of the bistability can be selectively chosen by tuning the experimental parameters, this could be interesting for applications. Following these ideas it is worth understanding how the two-cavity-photon process that has been neglected affects the limit cycle. It is known that for the linear stability analysis, it only amounts to a shift of the cavity detunings, which can be compensated by changing the sideband frequencies. However, beyond the normal phase, it gives rise to a second optical potential for the atoms, and it would therefore lead to perturbations to the coefficients of the Stuart-Landau equations. By tuning the values, these perturbations can certainly be made negligible, but one could investigate if tuning the two-cavity-photon process could give rise to steady states with an additional limit cycle in the amplitude equations.

# Chapter 5

## Polaron-polaritons

### 5.1 Introduction

In chapter 3, the focus was on the spectral features, while the occupation of the spectrum was included through classical equations in chapter 4. This last chapter considers a driven system with strong interactions between bosonic and fermionic degrees of freedom. The spectral properties of both degrees of freedom will change due to the interaction. Because the system is driven, it is also necessary to consider the change in the occupation of the spectrum. As it is necessary to capture the perturbation to the spectrum of fermionic degrees of freedom, it is not possible to approach the system using classical equations as in chapter 4. Instead, we solve the coupled Dyson equations for the retarded and the Keldysh propagator.

In this chapter, the type of system considered is a two-dimensional semiconductor inside a cavity. The research field of two-dimensional materials has evolved dramatically since the discovery of graphene [160] and monolayer transition metal dichalcogenides (TMD) [161]. From the perspective of polaritons, the TMD monolayers are exciting because they have very strong photoluminescence [162, 163]. The strong photoluminescence arises from the fact that these materials have a large exciton binding energy on the order of hundreds of meVs [164–166]. TMD monolayers also have an additional degree of freedom because they exhibit two different valleys within the first Brillouin zone [167, 168]. This gives rise to an effective description of the TMD monolayers with two different species of electrons. An important property of the TMD monolayers is that they are structurally stable at room temperature and can be embedded inside solid-state microcavities. It is experimentally possible to realize high-quality solid-state microcavities such that strong coupling between the exciton and the cavity can be achieved, giving rise to polaritons.

The main motivation for our work is the recent developments [99, 169–171], where experimental groups have been able to add a gate voltage to the TMD monolayer while it

is inside a cavity. The gate voltage makes it possible to inject electrons into a conduction band of a different valley than the electrons that form the exciton.

As the conduction electrons introduced by the voltage bias are not constituents of the excitons, the system can effectively be described as a two-dimensional Bose-Fermi mixture where the bosons are excitons, and the fermions are the conduction electrons in the other valley. In the limit where there is only a single exciton in the system, the exciton's interaction with the electrons leads to the formation of a quasiparticle known as a Fermi polaron. The Fermi polaron system has been widely studied in three dimensions and in two dimensions [172–178]. The experimental realization of a quasi two-dimensional quantum gas [179] has motivated several different theoretical approaches such as a variational ansatz [180–184], non-self-consistent ladder approximation [185], functional renormalization group [186] and even diagrammatic Monte Carlo [187]. Motivated by the above-mentioned experimental developments with TMD monolayers in cavities, the large interest in Fermi polarons has carried over into investigations of the effects of polariton formation either through a variational approach [188, 189] or with the non-self-consistent ladder approximation [190, 191]. Indeed, since the excitons can be created by absorbing a photon from the cavity, this gives rise to excitons-polaritons that couple to electrons. All the previous theoretical approaches have been restricted to thermal equilibrium. However, due to the finite lifetime of excitons and photons, the system must be driven for a finite density of exciton-polaritons to be present in the steady state. This chapter goes beyond the previous theoretical work by non-perturbatively including drive and dissipation via non-equilibrium field theory.

Apart from the TMD monolayers, two-dimensional polaritons also appear in quantum well systems [192], where the study of quantum polaritonic fluids has been made possible by the existence of non-equilibrium Bose-Einstein condensation even at room temperature [193–195]. This has attracted the attention of a large community in recent years, and exciton-polariton condensation has now also been observed with TMD monolayers [196]. Already for these systems, where no additional electrons are present to form polarons, the theoretical description of non-equilibrium condensation has been limited to either quantum kinetic theories [197] or semiclassical equations like the ones we introduced in chapter 4. Our approach extends previous theories by simultaneously describing the coupled dynamics of the response and correlation functions at and in the vicinity of condensation. It is also directly applicable to the present case of interest where gated electrons in TMD monolayers lead to the formation, and potentially condensation, of exciton-polaron-polaritons.

Doing the out-of-equilibrium self-consistent calculations comes with a host of challenges, and our work so far has been concerned with finding ways to make the calcula-

tions feasible and reasonably accurate. Section 5.2 is devoted to deriving the model and its action, while section 5.3 derives the self-energies for our non-equilibrium self-consistent ladder approximation. The numerical methods we have developed are described in section 5.4, and some first results are presented in section 5.5.

We find that our method can capture the known features of the Fermi polaron and that coupling the exciton to the cavity leads to the formation of a quasiparticle, the polaron-polariton. The polaron-polariton is an exciton strongly coupled to light and the Fermi sea simultaneously. Including the cavity leads to more than just a dressing of the polaron as it renormalizes the coupling to the Fermi sea. The cavity can significantly alter the polaron, and we can change the qualitative features of the lowest energy excitation by shifting the cavity detuning. We explore the system's behavior when a continuous laser drives the cavity and find an accumulation of excitations at finite momentum. The accumulation is explained by a competition between cavity loss and momentum relaxation induced by electron scattering. Because of the hybrid nature of the polaron-polariton, both the loss and the momentum relaxation can be qualitatively altered by changing the cavity detuning.

While implementing the non-equilibrium self-consistent ladder approximation is complicated, it is versatile as our method can also be applied to three-dimensional systems with only minor modifications. It, therefore, allows exploring non-equilibrium features in many-body physics. While this by itself is a major theoretical motivation, it is important that our models should describe current experiments with monolayer semiconductors in cavities well.

## 5.2 Model

The two-dimensional polaron-polariton system is complex because there is a strong coupling between the cavity and the exciton but also a strong coupling between the exciton and the electron gas in the conduction band. The exciton and photon are strongly coupled, leading to polariton formation, while the strong interaction between excitons and electrons leads to the formation of polarons. We seek to construct a method that treats both effects on the same level. In addition, a non-equilibrium treatment is essential due to the drive and loss of the cavity.

### 5.2.1 Non-interacting constituents

Choosing the simplest possible building blocks for the system is essential as the complexity arises due to their interactions. To do this, we first describe how the different bare parts of the system are modeled.



## Electrons

A significant experimental achievement is that by gating the TMD monolayer [99, 169], electrons of a different valley than those creating the exciton can be excited to the conduction band. These electrons are well described as a two-dimensional free fermion gas with an effective mass  $m_e$ . The electrons' chemical potential  $\mu_e$  is tuned by varying the gate voltage. The last free parameter for a free electron gas is the inverse temperature  $\beta = 1/Tk_B$ . With this simple description, the bare electron propagators are

$$\begin{aligned} G_{e,0}^R(p) &= \frac{1}{\omega + \mu_e - \frac{k^2}{2m_e} + i0^+}, \\ G_{e,0}^K(p) &= -2i\pi (1 - 2n_F(\omega)) \delta\left(\omega + \mu_e - \frac{k^2}{2m_e}\right), \end{aligned} \quad (5.1)$$

where  $n_F(\omega) = (e^{\beta\omega} + 1)^{-1}$  is the Fermi-Dirac distribution. To simplify the notation define  $\mathbf{p} = (\omega, \mathbf{k})$ ,  $p = (\omega, |\mathbf{k}|)$  and  $\mathbf{k} = (k_x, k_y)^T$ . The propagators are the generalization of the free propagators from eq. (A.40) to a spatially homogeneous system. The isotropy of space means that the propagators only depend on the magnitude of the momentum  $k = |\mathbf{k}|$  and not the direction.

## Excitons

An exciton is a tightly bound pair consisting of an electron in the conduction band and a hole in the valence band. Due to the dipole moment generated by separating the hole and electron, excitons interact with phonons. The microscopic description of the excitons themselves is therefore complicated [198]. TMD monolayers have the property that the exciton binding energy is on the order of several hundred meV's [196], which is exceptionally high. In these materials, the exciton binding energy is the largest energy scale, which makes the excitons stable quasiparticles with long lifetimes. To the lowest order, the excitons can be modeled as a single species of particles independent of the electrons in the other valley, and at low temperatures, the perturbation can be included as a phenomenological decay rate of the exciton.

In the TMD systems the effective mass of the hole is similar to effective electron mass  $m_e$  [199] such that the exciton mass is approximately  $m_x = 2m_e$ . In this simple model of the exciton, the bare propagators are

$$\begin{aligned} G_{x,0}^R(p) &= \frac{1}{\omega - \frac{k^2}{2m_x} + i0^+}, \\ G_{x,0}^K(p) &= -2i\pi \delta\left(\omega - \frac{k^2}{2m_x}\right), \end{aligned} \quad (5.2)$$

where the exciton chemical potential has been set to zero. As excitons consist of an electron-hole pair, they are bosonic quasiparticles. For bosons, the chemical potential is equivalent to a detuning, which should be interpreted as the cost of creating excitations with zero momentum.

The combination of high binding energy and low temperature means that the thermal energy is insufficient to create an exciton in a TMD monolayer. To occupy the exciton states, it is, therefore, necessary to drive the system, which is done through the cavity. In TMD bilayers, the excitons can be injected electrically, and their thermal condensation has been observed [200].

## Cavity

The most straightforward description of the cavity is as a slab of material with a refractive index  $\tilde{n}$  between two mirrors. Let the cavity dimensions be  $L_x \times L_y \times L_z$ , where  $L_z$  is the length between the mirrors perpendicular to the two-dimensional material. Due to the boundary set by the cavity, the modes have three discrete quantum numbers  $(n_x, n_y, n_z)$  and energy given by [85]

$$\omega_{k_x, k_y, k_z} = c/\tilde{n} \sqrt{k_x^2 + k_y^2 + k_z^2}, \quad (5.3)$$

with  $k_i = \frac{n_i \pi}{L_i}$ , where  $c$  is the speed of light in vacuum. If the slab is thin but long in the  $x$  and  $y$  directions such that  $L_z \ll L_x \sim L_y$ , the level spacing between different  $k_z$  is large compared to the spacing between the transverse directions. For thin enough slabs, the longitudinal energy spacing will be the largest scale in the system. The longitudinal mode index is then set by the one closest to the exciton's binding energy. If the cavity is approximated as infinitely large in the transverse directions, the transverse level spacing goes to zero, and the transverse spectrum becomes continuous. Expanding around zero transversal momentum, the cavity dispersion is approximated as

$$\omega(k_x, k_y) \approx \frac{cn_z \pi}{\tilde{n} L_z} + \frac{1}{2} \frac{cL_z}{\tilde{n} n_z \pi} (k_x^2 + k_y^2) = E_0 + \frac{k^2}{2m_c}, \quad (5.4)$$

where  $E_0$  is the constant energy offset due to the longitudinal mode and  $m_c = \frac{\tilde{n} n_z \pi}{cL_z}$  the corresponding photon mass.

The cavity mirrors are inherently lossy, so the system is not energy-conserving. To get non-trivial steady states, the loss has to be compensated by external driving. We consider driving non-resonantly away from modes that have an appreciable occupation, which means that the imprinted phase from the laser is lost through the relaxation process, and we can therefore model the laser as an incoherent environment with a narrow frequency distribution. To this extent, both loss and drive are approximated by coupling to an external electromagnetic environment. Assuming the coupling to the environment is

small, such that the cavity and environment do not hybridize (quasiparticle weight of bare cavity mode weight close to unity), the coupling leads to renormalization of the cavity propagators as shown in section 2.8. Under those conditions, the retarded self-energy of the cavity is constant

$$\Sigma_c^R = \sigma - i\gamma. \quad (5.5)$$

The constant shift is combined with  $E_0$  to give an effective photon detuning  $\Delta_c$ . This detuning can be freely tuned by varying the pump frequency as for the ultracold atom system considered previously. The loss rate  $\gamma$  describes photon leakage out of the cavity and is determined by the cavity geometry and quality. Here we assume that it is identical for all transverse modes, which is a good assumption because the energy scale of the transverse modes is small compared to the total energy in the cavity mode. As seen in section 2.8, incoherent pumping affects the Keldysh self-energy through the distribution function derived in eq. (2.114). This result can be modified to model a pump laser by writing the occupied part of the cavity Keldysh self-energy as

$$\delta\Sigma_c^K(p) = i2\kappa(p), \quad (5.6)$$

where  $\kappa(p)$  is a function describing the pump envelope in energy and momentum. To simplify the analysis, we assume that the pump does not break the isotropy of space and only depends on the magnitude of the momentum.  $\kappa(p)$  is proportional to  $\gamma$ , which is small, but also to the occupation of the modes, which is determined by the intensity of the laser. It is, therefore, possible to increase the effective drive strength of the cavity without requiring large  $\gamma$ .

Accounting for drive and dissipation, the bare cavity propagators are given as

$$\begin{aligned} G_{c,0}^R(p) &= \frac{1}{\omega - \Delta_c - \frac{k^2}{2m_c} + i\gamma}, \\ G_{c,0}^K(p) &= \frac{-2i(\gamma + \kappa(p))}{\left(\omega - \Delta_c - \frac{k^2}{2m_c}\right)^2 + \gamma^2}. \end{aligned} \quad (5.7)$$

## 5.2.2 Interactions

As already mentioned, the system contains two distinct types of interactions: interactions between the exciton and the cavity and interactions between the excitons and the electrons. In both cases the form is most intuitive in real-space  $\mathbf{r} = (r_x, r_y)^T$  and time  $t$ . Similar to the composite index introduced for momentum and energy, we use the composite variable  $\mathbf{x} = (t, \mathbf{r})$  for space and time.

## Exciton-cavity

The exciton is a localized particle with a Bohr radius on the order of a few nanometers [201]. Due to the small spatial extension, the interaction with the electromagnetic field can be approximated as a dipole interaction as discussed in section 3.2. The dipole interaction is not number conserving as it contains counter-rotating terms but similar to the discussion of the laser section 3.2, the counter-rotating terms can be neglected on the time scale the system is probed. The remaining process describes annihilation of an excitation of the complex exciton field  $b(\mathbf{x})$ , through creation of an excitation in the conjugate complex photon field  $\bar{a}(\mathbf{x})$  at the same point in space-time. The resulting interacting term in the action is of the form

$$S_{x-c} = -\Omega \sum_{\alpha,\beta=\{+,-\}} \int dt \int d^2\mathbf{r} \bar{a}_\alpha(\mathbf{x}) \sigma_{\alpha,\beta}^z b_\beta(\mathbf{x}) + H.c., \quad (5.8)$$

where  $\Omega$  is the coupling strength between exciton and cavity and  $\sigma_{\alpha,\beta}^z$  is the third Pauli matrix.

The bare constituents are diagonal in reciprocal space and frequency, which makes it advantageous to Fourier transform the interaction. To keep the notation compact and transparent, the Fourier transform is written as

$$f(\mathbf{x}) = \frac{1}{A} \sum_{\mathbf{p}} e^{i\mathbf{p}\cdot\mathbf{x}} f(\mathbf{p}), \quad (5.9)$$

where the dot-product is defined as  $\mathbf{p}\cdot\mathbf{x} = \mathbf{k}\cdot\mathbf{r} - \omega t$  and  $A^{-1} \sum_{\mathbf{p}} = \int \frac{d\omega}{2\pi} \int \frac{d^2\mathbf{p}}{(2\pi)^2}$ . Rotating from the  $\pm$  basis to the Keldysh basis gives an action with a similar form as the one discussed in section 2.8

$$S_{x-c} = -\Omega \frac{1}{A} \sum_{\mathbf{p}} \sum_{\alpha,\beta=\{c,q\}} \bar{a}_\alpha(\mathbf{p}) \sigma_{\alpha,\beta}^x b_\beta(\mathbf{p}) + H.c., \quad (5.10)$$

where  $\sigma^x$  is the first Pauli matrix. Crucially, this interaction is quadratic in fields and diagonal in  $\mathbf{p}$ . Similar to the case considered in section 2.8, this means that the interaction with the cavity can be included in an exciton self-energy given by diagrams equivalent to those in fig. 2.6b and fig. 2.6c

$$\begin{aligned} \Sigma_{xc}^R(p) &= \Omega^2 G_{c,0}^R(p), \\ \delta\Sigma_{xc}^K(p) &= \Omega^2 \delta G_{c,0}^K(p). \end{aligned} \quad (5.11)$$

Because of the linear coupling between exciton and cavity, the self-energies are exact.

The excitonic component of the polariton is of most interest because this is the part

that couples to the electrons. Conversely, given the full exciton propagator, the dressed cavity propagators are directly given by

$$\begin{aligned} G_c^R(p) &= \frac{1}{(G_{c,0}^R(p))^{-1} - \Omega^2 G_x^R(p)}, \\ G_c^K(p) &= (i2\gamma + i2\kappa(p) + \Omega^2 G_x^K(p)) |G_c^R(p)|^2, \end{aligned} \quad (5.12)$$

where we have anticipated that the approximation we will use for the exciton-electron interaction leaves the exciton propagator translation invariant. We will refer to the cavity-dressed exciton as the bare polariton, since the exciton propagator includes the cavity through the self-energies.

### Exciton-electron

The exciton consists of a spatially separated electron-hole pair. We have discussed that it is tightly bound and that we can therefore approximate it as a point-like particle. The interaction between the exciton and the electron is, therefore, like that of a dipole and a charge. For a quantitative treatment, one would have to treat the spatial dependence of the two-body potential, but if one only considers low energies and densities, then the short-range behavior of the potential will not be probed during the scattering event. At the lowest level of approximation the interaction can then be characterized by an s-wave contact-interaction [202]

$$H_{x-e} = g \int d^2\mathbf{r} b^\dagger(\mathbf{r}) c^\dagger(\mathbf{r}) c(\mathbf{r}) b(\mathbf{r}), \quad (5.13)$$

where  $c$  is the annihilation operator of the electrons. The corresponding interaction term in the action is

$$S_{x-e} = -g \sum_{\alpha=\{+,-\}} \int d\mathbf{x} \bar{b}_\alpha(\mathbf{x}) \bar{c}_\alpha(\mathbf{x}) c_\alpha(\mathbf{x}) b_\alpha(\mathbf{x}). \quad (5.14)$$

Opposite to the previously considered ultracold system with repulsive interactions, the collisions can now lead to bound states and are therefore essential to capture the main qualitative features of the system correctly. For the two-body scattering problem in two dimensions, any attractive interaction leads to the existence of a bound state [203, 204]. Differently from the three-dimensional case, the scattering length is directly related to the binding energy of the bound state  $E_B$  through  $a_s = 1/\sqrt{mE_B}$ , which for two dimensions is always positive.

For TMD monolayers, bound states between one hole and two electrons have been found to also have large binding energies on the order of tens of meVs [205–207] and are referred to as trions. These bound states correspond to a scattering process where

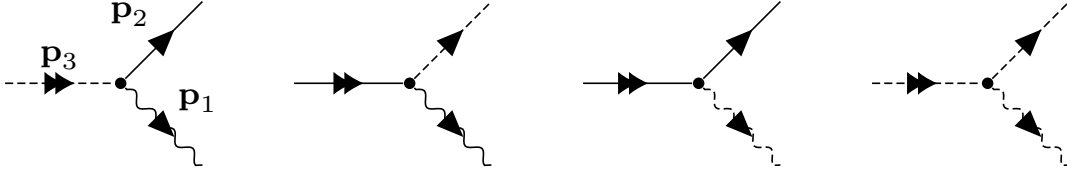


Figure 5.1: *The vertices between trions (double arrows), electrons (straight lines), and excitons (wavy lines). The dashed line represents a quantum field, and the solid line a classical field. Only the first vertex has the energy-momentum structure explicitly shown, but it is identical for all four vertices. The vertices are generated by the exciton-electron scattering in eq. (5.13) and described by eq. (5.16). Along with the four vertices shown here, there are another four vertices with the arrows reversed. These correspond to the conjugate processes.*

the exciton collides with an electron, and they move together. In the TMD monolayer system, both the electrons and the trions obey fermionic statistics. If we want to capture any perturbation to either the electron's or the trion's spectrum, then we have to go beyond classical approaches. To that extent, we will develop a self-consistent theory for the propagators based on the Dyson equation.

To efficiently write Dyson equations, it is convenient to include the trions directly in the action. This can be achieved through a Hubbard-Stratonovich transform, similarly to how the noise was included in the semiclassical equations in (4.3). The Hubbard-Stratonovich transform is a way of rewriting the two-body interactions between the electrons and excitons as an interaction with an auxiliary trion field  $\Delta(\mathbf{x})$  through

$$\begin{aligned} \exp(iS_{x-e}) &= \exp\left(-ig \sum_{\alpha,\beta=\{+,-\}} \int d\mathbf{x} \bar{b}_\alpha \bar{c}_\alpha \sigma_{\alpha,\beta}^z c_\beta b_\beta\right) \\ &= \int \mathcal{D}[\bar{\Delta}_\pm, \Delta_\pm] \exp\left(i \sum_{\alpha,\beta=\{+,-\}} \int dt \int d^2\mathbf{r} \frac{\bar{\Delta}_\alpha \sigma_{\alpha,\beta}^z \Delta_\alpha}{g} \right. \\ &\quad \left. - \bar{b}_\alpha \bar{c}_\alpha \sigma_{\alpha,\beta}^z \Delta_\beta - \bar{\Delta}_\alpha \sigma_{\alpha,\beta}^z c_\beta b_\beta\right), \end{aligned} \quad (5.15)$$

where the space-time dependence of the fields has been suppressed. After Fourier transforming and Keldysh rotating, the contact interaction leads to an energy and momentum conserving interaction

$$S_{x-e} = -\frac{1}{\sqrt{2}A^2} \sum_{\alpha,\beta,\gamma=\{c,q\}} \sum_{\mathbf{p}_1,\mathbf{p}_2,\mathbf{p}_3} M_{\alpha,\beta}^\gamma \bar{b}_\alpha(\mathbf{p}_1) \bar{c}_\beta(\mathbf{p}_2) \Delta_\gamma(\mathbf{p}_3) \delta(\mathbf{p}_1 + \mathbf{p}_2 - \mathbf{p}_3) + c.c., \quad (5.16)$$

where the factor of  $1/\sqrt{2}$  originates from the Keldysh rotation and the elements in  $M_{\alpha,\beta}^\gamma$

are

$$M_{\alpha,\beta}^c = \sigma_{\alpha,\beta}^x \text{ and } M_{\alpha,\beta}^q = \delta_{\alpha,\beta} \quad (5.17)$$

The interaction in eq. (5.16) leads to four different vertices that are shown in fig. 5.1.

Together with this interaction term, there is also a quadratic term for the bare trion, which defines the bare trion propagator

$$G_{\Delta,0}^R(p) = \frac{1}{1/g + i0^+}. \quad (5.18)$$

### Conservation laws

With the introduction of the trion field into the action, it is essential to understand the conservation laws different constituents of the system obey. The exciton-cavity coupling makes the exciton driven and dissipative, and it, therefore, obeys neither particle nor energy conservation. Electrons can scatter off the excitations, but electrons can not be exchanged into excitons or vice-versa, so the interaction conserves the electron number. What happens when one introduces the trion? This composite field contains one electron, so one could naively expect that the new conserved quantity is the sum of electrons and trions. However, the trions also contain an exciton that can be lost and generated, so one would not expect the trion number to be conserved. Our approach is based on the action, so this confusion can be cleared up using Noether's theorem [38]. The non-equilibrium nature of the cavity leads to additional coupling of the  $\pm$  branches for the exciton fields. Consequently, Noether's theorem for the contour fields of the exciton does not lead to conserved currents [82]. The electron and trion do not have direct coupling between the contour fields (apart from the contour endpoints). Consequently, the conserved currents will be independent of the branch index. To understand the conserved currents, it is thus sufficient to consider an action of the form

$$S = \int d\mathbf{x} L = \int d\mathbf{x} \bar{c}(\mathbf{x}) \left( i\partial_t - \frac{\nabla^2}{2m_e} + \mu_e \right) c(\mathbf{x}) + \frac{\bar{\Delta}(\mathbf{x})\Delta(\mathbf{x})}{g} - \bar{c}(\mathbf{x})\bar{b}(\mathbf{x})\Delta(\mathbf{x}) - \bar{\Delta}(\mathbf{x})b(\mathbf{x})c(\mathbf{x}), \quad (5.19)$$

where  $L$  is the Lagrangian. The Lagrangian is invariant under the global symmetry

$$\Psi = (c, \bar{c}, \Delta, \bar{\Delta}) \rightarrow (e^{i\epsilon}c, e^{-i\epsilon}\bar{c}, e^{i\epsilon}\Delta, e^{-i\epsilon}\bar{\Delta}) \forall \epsilon. \quad (5.20)$$

Because this is an infinitesimal transformation, it can be written as

$$\Psi_n \rightarrow \Psi_n + \epsilon \Gamma_n \Psi_n, \text{ with } \Gamma = (i, -i, i, -i)^T. \quad (5.21)$$

The theory then has a conserved current given by [38]

$$j_{\mu,n} = \frac{\partial L}{\partial (\partial_\mu \Psi_n)} \Gamma_n \Psi_n. \quad (5.22)$$

As the trion field does not have its own dynamics (no  $\partial_\mu \Delta$  in  $L$ ) there are no conserved currents for the trions. Furthermore, as the trion couples to the electron through  $c$  and not  $\partial_\mu c$ , the electron conservation laws are not affected by the trion field, and eq. (5.22) gives

$$\begin{aligned} j_{t,e} &= \bar{c}(\mathbf{x})c(\mathbf{x}), \\ j_{\mathbf{r},e} &= \frac{i}{2m_e} (\bar{c}(\mathbf{x})\nabla c(\mathbf{x}) - c(\mathbf{x})\nabla\bar{c}(\mathbf{x})). \end{aligned} \quad (5.23)$$

We thus find that the only conserved currents in the system are those of the electrons. The trion occupation can instead be shown to be related to a quantity known as Tan's contact [208–210], which relates the two-body physics to the many-body system.

## Two-body scattering

The bare retarded trion propagator is a constant, which leads to a lack of conserved quantities and a divergence of the bare action at large momentum and energy. Such a divergence invalidates any perturbative approach, and the theory has to be renormalized. One approach is to impose a UV cut-off, which means cutting off the integrals at a chosen large momentum and energy. To make the theory consistent, one must renormalize the contact interaction so that the correct scattering length is reproduced. We will take a slightly different approach, renormalizing the bare trion propagator through the vacuum self-energy. In theory, the two approaches are identical, but their numerical implementation is slightly different. For both cases, the renormalization relies on the solution of the two-dimensional scattering problem with an attractive  $\delta$ -potential at the origin.

In two dimensions, the s-wave vacuum T-matrix for a single particle of mass,  $m$ , is related to the energy of the bound state,  $E_B$ , through [211]

$$T(\omega) = \frac{2\pi}{m} \frac{1}{\log\left(\frac{E_B}{\omega}\right) + i\pi}. \quad (5.24)$$

This is derived by considering the scattering phase shift, which is connected to the measurable cross-section. The bound-state energy is, therefore, indirectly measurable. The vacuum T-matrix can equally be computed from the Lippmann-Schwinger equation [212]

$$T(\mathbf{q}, \mathbf{q}'; \omega) = \langle \mathbf{q} | V(\mathbf{r}) | \mathbf{q}' \rangle + \int \frac{d^2\mathbf{k}}{(2\pi)^2} \langle \mathbf{q} | V(\mathbf{r}) | \mathbf{q}' \rangle \frac{T(\mathbf{k}, \mathbf{q}'; \omega)}{\omega - \frac{\mathbf{k}^2}{2m} + i0^+}. \quad (5.25)$$



For an attractive regularized delta-function potential in two-dimensions  $\langle \mathbf{q} | V(r) | \mathbf{q}' \rangle = g$ . The Lippmann-Schwinger equation can then be rewritten in the same way as the Dyson equation in eq. (2.53)

$$T(\mathbf{q}, \mathbf{q}'; \omega) = \frac{1}{\frac{1}{g} - \int \frac{d^2\mathbf{k}}{(2\pi)^2} \frac{1}{\omega - \frac{\mathbf{k}^2}{2m} + i0^+}}. \quad (5.26)$$

The Lippmann-Schwinger equation can be set equal to the asymptotic result in eq. (5.24)

$$\frac{1}{\frac{1}{g} - \int \frac{d^2\mathbf{k}}{(2\pi)^2} \frac{1}{\omega - \frac{\mathbf{k}^2}{2m} + i0^+}} = \frac{2\pi}{m} \frac{1}{\log\left(\frac{E_B}{\omega}\right) + i\pi}. \quad (5.27)$$

This equation connects the contact interaction used in our theory to the physical bound state energy in the experimental setup. The bound state energy is connected to the two-dimensional scattering length  $a_s$  through [213]

$$E_B = \frac{1}{2ma_s^2}. \quad (5.28)$$

### 5.3 Dyson equations

Having dressed the exciton with the cavity, we can now derive the Dyson equations for the electron and exciton propagators. The first step is to find an approximation for the self-energy. As the interaction in eq. (5.16) contains three different fields, the lowest-order diagram that is fully connected requires two vertices. The  $\Phi$ -functional constructed from two vertices is shown in fig. 5.2a. Because of the self-consistent treatment, the next contribution to  $\Phi$  requires six vertices as seen in fig. 5.2b. Using fig. 5.2a our self-energy will capture three-body process illustrated by the trion self-energy diagram in fig. 5.2c [214]. However, the process shown fig. 5.2d also describes a three-body process but is not generated by self-energy insertions in fig. 5.2a. When the binding energy is large enough, the electron and the excitation can bind together so strongly that the trion becomes the new ground state, giving rise to a polaron to trion transition [174]. In two-dimensions, the importance of the corrections from fig. 5.2b is amplified to an extent where the self-consistent solution, using only fig. 5.2a, gives worse predictions for the phase transition than the non-self-consistent theory [181]. The reason the self-consistently solution is worse than the non-self-consistent solution is that the process in fig. 5.2d has been shown, through diagrammatic Monte Carlo methods [178], to almost exactly cancel against the process in fig. 5.2c. This cancellation has only been investigated in the impurity limit where there is no occupation of the exciton, and to our knowledge, it is unknown how the cancellation of the two processes in fig. 5.2c and fig. 5.2d is affected by finite exciton occupation. It is clear that when the three-body process becomes important, only using

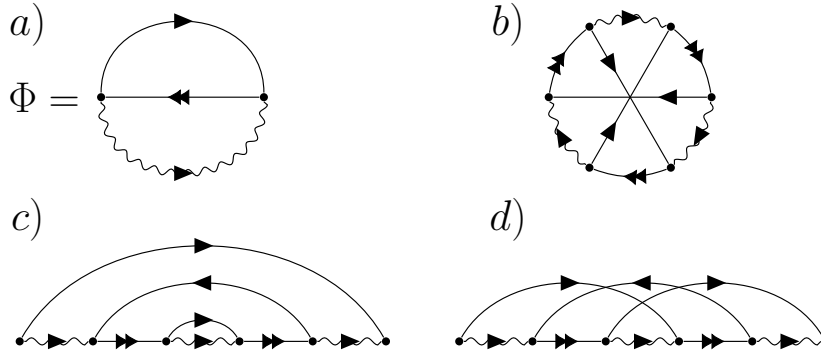


Figure 5.2: a) The lowest order  $\Phi$ -functional. Deriving self-energies from this functional and substituting all internal propagators with the full propagators constitutes a conserving theory. b) The next contribution is of significantly higher order. Notice that the crossing electron lines do not signal an interaction but the lines going over and under each other. c) The lowest order diagram generated by insertion of self-energies in a) which describes three-body processes. d) The lowest order diagram of b) that also describes three-body processes.

the two-vertex  $\Phi$ -functional in fig. 5.2a should not be expected to give good quantitative predictions [186]. For our numerical approach, it is challenging to include the diagrams in fig. 5.2b because their momentum structure is not a convolution. On top of the involved momentum and energy structure of the diagrams in fig. 5.2b, the Keldysh structure also leads to several hundreds of different configurations as discussed in section 2.7.

Even though the quantitative predictions might not be accurate in the high-binding energy limit, our method still seems to capture the qualitative features there.

Using the  $\Phi$ -functional in fig. 5.2a, the self-energy for particle  $\alpha \in \{x, e, \Delta\}$  is constructed by taking the functional derivative of  $\Phi$  with respect to the propagator  $G_\alpha$

$$\Sigma_\alpha = \frac{\delta\Phi}{\delta G_\alpha}. \quad (5.29)$$

Diagrammatically the functional derivative corresponds to cutting one propagator of type  $\alpha$  in fig. 5.2. Notice that the  $\Phi$ -functional only describes the topology of the diagrams and does not include any information about the Keldysh structure. The Keldysh structure is generated by considering the four different configurations of the vertices in fig. 5.1. When the self-energies are created from  $\Phi$ , and all internal bare propagators are promoted to full propagators, then conservation laws obeyed by the action are not broken by the approximation to the self-energy as discussed in 2.4.2.

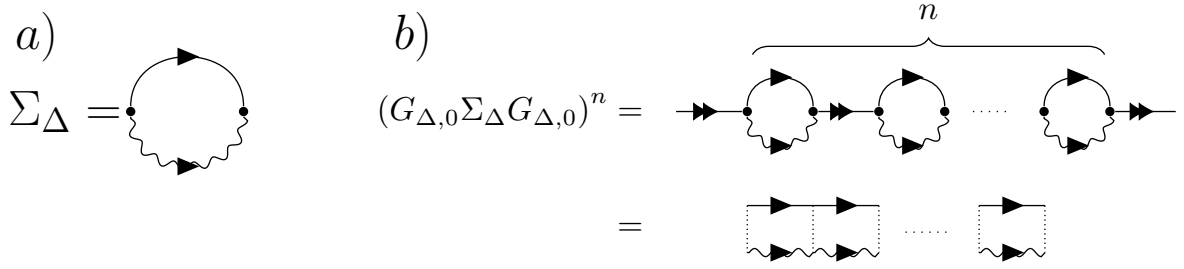


Figure 5.3: a) The topology of the single loop diagram that contributes to the trion self-energy. b) The resulting  $n$ th term of the perturbative series, and it is seen that the choice of self-energy leads to the well-known ladder approximation.

### 5.3.1 Trion

Our approximation for the full retarded trion propagator is

$$G_{\Delta}^R(\mathbf{p}) = \frac{1}{\frac{1}{g} - \Sigma_{\Delta}^R(\mathbf{p})}. \quad (5.30)$$

The topology of the self-energy is found by cutting the trion propagator in fig. 5.2a. The self-energy is shown in fig. 5.3a. The corresponding  $n$ th term of the series expansion of the Dyson equation is shown in fig. 5.3b. From the  $n$ th term, it is seen that the self-energy approximation corresponds to the self-consistent ladder approximation, also known as the self-consistent T-matrix approximation [61].

Taking the Keldysh structure of the vertices in fig. 5.1 into account, the diagrams contributing to the retarded trion self-energy are shown in fig. 5.4. Following section 2.4.2 the mathematical form of the self-energy is

$$\begin{aligned} \Sigma_{\Delta}^R(\mathbf{p}) &= \frac{i}{2A} \sum_{\mathbf{p}'} G_e^K(\mathbf{p} - \mathbf{p}') G_x^R(\mathbf{p}') + G_e^R(\mathbf{p} - \mathbf{p}') G_x^K(\mathbf{p}') \\ &= \frac{i}{2A} \sum_{\mathbf{p}'} \left( (\delta G_e^K(\mathbf{p} - \mathbf{p}') + G_e^R(\mathbf{p} - \mathbf{p}') - G_e^A(\mathbf{p} - \mathbf{p}')) G_x^R(\mathbf{p}') \right. \\ &\quad \left. + G_e^R(\mathbf{p} - \mathbf{p}') (\delta G_x^K(\mathbf{p}') + G_x^R(\mathbf{p}') - G_x^A(\mathbf{p}')) \right), \end{aligned} \quad (5.31)$$

where the vacuum contributions have been extracted from the Keldysh propagator according to eq. (2.82). The essential property of the self-energy is that it is a convolution in energy-momentum space, which is a direct consequence of using the contact interaction and  $\Phi$  in fig. 5.2.

As discussed in section 2.7, the causality of the retarded and advanced propagators can lead to cancellations of some of the diagrams. For the single loop diagrams in  $\Sigma_{\Delta}^R$ , the cancellations are particularly simple and found by Fourier transforming back to space-

$$\Sigma_{\Delta}^R(\mathbf{p}) = \begin{array}{c} G_e^K(\mathbf{p} - \mathbf{p}') \\ \curvearrowright \\ \bullet \\ \curvearrowleft \\ G_x^R(\mathbf{p}') \end{array} + \begin{array}{c} G_e^R(\mathbf{p} - \mathbf{p}') \\ \curvearrowright \\ \bullet \\ \curvearrowright \\ G_x^K(\mathbf{p}') \end{array}$$

Figure 5.4: The single loop diagrams that contribute to the retarded trion self-energy.

time. The transformation will be explicitly shown in eq. (5.47), and the result is

$$\frac{1}{A} \sum_{\mathbf{p}'} G^{\alpha}(\mathbf{p} \mp \mathbf{p}') G^{\beta}(\mathbf{p}') = \int dt \int d^2\mathbf{r} G^{\alpha}(\mathbf{x}) G^{\beta}(\pm\mathbf{x}) e^{-i\mathbf{p}\cdot\mathbf{x}}, \quad (5.32)$$

where  $\alpha, \beta \in R, A$ . The simple one-loop process comes in two different variations. One is the particle-hole process, where one of the internal propagators carries the sum of the energy. This process is identified in the diagram by the arrows of the two internal propagators pointing in opposite directions. The particle-hole diagram is only non-zero if the two propagators have poles in the opposite half-planes ( $\alpha \neq \beta$ ). The trion self-energy in fig. 5.3a is not of the particle-hole type but instead called a particle-particle diagram, meaning that one propagator carries the difference of the energies, and consequently, the two internal arrows point in the same direction. For the particle-particle diagram, causality dictates that the internal propagators must have poles in the same half-plane ( $\alpha = \beta$ ), which leads to cancellation of two of the vacuum diagrams in  $\Sigma_{\Delta}^R$  such that it takes the form

$$\begin{aligned} \Sigma_{\Delta}^R(\mathbf{p}) = & \frac{i}{2A} \sum_{\mathbf{p}'} 2G_e^R(\mathbf{p} - \mathbf{p}') G_x^R(\mathbf{p}') + \delta G_e^K(\mathbf{p} - \mathbf{p}') G_x^R(\mathbf{p}') \\ & + G_e^R(\mathbf{p} - \mathbf{p}') \delta G_x^K(\mathbf{p}'). \end{aligned} \quad (5.33)$$

All the propagators in this self-energy have to be the full propagators. In general, it is impossible to find analytical expressions for these, but the known bare parts can be separated out, which is essential for the renormalization scheme used here. The most convenient separation is to write the self-energy into four parts

$$\Sigma_{\Delta}^R(\mathbf{p}) = \Sigma_{\Delta,v}^R(\mathbf{p}) + \Sigma_{\Delta,v\delta}^R(\mathbf{p}) + \Sigma_{\Delta,x}^R(\mathbf{p}) + \Sigma_{\Delta,e}^R(\mathbf{p}). \quad (5.34)$$

The first term is the bare vacuum contribution

$$\Sigma_{\Delta,v}^R(\mathbf{p}) = \frac{i}{A} \sum_{\mathbf{p}'} G_{e,0}^R(\mathbf{p} - \mathbf{p}') G_{x,0}^R(\mathbf{p}') \quad (5.35)$$

Causality can be used to exchange the bare electron propagator with the bare electron spectral function:  $A_{e,0}(\mathbf{p}) = i (G_{e,0}^R(\mathbf{p}) - G_{e,0}^A(\mathbf{p})) = 2\pi\delta\left(\omega - \frac{\mathbf{k}^2}{2m_e}\right)$ .

$$\begin{aligned} \Sigma_{\Delta,v}^R(\mathbf{p}) &= \frac{i}{A} \sum_{\mathbf{p}'} (G_{e,0}^R(\mathbf{p} - \mathbf{p}') - G_{e,0}^A(\mathbf{p} - \mathbf{p}')) G_{x,0}^R(\mathbf{p}') \\ &= \int \frac{d\omega' d^2\mathbf{k}'}{(2\pi)^2} \frac{\delta\left(\omega - \omega' - \frac{(\mathbf{k}-\mathbf{k}')^2}{2m_e} + \mu_e\right)}{\omega' - \frac{\mathbf{k}'^2}{2m_x} + \mu_x + i0^+} \\ &= \int \frac{d^2\mathbf{k}'}{(2\pi)^2} \frac{1}{\omega - \frac{(\mathbf{k}-\mathbf{k}')^2}{2m_e} + \mu_e - \frac{\mathbf{k}'^2}{2m_x} + \mu_x + i0^+}. \end{aligned} \quad (5.36)$$

To make this expression more familiar we introduce the quantities  $m_\Delta = m_e + m_x$ ,  $M = \frac{m_e m_x}{m_e + m_x}$  and  $\mu_\Delta = \mu_x + \mu_e$  and the retarded vacuum self-energy for the trion takes the form

$$\Sigma_{\Delta,v}^R(\mathbf{p}) = \int \frac{d^2\mathbf{q}}{(2\pi)^2} \frac{1}{\omega - \frac{\mathbf{k}^2}{2m_\Delta} + \mu_\Delta - \frac{\mathbf{q}^2}{2M} + i0^+}. \quad (5.37)$$

The sum of this self-energy and the bare trion propagator is seen to have a form identical to the single particle scattering problem in eq. (5.27). The bare divergent propagator can therefore be renormalized by

$$1/g - \Sigma_{\Delta,v}^R(\mathbf{p}) = T_0^{-1} \left( \omega - \frac{\mathbf{k}^2}{2m_\Delta} + \mu_\Delta \right) = \frac{M}{2\pi} \left( \log \left( \frac{E_B}{\omega - \frac{\mathbf{k}^2}{2m_\Delta} + \mu_\Delta} \right) + i\pi \right). \quad (5.38)$$

The full renormalized trion propagator is then given by

$$G_\Delta^R(\mathbf{p}) = \frac{1}{T_0^{-1} \left( \omega - \frac{\mathbf{k}^2}{2m_\Delta} + \mu_\Delta \right) - \Sigma_{\Delta,v\delta}^R - \Sigma_{\Delta,x}^R - \Sigma_{\Delta,e}^R}, \quad (5.39)$$

where the self-energies dependence on  $\mathbf{p}$  has been suppressed. The remaining three self-energies can be read off from eq. (5.33). One term is due to the dressing of the retarded exciton and electron propagators, which is still a vacuum term

$$\Sigma_{\Delta,v\delta}^R(\mathbf{p}) = \frac{i}{A} \sum_{\mathbf{p}'} G_e^R(\mathbf{p} - \mathbf{p}') G_x^R(\mathbf{p}') - G_{e,0}^R(\mathbf{p} - \mathbf{p}') G_{x,0}^R(\mathbf{p}'). \quad (5.40)$$

On top of the dressed vacuum term, two self-energies arise due to finite densities in either



$$\begin{aligned}
\Sigma_x^R(p) &= \text{Diagram 1} + \text{Diagram 2} \\
\Sigma_x^K(p) &= \text{Diagram 3} + \text{Diagram 4} + \text{Diagram 5}
\end{aligned}$$

Figure 5.6: The retarded and Keldysh self-energy for the exciton that arises from scattering with the electrons.

### 5.3.2 Excitons and the dilute limit

The Dyson equation for the retarded exciton propagator contains both a contribution from the photon interaction and the electron scattering

$$G_x^R(\mathbf{p}) = \frac{1}{(G_{x,0}^R(\mathbf{p}))^{-1} - \Sigma_{xc}^R(\mathbf{p}) - \Sigma_x^R(\mathbf{p})}, \quad (5.44)$$

where  $\Sigma_{xc}^R$ , from eq. (5.11), leads to the polariton formation and  $\Sigma_x^R$  gives rise to polarons. To maintain the conservation laws, the topology of  $\Sigma_x$  is computed by cutting the exciton line in fig. 5.2a. The resulting retarded self-energy is shown in fig. 5.6. The exciton self-energy is different from the trion self-energy because it is of the particle-hole type and because both the electron and trion are fermions. Due to the closed fermionic loop, the self-energy acquires a sign-change as discussed in section 2.4.2. Separating out the vacuum contribution and using the causality conditions from the particle-hole nature of the diagrams, the retarded exciton self-energy due to electron scattering takes the form

$$\Sigma_x^R(\mathbf{p}) = \frac{-i}{2A} \sum_{\mathbf{p}'} G_{\Delta}^R(\mathbf{p}' + \mathbf{p}) \delta G_e^K(\mathbf{p}') + \delta G_{\Delta}^K(\mathbf{p}' + \mathbf{p}) G_e^R(\mathbf{p}'). \quad (5.45)$$

The form of the self-energy tells us that interaction can only modify the exciton by having a finite density of electrons. This intuition leads to the physical picture of a polaron that will be discussed in 5.5.

The Keldysh self-energy for the excitons is intuitive when the vacuum contribution is separated out. Following similar steps as for the trion, the occupied Keldysh self-energy is found to be

$$\delta\Sigma_x^K(\mathbf{p}) = \frac{-i}{2A} \sum_{\mathbf{p}'} \delta G_{\Delta}^K(\mathbf{p}' + \mathbf{p}) (\delta G_e^K(\mathbf{p}') - i2A_e(\mathbf{p}')). \quad (5.46)$$

The modification of occupation of the exciton due to the electron interactions require occupation in the trion but not the electron. This is understood as the only scattering process that can increase the exciton occupation is a trion decaying into an exciton and electron. This process is also possible even if there is no finite electron occupation, which explains the term in eq. (5.46) that is proportional to the electron spectral function.

At this point, the trion and exciton are fully defined, and only the electrons remain. Because the interaction is symmetric with respect to electrons and excitons, the self-energies for the electrons are equal to the exciton self-energies with the electron propagators replaced by exciton propagators. However, the goal is to model systems similar to the TMD-cavity systems under continuous driving. To this extent, we have attempted to define the minimal model but still have many parameters to tune. The bare dispersions and chemical potentials/detunings/losses give us eight parameters, whereas the driving gives three (frequency/momentum profile and strength). Additionally, there is also the photon-exciton interaction strength, binding energy for the exciton-electron scattering, and the temperature. In its current form, the model has fourteen parameters. The bare masses, cavity loss, exciton lifetime, and interaction parameters are known for the experimental setups. This leaves six parameters that can be more or less freely tuned. If the system is strongly driven, the many excitons scattering with the electrons will significantly heat the electrons. No energy dissipation mechanism has been included for the electrons, meaning they can only cool down by coupling to excitons that can dissipate energy through the cavity interaction. Experimentally the TMD monolayer is embedded in a solid-state material inside a cryostat, which will act as a heatsink for the electrons. The simplest way to implement this mechanism is by coupling the electrons to an environment through contact interactions. This interaction gives rise to an additional self-energy for the electrons. The challenge is not implementing this mechanism but choosing the appropriate interaction strength between the environment and the electrons. The electron-environment coupling strength is currently not known by the experimentalist and is something that will have a significant impact on the steady-state results. It will have a large impact because the steady-state obeys a balance between the incoming pump energy and the outgoing energy through the cavity loss and the cooling of the electrons. The balance will be very sensitive to the specific choice of the interaction strength between electron and environment. To



keep the model as minimal as possible, we seek a regime where our results will not be sensitive to the electron cooling rate. Such a regime exists when the perturbation of the electrons is negligible. Looking at the self-energies in eqs. (5.45) and (5.46) and exchanging  $x \rightarrow e$  in the propagators, it is seen that both self-energies vanish when there is no occupation of the excitons and trions. The trion occupation is linked through eq. (5.43) to the exciton occupation, so if there are no excitons, then the trion occupation also vanishes. In this limit, often called the impurity limit, the electrons will not be perturbed. If there is a large number of electrons in the system, then a small occupation of the exciton and trions will not significantly perturb the electrons, and heating of the electrons can be neglected. This dilute limit is achieved as long as the exciton density is small compared to the electron density, which clearly indicates how strongly we can drive the system without considering heating. Within this regime, the only consistent treatment of electrons is to neglect the self-energies such that the electrons remain in the same thermal state.

Our developed methods can directly be applied beyond the dilute limit (including the self-consistent treatment of the electrons). However, for the current consideration, this is only sensible to investigate once the non-equilibrium nature of the dilute limit has been understood.

## 5.4 Self-consistent convolution method

The cavity-exciton problem has been solved exactly through the closed-form expression of the self-energies in 5.11. The hard problem is the self-consistent solution of the exciton-trion interaction. This section will discuss an efficient numerical method we developed to tackle the self-consistent non-equilibrium problem. It is exploiting the fact that all the self-energies take the form of convolutions in energy and momentum

$$\begin{aligned} C(\mathbf{p}) &= \frac{1}{A} \sum_{\mathbf{p}'} f(\mathbf{p}') g(\mathbf{p} \mp \mathbf{p}') = \frac{1}{A} \sum_{\mathbf{p}'} \int d\mathbf{x} d\mathbf{x}' F(\mathbf{x}) G(\mathbf{x}') e^{-i\mathbf{x} \cdot \mathbf{p}' - i\mathbf{x}' \cdot (\mathbf{p} \mp \mathbf{p}')} \\ &= \int d\mathbf{x} F(\pm \mathbf{x}) G(\mathbf{x}) e^{i\mathbf{x} \cdot \mathbf{p}} = \mathcal{F} \{F(\pm \mathbf{x}) G(\mathbf{x})\}(\mathbf{p}), \end{aligned} \quad (5.47)$$

where  $\mathcal{F} \{F(x)\}(\mathbf{p}) = \int d\mathbf{x} e^{i\mathbf{x} \cdot \mathbf{p}} F(\mathbf{x})$  is the forward Fourier transform from space and time to momentum and energy. To understand the structure, consider the inverse transform of the bare retarded electron propagator in eq. (5.1)

$$G_{e,0}^R(\mathbf{x}) = \frac{1}{A} \sum_{\mathbf{p}} e^{i\mathbf{p} \cdot \mathbf{x}} G_{e,0}^R(\mathbf{p}) = \int \frac{d\omega d^2k}{(2\pi)^3} \frac{e^{i\mathbf{k} \cdot \mathbf{r} - i\omega t}}{\omega + \mu_e - \frac{k^2}{2m_e} + i0^+}. \quad (5.48)$$

One can shift the frequency grid by the dispersion and perform the frequency integral

$$G_{e,0}^R(\mathbf{x}) = \int \frac{d^2k}{(2\pi)^2} e^{i\mathbf{k}\cdot\mathbf{r} - i\frac{k^2t}{2m_e} + i\mu_e t} \int \frac{d\omega}{2\pi} \frac{e^{-i\omega t}}{\omega + i0^+} = -i\theta(t) \int \frac{d^2k}{(2\pi)^2} e^{i\mathbf{k}\cdot\mathbf{r} - i\frac{k^2t}{2m_e} + i\mu_e t - 0^+ t}, \quad (5.49)$$

where the shifted frequency integral is solved by performing the contour integral in the lower half-plane around the single simple pole. At this point, one of the main challenges related to doing these calculations out of equilibrium has emerged. Because the calculation is done in real-time and real frequencies, the momentum integral has a fast oscillating factor of  $e^{-i\alpha k^2 t}$ . This fast oscillation is extremely difficult to handle numerically as the oscillation frequency grows with  $k^2$  and therefore requires the grids to be extremely dense for large momenta. Avoiding this is the main achievement of the imaginary time approach [215]. By going to imaginary time, the oscillating exponential turns into a Gaussian, which is ideal due to its fast decay. As the system is not in thermal equilibrium, we are left with the challenge of the fast oscillating exponential. To make the calculations easier, we restrict ourselves to isotropic systems and go to polar coordinates

$$\begin{aligned} G_{e,0}^R(\mathbf{x}) &= -i\theta(t) \int_0^\infty \frac{dk}{(2\pi)^2} k \int_0^{2\pi} d\phi e^{ikr \cos \phi - i\frac{k^2t}{2m_e} + i\mu_e t - 0^+ t} \\ &= -i\theta(t) \sum_{n=-\infty}^\infty i^n \int_0^\infty \frac{dk}{(2\pi)^2} k J_n(kr) e^{-i\frac{k^2t}{2m_e} + i\mu_e t - 0^+ t} \int_0^{2\pi} d\phi e^{in\phi} \\ &= -i\theta(t) \int_0^\infty \frac{dk}{2\pi} k J_0(kr) e^{-i\frac{k^2t}{2m_e} + i\mu_e t - 0^+ t}, \end{aligned} \quad (5.50)$$

where the Jacobi-Anger identity has been used to solve the angular integral [131] and  $J_0(x)$  is the zeroth order Bessel function of the first kind. For any isotropic two-dimensional system, the Fourier transform always takes the form<sup>1</sup>

$$F(r) = \int_0^\infty \frac{dk}{2\pi} k J_0(kr) f(k). \quad (5.51)$$

This transformation is known as the zeroth order Hankel transformation [155], and it has the property that the backward transform has the same form as the forward transform. For the bare propagator, the Hankel transform has a closed form solution [129](6.631.6)

$$G_{e,0}^R(\mathbf{x}) = \frac{-m_e \theta(t)}{2\pi t} e^{i\frac{r^2 m_e}{2t} + i\mu_e t - 0^+ t}. \quad (5.52)$$

The solution for the bare propagator has several important features. First, it is proportional to  $\theta(t)$  as any retarded propagator must be and decays on a time scale set by the

<sup>1</sup>For a three-dimensional system the only difference is that  $J_0(kr) \rightarrow \frac{2 \sin kr}{r}$ .

inverse lifetime (here  $0^+$ ). Secondly, at short time scales, the amplitude diverges, and so does the spatial oscillation frequency. For long-lived functions, it is, therefore, necessary to have a long time grid that is dense for short times.

The numerical procedure for computing the Fourier transforms must be efficient because the self-energies will be calculated repeatedly until all propagators converge. To achieve convergence, it is crucial to minimize the number of numerical errors introduced because the errors will accumulate and thereby either spoil the convergence or lead to a result far from the exact solution. The standard for numerical Fourier transforms is the highly celebrated Fast Fourier Transform (FFT) algorithm [216]. This algorithm scales as  $N \log N$ , with  $N$  being the length of the sampling grid. The disadvantage of this algorithm is that the grid length has to be of length  $2^n$  with  $n$  being a positive integer and that the grid spacing has to be equidistant. Furthermore, once the grid is chosen in space/time, then this fully determines the grid in momentum/energy. An equidistant grid is problematic for several reasons. The bare renormalized trion propagator in eq. (5.38) decays as  $1/\log(\omega)$  which requires a long grid in frequency. On the other hand, the photon-exciton interaction leads to hybridization, which requires a frequency resolution significantly below  $2\Omega$ . To resolve both of these bare features, it is necessary to have a dense frequency grid at the places where the spectral function has sharp features, and the grid must extend to large values to ensure the functions have properly decayed. It is also essential that the functions are properly sampled in  $(r, t)$  which, by looking at eq. (5.52), requires a time grid that is long and must be dense at the origin to sample the  $1/t$  behavior of the bare propagators decently. The FFT requires that the frequency grid and time grid are related to each other such that  $\Delta\omega\Delta t = \frac{2\pi}{N}$ , where  $N$  is the number of grid points and  $\Delta\omega$  ( $\Delta t$ ) is the grid spacing in frequency (time) and similarly for the transformation between momentum and space. To use an FFT reliably for our system would require a vast number of grid points for all grids. For the FFT itself, this is not detrimental due to its  $N \log N$  scaling, but the spatial transform cannot be done with an FFT as it is a Hankel transform. The input function for the Hankel transform depends not only on momentum but also on time which entangles the spatial and the temporal transforms. For it to be possible to use long time and frequency grids, it would therefore be necessary to perform the Hankel transform with a similar scaling as the FFT. Such algorithms do exist [217, 218] but rely on a logarithmic grid which we know will not be able to sample the fast oscillations  $e^{-i\alpha k^2 t}$  at large  $k$ . As long time grids are needed, the momentum grid would have to be extremely dense, especially at higher momentum.

Due to these challenges, we will develop a different strategy for performing the numerical Fourier transformations. The fundamental properties we require of the numerical method are that non-equidistant grids can be used, that the grids are not directly

constrained by each other, and that the fast oscillation from the bare propagators does not have to be sampled on the grid. To decouple the different grids, we will use spline interpolations to perform the integrals in the transforms. The disadvantage of spline interpolations is that the transformation cannot scale better than  $N^2$  (when both grids have  $N$  points). This disadvantage is outweighed by the spline interpolations allowing grids with much fewer points to be used. Instead of trying to have a high grid density everywhere, our approach is trying to estimate the functions as well as possible with a much smaller number of data points.

The structure of the numerical transformation is inspired by the analytical calculation for the bare propagator in eq. (5.52), in the sense that we first extract the dominant bare contribution by shifting the frequency grid. Afterward, the backward Fourier transform from energy to time is performed. The last step is the Hankel transform from momentum to position, which is done such that the bare fast oscillations are included semi-analytically.

### 5.4.1 Spline interpolation and the temporal Fourier transform

The foundation of the numerical transforms is the spline interpolation. The conceptual idea is to construct a continuous representation of a function, when only its values  $f(\nu_i) = f_i$  on a grid with  $N$  nodes defined by  $\nu_i$  are known. The spline interpolation is constructed by a set of  $N - 1$  piecewise polynomials with the spline on the  $j$ th interval being given by

$$S_j(\nu) = \sum_{l=0}^M a_j^l (\nu - \nu_j)^l, \text{ with } \nu_j \leq \nu < \nu_{j+1}. \quad (5.53)$$

The highest order,  $M$ , of polynomial possible on each interval determines the order of the spline. In appendix F, it is shown that all the spline coefficients can be written as matrix multiplication with the data points

$$a_j^l = A_{j,n}^l f_n \rightarrow \vec{a}^l = \mathbf{A}^l \vec{f}, \quad (5.54)$$

where the arrow indicates a vector and a bold letter represents a matrix. The coefficients  $a_j^l$  are defined by requiring continuity conditions between adjacent intervals. The first condition is that the spline evaluated at every node gives the corresponding function value

$$S_j(\nu_j) = f(\nu_j) \rightarrow a_j^0 = f(\nu_j). \quad (5.55)$$

To determine the remaining  $M - 1$  coefficients one requires that the  $M - 1$  derivatives are continuous

$$\frac{d^k}{d\nu^k} S_j(\nu)|_{\nu=\nu_{j+1}} = \frac{d^k}{d\nu^k} S_{j+1}(\nu)|_{\nu=\nu_{j+1}}. \quad (5.56)$$

The  $k$ th derivative of eq. (5.53) is straightforwardly calculated as

$$\frac{d^k}{d\nu^k} S_j(\nu) = \sum_{l=k}^M a_j^l \frac{l!}{(l-k)!} (\nu - \nu_j)^{l-k}. \quad (5.57)$$

Inserting this into eq. (5.56) one arrives at the spline continuity conditions

$$\Delta a_j^k = \sum_{l=k+1}^M a_j^l \binom{l}{k} \Delta \nu_j^{l-k}, \quad (5.58)$$

where  $\binom{l}{k} = \frac{l!}{k!(l-k)!}$  is the binomial coefficient and the nodal difference operator has been defined as  $\Delta \bullet_j = \bullet_{j+1} - \bullet_j$ . To determine coefficients that satisfy the continuity conditions, one can isolate the second highest-order coefficients and then solve the resulting linear system. The highest order coefficients are directly given from setting  $k = M - 1$  in eq. (5.58)

$$\Delta a_j^{M-1} = a_j^M M \Delta \nu_j \rightarrow a_j^M = \frac{\Delta a_j^{M-1}}{M \Delta \nu_j}. \quad (5.59)$$

Rewriting the remaining  $M - 2$  continuity equations for the  $M - 1$  coefficients can be done systematically for arbitrary  $M$ , but it generally has to be done by hand. We will use the cubic ( $M = 3$ ) and the quintic splines ( $M = 5$ ) for our calculations. The matrix forms of the matrices  $\mathbf{A}^l$  are derived in appendix F.

With an efficient way to compute the spline coefficients, one can compute the Fourier transform between time and frequency

$$F(t) = \int_{-\infty}^{\infty} \frac{d\omega}{2\pi} \exp(-i\omega t) f(\omega). \quad (5.60)$$

We consider functions with finite support and define the two end values where the function value becomes negligible as  $\omega_1$  and  $\omega_N$ . This interval can be split into  $N - 1$  pieces and the spline interpolation in eq. (5.53) can be used to represent the function [219, 220]

$$F(t) = \sum_{j=1}^N \sum_{l=0}^M a_j^l \int_{\omega_j}^{\omega_{j+1}} \exp(-i\omega t) (\omega - \omega_j)^l. \quad (5.61)$$

The piecewise integral has a closed form solution, and using the spline continuity con-

ditions, the sum over the spline order can be collapsed to only the largest coefficient. The calculation requires some care, and the interested reader is referred to [220] for the details. Under the assumption that the function vanishes at the boundaries, the Fourier transform can be written as

$$F(t) = \sum_{j=1}^N a_j^M \mathcal{J}(t) (E_j(t) - E_{j+1}(t)) \quad (5.62)$$

with

$$\begin{aligned} \mathcal{J}(t) &= (-i)^{M+1} \frac{M!}{t^{M+1}}, \\ E_j(t) &= e^{-i\nu_j t} - \sum_{k=0}^M \frac{(-i\nu_j t)^k}{k!} \end{aligned} \quad (5.63)$$

Notice that the divergence at  $\mathcal{J}(0)$  is exactly cancelled by  $E_j(0) - E_{j+1}(0) = 0$  such that the Fourier transform is well defined for all real values of  $t$  and  $\nu_i$ .

The temporal Fourier transform evaluated on the grid  $t_n$  can be found using

$$F_n = \sum_j \mathcal{E}_{n,j} f_j, \quad (5.64)$$

where the matrix transformation is defined as

$$\mathcal{E}_{n,j} = \sum_{k=1}^N \mathcal{J}(t_n) (E_k(t_n) - E_{k+1}(t_n)) A_{k,j}^M. \quad (5.65)$$

It is seen that  $\mathcal{E}$  only depends on the grid points, meaning that it only has to be computed once the grids are defined or if they are changed. The spline Fourier transform has no requirement on the grids having the same number of points nor on them being equidistant. Because the transformation is implemented as a matrix-vector multiplication, it scales as  $N_t N_\omega$ , with  $N_\alpha$  being the number of grid points in grid  $\alpha$ .

All the functions considered obey the causal structure of the propagators in eq. (2.39). This means that any advanced propagator is the conjugate of the retarded propagator

$$G^A(k, \omega) = \bar{G}^R(k, \omega). \quad (5.66)$$

Additionally, the negative time propagators can be mapped to positive time

$$G^A(k, -t) = \bar{G}^R(k, t). \quad (5.67)$$

Similarly, the anti-Hermitain nature of the Keldysh propagators allows one to write

$$\delta G^K(k, -t) = -\delta \bar{G}^K(k, t), \quad (5.68)$$

which makes it possible to only consider a grid with  $t \geq 0$  and only retarded and Keldysh propagators.

A typical retarded propagator has the form

$$G^R(\omega) = \frac{\omega - E - i\gamma}{(\omega - E)^2 + \gamma^2}, \quad (5.69)$$

which shows that the imaginary part decays as  $\omega^{-2}$  while the real part only decays as  $\omega^{-1}$ . The realization makes it possible to improve the Fourier transform from frequency to time by using the Kramers-Kronig relations from eq. (2.64)

$$\begin{aligned} G^R(t > 0) &= \int \frac{d\omega}{2\pi} e^{-i\omega t} G^R(\omega) = \int \frac{d\omega}{2\pi} e^{-i\omega t} (i \operatorname{Im} G^R(\omega) + \operatorname{Re} G^R(\omega)) \\ &= i\mathcal{F}^{-1} \{ \operatorname{Im} G^R(\omega) \} - \mathcal{F}^{-1} \left\{ \mathcal{P} \int \frac{d\omega'}{\pi} \frac{\operatorname{Im} G^R(\omega')}{\omega - \omega'} \right\} \\ &= i2\mathcal{F}^{-1} \{ \operatorname{Im} G^R(\omega) \}, \end{aligned} \quad (5.70)$$

where the relationship between the Kramers-Kronig relations and the Fourier transform from appendix B has been used.

## 5.4.2 Hankel transform

To deal with the fast oscillations, we recall that they originate from bare dispersions. The function that has to be transformed is therefore well described as

$$f(k, \omega) = f_s(k, \omega + \phi_\beta(k)), \quad (5.71)$$

where  $\phi_\beta(k) = -\frac{k^2}{2m_\beta} + \mu_\beta$ . By shifting the  $\omega$  grid,  $\phi_\beta$  enters only as a phase. The Fourier transformation from energy to time is then written as

$$f(k, t) = \int \frac{d\omega}{2\pi} e^{-i\omega t} f_s(k, \omega + \phi_\beta(k)) = e^{i\phi_\beta(k)t} \int \frac{d\omega'}{2\pi} e^{-i\omega' t} f_s(k, \omega') = e^{i\phi_\beta(k)t} f_s(k, t), \quad (5.72)$$

where  $\omega'$  is the shifted grid. Having chosen the appropriate mass and chemical potential in  $\phi_\beta(k)$ ,  $f_s(k, t)$  will be a slowly oscillating function. The resulting Hankel transform

that has to be performed takes the form

$$F(r, t) = e^{i\mu\beta t} \int \frac{dk}{2\pi} k J_0(kr) e^{-i\alpha(t)k^2} f_s(k, t) = e^{i\mu\beta t} \mathcal{H}_\alpha^{-1} \{f_s(k, t)\} \quad (5.73)$$

where  $\alpha$  for the backward transform is

$$\alpha(t) = \frac{t}{2m_\beta}. \quad (5.74)$$

If the forward transformation, to momentum from position, is performed then the transformation has the same form with the factor of  $2\pi$  removed,  $k \leftrightarrow r$  and  $\alpha(t)$  replaced by

$$\alpha_r(t) = -\frac{m_\beta}{2t}. \quad (5.75)$$

The form of the fast oscillation in the forward transformation follows from eq. (5.52). As the forward and backward transformations have the same form, the same method can be used to do the transformation.

To perform the backward transformation, space, time, and momentum are discretized

$$\begin{aligned} \mathcal{H}_\alpha^{-1} \{f_s\} (r_i, t_j) &= H_{\alpha; i, j} = \int_0^{k_N} \frac{dk}{2\pi} k J_0(kr_i) e^{-i\alpha_j k^2} f_s(k, t_j) \\ &= \sum_{n=0}^{N-1} \int_{k_n}^{k_{n+1}} \frac{dk}{2\pi} k J_0(kr_i) e^{-i\alpha_j k^2} f_s(k, t_j). \end{aligned} \quad (5.76)$$

As  $f_s$  is a slowly changing function it can be interpolated using a spline:  $k f_s(k, t_j) = \sum_{l=0}^M a_{n,j}^l (k - k_n)^l$  with  $k_n \leq k < k_{n+1}$ . The Hankel transform takes the form

$$H_{\alpha; i, j} = \sum_{n=0}^{N-1} \sum_{l=0}^M a_{n,j}^l \int_{k_n}^{k_{n+1}} \frac{dk}{2\pi} J_0(kr_i) e^{i\alpha_j k^2} (k - k_n)^l = \sum_{n=0}^{N-1} \sum_{l=0}^M a_{n,j}^l \mathcal{W}_{i,j,n}^l, \quad (5.77)$$

where

$$\mathcal{W}_{i,j,n}^l = \int_{k_n}^{k_{n+1}} \frac{dk}{2\pi} J_0(kr_i) e^{i\alpha_j k^2} (k - k_n)^l. \quad (5.78)$$

$\mathcal{W}$  depends on three grids and the order of the interpolation, and it is, therefore, a huge tensor object, making direct computation inefficient or even impossible. To solve this issue,  $\mathcal{W}$  must be factorized. As the fast oscillation must be treated exactly, the best option is to factorize the Bessel functions. The Bessel functions satisfy the recurrence relation [221, 10.6.2]

$$J_n^{(1)}(z) = -J_{n+1}(z) + \frac{n}{z} J_n(z), \quad (5.79)$$

where the exponent in parenthesis denotes the first derivative with respect to the argu-



ment. Using the derivatives, the naive factorization is a Taylor expansion around each node  $k_n$

$$J_0(kr_i) \approx \sum_{p=0}^{P-1} J_0^{(p)}(x)|_{x=k_n r_i} r_i^p \frac{(k - k_n)^p}{p!}, \text{ with } k_n \leq k \leq k_{n+1}. \quad (5.80)$$

The Taylor expansion is a poor choice because it does not guarantee that the resulting integrand is continuous. For it to be continuous, it would require that

$$J_0(k_n r_i) = \sum_{p=0}^{P-1} J_0^{(p)}(x)|_{x=k_{n+1} r_i} \frac{r_i^p (k_{n+1} - k_n)^p}{p!} \quad (5.81)$$

should be true for all grid choices, which is not the case for finite  $P$ . To guarantee the continuity of the expansion, one can instead use a two-point Hermite interpolation [222]. The Hermite interpolation has the property that it not only gives the correct function values at the given nodes but also that all the  $P - 1$  derivatives are continuous. For  $K$  nodes and  $P - 1$  derivatives at each node, this gives rise to a polynomial of order  $KP - 1$ . By choosing to do the Hermite interpolation between the two neighboring points  $k_n$  and  $k_{n+1}$ , it is guaranteed that the  $P - 1$  derivatives and the values are correct at all nodes, with the lowest order of the polynomial. As long as  $\Delta k_n = k_{n+1} - k_n < 1$ , then going to higher order in  $P$  is guaranteed to decrease the error as the errors are given by [222]

$$\begin{aligned} J_0(k) - h(k) &= \frac{J_0^{(2)}(a)}{2} (k - k_n)^P (k - k_{n+1})^P \\ &= \frac{J_2(a) - J_0(a)}{4} (k - k_n)^P (k - k_{n+1})^P, \text{ with } k_n \leq k \leq k_{n+1}, \end{aligned} \quad (5.82)$$

where  $h(k)$  is the Hermite interpolation. Robustness is essential to achieve convergence of the self-consistent iterations, so we use a high interpolation order  $P = 13$ . The coefficients of the  $2P - 1 = 25$  degree polynomial are found by computing the generalized divided differences as derived in appendix G.1 which gives

$$J_0(kr_i) = \sum_{p=0}^{2P-1} b_{i,n}^p (k - k_n)^p, \text{ with } k_n \leq k \leq k_{n+1}. \quad (5.83)$$

With this approximation for the Bessel function, the tensor  $\mathcal{W}$  is given by

$$\mathcal{W}_{i,j,n}^l = \sum_{p=0}^{2P-1} b_{i,n}^p \int_{k_n}^{k_{n+1}} \frac{dk}{2\pi} e^{i\alpha_j k^2} (k - k_n)^{l+p} = \sum_{p=0}^{2P-1} b_{i,n}^p I_{n,j}^{l+p}. \quad (5.84)$$

With this method,  $\mathcal{W}$  has successfully been decomposed into two matrices at the price of

the additional sum over  $p$ . The remaining element is the integrals in  $I$

$$\begin{aligned}
I_{n,j}^p &= \int_{k_n}^{k_{n+1}} e^{i\alpha_j k^2} (k - k_n)^p \frac{dk}{2\pi} \\
&= e^{i\alpha_j k_n^2} \int_0^{k_{n+1}-k_n} e^{i\alpha_j k^2 + 2i\alpha_j k_n k} k^p \frac{dk}{2\pi} \\
&= e^{i\alpha_j k_n^2} \frac{\partial^p}{\partial \eta^p} \int_0^{k_{n+1}-k_n} e^{i\alpha_j k^2 + \eta k} \frac{dk}{2\pi} \Big|_{\eta=2i\alpha_j k_n}.
\end{aligned} \tag{5.85}$$

This last integral can be solved exactly<sup>2</sup>

$$\int_0^{k_{n+1}-k_n} e^{i\alpha_j k^2 + \eta k} \frac{dk}{2\pi} = \frac{\sqrt{i\pi}}{8\pi\alpha_j} e^{i\eta^2/(4\alpha_j)} \left( \operatorname{erf} \left( \sqrt{\frac{i}{\alpha_j}} \frac{\eta}{2} \right) - \operatorname{erf} \left( \sqrt{\frac{i}{\alpha_j}} \frac{2i\alpha_j \Delta k_n + \eta}{2} \right) \right), \tag{5.86}$$

where erf is the error function [223]. Using this integral one can efficiently compute  $I_{n,j}^p$ , which is shown in appendix G.2. As the integral is solved exactly, we are not relying on a sufficient sampling of the fast oscillation, and the full Hankel transform can be written as

$$H_{\alpha;i,j} = \sum_{n,m=0}^{N_k-1} \sum_{p=0}^{2P-1} \sum_{l=0}^M b_{i,n}^p I_{n,j}^{p+l} A_{n,m}^l f(k_m, t_j) = \sum_{p=0}^P \sum_{l=0}^M \left( \mathbf{B}^p \circ \left( \mathbf{I}^{p+l} \odot (\mathbf{A}^l \circ \mathbf{f}) \right) \right), \tag{5.87}$$

where  $\circ$  denotes matrix contraction as in the previous chapters, and  $\odot$  denotes the Hadamard (element-wise) product.

The complexity of the Hadamard product is given by the number of elements in the arrays and is, therefore,  $O(N_k N_t)$ . The complexity of the first matrix-matrix multiplication is  $O(N_k^2 N_t)$ . While the last matrix-matrix multiplication is  $O(N_r N_k N_t)$ . The matrix-matrix multiplication in the spline Fourier transforms scales as  $O(N_t N_\omega N_k)$ . Considering the complexity, one would conclude that they are equally fast. However, the Fourier transform has no additional overhead, while the Hankel transform has an overhead of around  $2P - 1 + M$ , which is  $\sim 30$ . Because of this overhead, the Hankel transform will be around an order of magnitude slower than the Fourier transform.

Constructing the arrays  $\mathbf{B}$  and  $\mathbf{I}$  is described in appendix G. Building these arrays is time-consuming and takes around 30 minutes for grids with a length of  $N \sim 500$ .  $\mathbf{B}$  and  $\mathbf{I}$  depend on the grids,  $m_e$  and  $m_x$ , which means that if the exciton and electron masses and time, space, and momentum grids are unchanged during the calculation, then the arrays only have to be computed once for each choice of grids and masses.

<sup>2</sup>For example Using Mathematica

### 5.4.3 Structure of a self-energy computation

The  $\omega$  grid has to be long to avoid introducing errors in the Fourier transform due to finite boundary terms. To capture narrow features, each type of propagator is shifted by the dispersion and the chemical potential. The sharp features are then close to  $\omega = 0$  on the shifted grids, meaning that the  $\omega$  grid only has to be dense around  $\omega = 0$  and can then be logarithmically spaced away from the center. By shifting the frequency grids, the fast oscillation naturally emerges in transforms. To illustrate how the numerical transforms are used, consider the vacuum contribution to the retarded trion self-energy in eq. (5.40). In the dilute limit, the electron propagator is the bare propagator, which was transformed in eq. (5.52). The first step is then to find the space-time representation of  $\delta G_x^R(k, \omega) = G_x^R(k, \omega) - G_{x,0}^R(k, \omega)$ . It is sampled on the shifted grid with  $\phi_x = -\frac{k^2}{2m_x}$ , and one can immediately do the backward transformation to time

$$\delta G_x^R(k, t) = \mathcal{F}^{-1} \{ \delta G_x^R(k, \omega) \} (k, t). \quad (5.88)$$

$\delta G_x^R(k, t)$  is then the slowly oscillating function which must be multiplied with the fast oscillation  $\exp(-ik^2t/2m_x)$  to get the full time-dependence. Using the modified Hankel transform, the real-space representation is

$$\delta G_x^R(r, t) = \mathcal{H}_x^{-1} \{ \delta G_x^R(k, t) \} (r, t). \quad (5.89)$$

The self-energy is now a simple product

$$\Sigma_{\Delta, \delta v}^R(r, t) = iG_{e,0}^R(r, t)\delta G_x^R(r, t). \quad (5.90)$$

To transform the self-energy back to momentum, we are precomputing four different transformations defined by eq. (5.75) with the possible options

$$\alpha_r(t) = \left\{ \frac{m_x}{2t}, \frac{m_2}{2t}, \frac{m_e + m_x}{2t}, 0 \right\}. \quad (5.91)$$

For the vacuum case considered here the slowest oscillating function is found when  $\alpha_r(t) = (m_e + m_x)/2t = m_\Delta/2t$ , and the oscillation due to the electron chemical potential is removed. Because both constituents of the self-energy are retarded propagators, the optimal phase will generally be the one that removes oscillation due to the bare dispersion.

When the self-energy is not only made up of retarded propagators, the optimal phase to remove the fast oscillation is less obvious. The ideal phase is less evident because the Keldysh propagators are connected to the occupation and vanish for high momentum. In practice, we consider each self-energy term independently and check which of the four

options removes the most oscillations in real space. As the oscillation is a generic feature of that specific self-energy, the optimal phase is mainly independent of parameters and interactions. Therefore, the optimal phases only have to be determined when implementing the algorithm. Having found the optimal phase for the self-energy, its representation in momentum and time is

$$\Sigma_{\Delta,\delta v}^R(k, t) = e^{i\mu_e t} \mathcal{H}_\Delta \left\{ e^{-i\frac{r^2 m \Delta}{2i} - i\mu_e t} \Sigma_{\Delta,\delta v}^R(r, t) \right\}, \quad (5.92)$$

where the oscillation inside the transform cancels the one in  $\Sigma_{\Delta,\delta v}^R(r, t)$ , such that only the slowly oscillating function is passed to the modified Hankel transform. The temporal oscillation from the chemical potential that was removed has to be multiplied back by hand, while the fast oscillation due to  $r^2$  is taken care of by the Hankel transform.

Adding and removing the different phases has the purpose of reducing errors in our transforms. The slower oscillating the sampled functions are, the fewer errors will be introduced due to the spline interpolation, thus leading to more accurate transformations.

The last step is the forward Fourier transform to frequency. As we work on different shifted grids in frequency, we must shift the self-energies to the same grid as the other terms in the Dyson equation. Shifting to the correct grid can be done without significant overhead by multiplying with a phase before Fourier transforming

$$f(\omega - k^2 + \mu) = \int dt e^{i\omega t} \left( e^{-ik^2 t + i\mu t} f(t) \right). \quad (5.93)$$

Shifting the grid can lead to sub-optimal accuracy if  $e^{-ik^2 t + i\mu t} f(t)$  is not optimally sampled on the time grid. This is generally the case if the self-energy differs significantly from the bare dispersion. To avoid this loss of accuracy, an alternative approach would be to shift the self-energy to the optimal grid and do the Fourier transform. Having found a good representation in frequency, one could interpolate the self-energy on this grid and evaluate it on the dispersion-shifted grid. Such a procedure comes with high overhead in computation time because the self-energies can significantly change throughout the iterations, which requires one to interpolate between different grids at each iteration. Instead, we choose a time grid that is sufficient to keep these errors small.

For the trion, we rely on the bare dispersion of the bound state. Fourier transforming and shifting to the proper grid, the self-energy takes the form

$$\Sigma_{\Delta,\delta v}^R(k, \omega) = \mathcal{F} \left\{ e^{-i\frac{k^2}{2m\Delta} t + i\epsilon_\Delta t} \Sigma_{\Delta,\delta v}^R(k, t) \right\} (k, \omega), \quad (5.94)$$

where  $\epsilon_\Delta$  is a shift such that the trion propagator is most ideally sampled on the frequency

grid. By repeating this procedure for all the self-energies and finding the optimal phases, all the self-energies can be computed. Having computed all self-energies, all the propagators can be computed. This process is then iterated until the propagators no longer change on the level of our numerical precision.

#### 5.4.4 Subtraction schemes

If our transforms were exact, then this would be everything needed for the calculation. However, the physical system we consider has various features that give rise to errors in the transformations. To minimize these error, a variety of different numerical tricks have to be used. We denote these tricks as subtraction schemes. This section will briefly discuss the main ideas behind the most essential subtraction schemes. We will start with two generic features and then consider more specific cases afterward.

One important technical detail is that even though the momentum, time, and position grids are only computed at the initialization, the frequency grid can be recomputed at a low cost. Depending on the features seen in the spectral functions and  $\delta G^K$ s, during the iterations, one can then optimize the grid by adding points on the fly to ensure that all sharp features are resolved properly on the frequency grid. This is possible because we use the spline Fourier transform that does not link the  $\omega$  and  $t$  grids, unlike a normal DFT/FFT.

Another technical detail is that using Fourier transforms makes it challenging to go to zero temperature for the electrons. This is because, at zero temperature, the Fermi surface is a Heaviside function. Fourier transforming a Heaviside function numerically is difficult as it is sensitive to truncation at high energy. As soon as the temperature increases, the Fermi surface smoothens, and the numerical Fourier transform becomes much better behaved. This does not pose a significant drawback as long as we can consider temperatures much smaller than the other energy scales in the system.

The remaining tricks described in this section are features of a different physical origin and will therefore be discussed separately.

#### Artificial linewidths

In the dilute limit, the electron spectral function is proportional to  $\delta(\omega - k^2 + \mu_e)$ , which is impossible to sample reliably on a grid. It is, therefore, necessary to give it some finite linewidth, which should be as small as possible. Apart from being able to sample the spectral function, our method also has one more requirement, namely that everything must vanish at the end of the grids. The ideal artificial linewidth is one that broadens the spectral function enough that it can be well interpolated near the pole but still has

the spectral function decay quickly away from the pole. The simplest choice to broaden the pole is to add a constant imaginary part

$$G_{e,Markov}^R(\omega) = \frac{1}{\omega + i\gamma_e}, \quad (5.95)$$

where we are working on the shifted grid and therefore have no explicit momentum dependence. Adding a small constant imaginary part resembles coupling weakly to an environment with a flat spectral density as discussed in section 2.8. A constant imaginary part effectively gives rise to a Lorentzian broadening of the spectral function

$$A_{e,Markov}(\omega) = \frac{2\gamma_e}{\omega^2 + \gamma_e^2}. \quad (5.96)$$

However, for large  $\omega$ , this only decays as  $\omega^{-2}$ . To improve upon this, we instead broaden the linewidth in a non-Markovian fashion and write the electron propagator as

$$G_{e,nM}^R(\omega) = \frac{1}{\omega - \frac{\gamma_e}{\alpha\omega - \frac{1}{\omega + i}}}. \quad (5.97)$$

Using such a broadening is a good choice in the limit of  $\alpha \gg 1 \gg \gamma_e$  because the spectral function takes the form

$$A_{e,nM}(\omega) = \frac{2\gamma_e}{\gamma_e^2 + \omega^2 + \alpha^2(\omega^4 + \omega^6)}. \quad (5.98)$$

Close to the dispersion ( $\omega \ll 1$ ) this has the same Lorentzian form as the Markovian approximation in eq. (5.96) but for  $\omega > 1$  this instead decays as  $\omega^{-6}$ .

The excitons are coupled to the cavity, which gives rise to broadening, and they also have a finite but long lifetime in the experiments. Because the effective photon mass is much smaller than the exciton mass, the cavity broadening is only prominent at low momentum. If the exciton develops an extremely long lifetime due to the driving, then the functions do not decay before the truncation of our time grid which leads to a dramatic loss of accuracy when transforming the self-energy to  $\omega$  space. To optimize for the smallest possible linewidth, we only add an artificial broadening to the self-energy parts below our resolution threshold. This finite exciton lifetime carries over into the bare trion, which guarantees that we do not move past the branch cut of the logarithm for negative energies.

### Analytical subtractions

The best case scenario is when a challenging step for the numerical transforms can be done analytically. This is the case for the bare electron and exciton propagators, as they

have an infinite lifetime. To separate out the bare parts of the propagators, the Dyson equation can be rewritten

$$\begin{aligned}
G &= \frac{1}{G^{-1} - \Sigma} = G_0 \frac{1}{1 - G_0 \Sigma} \\
&= G_0 + G_0 \sum_{n=1} (G_0 \Sigma)^n = G_0 + G_0^2 \Sigma \sum_{n=0} (G_0 \Sigma)^n \\
&= G_0 + \frac{G_0^2 \Sigma}{1 - G_0 \Sigma} = G_0 + \frac{G_0 \Sigma}{G_0^{-1} - \Sigma} = G_0 + \delta G.
\end{aligned} \tag{5.99}$$

Applying this to the exciton propagator, the correction takes the form

$$\delta G_x^R(\mathbf{p}) = \frac{G_{x,0}^R(\mathbf{p}) (\Sigma_x^R(\mathbf{p}) + \Sigma_{xc}^R(\mathbf{p}))}{(G_{x,0}^R(\mathbf{p}))^{-1} - \Sigma_x^R(\mathbf{p}) - \Sigma_{xc}^R(\mathbf{p})}. \tag{5.100}$$

The bare exciton propagator can then be analytically transformed to  $\mathbf{x}$  following the same calculation as the electron propagator in eq. (5.52) and only  $\delta G_x^R(\mathbf{p})$  has to be transformed numerically.

Besides directly taking care of the bare exciton propagator the rewriting in eq. (5.100) is also useful because  $\Sigma_{xc}^R(\mathbf{p})$  is known analytically from eqs. (5.7) and (5.11), which allows us to subtract another closed-form term

$$\delta G_x^R(\mathbf{p}) = \frac{(G_{x,0}^R(\mathbf{p}) + \delta G_{xc}^R(\mathbf{p})) \Sigma_x^R(\mathbf{p})}{(G_{x,0}^R(\mathbf{p}))^{-1} - \Sigma_x^R(\mathbf{p}) - \Sigma_{xc}^R(\mathbf{p})} + \delta G_{x,c}^R(\mathbf{p}), \tag{5.101}$$

with

$$\begin{aligned}
\delta G_{x,c}^R(\mathbf{p}) &= \frac{\Sigma_{xc}^R(\mathbf{p}) G_{x,0}^R(\mathbf{p})}{(G_{x,0}^R(\mathbf{p}))^{-1} - \Sigma_{xc}^R(\mathbf{p})} = \frac{\Omega^2 G_{x,0}^R(\mathbf{p})}{(G_{x,0}^R(\mathbf{p}))^{-1} (G_{c,0}^R(\mathbf{p}))^{-1} - \Omega^2} \\
&= \frac{\Omega^2}{\left(\omega - \frac{k^2}{2m_x} + i0^+\right) \left(\omega + \Delta_c - \frac{k^2}{2m_c} + i\gamma\right) - \Omega^2 \left(\omega - \frac{k^2}{2m_x} + i0^+\right)},
\end{aligned} \tag{5.102}$$

where the bare cavity propagator is given in eq. (5.7). Shifting this onto the bare dispersion of the exciton and finding the roots of the cubic denominator ( $\lambda_i$ ), this correction can be analytically transformed to the time domain

$$\delta G_{x,c}^R(k, t) = \Omega^2 e^{\frac{-ik^2 t}{2m_x}} \left( \frac{e^{-i\lambda_1 t}}{(\lambda_1 - \lambda_2)(\lambda_1 - \lambda_3)} + \frac{e^{-i\lambda_2 t}}{(\lambda_2 - \lambda_1)(\lambda_2 - \lambda_3)} + \frac{e^{-i\lambda_3 t}}{(\lambda_3 - \lambda_2)(\lambda_3 - \lambda_1)} \right), \tag{5.103}$$

which can be numerically transformed with the Hankel transform using  $\alpha = x$ .

The non-Markovian bare electron propagator also has a known analytical form given by eq. (5.97), and this propagator can be Fourier transformed to time in a similar manner.

For the  $G_{e,nM}^R$ , the slow oscillation is independent of momentum, and the Hankel transform can be done analytically as in 5.52. The space-time representation of the non-Markovian electrons is then given as

$$G_{e,nM}^R(r, t) = -\frac{m_e}{2\pi} e^{i\frac{r^2 m_e}{2t} + i\mu_e t} G_{e,nM}^R(t). \quad (5.104)$$

It is worth noting that using non-Markovian electrons means that, even in the dilute limit, one can no longer take out of a common factor of  $G_{e,0}^R$  in eq. (5.40).

### Log continuum of trion

As the bare trion propagator inherits a minimum broadening from the exciton, the pole at  $-E_B$  can be integrated numerically. However, the bare trion propagator poses another challenge: the continuum's spectral function decays as a  $1/\log \omega$  for large  $\omega$ . This requires extremely long frequency grids, compromising the quality of the transforms with more well-behaved numerical self-energies. To avoid using such long grids, the Fourier transform to time of the bare trion propagator is carried out separately. Using the causality structure discussed in eq. (5.70), we do the integral around the pole separately and therefore split the integration into three parts

$$G_{\Delta,0}^R(k, t) = 2ie^{i\phi_{\Delta}(k)t} \left( \int_{-E_b+c}^{\infty} \frac{d\omega}{2\pi} \text{Im} G_{\Delta,0}^R(\omega) e^{-i\omega t} + \int_{-E_b-c}^{-E_b+c} \frac{d\omega}{2\pi} \text{Im} G_{\Delta,0}^R(\omega) e^{-i\omega t} + \int_{-\infty}^{-E_b-c} \frac{d\omega}{2\pi} \text{Im} G_{\Delta,0}^R(\omega) e^{-i\omega t} \right), \quad (5.105)$$

with  $c > 0$  being chosen such that the peak is properly captured by the integration routine. To evaluate the two integrals that contain the tails, we take advantage of the fact that the derivative of the propagator decays faster than the propagator itself and therefore integrate by parts

$$\int_{-E_b+c}^{\infty} \frac{d\omega}{2\pi} \text{Im} G_{\Delta,0}^R(\omega) e^{-i\omega t} = \left[ \text{Im} G_{\Delta,0}^R(\omega) \frac{i}{t} e^{-i\omega t} \right]_{-E_b+c}^{\infty} - \int_{-E_b+c}^{\infty} \frac{d\omega}{2\pi} \text{Im} \left( \frac{d}{d\omega} G_{\Delta,0}^R(\omega) \right) \frac{i}{t} e^{-i\omega t}. \quad (5.106)$$



As the propagator goes to zero at  $\omega = \infty$ , the upper limit of the boundary term vanishes. This can be repeated  $N$  times until the integral is accurate enough

$$\int_{-E_b+c}^{\infty} \frac{d\omega}{2\pi} \text{Im} G_{\Delta,0}^R(\omega) e^{-i\omega t} = \sum_{n=0}^N \text{Im} \left( \frac{d^n}{d\omega^n} G_{\Delta,0}^R(\omega) \right) \frac{e^{-i\omega t}}{(it)^{n+1}} \Big|_{\omega=-E_b-c} + \int_{-E_b+c}^{\infty} \frac{d\omega}{2\pi} \text{Im} \left( \frac{d^{(N+1)}}{d\omega^{(N+1)}} G_{\Delta,0}^R(\omega) \right) \frac{e^{-i\omega t}}{(it)^{N+1}}. \quad (5.107)$$

With this result, it is possible to compute the transformation of the bare trion with high accuracy without affecting the performance of the rest of the calculation.

### Optimized sampling of multiple poles

A characteristic feature of all the systems considered in this thesis is that interactions give rise to multiple poles in the propagator. The photon coupling gives rise to the upper and lower polariton, while the electron interaction leads to the formation of attractive and repulsive polaron branches. As these poles can be far separated in energy, it can be challenging to sample both properly on the same grid. To overcome this issue, the propagator can be split into several pieces. In the case of two well-separated branches, the "lower" and "upper" propagators are defined through

$$G^R(k, \omega) = \left( 1 - \theta(\omega - \omega_0) \right) G^R(k, \omega) + \theta(\omega - \omega_0) G^R(k, \omega) = G_L^R(k, \omega) + G_U^R(k, \omega), \quad (5.108)$$

where  $\omega_0$  is a suitable point between the two branches, which is updated through the iterations. For clarity, the split has been written using a Heaviside function, but as discussed at the start of the section, this leads to artifacts in the Fourier transforms. To avoid this, the Heaviside is replaced by a Fermi function at a temperature where the broadening of the distribution is small compared to  $\omega_0$ .

Once the two new propagators have been defined, they can be shifted such that they are both optimally sampled on the frequency grid.

## 5.5 Results

Having described the main ideas of our numerical method, we now show some first results. We will start by considering the polaron without the cavity, which has been thoroughly investigated in the literature. Having seen that our results are in good qualitative agreement with previous results, the cavity coupling will then be included such that the polaron-polaritons are formed. Finally, driving of the system through the cavity will be considered.

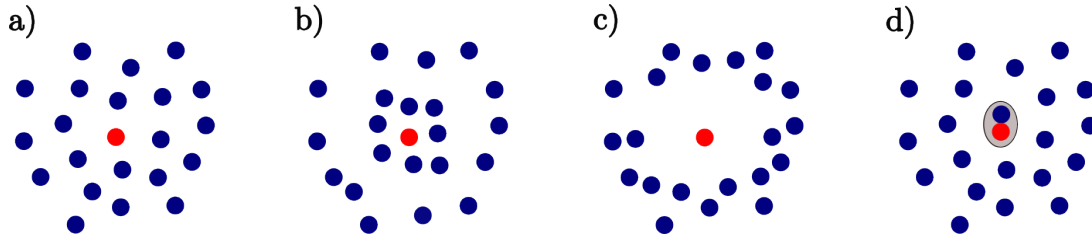


Figure 5.7: *The attractive contact interactions between the exciton (red) and the Fermi sea of electrons (blue) give rise to new states depending on the binding energy. At small binding energies, the Fermi sea is almost unperturbed by the exciton as sketched in a). When the binding energy is increased, the attractive interaction makes the electrons closest to the exciton move towards it, and the exciton ends up being dressed by a cloud of fermions, as shown in b). This configuration is known as the attractive polaron. At these intermediate binding energies, the system has an excited state known as the repulsive polaron sketched in c). In this excited state, the electrons are pushed away from the exciton, making it metastable. Apart from the attractive and repulsive polarons, the exciton can also form a bound state with just a single electron which is the trion state illustrated in d).*

For all calculations, a finite gate voltage will be assumed such that all parameters can be expressed in units of the Fermi energy  $\epsilon_F$ .

### 5.5.1 Polarons

Without driving and at low temperatures, the self-energies that depend on  $\delta G_x^K$  vanish, and the system enters the impurity limit. In this limit, the system can have different states depending on the magnitude of the binding energy compared to the Fermi energy. The electrons weakly interact with the exciton for small binding energy, so the system's state is close to the non-interacting system as sketched fig. 5.7a. As the binding energy is increased, the attractive interactions make it energetically favorable for the electrons to move closer to the exciton, which leads to a dressing of the exciton by a cloud of electrons. This state is known as the attractive polaron (AP) and is shown in fig. 5.7b. While the AP is energetically favorable, the system can have an excited state known as the repulsive polaron (RP), shown in fig. 5.7c, that can be metastable. The RP is physically understood as the exciton repelling the nearby electrons, which is the reason why it is energetically unfavorable. As the binding energy is increased, the dressing cloud of APs gets denser until, at some point, the energetically preferable state is when the exciton forms a bound state with a single electron, namely the trion state that is sketched in fig. 5.7d. The trion only becomes energetically favorable at a very large binding energy. Below this critical binding energy, the trion state is an excited state of the system.

These are the different states we describe in our theory, but it is worth pointing out

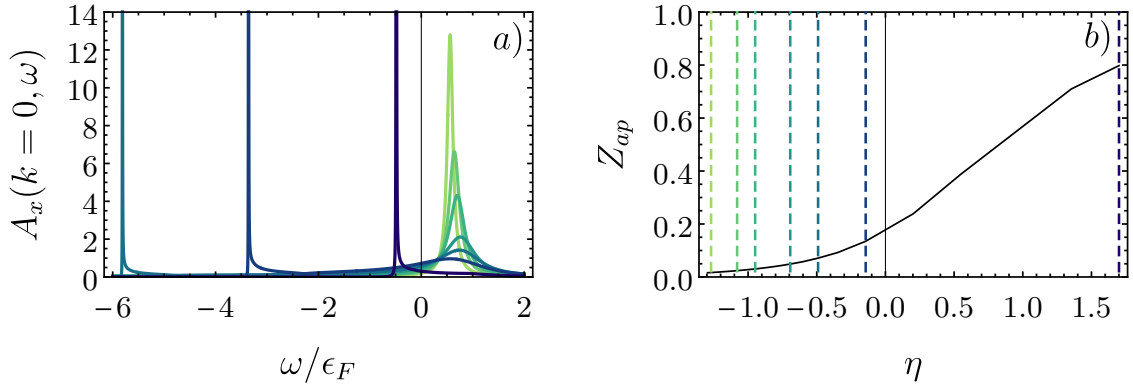


Figure 5.8: a) Spectral function of the exciton at zero momentum for different binding energies. The value of the binding energy is determined by the color coding, such that a brighter color is equivalent to a larger binding energy. The corresponding value of  $\eta$  can be read off by the dashed vertical lines in b). In b), the quasiparticle weight of the attractive polaron is shown as a function  $\eta$ .

that the system can have more bound states. These become energetically favorable if the exciton/impurity mass is significantly larger than the electrons in the gas. The trimer state consisting of one impurity and two electrons becomes favorable when  $m_x/m_e > 3.33$  [224] and the tetramer, consisting of one impurity and three electrons, becomes the ground state when the ratio is greater than five [225]. The mass ratio is two for the TMD monolayer setup, and these additional bound states can therefore be neglected.

To see that our calculations qualitatively capture the known physical features, we first consider the exciton spectral function at  $k = 0$  and at a low temperature of  $\beta = 200\epsilon_F$  in fig. 5.8a. Here the exciton spectral function is plotted for different values of the binding energy indicated by the colored dashed vertical lines in fig. 5.8ab. For small binding energy,  $A_x$  contains a single sharp peak close to  $\omega = 0$ . This peak is the AP and shows that the AP emerges from the non-interaction bare state. As  $E_B$  increases, the AP peak is pushed towards lower energy, and a broad continuum feature emerges around  $\omega \approx 1$ . It is from this continuum that the repulsive branch emerges.

In the standard Fermi-polaron field, it is more common to work with the scattering length instead of the binding energy. For a two-dimensional system, one can then define the logarithm of the product of the scattering length and Fermi momentum ( $k_F$ )

$$\eta = \log(k_F a_s) = \log\left(\frac{k_F}{\sqrt{2E_B\epsilon_F M}}\right) = -\frac{\log\left(\frac{E_B m_x}{m_e + m_x}\right)}{2}, \quad (5.109)$$

where the binding energy's relation to the scattering length through eq. (5.28) was used, and  $E_B$  was written in units of  $\epsilon_F$ . This quantity is insightful because it is inversely related

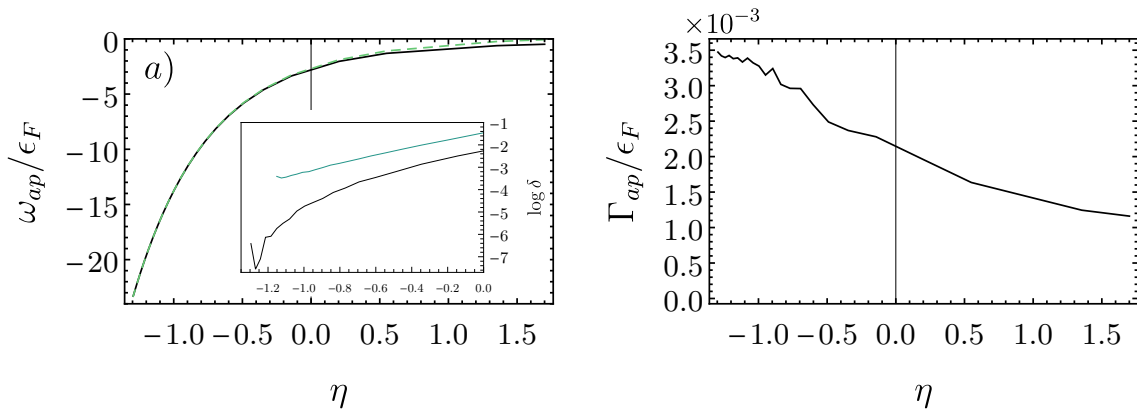


Figure 5.9: The energy and linewidth of the attractive polaron as a function of  $\eta$ . In a) the dark line is the energy of the AP and the dashed line is the energy of the bound state in the trion. The inset shows the logarithm of the absolute difference  $\delta = |\omega_{AP} - \omega_{\Delta}|/\epsilon_F$ . The dark line in the inset is the logarithm of the difference between the solid and dashed line in the main plot. Here it is seen that at around  $\eta = -1.25$  the trion becomes more energetically favorable than AP, which is seen by the change in sign of the slope. The bright line in the inset is the same difference but for a mass-balanced system. Here no crossing is observed. In b), the linewidth of the AP is shown. The linewidth should be compared to the artificial broadening used for the bare exciton, which is  $10^{-3}\epsilon_F$ .

to scattering amplitude in the presence of a Fermi sea, and the system is strongly interacting when  $|\eta|$  is small. Conversely, when  $|\eta| \gg 1$ , one can treat the system perturbatively in powers of  $1/\eta$  [226].

In 5.8a, it is observed that the linewidth of the RP only becomes narrow for large binding energy ( $\eta < 0$ ) and is, therefore, a bad quasiparticle for  $\eta \approx 0$ . While the linewidth decreases, it is also seen that the peak position of the RP moves towards 0. Both of these features are similar to experiments [179] and the non-self-consistent ladder approximation [185] for equal masses.

Oppositely to the RP, the attractive polaron is narrow for all  $\eta$ , and one can reliably extract meaningful quasiparticle parameters. The quasiparticle weight as a function of  $\eta$  is shown in fig. 5.8b, and it is seen that for small binding energy,  $Z_{ap}$  is close to 1. This is as expected as the AP emerges from the bare exciton such that  $\lim_{E_B \rightarrow 0} Z_{ap} = 1$ . As the interactions increase, we observe a decrease of  $Z_{ap}$ , understood as the quasiparticle weight being transferred into the repulsive continuum. The same behavior is observed in three dimensions [227]. While the AP is losing quasiparticle weight, its energy quickly decreases, as shown in fig. 5.9a. Just like the AP is decreasing in energy, so is the trion. This is illustrated by the dashed line in fig. 5.9a. For large binding energy, we expect the trion to become energetically favorable, signaling the polaron to trion transition. We observe this in the inset of fig. 5.9a. Here the logarithm of the difference between the

energies of the AP and the trion is plotted, and a change of sign of the slope for large binding energies means that we predict the trion to be energetically favorable. As we are plotting a function of the absolute value of the difference  $\omega_{AP} - \omega_{\Delta}$ , a node in the difference translates into a sign change of the slope in the absolute value. The intersection angle of the crossing is extremely shallow in two dimensions and is also at large binding energies. Furthermore, the phase transition is only a true phase transition for zero temperature. We are considering a finite but low temperature and include a finite width to the exciton. The combination of these two effects is that the linewidth of the AP, shown in fig. 5.9b, is finite even when the AP is the system's ground state. We also observe a slight broadening of the AP as the binding energy is increased, which we attribute to a combination of using finite temperature and, at large binding energy, not capturing three-body processes of the form fig. 5.2d. The three-body processes describe the broadening of the AP and the trion, so we cannot quantitatively rely on our method when the missing processes in fig. 5.2d become important. That our calculations are struggling in the large binding energy regime is made more evident by considering the mass-balanced system ( $m_x = m_e$ ). The bright line in the inset of fig. 5.9a is the logarithm of the difference between the AP and trion energy for the mass balanced case. Here we observe no transition as the intersection angle is even shallower for this mass ratio. However from both FRG [186] and Diag-MC [187, 228] the transition is found to be  $\eta = -1.0 \pm 0.2$ . The polaron to trion transition is challenging in two dimensions because the shallow intersection angle makes the predictions very sensitive to errors. For our method, it is further problematic as the transition also happens in the parameter region where our current implementation is the most susceptible to errors. It is susceptible to errors because the results have a strong dependence on the artificial linewidth, as it sets the scale for the linewidth of the interacting system as seen in fig. 5.9b. Here we see that the AP linewidth for small binding energy (large  $\eta$ ) starts at  $10^{-3}\epsilon_F$ , which is the value of the artificial broadening used in the exciton. Even though we observe an increase in the linewidth, it remains on the same order of magnitude as the introduced linewidth. With a small linewidth being important, it is also necessary to use very low temperatures, which further increases the numerical errors in our current implementation.

While the polaron to trion transition requires more careful investigations, one significant advantage of our real-time approach is that it gives direct access to the spectral function without having to perform an analytic continuation. The analytic continuation is an ill-defined procedure numerically and, therefore, very challenging in general. In fig. 5.10a the full momentum resolved spectral function, for the exciton at  $\eta = 0$  is plotted. At  $k = 0$ , the AP is narrow, while the RP is broad and without a well-defined quasiparticle peak. As the momentum increases, the AP broadens due to scattering with

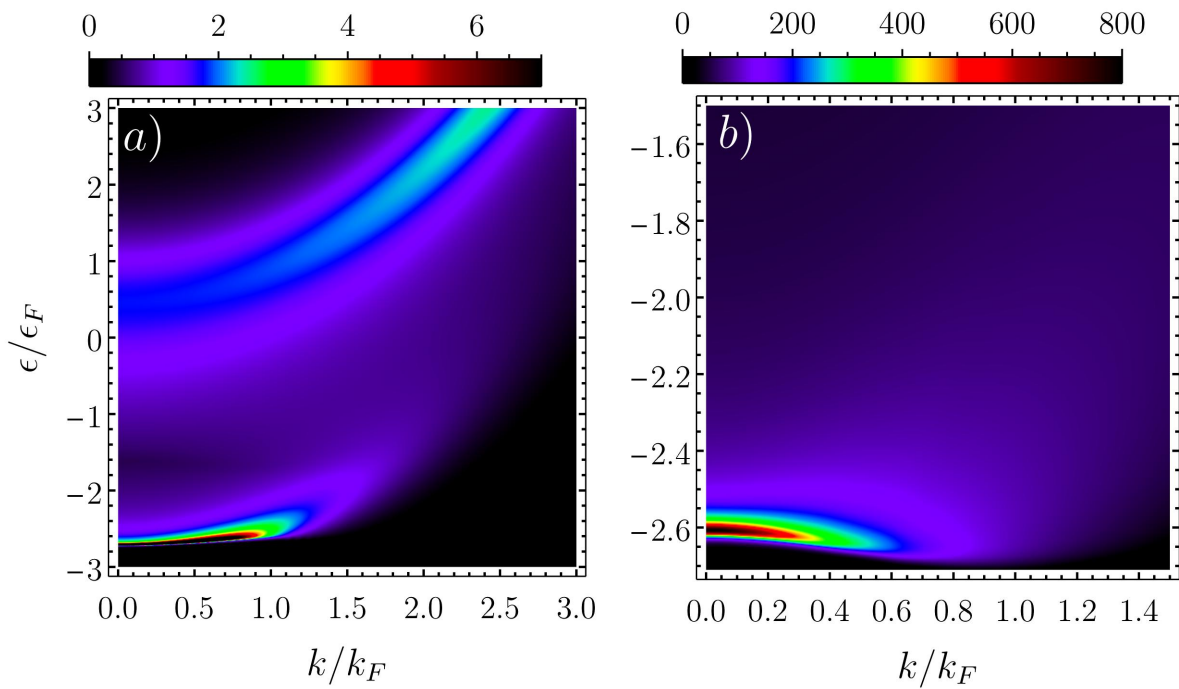


Figure 5.10: The spectral functions for the exciton ( $A_x(k, \omega)$ ) and the trion ( $A_\Delta(k, \omega)$ ) at  $\eta = 0$  in plot a) and b) respectively. a) The exciton spectral function shows the narrow linewidth of the AP at  $k = 0$  and a broad repulsive continuum at higher energy. At higher momentum, the AP broadens and is no longer a good quasiparticle at  $k \sim 0.7k_F$ . b) The trion shows a sharp onset at low energy followed by a large continuum. The trion spectral function vanishes at larger momentum. Both colorbars have been truncated to resolve the broader features.

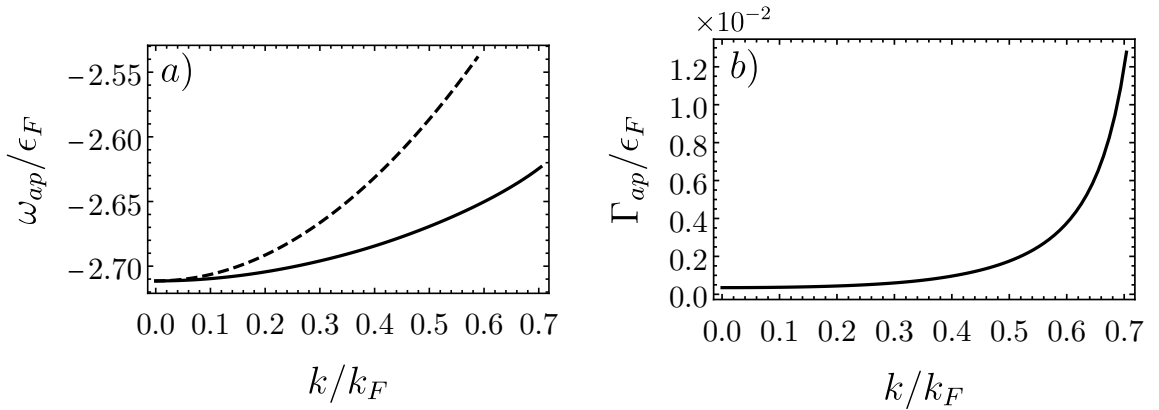


Figure 5.11: *The quasiparticle properties of the AP at  $\eta = 0$  as a function of momentum. In a) the solid line is the dispersion of the AP extracted from the spectral function fig. 5.10a, and the dashed line is the bare dispersion shifted down. This demonstrates the large effective mass of the AP, which is  $m_{ap} \approx 2.9m_x$ . b) shows the lifetime of the AP, which starts to increase super exponentially for  $k > 0.7k_F$ .*

the electrons. As quantified in fig. 5.11b, this broadening is highly non-linear, and for momentum above  $0.7k_F$ , the AP starts losing its quasiparticle nature. After this point, it enters into the continuum and no longer exists. The linewidth of the AP is not the only thing that is significantly changed compared to the bare exciton, also the effective mass of the AP is significantly altered as seen in fig. 5.11a. For the considered parameters we find an effective mass  $m_{ap} \approx 2.9m_x$ . The mass of the AP increasing with the binding energy is a well-known feature [229]. Looking at fig. 5.10a, one observes that while the AP broadens for large momentum, the broad RP continuum gets narrower until it recovers the bare dispersion. The RP merging with the bare dispersion at large momentum is the main reason our numerical method is successful, as we rely on the bare dispersions for large momentum to avoid sampling highly oscillatory functions on finite grids.

The same physical features are visible in the trion spectral function shown in fig. 5.10b. For small momentum, the trion has a narrow feature that shifts the AP down, while for large momentum, the trion is in the particle-particle scattering continuum. As there is only a small weight at large momenta, the trion has minimal effect on the exciton, which explains why the RP connects to the bare dispersion. As observed in [182], where the system was investigated using a variational ansatz, the trion spectral function has a minimum at finite momentum. The effective mass of the trion at zero momentum is, therefore, negative. This effective mass becomes positive at large binding energy as the trion spectral function approaches that of the bare trion. One feature worth pointing out in the trion spectral function is that the bound state of the trion is sitting on the edge of the continuum. For non-self-consistent and variational calculations, one finds a clear

separation between the log continuum and the bound state for large binding energy. The clear separation is because, for a non-self-consistent calculation, the scattering is among the bare excitons and bare electrons. The continuum, therefore, also starts at zero. In a self-consistent calculation, the scattering continuum of the trion arises due to scattering between polarons and electrons. The attractive polaron has an energy that is  $\sim E_B$  lower than the bare exciton. Scattering between the attractive polaron and bare electrons, therefore, leads to a continuum starting close to the energy of the attractive polaron.

With this, we close our comparison to the equilibrium polaron problem. Our self-consistent approach captures all the features qualitative level, and most of them even quantitatively. To achieve a good quantitative agreement for the polaron-trion transition, it would be necessary to include the missing three-body scattering effects and do a more thorough investigation of how the small artificial linewidth and finite temperature affect the predictions for the transition.

### 5.5.2 Undriven polaron-polaritons

The attractive and repulsive polarons are the emerging quasiparticles arising from the contact interaction with the Fermi sea. We now investigate what happens when the cavity is coupled to the exciton. To contain the discussion we will consider parameters that are inspired by the recent experiments [99, 169, 171] and choose:  $\epsilon_F = 5\text{meV}$ ,  $\gamma = 0.08\epsilon_F$ ,  $\Omega = 0.8\epsilon_F$  and  $\beta\epsilon_F = 50$ . For the binding energy, we stay at unitarity  $E_B = 3/2\epsilon_F$ , which is smaller than the explored TMD materials that have  $E_B = 7\epsilon_F$ . The one other parameter which is chosen more liberally is the effective photon mass. In the current experiments, the photon mass is around  $10^{-5}m_e$ , which requires a very dense momentum grid at small values, and we, therefore, chose  $m_c = 1/2 \times 10^{-3}m_e$  to speed up the computations. To ensure that the larger photon mass does not qualitatively alter the effects seen, a few data points with  $m_c = 1/2 \times 10^{-4}$  have been computed, and the same qualitative features were found but at a smaller momentum.

With these parameters, we first investigate how the AP spectral function is affected when the cavity has two different detunings  $\Delta_c$  as shown in fig. 5.12. In fig. 5.12a, the cavity detuning is chosen such that the bare cavity is  $0.3\epsilon_F$  higher in energy than the AP at zero momentum. The choice of detuning in fig. 5.12a will be referred to as positive cavity detuning as the cavity has higher energy than the AP. Because of the strong coupling between the exciton and the cavity of  $\Omega = 0.8\epsilon_F$ , the quasiparticle that emerges in the exciton spectral function is pushed down in energy at small momenta. The emerging quasiparticle is the lower polariton arising from the cavity interacting with an exciton dressed by electrons and forming the AP. It is denoted as the lower attractive polaron-polariton (LAPP). To compute the dispersion the quasiparticle approximation



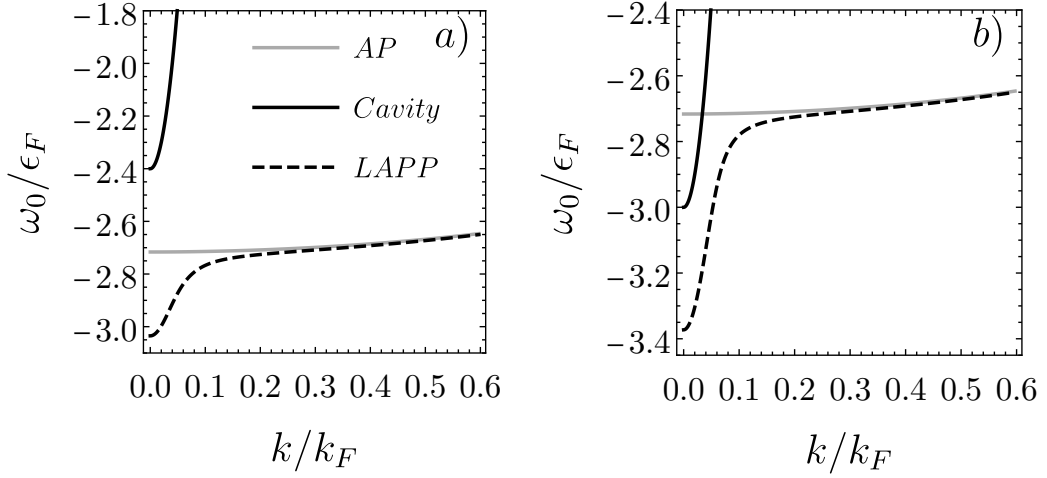


Figure 5.12: The bare dispersion of the attractive polaron from fig. 5.11, the bare cavity and the resulting lower attractive polaron-polariton dispersion arising from the coupling between the cavity and the exciton. The resulting dispersion is determined using the quasiparticle approximation from section 2.5. In a) the cavity is detuned such that it is  $0.3\epsilon_F$  above the attractive polaron, and in b) the cavity is detuned to be below the attractive polaron by  $0.3\epsilon_F$ .

from section 2.5 has been applied to the converged result for  $G_x^R(\omega, k)$ . In fig. 5.12b  $\Delta_c$  is chosen such that the bare cavity mode is  $0.3\epsilon_F$  lower in energy than the AP at  $k = 0$  and will be referred to as negative cavity detuning. In this case, the emerging LAPP is pushed below the bare cavity because  $\Omega > \omega_{AP} - \Delta_c$ . Because of the strong cavity coupling, the LAPP dispersion differs from the AP up to much greater momentum than the extent of the cavity dispersion. For both cavity detunings, the LAPP dispersion does not fully join the AP dispersion until momentum  $k \sim 0.3k_F$ .

In section 5.5.1, it was found that the AP was a good quasiparticle, and one could therefore imagine that retarded propagator for the LAPP can be found by adding the cavity self-energy in eq. (5.11) to the AP quasiparticle

$$G^R(k, \omega) = \frac{Z_{ap}}{\omega - \omega_{ap}(k) + i\gamma_{ap} - \frac{\Omega^2}{\omega - \Delta_c - \frac{k^2}{2m_c} + i\gamma}}. \quad (5.110)$$

Applying the quasiparticle approximation to this propagator at  $k = 0$  and looking at the

lowest energy  $\omega_-$  one finds

$$\begin{aligned} \omega_- - \omega_{ap}(k=0) - \frac{\Omega^2}{\omega_- - \Delta_c} &= 0 \\ \rightarrow \omega_- &= \frac{\omega_{ap} + \Delta_c - \sqrt{(\omega_{ap} - \Delta_c)^2 + 4\Omega^2}}{2}, \end{aligned} \quad (5.111)$$

where the cavity and AP linewidth have been neglected as they are both small compared to the energy difference  $|\omega_{ap} - \Delta_c| = 0.3\epsilon_F$ . For the positive detuning case in fig. 5.12a, the result is  $\omega_- = -3.36\epsilon_F$  which suggests that the LAPP should be pushed significantly further down than the  $-3.03\epsilon_F$  found in fig. 5.12a. Similarly for the negative case in fig. 5.12b, where eq. (5.111) predicts an energy of the LAPP of  $-3.66\epsilon_F$  while the self-consistent calculation gives  $\omega_- = -3.37\epsilon_F$ .

One can also compute the new quasiparticle weight of the LAPP according to eq. (5.110)

$$Z_- = Z_{ap} (1 - \partial_\omega \text{Re} \Sigma(0, \omega_-))^{-1} = Z_{ap} \left( 1 + \frac{\Omega^2}{(\omega_- - \Delta_c)^2} \right)^{-1} \leq Z_{ap}, \quad (5.112)$$

which predicts that the LAPP's quasiparticle weight must always be smaller than the  $Z_{ap}$ . By including the  $k$ -dependence to the dispersion, the prediction is unchanged because  $(\omega_- - \Delta_c)^2 \geq 0$  for all values of  $\omega_-(k)$ . This prediction is consistent with considering the system in terms of hybridizing the AP with the cavity. The prediction states that the weight in the AP is shared between the two new quasiparticles, the LAPP and the upper attractive polaron-polariton (UAPP) that one would have found if the larger energy solution in eq. (5.111) was used instead of  $\omega_-$ . As the coupling redistributes the spectral weight, neither of the new quasiparticles can have a  $Z$  greater than  $Z_{ap}$ . The quasiparticle weight found from the converged self-consistent solution is shown in fig. 5.13a. Here one sees that the prediction from eq. (5.112) is qualitatively wrong in the sense that for both the positive and negatively detuned cavity case, the LAPP acquires a  $Z > Z_{ap}$  for most values of  $k$ . Combined with the overestimation of the splitting from eq. (5.111) it is clear that the approximation in eq. (5.110) is both quantitatively and qualitatively wrong.

The approach in eq. (5.110) fails because it does not account for how the hybridization between the cavity and the exciton affects the polaron formation. The correct physical picture requires one to consider the exciton's hybridization with the cavity when interacting with the Fermi sea as done in section 5.2.2. The phenomenology is that the exciton in the AP is hybridized with the cavity. The LAPP then emerges from the lower polariton (LP) part of the exciton in the AP when the system interacts with the Fermi sea. Because the LP is part cavity part exciton, it interacts less efficiently with the Fermi sea. The less efficient interaction with the Fermi sea leads to an effective binding energy for the

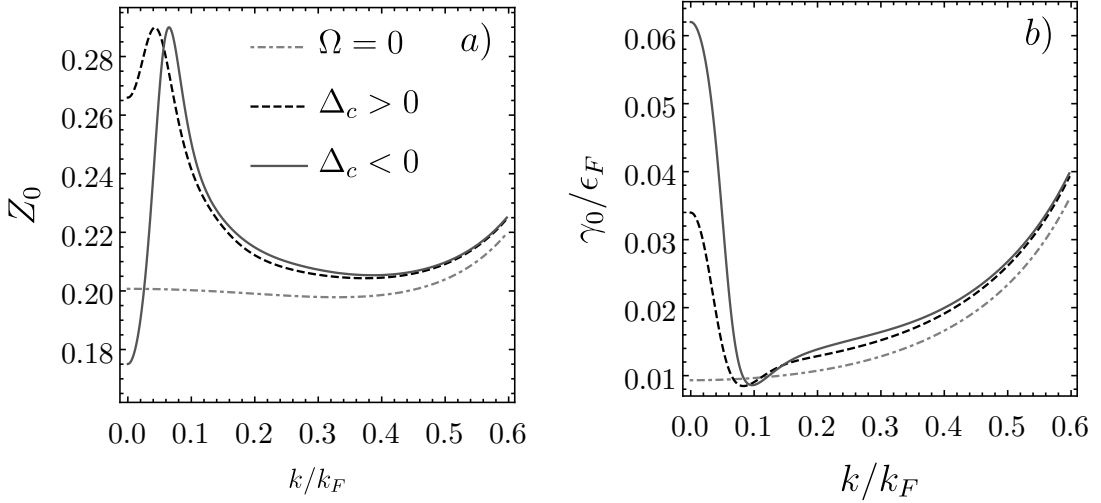


Figure 5.13: *The remaining two quasiparticle parameters ( $Z$  and  $\gamma$ ) for the attractive polaron and the lower attractive polaron-polariton in the case with different cavity detunings as shown in fig. 5.12. The quasiparticle weight is plotted in a) and the linewidth is shown in b).*

LAPP that is less than that of the AP. In fig. 5.9a, it was shown that smaller binding energy (larger  $\eta$ ) decreases the splitting between the repulsive and attractive polaron. The effective decrease of the binding energy, due to the cavity coupling, therefore, pushes the LAPP up in energy, which explains why eq. (5.111) overestimated the lowering of the LAPP energy.

Similarly, in fig. 5.8b, it was shown that decreasing the binding energy added more quasiparticle weight to the AP, so an effective smaller binding energy is also consistent with the increase of  $Z$  seen in fig. 5.13a. This argument does not explain the highly non-monotonic nature of the quasiparticle weight nor why  $Z_0$  is smaller than  $Z_{ap}$  for the negatively detuned case. If the cavity only leads to an effective decrease of the binding energy, then one would expect that the quasiparticle weight would continuously increase as the momentum is lowered. A continuous increase would be expected because, at smaller momentum, the LAPP is more photonic. However, as momentum gets smaller, the UP polariton acquires more spectral weight, meaning that even if the AP-part of the LAPP acquires more spectral weight due to the decreased electron dressing, the polariton spectral weight has to be shared with the upper polariton. The peak in the quasiparticle weight is an effect of the fact that there is a trade-off between having less electron dressing and having more weight in the UP.

With this understanding, one can also explain the qualitative difference between the positive and negatively detuned case seen in fig. 5.13a, where the spectral weight of the

negatively detuned cavity is much smaller than it is in the case for a positively detuned cavity, even though their parameters are very similar. In the positive detuned case, the cavity sits above the AP as seen in fig. 5.12a. The effect of having the cavity sitting above the AP is that the LAPP is mostly excitonic at low momenta, whereas the higher energy UAPP is mostly photonic. The quasiparticle weight of the LAPP at small momentum is, therefore, fairly large as most of the quasiparticle weight remains in the excitonic part of the particle. This feature is qualitatively changed by having a negative detuning of the cavity as in fig. 5.12b. Because the photon is below the AP, the LAPP at small momenta is now mostly photonic. The effect is that most of the quasiparticle weight now goes to the UAPP because of its more excitonic character, resulting in a significant decrease in the quasiparticle weight.

The different nature of the LAPP at small momentum for the two different detunings is observed in the linewidth of the LAPP shown in fig. 5.13b. Because the cavity has a much larger linewidth than the AP, the LAPP is lossier at low momentum when  $\Delta_c < 0$  because it is more photonic. Conversely, the more excitonic nature of the LAPP in the  $\Delta_c > 0$  case means it inherits less cavity loss.

### 5.5.3 Driving of polaron-polaritons

We have seen how the cavity coupling significantly changes the nature of the quasiparticle and that changing the cavity detuning can significantly alter the nature of the lowest energy excitation. We will now explore how the system reacts to continuous driving. We consider a narrow laser profile with a Gaussian frequency distribution

$$\kappa(\omega) = \kappa_0 \exp\left(-\frac{1}{2}\left(\frac{\omega - \delta_\kappa}{\gamma_\kappa}\right)^2\right), \quad (5.113)$$

which is independent of momentum. The driving strength of the laser is determined by  $\kappa_0$ , which is proportional to the laser intensity. The carrier frequency of the laser is set by  $\delta_\kappa$ , and  $\gamma_\kappa$  sets the linewidth of the laser. A narrow linewidth of  $\gamma_\kappa = 0.05\epsilon_F$  is chosen such that the cavity can be driven at well-defined energies. The exciton is indirectly driven through the cavity's contribution to the exciton Keldysh self-energy in eq. (5.11). Computing the cavity Keldysh propagator using eqs. (2.83) and (5.6) one finds that the self-energy responsible for driving takes the form

$$\delta\Sigma_{xc}^K(k, \omega) = i2\kappa(\omega)\Omega^2 |G_{c,0}^R(k, \omega)| = \frac{i2\kappa(\omega)\Omega^2}{\left(\omega - \Delta_c - \frac{k^2}{2m_c}\right)^2 + \gamma^2}. \quad (5.114)$$

Due to the indirect nature of the drive, the exciton only experiences the drive along the bare cavity dispersion and, as a consequence of the small photon mass, can only be driven at small momentum.

The loss of photons in the cavity allows the system to dissipate energy. By driving the system, the steady state will be a state with a balance between dissipation and driving and a finite occupation of excitons. The steady state is non-trivial because the exciton's interaction with the electrons allows the exciton to relax down in energy by transferring momentum to the electrons. This relaxation has been explored using a quantum kinetic equation in [230]. In this work, there is no strong coupling to the cavity, and the quasi-particles are the repulsive and attractive polaron and not polaron-polaritons considered here. Furthermore, in [230], it was assumed that the finite density of excitons did not change the spectral function, which is a common assumption when working with kinetic equations. Because of the strong hybridization with the cavity, we can explore how the photonic nature of the LAPP affects the driven steady state and can investigate how the spectrum is modified by driving.

To explore this, we consider the two cases in fig. 5.12 and drive the system above the LAPP with  $\delta_\kappa = -2.4\epsilon_F$ . The driving is then gradually increased until our self-consistent method fails to converge. The code fails to converge because the driving leads to the accumulation of occupation of a specific mode. When this happens, then the effective driving of this mode leads to a decrease in its linewidth. At some point, this linewidth becomes so small that our numerical integrals contain errors that accumulate faster than the convergence rate. A small linewidth indicates that the bosonic mode that is being occupied is close to being unstable. The difficulty we face is, therefore, equivalent to the difficulties that arise close to a phase transition, where the correlation length of the fluctuations diverges. How close we can drive the system to an actual phase transition is an interesting question that is best addressed within the scope of thermal equilibrium, as the behavior of the systems is better understood. In thermal equilibrium, it is easier to differentiate between the numerical calculations becoming unstable due to error accumulation and the physical instability due to a nearby phase transition. The question of how close our current numerical implementation can go to a phase transition is left for further work. For the remainder of the section, we will focus on how the steady state of the positive and negatively detuned cavity is affected by the drive.

The first property we consider is the exciton density computed by integrating  $-\delta G_x^K(k, \omega)/2$  over frequency and momentum. The resulting density as a function of the drive strength is shown in fig. 5.14a. Both densities are only a few percent of the electron density which justifies using the thermal non-interacting electron propagator in the self-energies.

The first striking feature is that the densities increase sub-linearly with the drive

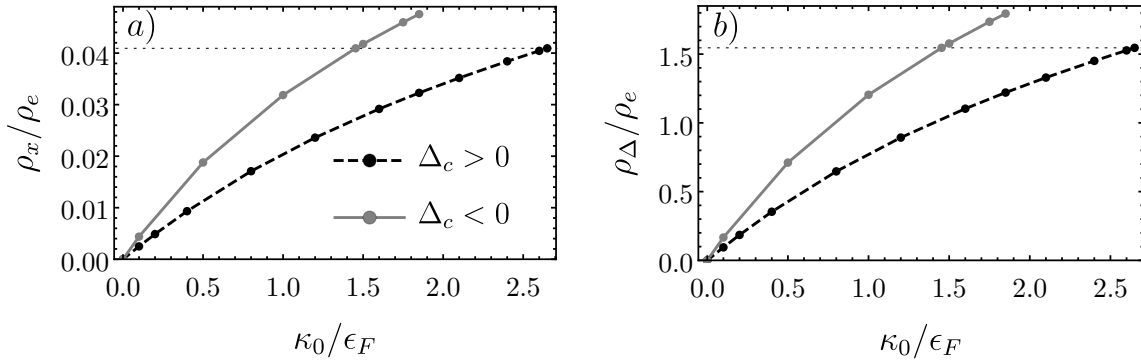


Figure 5.14: *The density of the exciton in a) and the density of the trion in b) as a function of the pump power. The horizontal dashed lines indicate the density  $\rho_x = 0.0409\rho_e$ , which will be used to compare the two different cases. The dots indicates the actual data points computed which are connected with lines to guide the eye.*

strength. The sub-linear scaling can indicate that either the drive becomes less efficient for higher densities or that the LAPP effectively interacts repulsive with each other. At the end of our analysis, we will see that the non-equilibrium nature of the polariton can explain this sub-linear response of the drive.

The density is the momentum and frequency integrated Keldysh propagator, which means that most information about the system is lost. To understand the sub-linear behavior and differentiate between the possible explanations, it is necessary to investigate the properties of the systems in momentum and frequency.

Before moving on, we first explain the other features of the density. For example, the fact that the density of the negatively detuned case increases significantly faster than the positively detuned case. It increases faster because the exciton is driven at different momentum in the two cases. In the positively detuned case, the drive is centered at  $\delta_\kappa = \Delta_c$ , and the photon is therefore driven at the bottom of its dispersion at  $k = 0$ . In the negatively detuned case, the laser is driving at the same frequency but  $\Delta_c = \delta_\kappa - 0.6\epsilon_F$ , such that the laser is driving the photon at a finite momentum around  $k = \sqrt{0.6\epsilon_F 2m_c} \sim 0.05k_F$ . As the laser is driving all momentum equally, the large phase space at finite momentum effectively means that exciton in the  $\Delta_c < 0$  case is driven much harder. This suggests that to compare the two cases, one should not compare them for equal drive strengths but instead for equal densities. The point chosen for the comparison is indicated in fig. 5.14a by the dotted horizontal line where both the negative and the positive case have an exciton density of  $\rho_x/\rho_e = 0.0409$ .

In fig. 5.14b the density of the trion is computed and seen to imitate the behavior of the exciton. The trion density is expected to follow the exciton density closely because the photon only affects  $G_x^R$  for small values of momentum, and the perturbation of  $G_\Delta^R$

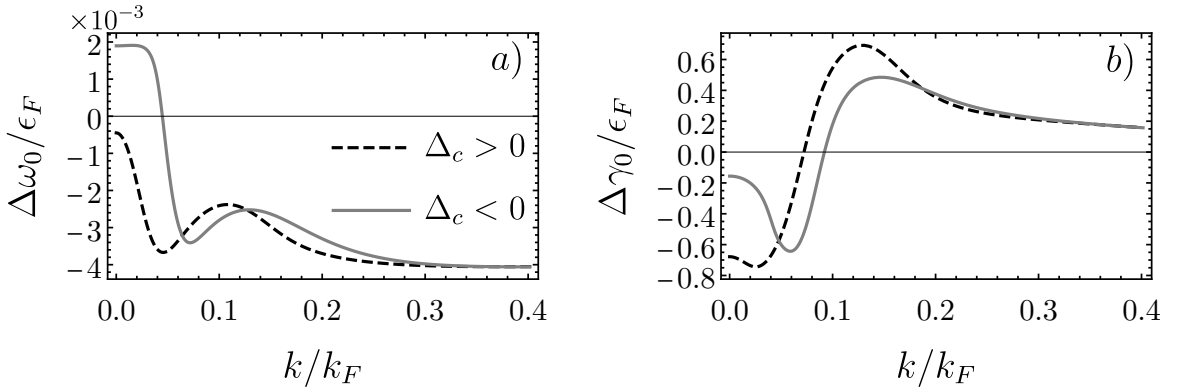


Figure 5.15: *Spectral features at finite driving.* In a) the relative change of the LAPP quasiparticle energy between zero exciton density and an exciton density of  $0.0409\rho_e$  (the horizontal line in fig. 5.14) is shown. The change in the LAPP quasiparticle linewidth is shown for the same densities in b).

due to the polariton formation is therefore small. As the electron density is kept constant and at a low temperature, the Keldysh self-energy of the trion in eq. (5.43) is related to exciton density. The absolute value of the trion density should not be understood as the trion's physical density of trions as the trion has no physical bare dispersion. Instead, the absolute value of the trion density is related to the Tan contact [208]. Even though the absolute value of the density is not equivalent to the number of trions per area, the way the trion is occupied can still be directly inferred from  $\delta G_{\Delta}^K$ .

Having considered the total density, we now investigate momentum and frequency-resolved features. The first element considered is the dispersion of the LAPP. We are interested in how the system is changed by having a finite exciton density and therefore consider the relative change between  $\rho_x = 0$  and  $\rho_x = \rho = 0.0409\rho_e$  given by

$$\Delta\omega_0(k) = \frac{\omega_{0,\rho}(k) - \omega_{0,0}(k)}{\omega_0(k)}, \quad (5.115)$$

where  $\omega_{0,0}(k)$  is the LAPP dispersion at zero exciton density. The relative change of the quasiparticle energy is plotted in fig. 5.15a. The relative change is observed to be on the order of 0.1%, which validates thinking of the LAPP energies as mostly unperturbed by the considered densities.

Even though the changes are small, they are by no means trivial. Independent of the polariton nature (negative or positive detuned cavity), the dispersion is shifted down by a constant for large momentum. Because the shift is independent of the polariton nature, the shift is understood as the effect of changing the trion self-energy by having a finite occupation in the exciton according to eq. (5.41) and the self-energy correction of the exciton due to a finite occupation of trions in eq. (5.45). At small momentum,

the two different detunings do behave qualitatively differently. In the positive case, the quasiparticle energy at  $k = 0$  is decreased slightly, whereas, in the negatively detuned case, the energy is increased. This means that for the negatively detuned cavity, the zero momentum mode becomes less favorable for increasing exciton density.

While the changes in the quasiparticle energy are small and negligible, this is not the case for the quasiparticle linewidth. The relative change of the quasiparticle linewidth, defined analogously to eq. (5.115), is shown in fig. 5.15b and seen to change by up to 80% of the undriven linewidth. Consistent with the previous interpretation, the change of the linewidth also goes to a constant for large momentum. As momentum is decreased, the linewidth increases until it suddenly starts decreasing. The increased linewidth for intermediate momentum is due to the drive happening at higher energy than the LAPP. This leads to a quick relaxation down to the LAPP dispersion at large momentum<sup>3</sup>. From there, the excitons have to scatter off the electrons to decrease their momentum. This is energetically favorable as the dispersion bends down, and the lower momentum modes are therefore driven by the relaxation of the higher momentum modes, which in turn gives rise to a large linewidth of the high momentum mode. Following this reasoning, one would expect that the excitons would continue decaying down until they hit zero momentum. If this was the case, then the finite momentum modes should always have a larger linewidth when there is a finite exciton density in the system compared to when the system is not driven. This is the case for polaron as discussed in section 5.5.1. However, the hybridization of the cavity increases the linewidth at small momentum, as discussed in fig. 5.13b. The increased loss that happens when the LAPP starts bending down means that the occupation accumulates at a finite momentum which is seen in the momentum distribution in fig. 5.16a. The accumulation at finite momentum means that all these modes are driven by those at higher momentum, and their linewidth is, therefore, significantly decreased compared to when there is no occupation. Because the LAPP becomes more photonic at small momentum, its linewidth again increases as the momentum decreases, as seen in fig. 5.13b. The effect is a minimum linewidth at finite momentum because the excitons move down the dispersion due to relaxation, but they are lost with a higher rate, and the low momentum modes are not as efficiently driven because there are fewer particles to drive them. The cavity hybridization can therefore be understood as leading to a competition between momentum relaxation rate and loss rate.

By just considering the energy of the quasiparticle, one would have expected that the negatively detuned case would be much better at getting the population to  $k = 0$  because its dispersion is much steeper. Instead, one observes the opposite in fig. 5.16a. Based on

---

<sup>3</sup>On the scale of the characteristic photon momenta



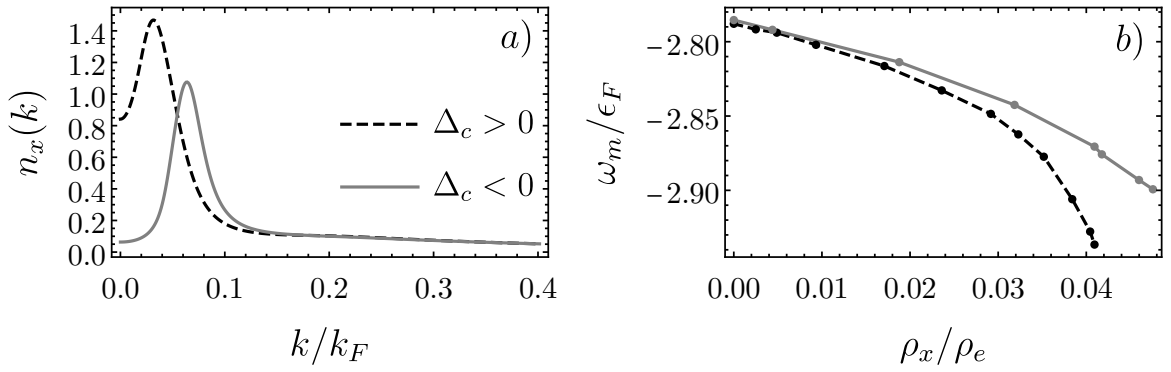


Figure 5.16: a) shows the momentum distribution for the LAPP at the same two densities as in fig. 5.15 while b) shows the frequency of the minimum of the quasiparticle linewidth as a function of the density.

the above discussion, one could expect that this is because of the increased loss of the  $\Delta_c < 0$  case seen in fig. 5.13b. This argument is insufficient to explain the qualitative difference between the detunings seen in both fig. 5.15b and fig. 5.16a. The negatively detuned case has a much smaller change of its linewidth at small momentum, and its momentum distribution is centered at larger momentum because the negative case has a much lower relaxation rate at small momentum because it is less excitonic. This means that even if the two cases were engineered to have the same linewidths, the negatively detuned case would accumulate at large momentum and effectively drive the  $k = 0$  mode very inefficiently. Another indicator for this effect is observed by looking at the frequency of the minimum of the linewidth as a function of the density as shown in fig. 5.16b. Because the dispersion is barely modified, it is sufficient to consider the frequency of the minimum linewidth, as the momentum changes accordingly. Here, the minimum moves down along the LAPP dispersion with increasing density. As explained above, it moves down because the increased density can compensate for a larger loss rate, meaning the particles reach further down the dispersion before being lost through the cavity. Because the relaxation rate is less efficient for the negative detuning, one observes a much smaller non-linear impact on  $\omega_m$  even though the dispersion is much steeper.

Having understood how the system is affected by the drive, we can now explain the sub-linear dependence of the density as a function of the drive strength seen in fig. 5.14a. At large drive strength, the population is pushed further into the lossy region, which means that more particles are lost. It is, therefore, necessary to drive the system harder when the density is increased because the average loss rate per particle is increased. From this understanding, we can also predict that the system should not be able to condense at finite momentum. The system can not condense at finite momentum because if the occupation grows, then it will move further down the dispersion, and the particles will

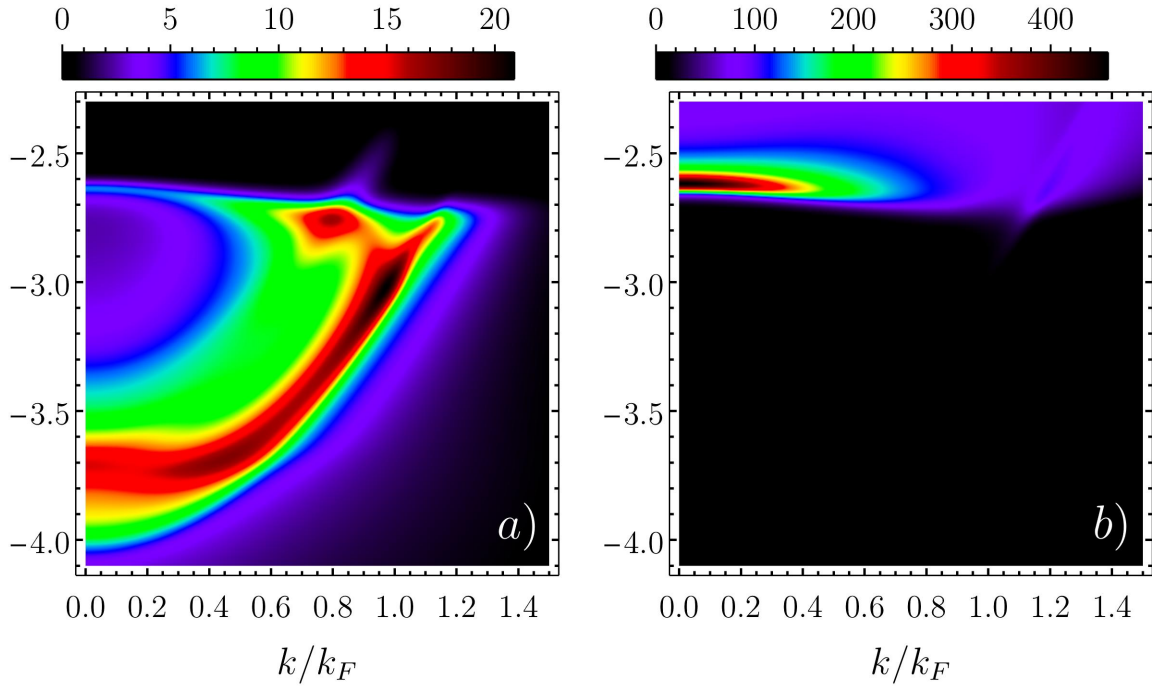


Figure 5.17: *The occupation and spectrum of the trion when the excitons are driven to a density of  $\rho_x/\rho_e = 0.0409$ . a) A plot of  $\delta G_{\Delta}^K(k, \omega)$ , which is occupied below the trion continuum. b) The trion spectral function  $A_{\Delta}(k, \omega)$  which is similar to the  $\rho_x = 0$  one in fig. 5.10b but shows an emerging feature near  $k = 1.2k_F$ . This feature arises due to the finite density of the excitons.*

experience more loss. The only way for the system to condense is, therefore, when the peak of the population is at  $k = 0$ . When that is the case, increasing the drive strength directly corresponds to adding more particles at  $k = 0$ , and the effective loss rate is therefore unchanged by increasing the drive strength.

These results show that modifying the spectral function is important for the driven system, as the linewidth is significantly perturbed by driving. We have seen how various non-trivial observations can be understood by the interplay between loss and the effective momentum relaxation rate. Both these features can be qualitatively changed by simply changing the cavity detuning.

To close off the section, we will point out that while the trion is a slave to the exciton, the trion propagators are qualitatively changed when the exciton has a finite density. This is shown in the spectral function and occupied Keldysh propagator shown in fig. 5.17. Because the exciton has occupation at small momentum, it is possible to create trions formed by an exciton at  $k = 0$  and an electron at  $k = k_F$ . The trion keldysh propagator then starts forming occupation along a parabolic band seen in fig. 5.17a. Because the occupation of the excitons is not at  $k = 0$ , there is a significant deviation from a simple

parabolic band.

This occupation is along a dispersion that does not exist for the undriven trion spectral function shown in fig. 5.10b. The finite exciton occupation, therefore, also leads to a modification of the trion spectrum seen in fig. 5.17b at  $k > k_F$ . The effect here is small because our occupation is small and is distributed over many momentum modes. With this we show that, even within the dilute limit, where the electrons are assumed unperturbed, the occupation of the trion does not happen by filling up the undriven trion spectral function; instead, one has to include the self-energy corrections that arise from a finite exciton density.

## 5.6 Summary and discussion

In this chapter, we have described a method to self-consistently compute the steady states' spectral properties and occupation of a many-body driven-dissipative system using real frequencies. The method presented applies to any system where the interaction can be approximated as a contact interaction in space and time. Inspired by the recent experimental progress in setting up gated TMD monolayers inside cavities, we have focused on the specific case of polaron-polaritons in two dimensions in the dilute limit. We have shown that our self-consistent calculation can capture the qualitative features of the polaron system and that including the cavity leads to interesting effects that arise from the interplay between the non-equilibrium nature of the cavity and the many-body-driven momentum relaxation through electron interaction.

We have here shown some first results but also remark that there is a long list of exciting things that should be studied. We have focused on non-equilibrium effects, but even in equilibrium, there are interesting questions one should investigate. Our method has the advantage of having direct access to the spectral functions without performing an analytic continuation. One should study how close our current numerical method can go to a condensation transition of the excitons within thermal equilibrium. By understanding this, one could investigate the properties of condensation in two dimensions which happens through a BKT transition [231]. This would lead to investigations of two-dimensional Bose-Fermi mixtures both in and out of equilibrium. Having seen that the trion is not simply occupied along its undriven spectral function, it is also relevant to investigate how the occupation of the system is affected by going across the polaron to trion transition seen for  $m_x = 2m_e$  in fig. 5.9.

# Chapter 6

## Conclusion

In this thesis, we studied two systems with strong interactions between a cavity light field and a many-particle system. These hybrid systems require that drive and dissipation are treated together with the interactions in the many-particle system. To this extent, we have used non-equilibrium field theory for the theoretical description of the systems. The construction and properties of the non-equilibrium field theory have been discussed in chapter 2. Considering the example of a linearly coupled environment, we showed how incoherent loss and drive emerged from the microscopic theory and how the field theory relates to the master equation from open quantum system.

In chapter 3 we focused on a system consisting of an ultracold bosonic atom cloud trapped inside a near-planar cavity. Inspired by the experimental realizations, we considered driving the atom cloud with a transverse pump laser. The combination of a large number of atoms in the cloud and the external pumping made it possible to strongly couple the light field and the atomic motion, leading to the formation of polaritons. By using a periodic phase modulation of the laser with a frequency similar to the transverse cavity mode splitting, we derived an effective model with tuneable interactions between the different transverse cavity modes. The derivation relied on the large energy scale separation between the detuning of the laser to the electronic transition, the transverse cavity mode splitting, and the recoil energy of the atomic cloud. It was shown how the effective interactions between the transverse cavity modes led to polaritons that consisted of several different cavity modes. In the regime where the cavity linewidth was smaller than the atomic recoil energy, we showed how strong coupling between the different cavity modes led to avoided crossings between the polaritons.

In chapter 3, we found that the phase diagram for the superradiant transition was drastically modified when some cavity modes acquired an effective negative detuning. The modification to the superradiant phase was explained in chapter 4, using the microscopic quantum action to derive classical equations for the atom motion and the cavity field.

---

From these we derived analytical equations for the critical coupling and frequency of the unstable polariton mode in the multimode model. By investigating the eigenvalues of the linearized equations around the normal phase, we developed a qualitative description of how the multimode polariton becomes unstable at a finite frequency, due to the coupling to both a positively- and a negatively-detuned cavity mode. The qualitative description allowed us to fully explain the phase diagram found in chapter 3. With this description we showed that there were parameter regions where two finite-frequency polariton modes could become unstable simultaneously. By deriving the two-mode generalization of the Stuart-Landau equations, it was shown that the finite-frequency unstable polariton modes led to the emergence of stable limit cycles inside the superradiant phase. The two-mode Stuart-Landau equations also showed that two limit cycles could co-exist and that at the level of the classical equations, the transition into the superradiant phase was equivalent to a double Hopf bifurcation. To understand all the possible steady states for the two-limit-cycle system, we mapped the results from the two-mode Stuart-Landau equations to the normal form of the double Hopf bifurcation. This mapping showed that for our parametrization of the two-limit-cycle case, the steady state could be either a single limit-cycle or the co-existence of two limit cycles. There were also parameters for which we proved that the system was bistable and, therefore, sensitive to the initial state. Lastly, we explored how interactions within the atom cloud affect the finite-frequency polariton instability. The resulting analytical equations for the critical coupling and frequency were similar to the previous equations without atom interactions. The only change was that the bare dispersion of the atom cloud was modified to be that of the Bogoliubov dispersion. Transitioning into superradiance at finite frequency was shown to be more sensitive to the form of the dispersion than the normal zero-frequency transition. While the features of the linear stability were not significantly affected by the atom interactions, we showed that the combination of a limit cycle and atom interactions opened new scattering channels for the atoms. These allowed the atoms to scatter into modes that did not belong to the limit cycle and suggested that the generic limit cycle is only metastable. Using the Stuart-Landau result, we discussed the scaling of the scattering rates and showed that the dominant scattering channel could be closed by changing the frequency of the limit cycle. We hypothesized that this should lead to a qualitatively different scaling of the scattering rates, which could significantly extend the limit cycle's lifetime.

In chapter 5 we moved from the ultracold gas to considering a two-dimensional semiconductor inside a cavity. This was inspired by recent experiments where a Transition-metal dichalcogenide (TMD) monolayer was placed inside a cavity. The TMD monolayer coupled strongly to the cavity by optical excitation of an exciton in the TMD, forming exciton-polaritons. By gating the monolayer, the experiments could generate a back-

ground gas of electrons that interacted strongly with the exciton, dressing it to form polarons. The strong interaction between the electrons and the excitons, and in turn the polaritons, required us to solve out-of-equilibrium coupled Dyson equations both the spectrum and the occupation simultaneously. To do this, we considered the coupled equations within a non-perturbative ladder approximation. The drive and dissipation made it impossible to use an imaginary time formulation, and the coupled equations had to be solved in real time. Solving the equations in real time is numerically challenging due to fast oscillations in time and space. To deal with these oscillations, we developed a numerical method to Fourier transform functions that did not rely on sampling the fast oscillations. The numerical method works for any isotropic system in two and three dimensions. We compared the results of our method to the known results for the Fermi polaron problem and found that it captured the qualitative features well. In the regime close to the polaron-trion transition, our non-perturbative ladder approximation missed important processes, and the quantitative prediction power of our theory was poor in this parameter region. With this knowledge, the system was considered far from the polaron-trion transition. We investigated the spectrum of the emerging polaron-polariton that arose due to the strong cavity-exciton-electron coupling. It was shown that the cavity dressing of the exciton led to an effective decrease of the trion binding energy, meaning that the interplay between the strong cavity-exciton coupling and the strong exciton-electron coupling required that both interactions were treated at the same level in the calculation. We found that by changing the detuning of the cavity, it was possible to drastically change the nature of the lowest energy excitation, which we used to explain the qualitatively different behavior of the steady state when the system was driven. The combination of cavity loss at small momentum and the effective decrease of the trion binding energy led to the accumulation of occupation at a small finite value of momentum. We showed that by driving the system harder, the occupation accumulated at lower momentum, which was explained by the increased number of particles that drove the low-momentum modes. Based on our results, we hypothesized that in the considered cases, the polaritons could not condense unless they reached zero momentum.

# Appendix A

## Action for a free theory

The derivation presented here is based on a previous work [232] and follows [33] and [34]. Here we will construct a correct continuum representation of the free action. The focus here is on a single mode with the Hamiltonian given as

$$H = \omega_0 a^\dagger a, \quad (\text{A.1})$$

where  $\omega_0$  is the energy required to add one excitation to the mode. We write the thermal state of a free system (with  $\beta = 1/k_B T$ ) as

$$\rho_0 = \frac{e^{-\beta(H - \mu a^\dagger a)}}{\text{Tr} [e^{-\beta(H - \mu a^\dagger a)}]} = e^{-\beta(H - \mu a^\dagger a)} (1 \mp \kappa)^{\pm 1} = \frac{e^{-\beta(H - \mu a^\dagger a)}}{\mathcal{N}}, \quad (\text{A.2})$$

with  $\kappa = e^{-\beta(\omega_0 - \mu)}$  and  $\mathcal{N} = (1 \mp \kappa)^{\mp 1}$ .  $\mu$  is the chemical potential. The upper sign is for a bosonic system, and the lower sign is for a fermionic one. The discrete partition function is then defined by eq. (2.29). The last remaining element there is the initial state overlap

$$\langle \phi_1^+ | \rho_0 | \pm \phi_1^- \rangle = \frac{e^{\pm \bar{\phi}_1^+ \phi_1^- \kappa}}{\mathcal{N}}, \quad (\text{A.3})$$

here the normalization and notation for the thermal state from eq. (A.2) has been used.

Inserting the results of all the overlaps and multiplying together all the resulting exponentials, the partition function takes the form of a multidimensional Gaussian integral

$$\mathcal{Z} = \frac{1}{\mathcal{N}} \int \left( \prod_{j=1}^N d[\bar{\phi}_j^+, \phi_j^+] d[\bar{\phi}_j^-, \phi_j^-] \right) \exp(i\mathcal{S}_d), \quad \mathcal{S}_d = \sum_{\alpha, \beta} \bar{\phi}_\alpha G_{\alpha, \beta}^{-1} \phi_\beta. \quad (\text{A.4})$$

$\mathcal{S}_d$  is the discrete action for our theory. The  $\alpha/\beta$  indices contain all degrees of freedom

( $\pm$  and time index).  $G^{-1}$  is thus a  $2N \times 2N$  matrix which takes the form

$$iG^{-1} = \left( \begin{array}{ccc|ccc} -1 & & & \pm\kappa & & \\ h_+ & -1 & & & & \\ & h_+ & -1 & & & \\ & & & \cdot & \cdot & \\ & & & & \cdot & \cdot \\ \hline & & & & -1 & h_- \\ & & & & & -1 & h_- \\ & & & & & & -1 & \cdot \\ & & & & & & & \cdot & \cdot \\ & & & & & & & & \cdot \\ & & & & & & & & 1 \\ & & & & & & & & & \cdot \end{array} \right) = \left( \begin{array}{c|c} -A & B \\ \hline C & -D \end{array} \right). \quad (\text{A.5})$$

The inverse  $G^{-1}$  is a  $2 \times 2$  block matrix, where the diagonal elements emerge from the overcounting corrections in the identity resolutions in eq. (2.21). The  $h_{+(-)}$  elements originate from the evolution overlaps along the forward (backward) leg of the contour. The two off-diagonal blocks contain only one non-zero element each. The fields corresponding to the initial time couple through  $\kappa$ , while the fields at the end of the contour couple through an identity. All other entries in this matrix are zero.

By including source terms to the partition function we can promote it to a generating functional

$$\mathcal{S}_d[\bar{J}, J] = \sum_{\alpha, \beta} \bar{\phi}_\alpha G_{\alpha, \beta}^{-1} \phi_\beta + \sum_\alpha (\bar{\phi}_\alpha J_\alpha + \bar{J}_\alpha \phi_\alpha). \quad (\text{A.6})$$

The generating functional still has the form of a Gaussian integral and can be solved exactly [33]

$$\mathcal{Z}[\bar{J}, J] = \int \prod_{j=1}^N d[\bar{z}_j, z_j] e^{-\sum_{i,j} \bar{z}_j M_{ji} z_i + \sum_j (\bar{z}_j J_j + \bar{J}_j z_j)} = \frac{e^{\sum_{i,j} \bar{J}_i (M^{-1})_{ij} J_j}}{\det(M)^{\pm 1}}, \quad (\text{A.7})$$

Where the elements are identified as  $M = -iG^{-1}$  and  $z_j = \phi_\alpha$ . For bosons, the result is valid when all eigenvalues of  $M$  have non-negative real parts, and for fermions, it is valid for any invertible  $M$ . This difference is because Grassmann integrals are always convergent [233]. Correlation functions can now be evaluated by taking derivatives of the generating functional followed by setting the sources to zero

$$\begin{aligned} \langle \phi_\gamma \bar{\phi}_\lambda \rangle &= \frac{1}{\mathcal{N}} \int \left( \prod_{j=1}^N d[\bar{\phi}_j^+, \phi_j^+] d[\bar{\phi}_j^-, \phi_j^-] \right) \phi_\gamma \bar{\phi}_\lambda \exp(i\mathcal{S}_d[0, 0]) \\ &= \frac{\partial^2}{\partial \bar{J}_\gamma \partial J_\lambda} \mathcal{Z}[\bar{J}, J] \Big|_{J=\bar{J}=0}. \end{aligned} \quad (\text{A.8})$$



Using eq. (A.7) the correlation function is found to be given by the inverse of  $G^{-1}$

$$\langle \phi_\gamma \bar{\phi}_\lambda \rangle = \frac{\partial^2}{\partial \bar{J}_\gamma \partial J_\lambda} \frac{e^{\sum_{i,j} \bar{J}_i (iG)_{ij} J_j}}{\mathcal{N} \det(-iG^{-1})^{\pm 1}} \Big|_{J=\bar{J}=0} = \frac{iG_{\gamma\lambda}}{\det(-iG^{-1})^{\pm 1} \mathcal{N}}. \quad (\text{A.9})$$

Considering correlation functions different from the two-point function, it is seen that with a quadratic theory, the odd-point functions vanish. The higher-order even correlation functions are also accessible from the generating functional e.g. the four-point function is given by

$$\begin{aligned} \langle \phi_{\gamma_1} \phi_{\gamma_2} \bar{\phi}_{\lambda_1} \bar{\phi}_{\lambda_2} \rangle &= \frac{\partial^4}{\partial \bar{J}_{\gamma_1} \partial \bar{J}_{\gamma_2} \partial J_{\lambda_1} \partial J_{\lambda_2}} \frac{e^{\sum_{i,j} \bar{J}_i (iG)_{ij} J_j}}{\mathcal{N} \det(-iG^{-1})^{\pm 1}} \Big|_{J=\bar{J}=0}, \\ &= \frac{\partial^2}{\partial \bar{J}_{\gamma_1} \partial \bar{J}_{\gamma_2}} \frac{\sum_{i,j} \bar{J}_i (iG)_{i\lambda_1} \bar{J}_j (iG)_{j\lambda_2}}{\mathcal{N} \det(-iG^{-1})^{\pm 1}} \Big|_{\bar{J}=0}, \\ &= \frac{(iG)_{\gamma_2\lambda_1} (iG)_{\gamma_1\lambda_2} \pm (iG)_{\gamma_1\lambda_1} (iG)_{\gamma_2\lambda_2}}{\mathcal{N} \det(-iG^{-1})^{\pm 1}}. \end{aligned} \quad (\text{A.10})$$

This generalizes to all higher order  $2n$ -point functions such that one has to sum over all possible combinations of  $iG$ . For fermions, one has to consider the anti-commutation, which leads to each term being multiplied by the parity of its corresponding permutation. This is known as Wick's theorem and is exact as long as the theory is quadratic. It means that for a quadratic theory, the only elements needed are the two-point functions.

The two-point functions are usually called the propagators, as they give the probability of finding an excitation created at a specific point  $\mathbf{x}_0$  at a later point  $\mathbf{x}_f$ . The correlations thus carry information about how excitations propagate through the system.

## A.1 Propagators for the free system

To avoid errors introduced by the Trotter decomposition in eq. (2.16) it is necessary to take the continuum limit.

From eq. (A.9) it is seen that all the propagators can be read out if the determinant and inverse of eq. (A.5) are found. To compute the determinant the relation  $\det(\mathcal{O}) = \exp[\text{Tr} \log(\mathcal{O} - \mathbb{1} + \mathbb{1})]$  for a matrix  $\mathcal{O}$ , is used and  $\log(x + 1)$  is expanded around  $x = 0$

$$\det(-iG^{-1}) = \exp \left( \text{Tr} \left[ \sum_{i=1}^{\infty} \frac{(-1)^{i+1}}{i} (-iG^{-1} - \mathbb{1})^i \right] \right). \quad (\text{A.11})$$

Inspecting the form of the matrix power, one finds that the first case where it has a non-zero trace is at  $i = 2N$ , with  $2N$  being the size of  $G^{-1}$ . For this case the matrix is a purely diagonal with the constant elements  $(h_+ h_-)^{N-1} \kappa$ . Therefore, the trace inside the

exponential will only be non-zero when  $i = n2N$  with  $n$  being an integer. Re-summing these terms, the sum can be written as a logarithm

$$\begin{aligned} \det(-iG^{-1}) &= \exp\left(\sum_{i=1}^{\infty} \frac{(-1)^{i+1}}{i} \left(- (h_+ h_-)^{N-1} (\pm\kappa)\right)^i\right) \\ &= \exp\left(\log\left(1 - (h_+ h_-)^{N-1} (\pm\kappa)\right)\right), \\ &= 1 - (h_+ h_-)^{N-1} (\pm\kappa). \end{aligned} \quad (\text{A.12})$$

The form of  $h_{\pm}$  is given by eq. (2.28) such that

$$\det(-iG^{-1}) = 1 - (1 + \Delta^2 \omega_0^2)^{N-1} (\pm\kappa). \quad (\text{A.13})$$

Before taking the limit of  $n \rightarrow \infty$  it is important to remember that the time slice length,  $\Delta = (t - t_0)/N$ , is inversely proportional to  $N$ . The limit where  $N \rightarrow \infty$  is, therefore, equal to  $\Delta \rightarrow 0$ , which implies that

$$\begin{aligned} \det(-iG^{-1}) &= \lim_{N \rightarrow \infty} 1 - (1 + \Delta^2 \omega_0^2)^{N-1} (\pm\kappa) \\ &= \lim_{N \rightarrow \infty} 1 - e^{(N-1)\Delta^2 \omega_0^2} (\pm\kappa) = 1 \mp \kappa. \end{aligned} \quad (\text{A.14})$$

As a result, the determinant exactly cancels the normalization ( $\mathcal{N}$ ) from the thermal state eq. (A.2). This is a consistency check of the theory as the partition function is the "zero-point" correlation and must be unity due to the identical Hamiltonian on both legs of the contour

$$\mathcal{Z} = \frac{1}{\mathcal{N} \det(-iG^{-1})^{\pm 1}} = 1. \quad (\text{A.15})$$

To compute the inverse of eq. (A.5), it is advantageous to use its  $2 \times 2$  block structure. With  $D$  being invertible  $N \times N$  matrices, the inverse is given by [234]

$$\begin{aligned} (-iG^{-1})^{-1} = iG &= \left( \begin{array}{c|c} A & -B \\ \hline -C & D \end{array} \right)^{-1}, \\ &= \left( \begin{array}{c|c} (A - BD^{-1}C)^{-1} & (A - BD^{-1}C)^{-1}BD^{-1} \\ \hline D^{-1}C(A - BD^{-1}C)^{-1} & D^{-1} + D^{-1}C(A - BD^{-1}C)^{-1}BD^{-1} \end{array} \right) \end{aligned} \quad (\text{A.16})$$

As  $A$  and  $D$  are both triangular matrices, they can be written as  $\mathbb{1} + \mathcal{T}$ , with  $\mathcal{T}$  being a strictly triangular matrix (zero in diagonal). For a strictly triangular matrix of dimension  $N$ , it is known that the matrix power vanishes for an exponent  $\geq N$  [156]. Using the

general property

$$(\mathbb{1} - x^N) = (\mathbb{1} - x) (\mathbb{1} + x + x^2 + x^3 + \dots + x^{N-1}), \quad (\text{A.17})$$

and substituting  $x = -\mathcal{T}$ , the inverse is found as

$$\begin{aligned} \mathbb{1} &= (\mathbb{1} + \mathcal{T}) \left( \mathbb{1} + \sum_{i=1}^{N-1} (-1)^i \mathcal{T}^i \right) \\ &\rightarrow (\mathbb{1} + \mathcal{T})^{-1} = \mathbb{1} + \sum_{i=1}^{N-1} (-1)^i \mathcal{T}^i. \end{aligned} \quad (\text{A.18})$$

$iG$  can now be computed for a finite dimensionality. For  $N = 6$ , one finds

$$iG = \frac{1}{\det(-iG^{-1})} \times \left( \begin{array}{ccc|ccc} 1 & \pm h_+ h_-^2 \kappa & \pm h_-^2 \kappa & \pm \kappa & \pm h_- \kappa & \pm h_-^2 \kappa \\ h_+ & 1 & \pm h_+ h_-^2 \kappa & \pm h_+ \kappa & \pm h_- h_+ \kappa & \pm h_-^2 h_+ \kappa \\ h_+^2 & h_+ & 1 & \pm h_+^2 \kappa & \pm h_- h_+^2 \kappa & \pm h_+^2 h_-^2 \kappa \\ \hline h_+^2 h_-^2 & h_+ h_-^2 & h_+^2 & 1 & h_- & h_-^2 \\ h_+^2 h_- & h_+ h_- & h_- & \pm h_+^2 h_- \kappa & 1 & h_- \\ h_+^2 & h_+ & 1 & \pm h_+^2 \kappa & \pm h_+^2 h_- \kappa & 1 \end{array} \right). \quad (\text{A.19})$$

Notice that because the determinant here is a consequence of the inversion and not the functional integral, it is in the denominator for both bosons and fermions.

Generalizing this result to arbitrary  $N$  does not require inverting larger matrices, as the structure of the matrix is extendible. The two diagonal blocks in eq. (A.19) describe propagation between a field configuration on the same branch (upper block = forward leg, lower block = backward leg), while the off-diagonal blocks describe propagation between the two contour legs. The four different propagators are necessary to accommodate for the non-equilibrium situation. Inspecting the form of eq. (A.19) the four different propagators, for arbitrary  $N$ , are taking the form

$$\begin{aligned} iG_{k,l}^{++} &= (\theta(k \geq l) h_+^{k-l} \pm \theta(l > k) (h_- h_+)^{N-1} h_+^{k-l} \kappa) / \det(-iG^{-1}), \\ iG_{k,l}^{--} &= (\theta(l \geq k) h_-^{l-k} \pm \theta(k > l) (h_- h_+)^{N-1} h_-^{l-k} \kappa) / \det(-iG^{-1}), \\ iG_{kl}^{\leq} &= iG_{k,l}^{+-} = (\pm h_-^{l-1} h_+^{k-1} \kappa) / \det(-iG^{-1}), \\ iG_{kl}^{\geq} &= iG_{k,l}^{-+} = ((h_+ h_-)^N h_+^{-l} h_-^{-k}) / \det(-iG^{-1}), \end{aligned} \quad (\text{A.20})$$

where  $\theta(x)$  is a discrete Heaviside function which is unity when the argument condition is satisfied and zero otherwise. In the continuum limit the propagators can be found using

$$\lim_{N \rightarrow \infty} h_{\pm} = e^{\mp i \Delta \omega_0}$$

$$\begin{aligned} iG^{++}(t, t') &= \frac{(\theta(t-t') \exp[-i\omega_0(t-t')] \pm \theta(t'-t) \exp[-i\omega_0(t-t')]) \kappa}{1 \mp \kappa} \\ &= \exp[-i\omega_0(t-t')] \left( \theta(t-t')(1 \pm n_{B/F}) \pm \theta(t'-t)n_{B/F} \right), \\ iG^{--}(t, t') &= \exp[-i\omega_0(t-t')] \left( \theta(t'-t)(1 \pm n_{B/F}) \pm \theta(t-t')n_{B/F} \right), \\ iG^{<}(t, t') &= \pm \exp[-i\omega_0(t-t')] n_{B/F}, \\ iG^{>}(t, t') &= \exp[-i\omega_0(t-t')] (1 \pm n_{B/F}), \end{aligned} \tag{A.21}$$

where  $n_{B/F}$  is thermal occupation given by the Bose/Fermi distribution

$$n_{B/F} = \frac{1}{e^{\beta(\omega_0 - \mu)} \mp 1}. \tag{A.22}$$

It is important to notice that the continuum representation is not completely reflecting the discrete theory. This is seen by considering  $t = t'$ . In the discrete version, one Heaviside is zero while another one is unity, whereas, in the continuum representation, both Heaviside functions look identical. Considering properties in the continuum limit can be misleading, as it hides several features present in the discrete version. The continuum theory can therefore be considered a representation of the discrete version. As mentioned, this is especially important when considering equal time. A consequence is the explicit correlation between the propagators. When discussing the construction of the time contour, the correlation among the two legs was already noted as unavoidable. In the continuum representation one finds the redundancy relation

$$C_{\text{cont}} = G^{++}(t, t') + G^{--}(t, t') - G^{<}(t, t') - G^{>}(t, t') = 0. \tag{A.23}$$

However, there is some ambiguity for  $t = t'$  due to the interpretation of the Heavisides. To resolve this ambiguity, one considers the discrete case where the same quantity is given by

$$\begin{aligned} C_{\text{discrete}} &= \frac{1}{\det(-iG^{-1})} \left( \theta(k \geq l) h_+^{k-l} + \theta(l \geq k) h_-^{l-k} \right. \\ &\quad \pm \theta(k > l) (h_- h_+)^{N-1} h_+^{k-l} \kappa \\ &\quad \pm \theta(l > k) (h_- h_+)^{N-1} h_-^{l-k} \kappa \\ &\quad \left. \mp h_-^{l-1} h_+^{k-1} \kappa - (h_- h_+)^N h_+^{-l} h_-^{-k} \right). \end{aligned} \tag{A.24}$$

Considering the different values of  $k, l$  and taking the continuum limit, one finds the

relations

$$C_{\text{discrete}} \stackrel{N \rightarrow \infty}{=} \begin{cases} \frac{e^{-i\omega_0(t-t')}}{\det(-iG^{-1})} (1 \pm \kappa \mp \kappa - 1) = 0, & k \neq l, \\ \frac{1}{\det(-iG^{-1})} (1 + 1 \mp \kappa - 1) = 1, & k = l. \end{cases} \quad (\text{A.25})$$

This shows that, due to the diagonal elements in the blocks of  $G^{-1}$ , the relation eq. (A.23) is not true for the point  $t = t'$ . In special cases, this results in disagreements between the continuum and discrete representations. A relevant example is the occupation number. This is given by the equal time correlation function

$$\begin{aligned} \langle a^\dagger a \rangle(t) &= \langle \phi(t) \bar{\phi}(t) \rangle = \frac{1}{2} (\langle \phi^+(t) \bar{\phi}^+(t) \rangle + \langle \phi^-(t) \bar{\phi}^-(t) \rangle) \\ &= \frac{i}{2} (G^{++}(t, t) + G^{--}(t, t)) = 1 \pm n_{B/F} \end{aligned} \quad (\text{A.26})$$

where the continuum representation has been used directly. In the discrete form, the operators  $a^\dagger$  and  $a$  do not sample the same field configuration but instead two neighboring time slices. The consequence is that in the discrete form, the occupation number expectation value is found to be

$$\begin{aligned} \langle a^\dagger a \rangle(j\Delta) &= \frac{1}{2} (\langle \phi_j^+ \bar{\phi}_{j+1}^+ \rangle + \langle \phi_{j+1}^- \bar{\phi}_j^- \rangle) = \frac{i}{2} (G_{j,j+1}^{++} + G_{j+1,j}^{--}) \\ &\stackrel{N \rightarrow \infty}{=} \pm n_{B/F}. \end{aligned} \quad (\text{A.27})$$

Compared to the continuum result, this is the correct one and therefore supports thinking of the discrete representation as more reliable. However the difference between eq. (A.23) and eq. (A.25) is a Kronecker delta. In the continuum representation this turns into  $\lim_{\Delta \rightarrow 0} \Delta \delta(t-t')$  [235], which means that the continuum violation is a manifold of measure zero [33].

This argument justifies extending the redundancy relation eq. (A.23) to include  $t = t'$  when building the theory. The redundancy relation is not a model-specific result but a property of the non-equilibrium formalism, which also holds for interacting theories.

### A.1.1 Keldysh rotation

We now seek a representation that makes the redundancy in eq. (A.23) explicit. This can be achieved through a linear transformation

$$\begin{pmatrix} \phi^{cl} \\ \phi^q \end{pmatrix} = \frac{1}{\sqrt{2}} \begin{pmatrix} 1 & 1 \\ 1 & -1 \end{pmatrix} \begin{pmatrix} \phi^+ \\ \phi^- \end{pmatrix}. \quad (\text{A.28})$$

The indices are commonly denoted as  $c$  for classical and  $q$  for quantum. The transformation is referred to as the Keldysh rotation [236]. It effectively uses the redundancy

eq. (A.23) to reduce the number of propagators. Applying the transformation to the  $+/-$  propagators eq. (A.21), the propagator coupling two quantum fields is given by [237]

$$\begin{aligned}
iG^q(t, t') &= \langle \phi^q(t) \bar{\phi}^q(t') \rangle = iG(t, t')^{q,q} \\
&= \frac{1}{2} (iG^{++}(t, t') + iG^{--}(t, t') - iG^<(t, t') - iG^>(t, t')) \\
&= \begin{cases} 0, & t \neq t' \\ -1/2, & t = t' \end{cases}.
\end{aligned} \tag{A.29}$$

This propagator is, therefore, only important when evaluating equal time correlation functions, and as discussed, it only has a finite value on a measure of zero. So we can therefore neglect this propagator. The next propagator is the one coupling two classical fields

$$\begin{aligned}
\langle \phi^c(t) \bar{\phi}^c(t') \rangle &= iG^{c,c}(t, t') \\
&= \frac{1}{2} \left( iG^{++}(t, t') + iG^{--}(t, t') + iG^<(t, t') + iG^>(t, t') \right. \\
&\quad \left. + iG^{+-}(t, t') + iG^{-+}(t, t') - iG^<(t, t') - iG^>(t, t') \right) \\
&= iG^<(t, t') + iG^>(t, t') + iG^q(t, t') \\
&= iG^K(t, t'),
\end{aligned} \tag{A.30}$$

where the  $G^q$  has been set to zero and the  $G^K$  has the form

$$iG^K(t, t') = iG^<(t, t') + iG^>(t, t') = (1 \pm 2n_{B/F})e^{-i\omega_0(t-t')}. \tag{A.31}$$

This propagator is known as the Keldysh propagator, and when neglecting  $G^q$ , it is the propagator that creates and removes an excitation in the classical field at two points in time. The propagator that creates an excitation in a quantum field at time  $t'$  and removes an excitation of a classical field at time  $t$  is known as the retarded propagator

$$\begin{aligned}
iG^R(t, t') &= \langle \phi^c(t) \bar{\phi}^q(t') \rangle = iG^{c,q}(t, t') \\
&= \frac{1}{2} (iG^{++}(t, t') - iG^{--}(t, t') - iG^<(t, t') + iG^>(t, t')) \\
&= \theta(t - t') (iG^>(t, t') - iG^<(t, t')) \\
&= \theta(t - t') e^{-i\omega_0(t-t')}.
\end{aligned} \tag{A.32}$$

Here the name eludes to the fact that such a propagation path is only possible if the  $t > t'$ . Conversely, one can create an excitation in a classical field and remove it in the

quantum field, which gives the result

$$\begin{aligned}
 iG^A(t, t') &= \langle \phi^q(t) \bar{\phi}^c(t') \rangle = iG^{q,c}(t, t') \\
 &= \frac{1}{2} (iG^{++}(t, t') - iG^{--}(t, t') + iG^{<}(t, t') - iG^{>}(t, t')) \\
 &= \theta(t' - t) (iG^{<}(t, t') - iG^{>}(t, t')) \\
 &= -\theta(t' - t) e^{-i\omega_0(t-t')}.
 \end{aligned} \tag{A.33}$$

This propagator is referred to as the advanced propagator.

The free propagators satisfy the causality conditions in eq. (2.39).

The Keldysh transformation is unitary and does not affect the magnitude of the integration measure in the field integral. It is therefore only necessary to find an appropriate action that satisfies

$$iG^{\alpha\beta}(t, t') = \int \mathcal{D} [\bar{\phi}, \phi] \phi^\alpha(t) \bar{\phi}^\beta(t') \exp(iS) = i \begin{pmatrix} G^K(t, t') & G^R(t, t') \\ G^A(t, t') & 0 \end{pmatrix}. \tag{A.34}$$

Here the new measure  $\mathcal{D} [\bar{\phi}, \phi]$  is a shorthand notation for the continuum limit of the measure in the discrete case eq. (A.8).

A general quadratic action can be written as

$$\mathcal{S} = \int_{-\infty}^{\infty} i \begin{pmatrix} \bar{\phi}^{cl} & \bar{\phi}^q \end{pmatrix}_t \begin{pmatrix} (G^{-1})^a & (G^{-1})^b \\ (G^{-1})^c & (G^{-1})^d \end{pmatrix}_{(tt')} \begin{pmatrix} \phi^{cl} \\ \phi^q \end{pmatrix}_{t'}. \tag{A.35}$$

These four objects are directly related to the propagators through the Gaussian integral in eq. (A.7). Here the Gaussian integral is no longer multidimensional but has been generalised to a functional Gaussian integral. This amounts to simply changing all sums to integrals, and all indices to continuous variables [34]. The connection to the propagators is that the matrix in  $\mathcal{S}$  is the inverse of the propagator matrix eq. (A.34). This gives the following set of equations for the components in  $\mathcal{S}$

$$\begin{aligned}
 &\int d\tau \begin{pmatrix} G^K & G^R \\ G^A & 0 \end{pmatrix}_{(t\tau)} \begin{pmatrix} (G^{-1})^a & (G^{-1})^b \\ (G^{-1})^c & (G^{-1})^d \end{pmatrix}_{(\tau t')} \\
 &= \int d\tau \begin{pmatrix} G_{t\tau}^K (G^{-1})_{\tau t'}^a + G_{t\tau}^R (G^{-1})_{\tau t'}^c & G_{t\tau}^K (G^{-1})_{\tau t'}^b + G_{t\tau}^R (G^{-1})_{\tau t'}^d \\ G_{t\tau}^A (G^{-1})_{\tau t'}^a & G_{t\tau}^A (G^{-1})_{\tau t'}^b \end{pmatrix} \\
 &= \begin{pmatrix} 1 & 0 \\ 0 & 1 \end{pmatrix} \delta(t - t').
 \end{aligned} \tag{A.36}$$

Solving these equations, one finds a continuum form of  $\mathcal{S}$  that reproduces the discrete

propagators

$$\begin{aligned} & \begin{pmatrix} (G^{-1})^a & (G^{-1})^b \\ (G^{-1})^c & (G^{-1})^d \end{pmatrix}_{(tt')} = \begin{pmatrix} 0 & (G^A)^{-1} \\ (G^R)^{-1} & (G^{-1})^K \end{pmatrix}_{(tt')} \\ \rightarrow \mathcal{S} &= \int_{-\infty}^{\infty} i \begin{pmatrix} \bar{\phi}^c & \bar{\phi}^q \end{pmatrix}_t \begin{pmatrix} 0 & (G^A)^{-1} \\ (G^R)^{-1} & (G^{-1})^K \end{pmatrix}_{(tt')} \begin{pmatrix} \phi^c \\ \phi^q \end{pmatrix}_{t'} dt dt'. \end{aligned} \quad (\text{A.37})$$

The off-diagonal elements are the inverse' of the propagators, while the diagonal element is determined by the relation

$$\begin{aligned} & \int G_{(t\tau)}^K (G^A)^{-1}_{(\tau t')} + G_{(t\tau)}^R (G^{-1})^K_{(\tau t')} d\tau = 0, \\ \rightarrow (G^{-1})^K_{(\tau' t')} &= - \int (G^R)^{-1}_{(\tau' t)} G_{(t\tau)}^K (G^A)^{-1}_{(\tau t')} dt d\tau = -(G^R)^{-1} \circ G^K \circ (G^A)^{-1}. \end{aligned} \quad (\text{A.38})$$

The  $\circ$  is a shorthand notation for a continuum form of matrix multiplication overall degrees of freedom.

For a free theory in the steady state, the propagators will not depend on the specific times but only on the time difference  $t - t'$ . In that case, it is much easier to invert matrices in the frequency domain as one can do a Fourier transform of the variable  $t - t'$ . A free theory is pathological because the system has no mechanism through which it can relax. To avoid this problem, one can put in a relaxation mechanism by hand by defining the Fourier transform, and its inverse as [39]

$$f(\omega) = \int_{-\infty}^{\infty} e^{it(\omega \pm i\eta)} f(t) dt, \quad f(t) = \lim_{\eta \rightarrow 0^+} \frac{1}{2\pi} \int_{-\infty}^{\infty} e^{-i\omega t} f(\omega) d\omega, \quad (\text{A.39})$$

where a positive infinitesimal part ( $\eta$ ) has been added to the energy as an imaginary contribution with the appropriate signs. This suppresses perpetual oscillations at  $\pm\infty$ . Whether to use  $+/-$  depends on which part of the time axis the non-physical correlations are present. For this trick to make sense, it is important that any physical observable one computes should be essentially unaffected by this small infinitesimal value. For numerical calculations, it is often necessary to include it, and then one has to check that the value one uses for the infinitesimal decay is not altering the physics observed. To keep  $\eta$ 's infinitesimal nature in mind, we will write it as  $0^+$ . With this extension, the energy



representations of the propagators are well-defined and given by

$$\begin{aligned}
 G^K(\omega) &= -iF(\omega) \int_{-\infty}^{\infty} e^{it(\omega-\omega_0)} dt = -2\pi iF(\omega)\delta(\omega - \omega_0), \\
 G^R(\omega) &= -i \int_{-\infty}^{\infty} \theta(t)e^{it(\omega-\omega_0+i0^+)} = \frac{1}{\omega - \omega_0 + i0^+}, \\
 G^A(\omega) &= i \int_{-\infty}^{\infty} \theta(-t)e^{it(\omega-\omega_0-i0^+)} = \frac{1}{\omega - \omega_0 - i0^+}.
 \end{aligned} \tag{A.40}$$

where  $F(\omega) = \coth\left(\frac{\beta(\omega-\mu)}{2}\right)$  for bosons and  $F(\omega) = \tanh\left(\frac{\beta(\omega-\mu)}{2}\right)$  for fermions. Using these propagators, the inverse Keldysh propagator can now be derived using eq. (A.38)

$$\begin{aligned}
 (G^{-1})^K(\omega) &= -(G^R(\omega)^{-1} \circ G^K(\omega) \circ (G^A(\omega))^{-1}) \\
 &= (\omega - \omega_0 + i0^+)i2\pi F(\omega)\delta(\omega - \omega_0)(\omega - \omega_0 - i0^+) \\
 &= i2\pi F(\omega) \frac{1}{\pi} \frac{0^+}{(\omega - \omega_0)^2 + (0^+)^2} [(\omega - \omega_0)^2 + (0^+)^2] \\
 &= i20^+ F(\omega).
 \end{aligned} \tag{A.41}$$

On the second line, it has been used that  $0^+$  is a positive infinitesimal, and an infinitely narrow Lorentzian can thus represent the delta function. The result is that in a free theory, the inverse Keldysh propagator is an infinitesimal quantity.

# Appendix B

## Kramers-Kronig relation for the retarded propagator

A retarded propagator is any propagator that has the form  $G(t) \propto \theta(t)$ . The Fourier transform takes the form

$$G(\omega) = \int_{-\infty}^{\infty} dt e^{i\omega t} G(t) = \int_0^{\infty} dt e^{i\omega t} G(t). \quad (\text{B.1})$$

To ensure that the Fourier transform is well defined, an infinitesimal decay can be added

$$G(\omega) = \lim_{\eta \rightarrow 0^+} \int_0^{\infty} dt e^{i(\omega+i\eta)t} G(t). \quad (\text{B.2})$$

Using the inverse transform, this takes the form

$$\begin{aligned} G(\omega) &= \lim_{\eta \rightarrow 0^+} \int_0^{\infty} dt e^{i(\omega+i\eta)t} \int \frac{d\epsilon}{2\pi} e^{-i\epsilon t} G(\epsilon) = i \int \frac{d\epsilon}{2\pi} \frac{G(\epsilon)}{\omega - \epsilon + i\eta} \\ &= i \int \frac{d\epsilon}{2\pi} \frac{-i\eta G(\epsilon)}{(\omega - \epsilon)^2 + \eta^2} + \frac{(\omega - \epsilon) G(\epsilon)}{(\omega - \epsilon)^2 + \eta^2} \end{aligned} \quad (\text{B.3})$$

Taking the limit of  $\eta \rightarrow 0^+$ , the second term is seen to be a nascent delta function [155]. When the limit is taken, the first term turns into a principal value of  $G(\omega)$ . This is seen by considering the fraction with  $\eta$  in the denominator in two limits. First  $(\omega - \epsilon)^2 \gg \eta^2$  and secondly  $(\omega - \epsilon)^2 \ll \eta^2$ . For the first case, this fraction is unity, and for the second case, it is zero as  $(\omega - \epsilon)^2 / \eta^2 \rightarrow 0$  in this limit. This means that one integrates  $G(\omega)/(\omega - \epsilon)$  until one is infinitesimally close to the singularity, which is then "ignored". Lastly, it is seen to be a principal value integral because the singularity limit is approached symmetrically.

The general form of the result is

$$\lim_{\eta \rightarrow 0^+} \int_0^\infty \frac{f(\omega)}{\omega \pm \epsilon + i\eta} d\omega = \mp i\pi \int_0^\infty \delta(\omega \pm \epsilon) f(\omega) d\omega + \mathcal{P} \int_0^\infty \frac{f(\omega)}{\omega \pm \epsilon} d\omega, \quad (\text{B.4})$$

where  $\mathcal{P}$  denotes the principal value. The solution can also be proven with a contour integral [39, 238] in a similar fashion as the integration in appendix B.2.

The propagator is then given by

$$G(\omega) = \frac{G(\omega)}{2} + \mathcal{P} \int \frac{d\omega}{2\pi} \frac{iG(\epsilon)}{\omega - \epsilon} = \mathcal{P} \int \frac{d\omega}{\pi} \frac{iG(\epsilon)}{\omega - \epsilon}. \quad (\text{B.5})$$

The last step is to split the propagator into its real and imaginary parts

$$\text{Re } G(\omega) + i \text{Im } G(\omega) = -\mathcal{P} \int \frac{d\omega}{\pi} \frac{\text{Im } G(\epsilon)}{\omega - \epsilon} + i\mathcal{P} \int \frac{d\omega}{\pi} \frac{\text{Re } G(\epsilon)}{\omega - \epsilon}. \quad (\text{B.6})$$

Comparing real and imaginary parts, one arrives at the Kramers-Kronig relations in eqs. (2.63) and (2.64). The form of the principle value integral with a simple pole in the denominator is known as the Hilbert transform.

## B.1 Derivative relation

Consider a retarded propagator that is explicitly split into real and imaginary parts

$$G(\omega) = \sigma(\omega) + i\gamma(\omega). \quad (\text{B.7})$$

Using the Kramers-Kronig relations, the derivative of the real part can be rewritten as a derivative of the principal value integral of the imaginary part

$$\partial_\omega \sigma(\omega) = \partial_\omega \mathcal{P} \int \frac{d\epsilon}{\pi} \frac{\gamma(\epsilon)}{\epsilon - \omega} = \partial_\omega \lim_{\eta \rightarrow 0^+} \left( \int_{-\infty}^{\omega-\eta} \frac{d\epsilon}{\pi} \frac{\gamma(\epsilon)}{\epsilon - \omega} + \int_{\omega+\eta}^{\infty} \frac{d\epsilon}{\pi} \frac{\gamma(\epsilon)}{\epsilon - \omega} \right) \quad (\text{B.8})$$

As the integral limits contain  $\omega$ , one has to use the general form for integrating under the integral

$$\partial_\omega \int_{a(\omega)}^{b(\omega)} f(\omega, \epsilon) d\epsilon = f(\omega, b(\omega)) \partial_\omega b(\omega) - f(\omega, a(\omega)) \partial_\omega a(\omega) + \int_{a(\omega)}^{b(\omega)} \partial_\omega f(\omega, \epsilon) d\epsilon. \quad (\text{B.9})$$

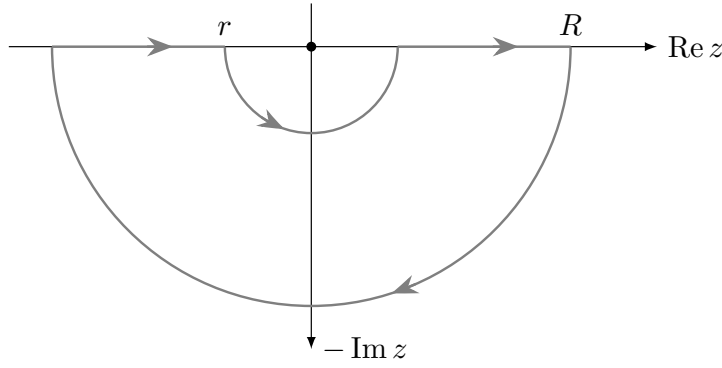


Figure B.1: *Contour choice for performing the principal value integral.*

Doing this for both terms gives

$$\begin{aligned} \partial_\omega \sigma(\omega) = \lim_{\eta \rightarrow 0^+} & \left( \frac{\gamma(\omega - \eta)}{\pi\eta} - \int_{-\infty}^{\omega - \eta} \frac{d\epsilon}{\pi} \frac{\gamma(\epsilon)}{(\epsilon - \omega)^2} \right. \\ & \left. - \frac{\gamma(\omega + \eta)}{-\pi\eta} - \int_{\omega + \eta}^{\infty} \frac{d\epsilon}{\pi} \frac{\gamma(\epsilon)}{(\epsilon - \omega)^2} \right). \end{aligned} \quad (\text{B.10})$$

The integrals can be put back together into a principal value

$$\partial_\omega \sigma(\omega) = \lim_{\eta \rightarrow 0^+} \left( \frac{\gamma(\omega + \eta) + \gamma(\omega - \eta)}{\pi\eta} \right) - \mathcal{P} \int_{-\infty}^{\infty} \frac{d\epsilon}{\pi} \frac{\gamma(\epsilon)}{(\epsilon - \omega)^2}. \quad (\text{B.11})$$

At first glance, the constant seems to diverge but consider the integral

$$\begin{aligned} \mathcal{P} \int \frac{d\epsilon}{\pi} \frac{1}{(\epsilon - \omega)^2} &= \lim_{\eta \rightarrow 0^+} \left( \int_{-\infty}^{\omega - \eta} \frac{d\epsilon}{\pi} \frac{1}{(\epsilon - \omega)^2} + \int_{\omega + \eta}^{\infty} \frac{d\epsilon}{\pi} \frac{1}{(\epsilon - \omega)^2} \right) \\ &= \lim_{\eta \rightarrow 0^+} \left( \int_{-\infty}^{-\eta} \frac{d\epsilon}{\pi} \frac{1}{u^2} + \int_{\eta}^{\infty} \frac{d\epsilon}{\pi} \frac{1}{u^2} \right) \\ &= \lim_{\eta \rightarrow 0^+} \left( - \left[ \frac{1}{\pi u} \right]_{-\infty}^{-\eta} - \left[ \frac{1}{\pi u} \right]_{\eta}^{\infty} \right) \\ &= \lim_{\eta \rightarrow 0^+} \left( \frac{2}{\pi\eta} \right). \end{aligned} \quad (\text{B.12})$$

As long as  $\gamma$  is analytic, this means that the derivative of the real part is given by

$$\partial_\omega \sigma(\omega) = \mathcal{P} \int_{-\infty}^{\infty} \frac{d\epsilon}{\pi} \frac{\gamma(\omega) - \gamma(\epsilon)}{(\epsilon - \omega)^2}. \quad (\text{B.13})$$

## B.2 Relation to Fourier transform

As a last property of the Kramers-Kronig relations, we discuss the relation to the Fourier transform. The goal is to derive the Fourier transform of the Hilbert transform

$$g(t > 0) = \int \frac{d\omega}{2\pi} e^{-i\omega t} \mathcal{P} \int \frac{d\omega'}{\pi} \frac{f(\omega')}{\omega - \omega'}. \quad (\text{B.14})$$

As both integrals convergence in the sense of the principal value, the order of integration can be exchanged

$$g(t > 0) = \int \frac{d\omega'}{\pi} f(\omega') \mathcal{P} \int \frac{d\omega}{2\pi} \frac{e^{-i\omega t}}{\omega - \omega'} = \int \frac{d\omega'}{2\pi^2} f(\omega') e^{-it\omega'} \mathcal{P} \int \frac{d\omega}{\omega} \frac{e^{-i\omega t}}{\omega}. \quad (\text{B.15})$$

The principal value integral can then be performed along the contour shown in fig. B.1. The large semicircle integral vanishes

$$\lim_{R \rightarrow \infty} \int_0^{-\pi} d\phi \frac{iR e^{i\phi - it \cos \phi} e^{t \sin \phi}}{R e^{i\phi}} \rightarrow 0. \quad (\text{B.16})$$

For the small semicircle, we can Laurent expand the fraction around  $z = 0$ . As the exponential factor is analytic, there is only the simple pole from the denominator

$$\frac{e^{-itz}}{z} = \frac{1}{z} + a_0 + a_1 z + \dots \quad (\text{B.17})$$

Inserting this expansion into the small semicircle integral

$$\lim_{r \rightarrow 0} \int_{-\pi}^0 d\phi i (1 + a_0 r e^{i\phi} + a_1 r^2 e^{i2\phi} \dots) = i\pi. \quad (\text{B.18})$$

As there are no poles inside the contour, the result is that

$$\mathcal{P} \int \frac{d\omega}{\omega} \frac{e^{-i\omega t}}{\omega} = -i\pi. \quad (\text{B.19})$$

Inserting this into the integral, we find

$$g(t > 0) = -i \int \frac{d\omega}{2\pi} f(\omega) e^{-i\omega t} = -i \mathcal{F}^{-1} \{f(\omega)\} (t). \quad (\text{B.20})$$

This shows that the Fourier transforming the Hilbert transform only gives rise to multiplication by a phase of  $e^{i\pi}$ .

# Appendix C

## Lehmann representation of contour propagators

In this appendix, the Lehmann representation of the steady-state diagonal part of the contour propagators and the spectral function are derived. The interacting system is assumed to be closed such that it can be described by the Hamiltonian  $H$ , which is formally diagonalized by the eigenvectors  $H|\alpha\rangle = E_\alpha|\alpha\rangle$ . The state of the system is described by the density matrix, which is assumed to be diagonal in Hamiltonian eigenbasis  $\rho = \sum_\alpha c(E_\alpha)|\alpha\rangle\langle\alpha|$ . The key idea of the Lehmann representation is that the eigenbasis of the Hamiltonian constitutes a complete basis, and one can therefore insert identities of this basis. As the Hamiltonian is time independent and diagonal in this basis, the eigenvalues of the time evolution operator are known through the spectral decomposition of  $U^\dagger(t) = e^{iHt}$ . As discussed in the main text, the Lehmann representation allows us to derive some generic properties for the propagators. These generic properties are strictly speaking only valid for closed systems in equilibrium, but it is seen that properties of interest are a consequence of the statics of the excitation, which is unchanged by going beyond those assumptions.

As we are focusing on a situation where  $G^R$  and  $G^K$  commute, it is sufficient to consider just a single mode, described by the bare annihilation operator  $a$ .

The first propagator considered is the retarded propagator, which is given by eq. (2.37)

$$\begin{aligned} G^R(t, t') &= -i\theta(t - t') \left\langle [a(t), a^\dagger(t')]_{\mp} \right\rangle \\ &= -i\theta(t - t') \text{Tr} (\rho U^\dagger(t) a U(t) U^\dagger(t') a^\dagger U(t') \mp \rho U^\dagger(t') a^\dagger U(t') U^\dagger(t) a U(t)). \end{aligned} \tag{C.1}$$

Inserting an identity resolution and writing out the trace and the density matrix, the

retarded propagator takes the form

$$\begin{aligned}
G^R(t, t') &= -i\theta(t - t') \sum_{\beta, \alpha} \left( c(E_\beta) e^{it(E_\beta - E_\alpha)} \langle \beta | a | \alpha \rangle \langle \alpha | a^\dagger | \beta \rangle e^{-it'(E_\beta - E_\alpha)} \right. \\
&\quad \left. \mp c(E_\beta) e^{it'(E_\beta - E_\alpha)} \langle \beta | a^\dagger | \alpha \rangle \langle \alpha | a | \beta \rangle e^{-it(E_\beta - E_\alpha)} \right) \quad (\text{C.2}) \\
&= -i\theta(t - t') \sum_{\alpha, \beta} e^{i(t-t')(E_\beta - E_\alpha)} |\langle \alpha | a^\dagger | \beta \rangle|^2 (c(E_\beta) \mp c(E_\alpha)).
\end{aligned}$$

Next, we Fourier transform from relative time to frequency

$$\begin{aligned}
G^R(\omega) &= -i \lim_{\eta \rightarrow 0^+} \int_0^\infty d\tau \sum_{\alpha, \beta} e^{i\tau(\omega + E_\beta - E_\alpha + i\eta)} |\langle \alpha | a^\dagger | \beta \rangle|^2 (c(E_\beta) \mp c(E_\alpha)) \\
&= - \lim_{\eta \rightarrow 0^+} \sum_{\alpha, \beta} \frac{|\langle \alpha | a^\dagger | \beta \rangle|^2 (c(E_\beta) \mp c(E_\alpha))}{\omega + E_\beta - E_\alpha + i\eta}. \quad (\text{C.3})
\end{aligned}$$

The spectral function is equal to twice the negative imaginary part of the retarded propagator. In the limit of  $\eta \rightarrow 0^+$  the Lorentzian turns into a  $\delta$ -functions as discussed in eq. (B.4)

$$\begin{aligned}
A(\omega) &= -2 \text{Im} G^R(\omega) \\
&= 2\pi \sum_{\alpha, \beta} |\langle \alpha | a^\dagger | \beta \rangle|^2 (c(E_\beta) \mp c(E_\alpha)) \delta(\omega + E_\beta - E_\alpha). \quad (\text{C.4})
\end{aligned}$$

The Lehmann representation of the Keldysh propagator is defined in eq. (2.38), and is the opposite commutator as for the retarded propagator and without the Heaviside function. This means that the form is similar to eq. (C.2)

$$G^K(t - t') = -i \sum_{\alpha, \beta} e^{i(t-t')(E_\beta - E_\alpha)} |\langle \alpha | a^\dagger | \beta \rangle|^2 (c(E_\beta) \pm c(E_\alpha)), \quad (\text{C.5})$$

which can directly be Fourier transformed

$$G^K(\omega) = -i \sum_{\alpha, \beta} |\langle \alpha | a^\dagger | \beta \rangle|^2 (c(E_\beta) \pm c(E_\alpha)) \delta(\omega + E_\beta - E_\alpha). \quad (\text{C.6})$$

This is seen to be sign-changing for fermions which is due to the vacuum contribution included in  $G^K$ . Separating the vacuum contribution as in eq. (2.82)

$$\begin{aligned}
\delta G^K(\omega) &= G^K(\omega) + iA(\omega) \\
&= \mp i \sum_{\alpha, \beta} 2c(E_\alpha) |\langle \alpha | a^\dagger | \beta \rangle|^2 \delta(\omega + E_\beta - E_\alpha). \quad (\text{C.7})
\end{aligned}$$

# Appendix D

## Contour configurations of diagrams: An algorithm

In this appendix, we will discuss an algorithm to generate all the different Keldysh variations of a specific diagram. We will discuss how the causality structure and different approximations drastically reduce the number of finite diagrams. The starting point is  $N_v$  vertices of a given type  $N_p$  propagators connecting the different vertices. These are then connected, which gives rise to the specific topology for which we want to find all the different contour variations. As an example, consider the same diagram as discussed in the main text, repeated in fig. D.1 for convenience.

To efficiently represent the diagrams mathematically, the standard methods from graph theory are the adjacency matrix, and the incidence matrix [239]. The adjacency matrix is a  $N_v \times N_v$  matrix. The  $i, j$  element of the adjacency matrix is one if the  $i$ th, and  $j$ th vertex are connected to each other and zero otherwise. The incidence matrix ( $\mathcal{I}$ ) is a  $N_v \times N_p$  matrix where the element  $\mathcal{I}_{ij}$  is 1 if the  $j$ th propagator attaches to the  $i$ th and its arrow points towards the vertex. If the arrow points away from the vertex, the element is -1. This means that each column of the incidence matrix sums to 0. Our goal is to describe the contour structure of a diagram. We do that by determining if a propagator is of the retarded, advanced, or Keldysh type, which is determined by the type of the ingoing and outgoing legs (quantum or classical). This information is encoded in the incidence matrix because it describes each propagator as having an incoming and an outgoing part. The only necessary addition to the incidence matrix is to distinguish between quantum and classical fields. Diagrams can contain propagators that start and end at the same vertex, giving rise to a closed loop consisting of one propagator. If the propagator in the loop is a retarded propagator, then it will cancel against the same diagram with an advanced propagator due to eq. (2.40). In these cases, the only non-zero diagrams are when the Keldysh propagator is in the loop. A keldysh loop can be included in the algorithm by



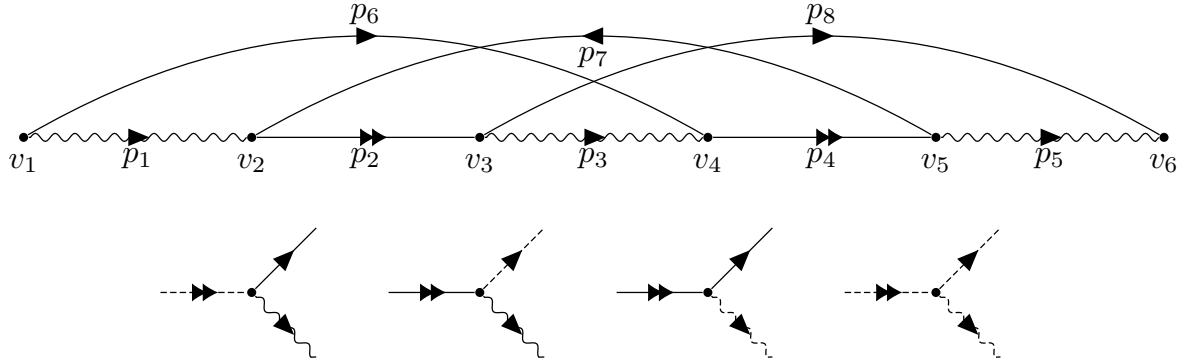


Figure D.1: A repetition of fig. 2.5 for convenience. The topology of a diagram for interaction between three different types of fields (differentiated by the arrow and line type) contributing to the self-energy. It consists of six vertices, each labeled by  $v_i$  and eight propagators labeled by  $p_i$ . Below the diagram is the four possible types of vertex structures arising from the contour degree of freedom. Due to causality, a configuration with only classical legs is impossible.

constricting the possible configurations for the vertex with the loop, similarly to how the end vertices' configurations will be constrained. Having discussed how to deal with loops consisting of single propagators, we will continue the discussion of diagrams without such loops.

To illustrate how the incidence matrix looks, consider the example diagram in fig. D.1. Here the incidence matrix takes the form

$$\mathcal{I} = \begin{pmatrix} -1 & 0 & 0 & 0 & 0 & -1 & 0 & 0 \\ 1 & -1 & 0 & 0 & 0 & 0 & 1 & 0 \\ 0 & 1 & -1 & 0 & 0 & 0 & 0 & -1 \\ 0 & 0 & 1 & -1 & 0 & 1 & 0 & 0 \\ 0 & 0 & 0 & 1 & -1 & 0 & -1 & 0 \\ 0 & 0 & 0 & 0 & 1 & 0 & 0 & 1 \end{pmatrix}. \quad (\text{D.1})$$

The  $i$ th row corresponds to the vertex  $v_i$  and the  $j$ th column corresponds to the  $p_j$ th propagator. As an example consider the vertex  $v_3$ . This is contained in the third row. The third row has a +1 for the second column because the  $p_2$  propagator is incident on this vertex and a -1 for the propagators  $p_3$  and  $p_8$ .

Next, we need to include a degree of freedom to distinguish between quantum and classical fields. One way of doing this is by making the incidence matrix complex and let real numbers represent classical fields and imaginary numbers quantum ones. To generate all possible structures, we first define an array  $V_c$  of length  $N_v$  containing all possible configurations for each vertex. It is not necessary to distinguish between in and

outgoing fields here because this is included in  $\mathcal{I}$ . In this way, the algorithm has no assumption about the form of each vertex, and we have a direct way of incorporating constraints. The constraints can be incorporated by limiting the possible configurations of the specific vertices in the diagram. For the diagram in fig. D.1 the internal vertices have four different configurations such that the entries for  $j_{\text{int}} \in \{2, \dots, 5\}$  in  $V_c$  are all given by

$$V_{c,j_{\text{int}}} = \begin{pmatrix} i & 1 & 1 \\ 1 & i & 1 \\ 1 & 1 & i \\ i & i & i \end{pmatrix}. \quad (\text{D.2})$$

Each row represents a different configuration, and each column represents a specific leg of the vertex. The two end vertices must be constrained because we want to separately compute the contribution to the retarded, advanced, and Keldysh self-energy.

As discussed in section 2.7, the self-energy diagram in fig. D.1 is a self-energy contribution to the double arrow (D) field. For the retarded self-energy  $\Sigma^R$ , we need the D leg of  $v_1$  to be classical, while for  $v_6$  we need the D leg to be a quantum field. This means that there is only a subset of allowed configurations for these two vertices, and they are effectively only two-legged. These two elements of  $V_c$  are therefore

$$V_{c,1} = \begin{pmatrix} i & 1 \\ 1 & i \end{pmatrix}, \quad V_{c,6} = \begin{pmatrix} 1 & 1 \\ i & i \end{pmatrix}. \quad (\text{D.3})$$

As alluded to previously, this is the same way one would deal with a diagram containing a propagator looping back to its initial vertex. For  $\Sigma^K$ , then both D legs at the ends of the diagram have to be quantum fields. In that case  $V_{c,1}$  would have the same possible configurations as  $V_{c,6}$ .

Now we need to build all possible configurations of the chosen diagram. This is done by looping over all possible combinations of the form

$$\mathcal{A}_j = \left( n_1, n_2, \dots, n_{N_v} \right), \quad (\text{D.4})$$

where each  $n_i$  takes on a single integer value from 1 up to the number of rows in  $V_{c,i}$ . Each vector  $\mathcal{A}_j$  then describes which vertex configurations the  $j$ th Keldysh configuration of the diagram has. For the considered diagram, this leads to

$$N_{D_0} = 2 \cdot 4 \cdot 4 \cdot 4 \cdot 4 \cdot 2 = 2^{10} = 1024, \quad (\text{D.5})$$

different combinations which makes  $\mathcal{A}$  in eq. (D.4) a matrix of dimension  $N_{D_0} \times N_v =$

$1024 \times 6$ . For each of the  $N_{D_0}$  combinations (each represented by a row in  $\mathcal{A}$ ), we then construct the sparse complex incidence matrix  $\mathcal{D}_i$ , which represents the  $i$ th configuration of the diagram. The  $i$ th row of  $\mathcal{A}$  generates  $\mathcal{D}_i$  by elementwise multiplication of the non-zero values in  $\mathcal{I}_j$  with  $V_{c,j,n_j}$ . This works because the number of non-zero values in  $\mathcal{I}_j$  is equivalent to the number of links in the vertex  $v_j$ . The direction is contained in the sign of  $\mathcal{I}_j$ , and the type of field is contained by the configuration  $V_{c,j,n_j}$  which picks the  $n_j$  configuration of the  $j$ th vertex. One now has  $N_{D_0}$  different complex incidence matrices, which can be efficiently sorted.

The first step in sorting the diagrams is that any configuration that contains a quantum-quantum propagator vanishes. In our matrix representation, these propagators are identified by both input and output legs being imaginary. Therefore, a diagram  $\mathcal{D}_j$  containing a q-q propagator can be identified by having at least one value of 2 in  $j$ th row of the matrix defined by

$$F_{qq,j;m} = \sum_n |\text{Im}\mathcal{D}_j|_{n,m}, \quad (\text{D.6})$$

where  $\text{Im}$  is the imaginary value and  $|\cdot|$  is the absolute value. Discarding all these diagrams drastically decreases the number of potentially relevant diagrams. For the considered example, the number of diagrams decreases from 1024 to 84.

After removing all q-q propagators, we consider the vacuum contribution in the Keldysh propagators. This vacuum contribution can cancel against other diagrams. Separating the vacuum is also useful because replacing  $G^K$  with  $\delta G^K$  generally makes the physical interpretation of the diagram significantly simpler and gives a good basis for further approximations. Analogous to the q-q case, a diagram that contains one or more Keldysh propagators will have two classical legs. They can therefore be identified by having at least one entry with value 2 in the  $j$ th row of

$$F_{cc,j;m} = \sum_n |\text{Re}\mathcal{D}_j|_{n,m}. \quad (\text{D.7})$$

Consequently, the diagrams can be split into two types: those containing a Keldysh propagator, which we define as  $\mathcal{D}_{K,j}$ , and the remaining ones  $\mathcal{D}_j$ .

For all the  $\mathcal{D}_{K,j}$  diagrams, one can now substitute each Keldysh propagator according to eq. (2.82). Notice that by inspecting each diagram, one will see that, effectively, new vertex configurations have emerged due to the separation of the vacuum contribution. To do the substitution successfully, one has to include one new degree of freedom to account for the fact that the diagrams now can acquire an overall negative sign. As the sign is already used to define direction, we introduce a variable called *minus*.

The separation of  $G_K$ 's can be done iteratively for diagrams with several Keldysh

propagators, and all the diagrams can then be sorted into two groups:  $\mathcal{D}_j^+$  which contain all diagrams (also those in  $\mathcal{D}_j$ ) where one can extract a prefactor of  $minus^{2n}$ , with  $n \in \{0, 1, 2, \dots\}$ , and  $\mathcal{D}_j^-$  where one can extract a prefactor of an odd power of  $minus$ . Any diagram that both appear in  $\mathcal{D}^+$  and  $\mathcal{D}^-$  then cancels. For the specific example in section 2.7, writing out the vacuums has increased the total number of non-zero diagrams from 84 to 236 with a positive prefactor and 152 diagrams with a negative prefactor.

One last generic feature that can lead to diagrams vanishing is the causal structure of the propagators, which means that combinations like  $G^R(t, t')G^A(t, t')$  vanishes. These cancellations only rely on the Heaviside dependence of  $G^R$  and  $G^A$  on relative time ( $\tau = t - t'$ ). To identify these cancellations for complicated diagrams, one has to consider the internal propagators' relative time arguments. The diagrams are usually written in the absolute energy  $\omega$  domain (Fourier transform of relative time) as done in eq. (2.62). It is, therefore, necessary to transform back to relative times to identify the causality cancellations. For diagrams with vertex strengths constant in relative time, we get conservation of the absolute energy at each vertex. To explain how this allows us to implement the causality, we consider the specific example in fig. D.1. Here the Fourier transform back to relative time leads to three  $\delta$ -functions because of the three closed loops. The  $\delta$ -functions can be used to constrain the relative time argument of three of the propagators, and we are left with  $N_{free} = 5$  free relative time variables. For the considered example we let the D and W (wavy) propagators in the diagram have free relative time variables such that  $p_{i_f}(\tau_{i_f})$  for  $i_f \in \{1, \dots, 5\}$ . The relative time dependence of the three S (straight) propagators can then be written in the form  $p_{i_c}(\sum_{i_f} \mathcal{B}_{i_c, i_f} \tau_{i_f})$ , where  $i_c$  only runs over propagators with constrained relative time index

$$p_6(\tau_1 + \tau_2 + \tau_3), p_7(-\tau_2 - \tau_3 - \tau_4), p_8(\tau_3 + \tau_4 + \tau_5). \quad (\text{D.8})$$

From which the elements of  $\mathcal{B}$  can be directly read off. For a diagram to vanish due to causality, it is then necessary to combine the first five propagators so that the product of at least one of the three S propagators vanishes. To make these constraints computationally efficient, we define the vector  $\tau_{free}$  which has the indices of the propagators that have free variables as their relative time index, which for the considered example gives

$$\tau_{free} = (1, 2, 3, 4, 5)^T. \quad (\text{D.9})$$

Together with the array  $\mathcal{B}$ ,  $\tau_{free}$  fully defines our constraints. To do this, we investigate each diagram in both  $\mathcal{D}^+$  and  $\mathcal{D}^-$  independently. For a specific diagram in  $\mathcal{D}^+$  or  $\mathcal{D}^-$  we know that a retarded (advanced) propagator is only non-zero if its relative time index is  $> 0$  ( $< 0$ ). So we first consider all the constrained propagators, which are directly given

the similar label columns of the complex matrix  $\mathcal{D}_j^\pm$ . The  $j$ th component of

$$F_{cp,j;i_c} = \sum_m (\text{Re}\mathcal{D}_j^\pm)_{m,i_c}, \quad (\text{D.10})$$

will then have a +1 when the propagator is retarded, a -1 for an advanced propagator, and for a Keldysh propagator, it will be zero. This means that if  $F_{cp,j;i_c} = +/- -1$  then the  $i_c$ th propagator in  $j$ th diagram is a retarded/advanced propagator. It is only non-zero when its relative time argument  $\tau_{i_c} = \sum_{i_f} \mathcal{B}_{i_c,i_f} \tau_{i_f} > / < 0$ . If  $F_{cp,j;i_c} = 0$  then the  $i_c$ th propagator in  $j$ th diagram is a  $\delta G^K$  propagator which can be non-zero for all values of  $\tau_{i_c}$ . We then do the same for the unconstrained propagators but also contract this with the signs of our constrained coefficients

$$F_{\mathcal{B},j;i_c} = \sum_{m,i_f} \text{sign}(\mathcal{B}_{i_c,i_f}) (\text{Re}\mathcal{D}_j^\pm)_{m,i_f}. \quad (\text{D.11})$$

$F_{\mathcal{B},j;i_c}$  is then equivalent to the  $\tau_{i_c}$  with the  $\tau_{i_f}$  being multiplied by +1, -1 or 0 depending on if the propagator  $p_{i_c}$  is retarded, advanced or Keldysh. For  $\tau_{i_c}$  to give rise to a vanishing diagram, it has to have a definite sign. This means that the only constrained times we can use are those where all  $\tau_{i_f}$ 's in the superposition belong to retarded or advanced propagators in such a way that when combined with the superposition coefficient,  $\mathcal{B}$ , the sum is always zero for either positive or negative times. This information is contained in  $F_{\mathcal{B},j;i_c}$  through its magnitude because for those definite constrained times the magnitude of  $F_{\mathcal{B},j;i_c}$  must equal the magnitude of  $\sum_{i_f} |\mathcal{B}_{i_c,i_f}|$ . We can therefore set all elements in  $F_{\mathcal{B},j;i_c}$  to zero that does not satisfy this equality and set the remaining components equal to just the sign of the element. After this procedure  $F_{\mathcal{B},j;i_c} = +/- -1$  means that  $\tau_{i_c} > / < 0$  for the  $i_c$ th propagator in the  $j$ th diagram. The condition for the  $j$ th diagram to vanish due to causality is that the condition

$$F_{cp,j;i_c} F_{\mathcal{B},j;i_c} > 0, \quad (\text{D.12})$$

is satisfied for at least one of the propagators (a specific value of  $i_c$ ). For the considered diagram, this takes us from 256 (152) to 134 (68) positive (negative) diagrams. This means that after removing all diagrams vanishing due to causality,  $\mathcal{D}$  has 220 entries left, each describing a contour variation of the diagram in fig. D.1. These all have to be calculated for a generic situation, but if certain parts of the system are not occupied, we can directly implement such an approximation by setting all  $\delta G^K$  propagators for this type equal to zero. Note that this is only possible because the vacuum contributions have been separated out. In the considered case, a physically realistic scenario is that the S

propagator represents a large medium that interacts with the impurity described by the  $W$  propagators. These attractive interactions can form a composite state described by the  $D$  propagator. If the system is in the impurity limit, the  $\delta G^K$  is zero for both the  $W$  and the  $D$  propagators. Using the same method as in eq. (D.7) to remove the diagrams with a Keldysh propagator for the  $D$  and  $W$  propagators, we are left with nine diagrams.

Our discussion has exemplified that diagrams with many internal propagators generally leads to an intractable amount of diagrams with different internal Keldysh configuration. However, many cancel due to the different aspects of the causal structure. To simplify this process, we have described an algorithm that does all the combinatorics when supplied with the boundary conditions. The boundary conditions consist of the incidence matrix for the diagram topology, the  $V_c$  array, and  $\mathcal{B}$ . Furthermore, we have seen that impurity limits are easy to implement in the algorithm and can significantly reduce the number of diagrams one needs to consider.

# Appendix E

## Stuart-Landau components

In this appendix, we will derive the three tensors needed for the Stuart-Landau equations in eq. (4.84). The equations of motion are the atom-number conserving equations on the center manifold in eq. (4.63). These are expanded and evaluated at the NP fixed point  $\mathbf{X}_0 = \mathbf{0}$ . The elimination of the homogeneous atom state means that factors  $\sqrt{2n_0}$  appear through eq. (4.62). To useful derivatives will therefore be

$$\frac{\partial}{\partial X_a} \sqrt{2n_0} = -\frac{X_a}{\sqrt{2n_0}}, \quad (\text{E.1})$$

and

$$\frac{\partial}{\partial X_a} \frac{1}{\sqrt{2n_0}} = \frac{X_a}{\sqrt{(2n_0)^{3/2}}}. \quad (\text{E.2})$$

The derivatives with respect to  $P_a$  are equivalent with the replacement  $X_a \rightarrow P_a$ . The first term is the Jacobian which is the linear term  $\nabla F(\mathbf{x})$ . The derivatives of the  $X_a$  component of  $F$  is

$$\begin{aligned} \frac{\partial F_{X_a}}{\partial X_a} &= -\kappa_a - \frac{P_a}{\sqrt{2n_0}} \sum_i \eta_i X_i - \frac{X_a^2 P_a}{(2n_0)^{3/2}} \sum_i \eta_i X_i, \\ \frac{\partial F_{X_a}}{\partial P_a} &= E_R - \frac{X_a}{\sqrt{2n_0}} \sum_i \eta_i X_i - \frac{X_a P_a^2}{(2n_0)^{3/2}} \sum_i \eta_i X_i, \\ \frac{\partial F_{X_a}}{\partial X_i} &= -\frac{X_a P_a \eta_i}{\sqrt{2n_0}}, \quad \frac{\partial F_{X_a}}{\partial P_i} = 0. \end{aligned} \quad (\text{E.3})$$

For the  $P_a$  component of  $F$ , the elements are

$$\begin{aligned}\frac{\partial F_{P_a}}{\partial X_a} &= -E_R + \frac{3X_a}{\sqrt{2n_0}} \sum_i \eta_i X_i + \frac{X_a^3}{(2n_0)^{3/2}} \sum_i \eta_i X_i, \\ \frac{\partial F_{P_a}}{\partial P_a} &= -\kappa_a + \frac{P_a}{\sqrt{2n_0}} \sum_i \eta_i X_i - \frac{X_a^2 P_a}{(2n_0)^{3/2}} \sum_i \eta_i X_i, \\ \frac{\partial F_{P_a}}{\partial X_i} &= \frac{X_a^2 \eta_i}{\sqrt{2n_0}} - \eta_i \sqrt{2n_0}, \quad \frac{\partial F_{P_a}}{\partial P_i} = 0.\end{aligned}\tag{E.4}$$

The cavity  $X_i$  component has the derivatives

$$\frac{\partial F_{X_i}}{\partial X_a} = \frac{\partial F_{X_i}}{\partial P_a} = 0, \quad \frac{\partial F_{X_i}}{\partial X_j} = -\delta_{i,j} \kappa_i, \quad \frac{\partial F_{X_i}}{\partial P_j} = \delta_{i,j} \Delta_i.\tag{E.5}$$

Lastly, the cavity  $P$ -quadrature components of gradient of  $F$  is

$$\begin{aligned}\frac{\partial F_{P_i}}{\partial X_a} &= -\eta_i \sqrt{2n_0} + \frac{X_a^2}{\sqrt{2n_0}}, \\ \frac{\partial F_{P_i}}{\partial P_a} &= \eta_i \frac{X_a P_a}{\sqrt{2n_0}}, \\ \frac{\partial F_{P_i}}{\partial X_j} &= -\delta_{i,j} \Delta_i, \quad \frac{\partial F_{P_i}}{\partial P_j} = -\delta_{i,j} \kappa_i.\end{aligned}\tag{E.6}$$

At the NP fixed point  $n_0 = 1$  and  $P_i = X_i = X_a = P_a = 0$ . The matrix form of the Jacobian, when only including the  $j$ th cavity block, is

$$\begin{pmatrix} -\kappa_j & \Delta_j & 0 & 0 \\ -\Delta_j & -\kappa_j & -\eta_j \sqrt{2} & 0 \\ 0 & 0 & -\kappa_a & E_R \\ -\eta_j \sqrt{2} & 0 & -E_R & -\kappa_a \end{pmatrix},\tag{E.7}$$

which is connected by the unitary transformation

$$U = \frac{1}{\sqrt{2}} \begin{pmatrix} 1 & i & 0 & 0 \\ 1 & -i & 0 & 0 \\ 0 & 0 & 1 & i \\ 0 & 0 & 1 & -i \end{pmatrix}\tag{E.8}$$

to the Jacobian in eq. (4.20). The Jacobian here generalizes to several modes in exactly the same way as eq. (4.20).



Next, we consider the quadratic non-linearity

$$M_{n,m}^i = \frac{1}{2} \frac{\partial^2 F_i}{\partial X_n \partial X_m} = \frac{\partial (\nabla F)_{i,n}}{\partial X_m}. \quad (\text{E.9})$$

As the derivatives can be exchanged  $M_{n,m}^i = M_{m,n}^i$ . Here we need the additional derivative

$$\frac{\partial}{\partial X} \frac{1}{(2n_0)^{3/2}} = 3 \frac{X}{(2n_0)^{5/2}}. \quad (\text{E.10})$$

First, we consider  $M_{n,m}^{x_a}$ , and to keep the indices more compact, we will use small  $x$  and  $p$  for the quadrature field indices.

$$\begin{aligned} M_{x_a, x_a}^{x_a} &= -\frac{3P_a X_a}{(2n_0)^{3/2}} \left(1 + \frac{X_a^2}{2n_0}\right) \sum_i \eta_i X_i, \\ M_{x_a, p_a}^{x_a} &= -\frac{1}{\sqrt{2n_0}} \left(1 + \frac{P_a^2}{2n_0}\right) \sum_i \eta_i X_i - \frac{X_a^2}{(2n_0)^{3/2}} \left(1 + 3\frac{P_a^2}{2n_0}\right) \sum_i \eta_i X_i, \\ M_{x_a, x_i}^{x_a} &= -\frac{\eta_i P_a}{\sqrt{2n_0}} \left(1 + \frac{X_a^2}{2n_0}\right), \\ M_{p_a, p_a}^{x_a} &= -\frac{P_a X_a}{(2n_0)^{3/2}} \left(2 + 3\frac{P_a^2}{2n_0}\right) \sum_i \eta_i X_i, \\ M_{x_i, p_a}^{x_a} &= -\frac{\eta_i X_a}{\sqrt{2n_0}} \left(1 + \frac{P_a^2}{2n_0}\right), \\ M_{x_a, p_i}^{x_a} &= M_{p_a, p_i}^{x_a} = M_{x_i, x_j}^{x_a} = M_{p_i, x_j}^{x_a} = M_{p_i, p_j}^{x_a} = 0. \end{aligned} \quad (\text{E.11})$$

All the elements are at least linear in a field from the center manifold, and all elements of  $M_{n,m}^{x_a}$ , therefore, vanish when evaluated at the NP fixed point. Next we consider  $M_{n,m}^{p_a}$

$$\begin{aligned} M_{x_a, x_a}^{p_a} &= \frac{1}{\sqrt{2n_0}} \left(3 + 4\frac{X_a^2}{2n_0} + 3\frac{X_a^4}{(2n_0)^2}\right) \sum_i \eta_i X_i, \\ M_{x_a, p_a}^{p_a} &= 3\frac{P_a X_a}{(2n_0)^{3/2}} \left(1 + \frac{X_a^2}{2n_0}\right) \sum_i \eta_i X_i, \\ M_{x_a, x_i}^{p_a} &= \frac{\eta_i X_a}{\sqrt{2n_0}} \left(3 + \frac{X_a^2}{2n_0}\right), \\ M_{p_a, p_a}^{p_a} &= \frac{1}{\sqrt{2n_0}} \left(\frac{X_a^2}{2n_0} + 3\frac{X_a^2 P_a^2}{(2n_0)^2} + 1 + \frac{P_a^2}{2n_0}\right) \sum_i \eta_i X_i, \\ M_{x_i, p_a}^{p_a} &= \frac{\eta_i P_a}{\sqrt{2n_0}} \left(1 + \frac{X_a^2}{2n_0}\right), \\ M_{x_a, p_i}^{p_a} &= M_{p_a, p_i}^{p_a} = M_{x_i, x_j}^{p_a} = M_{p_i, x_j}^{p_a} = M_{p_i, p_j}^{p_a} = 0. \end{aligned} \quad (\text{E.12})$$

Evaluated at the NP fixed point, all these elements again vanish. As  $(\nabla F)_{x_i, m}$  are all

constants  $M_{n,m}^{x_i} = 0$  for all values of  $n, m$ . The only remaining elements are  $M_{n,m}^{p_i}$ , which are given by

$$\begin{aligned}
M_{x_a, x_a}^{p_i} &= \frac{3\eta_i X_a}{\sqrt{2n_0}} \left( 1 + \frac{X_a^2}{2n_0} \right), \\
M_{x_a, p_a}^{p_i} &= \frac{\eta_i P_a}{\sqrt{2n_0}} \left( 1 + \frac{X_a^2}{2n_0} \right), \\
M_{p_a, p_a}^{p_i} &= \frac{\eta_i X_a}{\sqrt{2n_0}} \left( 1 + \frac{P_a^2}{2n_0} \right), \\
M_{x_a, p_j}^{p_i} &= M_{p_a, p_j}^{p_i} = M_{x_k, x_j}^{p_i} = M_{p_k, x_j}^{p_i} = M_{p_k, p_j}^{p_i} = M_{x_a, x_j}^{p_i} = M_{p_a, x_j}^{p_i} = 0.
\end{aligned} \tag{E.13}$$

Again all terms are at least linear in the center manifold fields, and all elements in  $M_{n,m}^i$ , therefore, vanish at the NP fixed point as expected from the reflection symmetry. The final tensor elements we have to contribute are the once in

$$N_{n,k,q}^i = \frac{1}{6!} \frac{\partial^3 F_i}{\partial X_n \partial X_k \partial X_q} = \frac{1}{3} \frac{\partial M_{n,k}^i}{\partial X_q}, \tag{E.14}$$

such that  $N_{n,k,q}^i$  is fully symmetric in subscripts. To have anything non-zero at the NP fixed point, the element of  $N_{n,k,q}^i$  can only depend on the center manifold fields through  $n_0$ . It is, therefore, sufficient to consider the terms of  $M_{n,m}^i$  that are linear in one of the fields (ignoring  $n_0$ ). These elements are

$$\begin{aligned}
M_{x_j, p_a}^{x_a} &= -\frac{X_a \eta_j}{2\sqrt{2n_0}}, & M_{x_j, x_a}^{x_a} &= -\frac{P_a \eta_j}{2\sqrt{2n_0}}, & M_{x_a, p_a}^{x_a} &= -\frac{\sum_j X_j \eta_j}{2\sqrt{2n_0}}, \\
M_{x_j, x_a}^{p_a} &= 3\frac{X_a \eta_j}{2\sqrt{2n_0}}, & M_{x_a, x_a}^{p_a} &= 3\frac{\sum_j X_j \eta_j}{2\sqrt{2n_0}}, & M_{p_a, p_a}^{p_a} &= \frac{\sum_j X_j \eta_j}{2\sqrt{2n_0}}, & M_{x_j, p_a}^{p_a} &= \frac{P_a \eta_j}{2\sqrt{2n_0}}, \\
M_{x_a, x_a}^{p_j} &= 3\frac{X_a \eta_j}{2\sqrt{2n_0}}, & M_{p_a, x_a}^{p_j} &= \frac{X_a \eta_j}{2\sqrt{2n_0}}, & M_{x_a, p_a}^{p_j} &= \frac{P_a \eta_j}{2\sqrt{2n_0}}.
\end{aligned} \tag{E.15}$$

Because of the symmetry, we only need to compute five elements of  $N_{n,k,q}^i$  as all others will either vanish at the NP fixed point or be a permutation of the subscripts. These five non-zero elements at the NP fixed point are

$$\begin{aligned}
N_{x_a, p_a, x_j}^{x_a} &= -\frac{\eta_j}{6\sqrt{2}}, & N_{x_a, x_a, x_j}^{p_a} &= \frac{\eta_j}{2\sqrt{2}}, & N_{p_a, p_a, x_j}^{p_a} &= \frac{\eta_j}{6\sqrt{2}}, \\
N_{x_a, x_a, x_a}^{p_j} &= \frac{\eta_j}{2\sqrt{2}}, & N_{x_a, p_a, p_a}^{p_j} &= \frac{\eta_j}{6\sqrt{2}}.
\end{aligned} \tag{E.16}$$

# Appendix F

## Spline interpolation

In this appendix, we derive the matrix form of the cubic and quintic spline interpolations.

### F.1 Cubic spline

The cubic spline is built of piecewise polynomials, with the highest order being a third-degree polynomial. Using the continuity conditions eq. (5.58) with  $k = 0$  directly gives an equation for the first order coefficients

$$a_j^1 = \frac{\Delta a_j^0}{\Delta \nu_j} - g_{1,j}, \quad (\text{F.1})$$

where  $g_{1,j}$  is defined as  $g_{1,j} = a_j^2 \Delta \nu_j + \frac{\Delta a_j^2}{3} \Delta \nu_j$ . This function is defined such that it only contains the second highest order coefficients and different node spacings. To eliminate  $a_j^1$  from the system we consider the continuity equation for  $k = 1$

$$\Delta a_j^1 = 2a_j^2 \Delta \nu_j + \Delta a_j^2 \Delta \nu_j. \quad (\text{F.2})$$

By applying the difference operator to eq. (F.1) we can equate it with eq. (F.2) and thereby arrive at a linear set of equations for  $a_j^2$

$$2a_j^2 \Delta \nu_j + \Delta a_j^2 \Delta \nu_j + \Delta g_{1,j} = \Delta \left[ \frac{\Delta a_j^0}{\Delta_j} \right]. \quad (\text{F.3})$$

As the third term on the left has a contribution where  $\Delta$  is applied twice, this leads to the  $j$ 'th coefficient coupling to  $j + 2$ . As the system is linear, it can be written using matrices

$$\mathbf{A} \vec{a}_2 = \mathbf{B} \vec{a}_0, \quad (\text{F.4})$$

where bold letters indicate matrices and the vectors of coefficients are indicated by the arrows. The continuity condition has therefore given rise to  $N - 3$  equations for the  $N - 1$   $a_j^2$  coefficients. This is a general feature of the spline interpolation, such that the equation system for the second highest coefficient always needs to be supplemented with  $M - 1$  boundary conditions. Which boundary to choose depends on the nature of the functions one is interpolating, but for our calculations, we are always attempting to choose grids where the function values are negligible at the grid boundaries. This makes the results independent of the specific choice of boundary conditions, and we, therefore, chose the most convenient boundary conditions. Currently our equations couple the  $j$ th to the  $j + M - 1$  component. One can instead write the equations for  $j + 1$ th coefficient, and the system of equations is then symmetric around  $n = j + 1$ . One can then use the boundary conditions to determine the undefined coefficients at both ends of the interval. Rewriting the equation system in eq. (F.3) for  $n = j + 1$  is unnecessary as it is very simple to implement the shift and boundary conditions on the matrix structure of the linear system. For convenience it is advantageous to use the continuity condition, eq. (5.59), to define the  $a_N^2$  coefficient. This allows one to work with quadratic matrices instead rectangular ones and also ensures the highest order coefficients are fully defined. Generating the internal part of the  $\mathbf{A}$  and  $\mathbf{B}$  matrices only requires the definition of one matrix, one vector, and a few standard numerical operations. As a starting point, one defines the  $(N, N)$  matrix representation of  $\Delta$ , which is a matrix ( $\mathbf{\Delta}$ ) with  $-1$  in the diagonal and  $+1$  in the band above the diagonal. The necessary vector is  $\vec{h} = \mathbf{\Delta}\vec{\nu}$ . This is nothing more than the vector  $\vec{\Delta}\vec{\nu}$  padded with one additional arbitrary element. The first operation one has to define is the cutting operation for matrices and vectors, which we here define as  $\mathbf{M}[n_r; ; -m_r, n_c; ; -m_c]$ . This is to be read as the matrix  $\mathbf{M}$  with the first  $n_r$  ( $n_c$ ) and the last  $m_r$  ( $m_c$ ) rows (columns) removed such that the dimension of  $\mathbf{M}[n_r; ; -m_r, n_c; ; -m_c]$  is  $N - n_r - m_r$ ,  $N - n_c - m_c$ . The next operation is a dimension independent version of the difference operator defined as  $\Delta[\mathbf{M}] = \mathbf{M}[:, ; -1] - \mathbf{M}[1; ; ]$ . Notice that this operation only acts on the rows of a matrix and, therefore, also is well defined for a vector. Lastly, one also needs the row-wise multiplication defined through

$$(\vec{\nu} \circ \mathbf{M})_{i,j} = \nu_i \mathbf{M}_{i,j}, \quad (\text{F.5})$$

which generalizes to an element-wise multiplication for two matrices

$$(\mathbf{M}_1 \circ \mathbf{M}_2)_{i,j} = (\mathbf{M}_1)_{i,j} (\mathbf{M}_2)_{i,j}. \quad (\text{F.6})$$

With these definitions the  $\mathbf{g}_1$  matrix is given from eq. (F.3) as

$$\mathbf{g}_1 = \vec{h} \circ \mathbb{1} + \frac{\vec{h}}{3} \circ \Delta, \quad (\text{F.7})$$

where the  $\mathbb{1}$  is just the  $(N, N)$  identity matrix. using this one can directly write off the internal part of  $\mathbf{A}$  from eq. (F.3) as

$$\mathbf{A}[1;; -1] = 2 \left( \vec{h} \circ \mathbb{1} \right) [;; -1] + (\vec{h} \circ \Delta)[;; -1] + \Delta [\mathbf{g}_1], \quad (\text{F.8})$$

and similarly for the internal part of  $\mathbf{B}$

$$\mathbf{B}[1;; -1] = \Delta \left[ \frac{1}{\vec{h}} \circ \Delta \right]. \quad (\text{F.9})$$

The boundary conditions set the last  $(M - 1)/2$  coefficients at each end of the grid. Here we choose the be  $a_N^2 = a_1^2 = 0$ . One can then solve the linear system of equations in eq. (F.4) which gives rise to a matrix  $\mathbf{A}_2$  that gives the  $a_j^2$  coefficients for any function evaluated on the same grid

$$\mathbf{A}_2[;; -1] \vec{a}_0 = \vec{a}_2. \quad (\text{F.10})$$

We are dealing with two-dimensional functions (momentum and frequency), so to find all the  $a_j^2$  coefficients in frequency for all momentum states, one has to do a matrix multiplication from the appropriate side.

Lastly, if one needs the remaining coefficients, they are easily found from the derived equations using the same "vectorization" method as the one used to find the internal parts of the linear system in eq. (F.4) and apply it to eq. (F.1). This gives the remaining three coefficients

$$\begin{aligned} \vec{a}_1 &= \left( \frac{1}{\vec{h}} \circ \Delta - \mathbf{g}_1 \cdot \mathbf{A}_2 \right) [;; -1] \vec{a}_0, \\ \vec{a}_3 &= \left( \frac{1}{3\vec{h}} \circ \Delta [\mathbf{A}_2] \right) \vec{a}_0. \end{aligned} \quad (\text{F.11})$$

Which again can be found by doing the matrix-vector product with the data points.

## F.2 Quintic spline

For the quintic spline, we use the same notation for the coefficients, as the two different splines do not appear together apart from a few cases. In those cases, we will differentiate them explicitly.

Like the cubic spline, the approach is to rewrite the continuity equations to a linear system for the second highest coefficient ( $a_j^4$ ). The continuity equation is the same as for

the cubic spline, namely eq. (5.58). The highest order coefficient is given by eq. (5.59) while the lowest order ( $a_j^0$ ) is just directly set by the data points. For the quintic spline, it makes the equations and manipulations slightly more compact if one already here introduces the first g-function

$$a_j^5 = \frac{g_j^0}{\Delta\nu_j}, \text{ with } g_j^0 = \frac{\Delta a_j^4}{5}. \quad (\text{F.12})$$

From the  $k = 0$  continuity equation the  $a_j^1$  equation is written as

$$a_j^1 = \frac{\Delta a_j^0}{\Delta\nu_j} - \Delta\nu_j a_j^2 - \Delta\nu_j^2 a_j^3 - \Delta\nu_j^3 g_j^1, \quad (\text{F.13})$$

with  $g_j^1 = g_j^0 + a_j^4$ . Applying the difference operator to this equation makes it possible to eliminate the  $a_j^1$  coefficients by equating it to the  $k = 1$  continuity equation, which is given as

$$\Delta a_j^1 = 2\Delta\nu_j a_j^2 + 3\Delta\nu_j^2 a_j^3 + 4\Delta\nu_j^3 a_j^4 + 5\Delta\nu_j^3 g_j^0. \quad (\text{F.14})$$

This leads to an equation containing  $a_j^2$  and  $a_{j+1}^2$ . To isolate the  $a_j^2$  coefficient we use the  $k = 2$  continuity equation

$$\Delta a_j^2 = 3\Delta\nu_j a_j^3 + 6\Delta\nu_j^2 a_j^4 + 10\Delta\nu_j^2 g_j^0. \quad (\text{F.15})$$

The result is the equation for  $a_j^2$

$$a_j^2 = \frac{\Delta \left[ \frac{\Delta a_j^0}{\Delta\nu_j} \right]}{\Delta\nu_{j+1} + \Delta\nu_j} - 3\Delta\nu_j a_j^3 - \frac{\Delta [\Delta\nu_j^2 a_j^3]}{\Delta\nu_{j+1} + \Delta\nu_j} - \frac{g_j^2}{\Delta\nu_{j+1} + \Delta\nu_j}, \quad (\text{F.16})$$

with

$$g_j^2 = 2\Delta\nu_j^2 (3\Delta\nu_{j+1} + 2\Delta\nu_j) a_j^4 + 5\Delta\nu_j^2 (2\Delta\nu_{j+1} + \Delta\nu_j) g_j^0 + \Delta [g_j^1 \Delta\nu_j^3]. \quad (\text{F.17})$$

The last remaining coefficient that has to be eliminated is  $a_j^3$ , and this is again done by applying the difference operator to the above-derived equation for the previous coefficient and then equating this to the  $k = 2$  continuity equation in eq. (F.15). This leads to an equation for  $a_j^3$  that contains  $a_j^3$ ,  $a_{j+1}^3$  and  $a_{j+2}^3$ . Like the previous coefficient, we need the higher order continuity equation to construct an equation for  $a_j^3$ . The  $k = 3$  continuity equation is

$$\Delta a_j^3 = 4\Delta\nu_j a_j^4 + 10\Delta\nu_j g_j^0. \quad (\text{F.18})$$

After having used this once for the  $a_{j+1}^3$  terms and twice for the  $a_{j+2}^3$  terms, we arrive at

$$a_j^3 = \frac{\Delta \left[ \frac{\Delta \left[ \frac{\Delta a_j^0}{\Delta \nu_j} \right]}{\Delta \nu_{j+1} + \Delta \nu_j} \right]}{\Delta \nu_{j+2} + \Delta \nu_{j+1} + \Delta \nu_j} - \frac{g_j^3}{\Delta \nu_{j+2} + \Delta \nu_{j+1} + \Delta \nu_j}, \quad (\text{F.19})$$

with the last of the g-functions being defined as

$$\begin{aligned} g_j^3 = & 2\Delta \nu_j (2\Delta \nu_{j+2} + 4\Delta \nu_{j+1} + 3\Delta \nu_j) a_j^4 \\ & + 10\Delta \nu_j (\Delta \nu_{j+2} + 2\Delta \nu_{j+1} + \Delta \nu_j) g_j^0 \\ & + \Delta \left[ \frac{\Delta \nu_{j+1}^2 (4\Delta \nu_j a_j^4 + 10\Delta \nu_j g_j^0) + g_j^2}{\Delta \nu_{j+1} + \Delta \nu_j} \right]. \end{aligned} \quad (\text{F.20})$$

Lastly we can eliminate the  $a_j^3$  coefficient by applying the difference operator to eq. (F.19) and equating it to the  $k = 3$  continuity equation in eq. (F.18). This gives the linear system where each coefficient is determined by the equation

$$4\Delta \nu_j a_j^4 + 10\Delta \nu_j g_j^0 + \Delta \left[ \frac{g_j^3}{\Delta \nu_{j+2} + \nu_{j+1} + \nu_j} \right] = \Delta \left[ \frac{\Delta \left[ \frac{\Delta \left[ \frac{\Delta a_j^0}{\Delta \nu_j} \right]}{\Delta \nu_{j+1} + \Delta \nu_j} \right]}{\Delta \nu_{j+2} + \Delta \nu_{j+1} + \Delta \nu_j} \right]. \quad (\text{F.21})$$

This gives  $N - 5$  equations for the  $N - 1$  coefficients, and one, therefore, has to supplement the quintic spline with four boundary conditions as discussed in appendix F.1. We can apply the same method developed there to write the linear system with matrices. We use similar boundary conditions as for the cubic case which translates into  $a_1^4 = a_2^4 = a_{N-1}^4 = a_N^4 = 0$ . One can then solve the linear system and compute the remaining coefficients from eqs. (F.12), (F.13), (F.16) and (F.19). Unlike the cubic case, these equations are not enough to determine all conditions. For the  $a_j^3$  coefficients eq. (F.19) only gives  $N - 3$  equations. This problem occurs because the boundary conditions are not included directly on the level of this equation; however, this is easily dealt with by using the continuity equation for  $a_j^3$  in eq. (F.18) to generate the two missing equations. This then incorporates the effect of the chosen boundary conditions into the  $a_j^3$  coefficients. For the  $a_j^2$  coefficients in eq. (F.16), one is, for the same reason, missing an equation that can be recovered by using eq. (F.15).

# Appendix G

## Hankel transform

In this appendix, we will construct the two arrays used in eq. (5.87).

### G.1 Hermite Interpolation of the Bessel function

The first element necessary is the Hermite interpolation of  $J_0(s) = h(s)$ . To find this interpolation, we are following the approach described in [240] but specified to our specific case of a two-point interpolation. To this extent we consider the two nodes  $\vec{x} = (x_0, x_1)^T$ . At each node, the values of the Bessel functions and  $P - 1$  derivatives are known. For this case, the two-point Hermite interpolation can be written

$$h(s) = \sum_{p=1}^{2P} f_{[\vec{x}, \vec{t}_p]} w^{(t_{p-1})}(s), \quad (\text{G.1})$$

where  $f_{[\vec{x}, \vec{t}_p]}$  are the general divided differences (GDDs).  $\vec{t}_p$  is a vector of length 2 that contains the combinations of powers at the different nodes and  $w^{(t_p)}(s) = (s - x_0)^{t_{p,0}}(s - x_1)^{t_{p,1}}$  gives the actual powers. To make this more concrete, consider the case with  $P = 3$ . In that case

$$\begin{pmatrix} \vec{t}_0 \\ \vec{t}_1 \\ \vec{t}_2 \\ \vec{t}_3 \\ \vec{t}_4 \\ \vec{t}_5 \\ \vec{t}_6 \end{pmatrix} = \begin{pmatrix} 0 & 0 \\ 1 & 0 \\ 2 & 0 \\ 3 & 0 \\ 3 & 1 \\ 3 & 2 \\ 3 & 3 \end{pmatrix}. \quad (\text{G.2})$$



The corresponding powers are

$$\begin{aligned}
 w^{\vec{t}_0}(s) &= 1, \\
 w^{\vec{t}_1}(s) &= s - x_0, \\
 w^{\vec{t}_2}(s) &= (s - x_0)^2, \\
 w^{\vec{t}_3}(s) &= (s - x_0)^3, \\
 w^{\vec{t}_4}(s) &= (s - x_0)^3(s - x_1), \\
 w^{\vec{t}_5}(s) &= (s - x_0)^3(s - x_1)^2, \\
 w^{\vec{t}_6}(s) &= (s - x_0)^3(s - x_1)^3.
 \end{aligned} \tag{G.3}$$

To complete the example the term for polynomial that is proportional to  $w^{\vec{t}_4}(s)$  is

$$f_{[x_0, x_0, x_0, x_1]}(s - x_0)^3(s - x_1). \tag{G.4}$$

A key feature of the GDDs is that they can be written as a linear transformation

$$\vec{\delta} = \mathbf{G}\vec{\phi}, \tag{G.5}$$

where  $\vec{\delta} = (f_{[\vec{x}, \vec{t}_1]}, \dots, f_{[\vec{x}, \vec{t}_{2P}]})^T$  is a vector of the GDD's and

$$\vec{\phi} = (J_0(x_n), \dots, J_0^{(P-1)}(x_n), J_0(x_{n+1}), \dots, J_0^{(P-1)}(x_{n+1}))^T \tag{G.6}$$

are all the known function values at the nodes. The matrix  $\mathbf{G}$  takes the form of a lower triangular block matrix

$$\mathbf{G} = \begin{pmatrix} \mathbf{L}_{00} & \mathbf{0} \\ \mathbf{L}_{10} & \mathbf{L}_{11} \end{pmatrix}, \tag{G.7}$$

with each  $\mathbf{L}_{nm}$  being a block of size  $P \times P$ .  $\mathbf{L}_{00}$  is nothing but the block describing a Taylor expansion to order  $P$  around  $x_0$

$$\mathbf{L}_{00} = \begin{pmatrix} 1 & 0 & \cdot & \cdot \\ 0 & \frac{1}{1!} & \cdot & \cdot \\ \cdot & \cdot & \ddots & \cdot \\ \cdot & \cdot & \cdot & \frac{1}{(P-1)!} \end{pmatrix}. \tag{G.8}$$

To write the two other blocks, we define

$$w_q^{(\vec{t}_p)} = \frac{w^{(\vec{t}_p)}}{(s - x_q)^{t_{pq}}}, \tag{G.9}$$

and

$$\alpha^{(\vec{t}_p)}(r; q) = \frac{d^r}{ds^r} \frac{1}{w_q^{(\vec{t}_p)}(s)} \Big|_{s=x_q}. \quad (\text{G.10})$$

The second block in the diagonal is lower triangular

$$(\mathbf{L}_{1,1})_{ij} = \begin{cases} \frac{\alpha^{(\vec{t}_{P+i})}(j-1,1)}{j!i!} & \text{if } j \leq i \\ 0 & \text{otherwise} \end{cases}. \quad (\text{G.11})$$

The off-diagonal block is dense with each element given by

$$(\mathbf{L}_{1,0})_{ij} = \frac{\alpha^{(\vec{t}_{P+i})}(P-j, 0)}{(P-j)!i!}. \quad (\text{G.12})$$

Considering again the example of  $P = 3$ , the second diagonal block takes the form

$$\mathbf{L}_{11} = \begin{pmatrix} \frac{\alpha^{(\vec{t}_4)}(0, 1)}{0!0!} & 0 & 0 \\ \frac{\alpha^{(\vec{t}_5)}(1, 1)}{1!0!} & \frac{\alpha^{(\vec{t}_5)}(0, 1)}{0!1!} & 0 \\ \frac{\alpha^{(\vec{t}_6)}(2, 1)}{2!0!} & \frac{\alpha^{(\vec{t}_6)}(1, 1)}{1!1!} & \frac{\alpha^{(\vec{t}_6)}(0, 1)}{0!2!} \end{pmatrix}, \quad (\text{G.13})$$

while the off-diagonal block is

$$\mathbf{L}_{10} = \begin{pmatrix} \frac{\alpha^{(\vec{t}_4)}(2, 0)}{2!0!} & \frac{\alpha^{(\vec{t}_4)}(1, 0)}{1!1!} & \frac{\alpha^{(\vec{t}_4)}(0, 0)}{0!2!} \\ \frac{\alpha^{(\vec{t}_5)}(2, 0)}{2!0!} & \frac{\alpha^{(\vec{t}_5)}(1, 0)}{1!1!} & \frac{\alpha^{(\vec{t}_5)}(0, x)}{0!2!} \\ \frac{\alpha^{(\vec{t}_6)}(2, 0)}{2!0!} & \frac{\alpha^{(\vec{t}_6)}(1, 0)}{1!1!} & \frac{\alpha^{(\vec{t}_6)}(0, 0)}{0!2!} \end{pmatrix}. \quad (\text{G.14})$$

Using these blocks to construct the full matrix  $\mathbf{G}$ , one can find the Hermite interpolation of function when the  $P - 1$  derivatives are known. This same procedure can, therefore, also be used for doing translationally invariant Fourier transforms in 3D.

## G.2 Oscillating integrals

The other array that has to be precomputed for our Hankel transform is the fast oscillating integrals in eq. (5.85). An element in this tensor is given by

$$I_{nj}^p = \frac{\sqrt{i\pi}}{8\alpha_j} e^{i\alpha_j k_n^2} \left. \frac{\partial^p}{\partial \eta^p} G_j(\eta) E_{n,j}(\eta) \right|_{\eta=2i\alpha_j k_n}, \quad (\text{G.15})$$

with

$$E_{jn} = \operatorname{erf}\left(\sqrt{\frac{i}{\alpha_j}} \frac{\eta}{2}\right) - \operatorname{erf}\left(\sqrt{\frac{i}{\alpha_j}} \frac{2i\alpha_j \Delta k_n + \eta}{2}\right) \quad (\text{G.16})$$

and

$$G_j = e^{i\eta^2/(4\alpha_j)}. \quad (\text{G.17})$$

The derivative of the product leads to binomial coefficients

$$I_{jn}^p = \frac{\sqrt{i\pi}}{8\alpha_j} e^{i\alpha_j k_n^2} \sum_{q=0}^p \binom{p}{q} \left. \left( \frac{\partial^{p-q} G_j(\eta)}{\partial \eta^{p-q}} \right) \left( \frac{\partial^q E_{jn}(\eta)}{\partial \eta^q} \right) \right|_{\eta=2i\alpha_j k_n}. \quad (\text{G.18})$$

The derivatives of  $G_j$  can be expressed through Hermite polynomials  $H_p(x)$

$$\mathcal{G}_{jnp} = \left. \frac{\partial^p G_j(\eta)}{\partial \eta^p} \right|_{\eta=2i\alpha_j k_n} = (-1)^p H_p\left(\sqrt{i\alpha_j} k_n\right) e^{-i\alpha_j k_n^2} (i4\alpha_j)^{-p/2}, \quad (\text{G.19})$$

The derivatives of  $E$  are less compact but can also be expressed through Hermite polynomials

$$\begin{aligned} \mathcal{E}_{jnp} = & \frac{2(-1)^{p-1}}{\pi} (-i4\alpha_j)^{-p/2} e^{i\alpha_j k_n^2} \left( H_{p-1}(i\sqrt{i\alpha_j} k_n) \right. \\ & \left. - H_{p-1}(i\sqrt{i\alpha_j}(k_{n+1} - 2k_n)) e^{i\alpha_j(k_n + k_{n+1})} \right), \end{aligned} \quad (\text{G.20})$$

$I$  can then be written as

$$I_{nj}^p = \frac{\sqrt{i\pi}}{8\alpha_j} e^{i\alpha_j k_n^2} \left( \mathcal{G}_{jnp} E_{jn} + \sum_{q=1}^p \binom{p}{q} \mathcal{G}_{jn(p-1)} \mathcal{E}_{jnq} \right). \quad (\text{G.21})$$

One can significantly decrease the computation time by taking advantage of the fact that the same Hermite polynomials occur in both  $\mathcal{E}$  and  $\mathcal{G}$ .



# Bibliography

- [1] S. Tomonaga. On a Relativistically Invariant Formulation of the Quantum Theory of Wave Fields. *Progress of Theoretical Physics*, 2, 1946.
- [2] Julian Schwinger. On Quantum-Electrodynamics and the Magnetic Moment of the Electron. *Physical Review*, 73:416–417, 1948.
- [3] Julian Schwinger. Quantum electrodynamics. I. A covariant formulation. *Physical Review*, 74(10), 1948.
- [4] R. P. Feynman. Space-time approach to quantum electrodynamics. *Physical Review*, 76(6), 1949.
- [5] R. P. Feynman. Mathematical formulation of the quantum theory of electromagnetic interaction. *Physical Review*, 80(3), 1950.
- [6] F. J. Dyson. The radiation theories of Tomonaga, Schwinger, and Feynman. *Physical Review*, 75(3), 1949.
- [7] F. J. Dyson. The S matrix in quantum electrodynamics. *Physical Review*, 75(11), 1949.
- [8] Alberto De La Torre, Dante M. Kennes, Martin Claassen, Simon Gerber, James W. McIver, and Michael A. Sentef. Colloquium: Nonthermal pathways to ultrafast control in quantum materials. *Reviews of Modern Physics*, 93(441002), 2021.
- [9] K. Nasu, H. Ping, and H. Mizouchi. Photoinduced structural phase transitions and their dynamics. *Journal of Physics Condensed Matter*, 13:693–721, 2001.
- [10] Xian Li, Tian Qiu, Jiahao Zhang, Edoardo Baldini, Jian Lu, Andrew M. Rappe, and Keith A. Nelson. Terahertz field-induced ferroelectricity in quantum paraelectric SrTiO<sub>3</sub>. *Science*, 364(6445), 2019.
- [11] M. Mitranò, A. Cantaluppi, D. Nicoletti, S. Kaiser, A. Perucchi, S. Lupi, P. Di Pietro, D. Pontiroli, M. Riccò, S. R. Clark, D. Jaksch, and A. Cavalleri. Possible

- light-induced superconductivity in K<sub>3</sub>C<sub>60</sub> at high temperature. *Nature*, 530:461–464, 2016.
- [12] Jacqueline Bloch, Andrea Cavalleri, Victor Galitski, Mohammad Hafezi, and Angel Rubio. Strongly correlated electron–photon systems. *Nature*, 606:41–48, 2022.
- [13] Farokh Mivehvar, Francesco Piazza, Tobias Donner, and Helmut Ritsch. Cavity QED with Quantum Gases: New Paradigms in Many-Body Physics. *Advances in Physics*, 70(1), 2021.
- [14] F. Schlawin, D. M. Kennes, and M. A. Sentef. Cavity quantum materials. *Applied Physics Reviews*, 9(1), 2022.
- [15] Kevin Roux, Hideki Konishi, Victor Helsen, and Jean Philippe Brantut. Strongly correlated Fermions strongly coupled to light. *Nature Communications*, 11(2974), 2020.
- [16] Serge Haroche and Daniel Kleppner. Cavity quantum electrodynamics. *Physics Today*, 42(1), 1989.
- [17] E. T. Jaynes and F. W. Cummings. Comparison of Quantum and Semiclassical Radiation Theories with Application to the Beam Maser. *Proceedings of the IEEE*, 51:89–109, 1963.
- [18] Gerhard Rempe, Herbert Walther, and Norbert Klein. Observation of quantum collapse and revival in a one-atom maser. *Physical Review Letters*, 58(4), 1987.
- [19] Y. Kaluzny, P. Goy, M. Gross, J. M. Raimond, and S. Haroche. Observation of self-induced Rabi oscillations in two-level atoms excited inside a resonant cavity: The ringing regime of superradiance. *Physical Review Letters*, 51(13), 1983.
- [20] D. Meschede, H. Walther, and G. Muller. One-atom maser. *Physical Review Letters*, 54(6), 1985.
- [21] R.J. Thompson, G. Rempe, and H. J. Kimble. Observation of normal-mode splitting for an atom in an optical cavity. *Physical Review Letters*, 68(8), 1992.
- [22] T. Yoshle, A. Scherer, J. Hendrickson, G. Khitrova, H. M. Gibbs, G. Rupper, C. Ell, O. B. Shchekin, and D. G. Deppe. Vacuum Rabi splitting with a single quantum dot in a photonic crystal nanocavity. *Nature*, 432:200–203, 2004.
- [23] S. Kuhr, S. Gleyzes, C. Guerlin, J. Bernu, U. B. Hoff, S. Deléglise, S. Osnaghi, M. Brune, J. M. Raimond, S. Haroche, E. Jacques, P. Bosland, and B. Visentin.

- Ultrahigh finesse Fabry-Pérot superconducting resonator. *Applied Physics Letters*, 90(164101), 2007.
- [24] D. N. Basov, Ana Asenjo-Garcia, P. James Schuck, Xiaoyang Zhu, and Angel Rubio. Polariton panorama. *Nanophotonics*, 10(1), 2020.
- [25] William L. Barnes, Alain Dereux, and Thomas W. Ebbesen. Surface plasmon sub-wavelength optics. *Nature*, 424:824–830, 2003.
- [26] N. Ocelic and R. Hillenbrand. Subwavelength-scale tailoring of surface phonon polaritons by focused ion-beam implantation. *Nature Materials*, 3:606–609, 2004.
- [27] E. Knill, R. Laflamme, and G. J. Milburn. A scheme for efficient quantum computation with linear optics. *Nature*, 409:46–52, 2001.
- [28] Michael Reck, Anton Zeilinger, Herbert J. Bernstein, and Philip Bertani. Experimental Realization of Any Discrete Unitary Operator. *Physical Review Letters*, 73(1), 1994.
- [29] H. J. Kimble. The quantum internet. *Nature*, 453:1023–1030, 2008.
- [30] Darrick E. Chang, Vladan Vuletić, and Mikhail D. Lukin. Quantum nonlinear optics - Photon by photon. *Nature Photonics*, 8(9):685–694, 2014.
- [31] S. Sun, H. Kim, Z. Luo, G.S. Solomon, and E. Waks. A single-photon switch and transistor enabled by a solid-state quantum memory. *Science*, 361(6397), 2018.
- [32] Julien Claudon, Joël Bleuse, Nitin Singh Malik, Maela Bazin, Périne Jaffrennou, Niels Gregersen, Christophe Sauvan, Philippe Lalanne, and Jean Michel Gérard. A highly efficient single-photon source based on a quantum dot in a photonic nanowire. *Nature Photonics*, 4:174–177, 2010.
- [33] Alex Kamenev. *Field Theory of Non-Equilibrium Systems*. Cambridge University Press, 2011.
- [34] Alexander Altland and Ben Simons. *Condensed matter field theory*. Cambridge University Press, 2010.
- [35] P. Danielewicz. Quantum theory of nonequilibrium processes. *Annals of Physics*, 152:239–304, 1984.
- [36] N. P. Landsman and Ch G. van Weert. Real- and imaginary-time field theory at finite temperature and density. *Physics Reports*, 145:141–249, 1987.

- 
- [37] Leslie E. Ballentine. *Quantum Mechanics: A modern development*. World Scientific, 2000.
- [38] Steven Weinberg. *Lectures on Quantum Mechanics*. Cambridge University Press, 2nd edition, 2015.
- [39] Henrik Bruus and Karsten Flensberg. *Many-Body Quantum Theory in Condensed Matter Physics*. Oxford University Press, 2002.
- [40] H.-P. Breuer and F. Petruccione. *The Theory of Open Quantum Systems*. Oxford University Press, 2007.
- [41] Jung Hoon Jung and Jae Dong Noh. Guide to Exact Diagonalization Study of Quantum Thermalization. *Journal of the Korean Physical Society*, 76(8), 2020.
- [42] Daniel Jaschke, Simone Montangero, and Lincoln D. Carr. One-dimensional many-body entangled open quantum systems with tensor network methods. *Quantum Science and Technology*, 4(013001), 2019.
- [43] Mathias R. Jørgensen and Felix A. Pollock. Exploiting the Causal Tensor Network Structure of Quantum Processes to Efficiently Simulate Non-Markovian Path Integrals. *Physical Review Letters*, 123(240602), 2019.
- [44] Mathias R. Jørgensen and Felix A. Pollock. Discrete memory kernel for multitime correlations in non-Markovian quantum processes. *Physical Review A*, 102(052206), 2020.
- [45] L V Keldysh. Diagram technique for nonequilibrium processes. *Soviet Physics JETP*, 20(4), 1964.
- [46] Julian Schwinger. Brownian motion of a quantum oscillator. *Journal of Mathematical Physics*, 2(3), 1961.
- [47] Joseph Maciejko. An Introduction to Nonequilibrium Many-Body Theory. *Springer*, page 58, 2007.
- [48] H. Haug and A.-P. Jauho. *Quantum Kinetics in Transport and Optics of Semiconductors*. Springer, 2007.
- [49] Klaus Morawetz. *Interacting systems far from equilibrium*. Oxford University Press, 2018.
- [50] Gianluca Stefanucci and Robert van Leeuwen. *Nonequilibrium many-body theory of quantum systems*. Cambridge University Press, 2013.



- 
- [51] I. M. Georgescu, S. Ashhab, and Franco Nori. Quantum simulation. *Reviews of Modern Physics*, 86:153–185, 2014.
- [52] H. F. Trotter. On the Product of Semi-Groups of Operators. *Proceedings of the American Mathematical Society*, 10(4), 1959.
- [53] M. Suzuki. Decomposition formulas of exponential operators and Lie exponentials with some applications to quantum mechanics and statistical physics. *J. Math. Phys.*, 26(601), 1985.
- [54] Richard P. Feynman and Albert R. Hibbs. *Quantum Mechanics and Path Integrals*. McGraw-Hill, 1965.
- [55] Ramamurti Shankar. *Quantum field theory and condensed matter: An introduction*. Cambridge University Press, 2017.
- [56] H Goldstein, C Poole, and J Safko. *Classical mechanics*. Addison Wesley, third edition, 2007.
- [57] Leon N. Cooper. Bound Electron Pairs in a Degenerate Fermi Gas. *Physical Review*, 104(4), 1956.
- [58] Anatoli Polkovnikov. Phase space representation of quantum dynamics. *Annals of Physics*, 325:1790–1852, 2010.
- [59] W. T. Coffey, Yu. P. Kalmykov, and J. T. Waldron. *The Langevin equation*. World Scientific, 2005.
- [60] Julian Schwinger. On the Green’s functions of quantized fields. I. *Proceedings of the National Academy of Sciences*, 37:452–455, 1951.
- [61] Alexander L Fetter and John Dirk Walecka. *Quantum theory of many-particle systems*. McGraw-Hill, New York, 1971.
- [62] Gordon Baym and Leo P. Kadanoff. Conservation laws and correlation functions. *Physical Review*, 124(2), 1961.
- [63] M. Pini, P. Pieri, and G. Calvanese Strinati. Fermi gas throughout the BCS-BEC crossover: Comparative study of  $t$ -matrix approaches with various degrees of self-consistency. *Physical Review B*, 99(094502), 2019.
- [64] R Mottl, F Brennecke, K Baumann, R Landig, T Donner, and T Esslinger. Roton-Type Mode Softening in a Long-Range Interactions. *Science*, 336(6088), 2012.

- [65] Renate Landig, Ferdinand Brennecke, Rafael Mottl, Tobias Donner, and Tilman Esslinger. Measuring the dynamic structure factor of a quantum gas undergoing a structural phase transition. *Nature Communications*, 6(7046), 2015.
- [66] L. Bürgi, O. Jeandupeux, H. Brune, and K. Kern. Probing hot-electron dynamics at surfaces with a cold scanning tunneling microscope. *Physical Review Letters*, 82(22), 1999.
- [67] J. Klierer. Dimensionality effects in the lifetime of surface states. *Science*, 288(5470), 2000.
- [68] Friedrich Reinert. Spin-orbit interaction in the photoemission spectra of noble metal surface states. *Journal of Physics Condensed Matter*, 15:693–705, 2003.
- [69] F. Reinert, B. Eltner, G. Nicolay, F. Forster, S. Schmidt, and S. Hüfner. The electron-phonon self-energy of metallic systems determined by angular resolved high-resolution photoemission. *Physica B*, 351:229–234, 2004.
- [70] L.D. Landau. The Theory of a Fermi Liquid. *Soviet Physics JETP*, 3(6):920–925, 1957.
- [71] Václav Špička and Pavel Lipavský. Quasiparticle Boltzmann equation in semiconductors. *Physical Review B*, 52(20), 1995.
- [72] H. B. Callen and T. A. Welton. irreversibility and generalized noise. *Physical Review*, 83(1), 1951.
- [73] J. Weber. Fluctuation dissipation theorem. *Physical Review*, 101(6), 1956.
- [74] Gerald D. Mahan. *Many-Particle Physics*. Plenum Publishers, 3rd edition, 2000.
- [75] Johannes Lang and Francesco Piazza. Critical relaxation with overdamped quasiparticles in open quantum systems. *Physical Review A*, 94(033628), 2016.
- [76] G. Lindblad. On the generators of quantum dynamical semigroups. *Communications in Mathematical Physics*, 48:119–130, 1976.
- [77] Vittorio Gorini, Andrzej Kossakowski, and E. C.G. Sudarshan. Completely positive dynamical semigroups of N-level systems. *Journal of Mathematical Physics*, 17:821–825, 1975.
- [78] Heinz Peter Breuer, Elsi Mari Laine, and Jyrki Piilo. Measure for the Degree of Non-Markovian Behavior of Quantum Processes in Open Systems. *Physical Review Letters*, 103(210401), 2009.

- [79] Anthony E Siegman. *Lasers*. University Science Books, 1986.
- [80] B.E.A. Saleh and M.C. Teich. *Fundamentals of photonics*. Wiley, 2nd edition, 2007.
- [81] J. Klinder, H. Keßler, Ch. Georges, J. Vargas, and A. Hemmerich. Bose-einstein condensates in an optical cavity with sub-recoil bandwidth. *Applied Physics B*, 122(299), 2016.
- [82] L M Sieberer, M Buchhold, and S Diehl. Keldysh Field Theory for Driven Open Quantum Systems. *Reports on Progress in Physics*, 79(096001), 2016.
- [83] Christian Høj Johansen, Johannes Lang, Andrea Morales, Alexander Baumgärenter, Tobias Donner, and Francesco Piazza. Multimode-polariton superradiance via Floquet engineering. *SciPost Physics*, 12(094), 2022.
- [84] Michael J. Hartmann, Fernando G.S.L. Brando, and Martin B. Plenio. Strongly interacting polaritons in coupled arrays of cavities. *Nature Physics*, 2:849–855, 2006.
- [85] Iacopo Carusotto and Cristiano Ciuti. Quantum fluids of light. *Reviews of Modern Physics*, 85:299–366, 2013.
- [86] Alexey V. Gorshkov, Rejish Nath, and Thomas Pohl. Dissipative many-body quantum optics in rydberg media. *Physical Review Letters*, 110(153601), 2013.
- [87] J. S. Douglas, H. Habibian, C. L. Hung, A. V. Gorshkov, H. J. Kimble, and D. E. Chang. Quantum many-body models with cold atoms coupled to photonic crystals. *Nature Photonics*, 9:326–331, 2015.
- [88] James S. Douglas, Tommaso Caneva, and Darrick E. Chang. Photon molecules in atomic gases trapped near photonic crystal waveguides. *Physical Review X*, 6(031017), 2016.
- [89] Changsuk Noh and Dimitris G. Angelakis. Quantum simulations and many-body physics with light. *Reports on Progress in Physics*, 80(016401), 2017.
- [90] S. Ostermann, F. Piazza, and H. Ritsch. Spontaneous crystallization of light and ultracold atoms. *Physical Review X*, 6(021026), 2016.
- [91] Emil Zeuthen, Michael J. Gullans, Mohammad F. Maghrebi, and Alexey V. Gorshkov. Correlated Photon Dynamics in Dissipative Rydberg Media. *Physical Review Letters*, 119(043602), 2017.

- [92] Kieran A. Fraser and Francesco Piazza. Topological soliton-polaritons in 1D systems of light and fermionic matter. *Communications Physics*, 2(48), dec 2019.
- [93] Ruichao Ma, Brendan Saxberg, Clai Owens, Nelson Leung, Yao Lu, Jonathan Simon, and David I. Schuster. A dissipatively stabilized Mott insulator of photons. *Nature*, 566:51–57, feb 2019.
- [94] Johannes Lang, Darrick Chang, and Francesco Piazza. Interaction-Induced Transparency for Strong-Coupling Polaritons. *Physical Review Letters*, 125(133604), 2020.
- [95] Ningyuan Jia, Nathan Schine, Alexandros Georgakopoulos, Albert Ryou, Logan W. Clark, Ariel Sommer, and Jonathan Simon. A strongly interacting polaritonic quantum dot. *Nature Physics*, 14:550–554, 2018.
- [96] Nathan Schine, Albert Ryou, Andrey Gromov, Ariel Sommer, and Jonathan Simon. Synthetic Landau levels for photons. *Nature*, 534:671–675, 2016.
- [97] Hyang Tag Lim, Emre Togan, Martin Kroner, Javier Miguel-Sanchez, and Atac Imamoglu. Electrically tunable artificial gauge potential for polaritons. *Nature Communications*, 8(14540), 2017.
- [98] A. Goban, C. L. Hung, S. P. Yu, J. D. Hood, J. A. Muniz, J. H. Lee, M. J. Martin, A. C. McClung, K. S. Choi, D. E. Chang, O. Painter, and H. J. Kimble. Atom-light interactions in photonic crystals. *Nature Communications*, 5(3808), 2014.
- [99] Li Bing Tan, Ovidiu Cotlet, Andrea Bergschneider, Richard Schmidt, Patrick Back, Yuya Shimazaki, Martin Kroner, and Atac İmamoğlu. Interacting Polaron-Polaritons. *Physical Review X*, 10(021011), 2020.
- [100] Logan W. Clark, Ningyuan Jia, Nathan Schine, Claire Baum, Alexandros Georgakopoulos, and Jonathan Simon. Interacting Floquet polaritons. *Nature Research Letter*, 571:532–536, 2019.
- [101] E. Urban, T. A. Johnson, T. Henage, L. Isenhower, D. D. Yavuz, T. G. Walker, and M. Saffman. Observation of Rydberg blockade between two atoms. *Nature Physics*, 5:110–114, 2009.
- [102] Peter Domokos and Helmut Ritsch. Collective Cooling and Self-Organization of Atoms in a Cavity. *Physical Review Letters*, 89(25), 2002.
- [103] Adam T. Black, Hilton W. Chan, and Vladan Vuletic. Observation of collective friction forces due to spatial self-organization of atoms: From Rayleigh to Bragg scattering. *Physical Review Letters*, 91(20), 2003.

- 
- [104] Kristian Baumann, Christine Guerlin, Ferdinand Brennecke, and Tilman Esslinger. Dicke quantum phase transition with a superfluid gas in an optical cavity. *Nature*, 464(7293):1301–1306, 2010.
- [105] D. Nagy, J. K. Asbóth, P. Domokos, and H. Ritsch. Self-organization of a laser-driven cold gas in a ring cavity. *Europhysics Letters*, 74(2), 2006.
- [106] J. K. Asbóth, P. Domokos, H. Ritsch, and A. Vukics. Self-organization of atoms in a cavity field: Threshold, bistability, and scaling laws. *Physical Review A*, 72(053417), 2005.
- [107] D. Nagy, G. Szirmai, and P. Domokos. Self-organization of a Bose-Einstein condensate in an optical cavity. *European Physical Journal D*, 48:127–137, 2008.
- [108] Francesco Piazza, Philipp Strack, and Wilhelm Zwerger. Bose-Einstein condensation versus Dicke-Hepp-Lieb transition in an optical cavity. *Annals of Physics*, 339:135–159, 2013.
- [109] Christoph Maschler, Igor B. Mekhov, and Helmut Ritsch. Ultracold atoms in optical lattices generated by quantized light fields. *European Physical Journal D*, 46:545–560, 2008.
- [110] Varun D. Vaidya, Yudan Guo, Ronen M. Kroeze, Kyle E. Ballantine, Alicia J. Kollár, Jonathan Keeling, and Benjamin L. Lev. Tunable-Range, Photon-Mediated Atomic Interactions in Multimode Cavity QED. *Physical Review X*, 8(011002), 2018.
- [111] Yudan Guo, Ronen M. Kroeze, Varun V. Vaidya, Jonathan Keeling, and Benjamin L. Lev. Sign-changing photon-mediated atom interactions in multimode cavity QED. *Physical Review Letters*, 122(193601), 2019.
- [112] P. Karpov and F. Piazza. Crystalline droplets with emergent topological color-charge in many-body systems with sign-changing interactions. *Physical Review A*, 100(061401), 2019.
- [113] Yudan Guo, Varun D. Vaidya, Ronen M. Kroeze, Rhiannon A. Lunney, Benjamin L. Lev, and Jonathan Keeling. Emergent and broken symmetries of atomic self-organization arising from Gouy phase shifts in multimode cavity QED. *Physical Review A*, 99(053818), 2019.
- [114] Julian Léonard, Andrea Morales, Philip Zupancic, Tilman Esslinger, and Tobias Donner. Supersolid formation in a quantum gas breaking a continuous translational symmetry. *Nature*, 543:87–90, 2017.

- [115] J. Lang, F. Piazza, and W. Zwerger. Collective excitations and supersolid behavior of bosonic atoms inside two crossed optical cavities. *New Journal of Physics*, 19(123027), 2017.
- [116] Farokh Mivehvar, Helmut Ritsch, and Francesco Piazza. Emergent Quasicrystalline Symmetry in Light-Induced Quantum Phase Transitions. *Physical Review Letters*, 123(210604), 2019.
- [117] Andrea Morales, Davide Dreon, Xiangliang Li, Alexander Baumgärtner, Philip Zupancic, Tobias Donner, and Tilman Esslinger. Two-mode Dicke model from nondegenerate polarization modes. *Physical Review A*, 100(013816), 2019.
- [118] Daniel Adam Steck. Rubidium 87 Line Data. Technical report, Los Alamos National Laboratory, 2009.
- [119] Daniel Adam Steck. *Quantum and Atom Optics*. <http://steck.us/teaching>, 2016.
- [120] Christopher C. Gerry and Peter L. Knight. *Introductory Quantum Optics*. Cambridge, 2005.
- [121] G.S. Agarwal. *Quantum Optics*. Cambridge, 2013.
- [122] Francesco Piazza and Philipp Strack. Quantum kinetics of ultracold fermions coupled to an optical resonator. *Physical Review A*, 90(4), 2014.
- [123] Julian Léonard. *A supersolid of matter and light*. PhD thesis, ETH, 2017.
- [124] M N Kiselev and R Oppermann. Schwinger-Keldysh semionic approach for quantum spin systems. *Physical review letters*, 85(26), 2000.
- [125] M.N. Kiselev. Semi-fermionic representation for spin systems under equilibrium and non-equilibrium conditions. *Int. J. Mod. Phys. B*, 20(4), 2006.
- [126] Piers Coleman. *Introduction to Many-Body Physics*. Cambridge University Press, 2015.
- [127] E. Karimi, R. W. Boyd, P. De La Hoz, H. De Guise, J. Řeháček, Z. Hradil, A. Aiello, G. Leuchs, and L. L. Sánchez-Soto. Radial quantum number of Laguerre-Gauss modes. *Physical Review A*, 89(063813), 2014.
- [128] Lev Pitaevski and Sandro Stringari. *Bose-Einstein Condensation and Superfluidity*. Oxford University Press, 2016.

- 
- [129] I. S. Gradshteyn and I.M. Ryzhik. *Table of Integrals, Series, and Products*. Elsevier, 8 edition, 2015.
- [130] Emanuele G.Dalla Torre, Sebastian Diehl, Mikhail D. Lukin, Subir Sachdev, and Philipp Strack. Keldysh approach for nonequilibrium phase transitions in quantum optics: Beyond the Dicke model in optical cavities. *Physical Review A*, 87(023831), 2013.
- [131] A. Cuyt, B.V. Petersen, B. Verdonk, H. Waadeland, and W.B. Jones. *Handbook of continued fractions for special functions*. Springer, 2008.
- [132] Peter Kirton, Mor M. Roses, Jonathan Keeling, and Emanuele G. Dalla Torre. Introduction to the Dicke model: from equilibrium to nonequilibrium, and vice versa. *Advanced Quantum Technologies*, 2(1800043), 2018.
- [133] Kristian Baumann, Christine Guerlin, Ferdinand Brennecke, and Tilman Esslinger. Dicke quantum phase transition with a superfluid gas in an optical cavity. *Nature*, 464:1301–1306, 2010.
- [134] Francesco Piazza and Helmut Ritsch. Self-Ordered Limit Cycles, Chaos, and Phase Slippage with a Superfluid inside an Optical Resonator. *Physical Review Letters*, 115(16), oct 2015.
- [135] Hans Keßler, Jayson G. Cosme, Michal Hemmerling, Ludwig Mathey, and Andreas Hemmerich. Emergent limit cycles and time crystal dynamics in an atom-cavity system. *Physical Review A*, 99(053605), 2019.
- [136] Phatthamon Kongkhambut, Jim Skulte, Ludwig Mathey, Jayson G. Cosme, Andreas Hemmerich, and Hans Keßler. Observation of a continuous time crystal. *Science*, 377:670–673, 2022.
- [137] V. M. Bastidas, C. Emary, B. Regler, and T. Brandes. Nonequilibrium quantum phase transitions in the Dicke model. *Physical Review Letters*, 108(043003), 2012.
- [138] R. Chitra and O. Zilberberg. Dynamical many-body phases of the parametrically driven, dissipative Dicke model. *Physical Review A*, 92(023815), 2015.
- [139] Jayson G. Cosme, Jim Skulte, and Ludwig Mathey. Time crystals in a shaken atom-cavity system. *Physical Review A*, 100(053615), aug 2019.
- [140] Jayson G. Cosme, Christoph Georges, Andreas Hemmerich, and Ludwig Mathey. Dynamical Control of Order in a Cavity-BEC System. *Physical Review Letters*, 121(153001), 2018.

- [141] Paolo Mognini, Luca Papariello, Axel U.J. Lode, and R. Chitra. Superlattice switching from parametric instabilities in a driven-dissipative Bose-Einstein condensate in a cavity. *Physical Review A*, 98(053620), 2018.
- [142] Hans Keßler, Phatthamon Kongkhambut, Christoph Georges, Ludwig Mathey, Jayson G. Cosme, and Andreas Hemmerich. Observation of a Dissipative Time Crystal. *Physical Review Letters*, 127(43602), 2021.
- [143] Christoph Georges, Jayson G. Cosme, Ludwig Mathey, and Andreas Hemmerich. Light-Induced Coherence in an Atom-Cavity System. *Physical Review Letters*, 121(220405), 2018.
- [144] Valentin Torggler and Helmut Ritsch. Adaptive multifrequency light collection by self-ordered mobile scatterers in optical resonators. *Optica*, 1(5), 2014.
- [145] Valentin Torggler, Sebastian Krämer, and Helmut Ritsch. Quantum annealing with ultracold atoms in a multimode optical resonator. *Physical Review A*, 95(032310), 2017.
- [146] R. L. Stratonovich. A method for the computation of quantum distribution functions. *Soviet Physics Doklady*, 115(6), 1957.
- [147] J. Hubbard. Calculation of partition functions. *Physical Review Letters*, 3(2), 1959.
- [148] Indrani Bose and Sayantari Ghosh. Bifurcation and criticality. *Journal of Statistical Mechanics: Theory and Experiment*, 043403, 2019.
- [149] Annick Lesne and Michel Lagües. *Scale invariance: From phase transitions to turbulence*. Springer, 2012.
- [150] Yuri A Kuznetsov. *Elements of Applied Bifurcation Theory, Second Edition*, volume 112. Springer, 1998.
- [151] G. Kónya, G. Szirmai, and P. Domokos. Damping of quasiparticles in a Bose-Einstein condensate coupled to an optical cavity. *Physical Review A*, 90(013623), 2014.
- [152] A J Lichtenberg and M A Lieberman. *Regular and chaotic dynamics*. Springer, 1992.
- [153] Y Kuramoto. *Chemical Oscillations, Waves and Turbulence*. Springer Berlin Heidelberg, 1984.



- [154] D. J.W. Simpson. A compendium of Hopf-like bifurcations in piecewise-smooth dynamical systems. *Physics Letters A*, 382(35), 2018.
- [155] George Arfken. *Mathematical Methods for Physicists*. Elsevier, 6 edition, 2005.
- [156] G. Strang. Linear Algebra and its applications. *Thomson Brooks/Cole*, 2006.
- [157] N.M. Bogoliubov. On the theory of superfluidity. *J. Phys. (USSR)*, 11(1), 1947.
- [158] Gábor Kónya, Dávid Nagy, Gergely Szirmai, and Peter Domokos. Nonequilibrium polariton dynamics in a Bose-Einstein condensate coupled to an optical cavity. *Physical Review A*, 98(063608), 2018.
- [159] M. Krämer, C. Menotti, L. Pitaevskii, and S. Stringari. Bose-Einstein condensates in 1D optical lattices: Compressibility, Bloch bands and elementary excitations. *European Physical Journal D*, 27:247–261, 2003.
- [160] K.S. Novoselov, A.K. Geim, S.V. Morozov, D. Jiang, Y. Zhang, S.V. Dubonos, I.V. Grigorieva, and A.A. Firsov. Electric Field Effect in Atomically Thin Carbon Films. *Science*, 306(5696), 2004.
- [161] K S Novoselov, D Jiang, F Schedin, T J Booth, V V Khotkevich, S V Morozov, and A K Geim. Two-dimensional atomic crystals. *PNAS*, 102(30), 2005.
- [162] Kin Fai Mak, Changgu Lee, James Hone, Jie Shan, and Tony F Heinz. Atomically Thin MoS<sub>2</sub>: A New Direct-Gap Semiconductor. *Physical Review Letters*, 105(136805), 2010.
- [163] Andrea Splendiani, Liang Sun, Yuanbo Zhang, Tianshu Li, Jonghwan Kim, Chi-yung Chim, Giulia Galli, and Feng Wang. Emerging Photoluminescence in Monolayer. *Nano Letters*, 10:1271–1275, 2010.
- [164] Miguel M Ugeda, Aaron J Bradley, Su-fei Shi, Felipe H Jornada, Yi Zhang, Diana Y Qiu, Wei Ruan, Sung-kwan Mo, Zahid Hussain, Zhi-xun Shen, Feng Wang, Steven G Louie, and Michael F Crommie. Giant bandgap renormalization and excitonic effects in a monolayer transition metal dichalcogenide semiconductor. *Nature materials*, 13:1091–1095, 2014.
- [165] Alexey Chernikov, Timothy C Berkelbach, Heather M Hill, Albert Rigosi, Yilei Li, Ozgur Burak Aslan, David R Reichman, Mark S Hybertsen, and Tony F Heinz. Exciton Binding Energy and Nonhydrogenic Rydberg Series in Monolayer WS<sub>2</sub>. *Physical Review Letters*, 113(076802), 2014.

- [166] Keliang He, Nardeep Kumar, Liang Zhao, Zefang Wang, Kin Fai Mak, Hui Zhao, and Jie Shan. Tightly Bound Excitons in Monolayer WSe<sub>2</sub>. *Physical Review Letters*, 113(026803), 2014.
- [167] A. Rycerz, J. Tworzydło, and C. W.J. Beenakker. Valley filter and valley valve in graphene. *Nature Physics*, 3:172–175, 2007.
- [168] Ting Cao, Gang Wang, Wenpeng Han, Huiqi Ye, Chuanrui Zhu, Junren Shi, Qian Niu, Pingheng Tan, Enge Wang, Baoli Liu, and Ji Feng. Valley-selective circular dichroism of monolayer molybdenum disulphide. *Nature Communications*, 3(887), 2012.
- [169] Meinrad Sidler, Patrick Back, Ovidiu Cotlet, Ajit Srivastava, Thomas Fink, Martin Kroner, Eugene Demler, and Atac Imamoglu. Fermi polaron-polaritons in charge-tunable atomically thin semiconductors. *Nature Physics*, 13:255–261, 2017.
- [170] Thibault Chervy, Patrick Knüppel, Hadis Abbaspour, Mirko Lupatini, Stefan Fält, Werner Wegscheider, Martin Kroner, and Atac Imamoglu. Accelerating Polaritons with External Electric and Magnetic Fields. *Physical Review X*, 10(011040), 2012.
- [171] R. P. A. Emmanuele, M. Sich, O. Kyriienko, V. Shahnazaryan, F. Withers, A. Catanzaro, P. M. Walker, F. A. Benimetskiy, M. S. Skolnick, A. I. Tartakovskii, I. A. Shelykh, and D. N. Krizhanovskii. Highly nonlinear trion-polaritons in a monolayer semiconductor. *Nature Communications*, 11(3589), oct 2020.
- [172] Pietro Massignan, Matteo Zaccanti, and Georg M. Bruun. Polarons, dressed molecules and itinerant ferromagnetism in ultracold Fermi gases. *Reports on Progress in Physics*, 77(3), 2014.
- [173] F. Scazza, G. Valtolina, P. Massignan, A. Recati, A. Amico, A. Burchianti, C. Fort, M. Inguscio, M. Zaccanti, and G. Roati. Repulsive Fermi Polarons in a Resonant Mixture of Ultracold Li 6 Atoms. *Physical Review Letters*, 118(083602), 2017.
- [174] Gal Ness, Constantine Shkedrov, Yanay Florshaim, Oriana K. Diessel, Jonas Von Milczewski, Richard Schmidt, and Yoav Sagi. Observation of a Smooth Polaron-Molecule Transition in a Degenerate Fermi Gas. *Physical Review X*, 10(41019), 2020.
- [175] Richard Schmidt, Michael Knap, Dmitri A. Ivanov, Jih Shih You, Marko Cetina, and Eugene Demler. Universal many-body response of heavy impurities coupled to a Fermi sea: A review of recent progress. *Reports on Progress in Physics*, 81(024401):1–43, 2018.

- 
- [176] Dimitri Pimenov and Moshe Goldstein. Spectra of heavy polarons and molecules coupled to a Fermi sea. *Physical Review B*, 98(220302), 2018.
- [177] N. V. Prokof'ev and B. V. Svistunov. Bold diagrammatic Monte Carlo: A generic sign-problem tolerant technique for polaron models and possibly interacting many-body problems. *Physical Review B*, 77(125101), 2008.
- [178] Kris Van Houcke, Félix Werner, and Riccardo Rossi. High-precision numerical solution of the Fermi polaron problem and large-order behavior of its diagrammatic series. *Physical Review B*, 101(4), 2020.
- [179] Marco Koschorreck, Daniel Pertot, Enrico Vogt, Bernd Fröhlich, Michael Feld, and Michael Köhl. Attractive and repulsive Fermi polarons in two dimensions. *Nature*, 485:619–622, 2012.
- [180] F. Chevy. Universal phase diagram of a strongly interacting Fermi gas with unbalanced spin populations. *Physical Review A*, 74(063628), 2006.
- [181] Meera M. Parish. Polaron-molecule transitions in a two-dimensional Fermi gas. *Physical Review A*, 83(051603), 2011.
- [182] Meera M. Parish and Jesper Levinsen. Highly polarized Fermi gases in two dimensions. *Physical Review A*, 87(033616), 2013.
- [183] Sascha Zöllner, G. M. Bruun, and C. J. Pethick. Polarons and molecules in a two-dimensional Fermi gas. *Physical Review A*, 83(021603), 2011.
- [184] Cheng Peng, Ruijin Liu, Wei Zhang, and Xiaoling Cui. Nature of the polaron-molecule transition in Fermi polarons. *Physical Review A*, 103(063312), 2021.
- [185] Richard Schmidt, Tilman Enss, Ville Pietilä, and Eugene Demler. Fermi polarons in two dimensions. *Physical Review A*, 85(021602), 2012.
- [186] Jonas von Milczewski, Félix Rose, and Richard Schmidt. Functional renormalization group approach to strongly-coupled Bose-Fermi mixtures in two dimensions. *Physical Review A*, 105(013317), 2022.
- [187] Jonas Vlietinck, Jan Ryckebusch, and Kris Van Houcke. Diagrammatic Monte Carlo study of the Fermi polaron in two dimensions. *Physical Review B*, 89(085119), 2014.
- [188] Guangyao Li, Jesper Levinsen, and Meera M. Parish. Theory of polariton-electron interactions in semiconductor microcavities. *Physical Review B*, 103(195307), 2021.

- [189] Guangyao Li, Meera M. Parish, and Jesper Levinsen. Microscopic calculation of polariton scattering in semiconductor microcavities. *Physical Review B*, 104(245404), 2021.
- [190] A. Camacho-Guardian, K. Knakkegaard Nielsen, T. Pohl, and G. M. Bruun. Polariton dynamics in strongly interacting quantum many-body systems. *Physical Review Research*, 2(023102), 2020.
- [191] M. A. Bastarrachea-Magnani, A. Camacho-Guardian, and G. M. Bruun. Attractive and repulsive exciton-polariton interactions mediated by an electron gas. *Physical Review Letters*, 126(127405), 2021.
- [192] Tony Low, Andrey Chaves, Joshua D. Caldwell, Anshuman Kumar, Nicholas X. Fang, Phaedon Avouris, Tony F. Heinz, Francisco Guinea, Luis Martin-Moreno, and Frank Koppens. Polaritons in layered two-dimensional materials. *Nature Materials*, 16:182–194, 2017.
- [193] J. Kasprzak, M. Richard, S. Kundermann, A. Baas, P. Jeambrun, J. M.J. Keeling, F. M. Marchetti, M. H. Szymńska, R. André, J. L. Staehli, V. Savona, P. B. Littlewood, B. Deveaud, and Le Si Dang. Bose-Einstein condensation of exciton polaritons. *Nature*, 443:409–414, 2006.
- [194] Max Waldherr, Nils Lundt, Martin Klaas, Simon Betzold, Matthias Wurdack, Vasilij Baumann, Eliezer Estrecho, Anton Nalitov, Evgenia Cherotchenko, Hui Cai, Elena A. Ostrovskaya, Alexey V. Kavokin, Sefaattin Tongay, Sebastian Klemmt, Sven Höfling, and Christian Schneider. Observation of bosonic condensation in a hybrid monolayer MoSe<sub>2</sub>-GaAs microcavity. *Nature Communications*, 9(3286), 2018.
- [195] Hui Deng, Gregor Weihs, Charles Santori, Jacqueline Bloch, and Yoshihisa Yamamoto. Condensation of Semiconductor Microcavity Exciton Polaritons. *Science*, 298(5591), 2002.
- [196] Christian Schneider, Mikhail M. Glazov, Tobias Korn, Sven Höfling, and Bernhard Urbaszek. Two-dimensional semiconductors in the regime of strong light-matter coupling. *Nature Communications*, 9(2695), 2018.
- [197] G. Malpuech, A. Kavokin, A. Di Carlo, and J. J. Baumberg. Polariton lasing by exciton-electron scattering in semiconductor microcavities. *Physical Review B*, 65(153310), 2002.

- [198] Thomas Mueller and Ermin Malic. Exciton physics and device application of two-dimensional transition metal dichalcogenide semiconductors. *npj 2D Materials and Applications*, 29, 2018.
- [199] Sara Conti, David Neilson, François M. Peeters, and Andrea Perali. Transition metal dichalcogenides as strategy for high temperature electron-hole superfluidity. *Condensed Matter*, 5(22), 2020.
- [200] Zefang Wang, Daniel A. Rhodes, Kenji Watanabe, Takashi Taniguchi, James C. Hone, Jie Shan, and Kin Fai Mak. Evidence of high-temperature exciton condensation in two-dimensional atomic double layers. *Nature*, 574:76–80, 2019.
- [201] Gang Wang, Alexey Chernikov, Mikhail M. Glazov, Tony F. Heinz, Xavier Marie, Thierry Amand, and Bernhard Urbaszek. Excitons in atomically thin transition metal dichalcogenides. *Reviews of Modern Physics*, 90(021001), 2018.
- [202] Christian Fey, Peter Schmelcher, Atac Imamoglu, and Richard Schmidt. Theory of exciton-electron scattering in atomically thin semiconductors. *Physical Review B*, 101(195417), 2020.
- [203] Mohit Randeria, Ji-min Duan, and Lih-Yir Shieh. Bound States, Cooper Pairing, and Bose Condensation in Two Dimensions. *Physical Review*, 62(9), 1989.
- [204] Sadhan K. Adhikari. Quantum scattering in two dimensions. *American Journal of Physics*, 54(4), 1986.
- [205] Jason S. Ross, Sanfeng Wu, Hongyi Yu, Nirmal J. Ghimire, Aaron M. Jones, Grant Aivazian, Jiaqiang Yan, David G. Mandrus, Di Xiao, Wang Yao, and Xiaodong Xu. Electrical control of neutral and charged excitons in a monolayer semiconductor. *Nature Communications*, 4(1474), 2013.
- [206] Kin Fai Mak, Keliang He, Changgu Lee, Gwan Hyoung Lee, James Hone, Tony F. Heinz, and Jie Shan. Tightly bound trions in monolayer MoS<sub>2</sub>. *Nature Materials*, 12:207–211, 2013.
- [207] Sefaattin Tongay, Jian Zhou, Can Ataca, Kelvin Lo, Tyler S. Matthews, Jingbo Li, Jeffrey C. Grossman, and Junqiao Wu. Thermally driven crossover from indirect toward direct bandgap in 2D Semiconductors: MoSe<sub>2</sub> versus MoS<sub>2</sub>. *Nano Letters*, 12:5576–5580, 2012.
- [208] Shina Tan. Large momentum part of a strongly correlated Fermi gas. *Annals of Physics*, 323:2971–2986, 2008.

- 
- [209] Eric Braaten and Lucas Platter. Exact relations for a strongly interacting fermi gas from the operator product expansion. *Physical Review Letters*, 100(205301), 2008.
- [210] Shizhong Zhang and Anthony J. Leggett. Universal properties of the ultracold Fermi gas. *Physical Review A*, 79(023601), 2009.
- [211] Mohit Randeria, Ji-min Duan, and Lih Yir. Superconductivity in a two-dimensional Fermi gas: Evolution from Cooper pairing to Bose condensation. *Physical Review B*, 41(1), 1990.
- [212] B. A. Lippmann and Julian Schwinger. Variational principles for scattering processes. I. *Physical Review*, 79(3), 1950.
- [213] Jesper Levinsen and Meera M. Parish. Strongly interacting two-dimensional fermi gasses. In *Annual Review of Cold Atoms and Molecules*. World Scientific, 3 edition, 2015.
- [214] G. M. Bruun and P. Massignan. Decay of polarons and molecules in a strongly polarized fermi gas. *Physical Review Letters*, 105(020403), 2010.
- [215] A. A Abrikosov, L. P Gorkov, and Dzyaloshinski I.E. *Methods of quantum field theory in statistical physics*. Pergamon Press, 2 edition, 1965.
- [216] James W. Cooley and John W. Tukey. An Algorithm for the Machine Calculation of Complex Fourier Series. *Mathematics of Computation*, 19(90), 1965.
- [217] Alex Townsend. A fast analysis-based discrete Hankel transform using asymptotic expansions. *SIAM Journal on Mathematical Analysis*, 53, 2015.
- [218] Michael O’Neil, Franco Woolfe, and Vladimir Rokhlin. An algorithm for the rapid evaluation of special function transforms. *Applied and Computational Harmonic Analysis*, 28:203–226, 2010.
- [219] R. Haussmann, W. Rantner, S. Cerrito, and W. Zwerger. Thermodynamics of the BCS-BEC crossover. *Physical Review A*, 75(023610), 2007.
- [220] Bernhard Frank. *Thermodynamics and Transport in Fermi Gases near Unitarity*. PhD thesis, TUM, 2018.
- [221] NIST Digital Library of Mathematical Functions, 2022.
- [222] Kendall E Atkinson. *An introduction to numerical analysis*. Wiley, 2nd edition, 1989.

- 
- [223] M. Abramowitz and I.S. Stegun. *Handbook of mathematical functions*. United States National Bureau of Standards, 1970.
- [224] Ludovic Pricoupenko and Paolo Pedri. Universal (1+2)-body bound states in planar atomic waveguides. *Physical Review A*, 82(033625), 2010.
- [225] Jesper Levinsen and Meera M. Parish. Bound states in a quasi-two-dimensional fermi gas. *Physical Review Letters*, 110(055304), 2013.
- [226] P. Bloom. Two dimensional fermi gas at 0K. *Physical Review B*, 12(1), 1975.
- [227] P. Massignan and G. M. Bruun. Repulsive polarons and itinerant ferromagnetism in strongly polarized Fermi gases. *European Physical Journal D*, 65:83–89, 2011.
- [228] Peter Kroiss and Lode Pollet. Diagrammatic Monte Carlo study of quasi-two-dimensional Fermi polarons. *Physical Review B*, 90(104510), 2014.
- [229] Kazuhiko Kamikado, Takuya Kanazawa, and Shun Uchino. Mobile impurity in a Fermi sea from the functional renormalization group analytically continued to real time. *Physical Review A*, 95(013612), 2017.
- [230] Tomasz Wasak, Falko Pientka, and Francesco Piazza. Fermi polaron laser in two-dimensional semiconductors. *arXiv:2103.14040*, 2021.
- [231] A. Zamora, L. M. Sieberer, K. Dunnett, S. Diehl, and M. H. Szymańska. Tuning across universalities with a driven open condensate. *Physical Review X*, 7(041006), 2017.
- [232] Christian H. Johansen. Msc Thesis: Non-Markovian methods for small one-dimensional systems out of equilibrium. Technical report, The Technical University of Denmark, 2018.
- [233] Franz Wegner. *Supermathematics and its applications in statistical physics : Grassmann variables and the method of supersymmetry*. Springer, 2016.
- [234] Tzon Tzer Lu and Sheng Hua Shiou. Inverses of 2 x 2 block matrices. *Computers and Mathematics with Applications*, 43:119–129, 2002.
- [235] Eric Smith. Doi-Peliti methods for non-commuting observables. *Santa Fe University*, 2006.
- [236] L V Keldysh. Real-Time Nonequilibrium Green's Functions. *Prog. Nonequilibrium Green's Funct. II*, 2003.

- 
- [237] Severin Jakobs. Functional RG for nonequilibrium transport through mesoscopic systems. *Lecture Notes*, 2015.
- [238] Steven Weinberg. *The quantum theory of fields I*. Cambridge University Press, 8th edition, 2015.
- [239] Jonathan L. Gross, Jay Yellen, and Mark Anderson. *Graph Theory and its applications*. CRC Press, 3rd edition, 2018.
- [240] Ömer Eğecioğlu, E. Gallopoulos, and Çetin K. Koç. Fast computation of divided differences and parallel hermite interpolation. *Journal of Complexity*, 5:417–437, 1989.



## Acknowledgements

I have been fortunate enough to have received help and support from many people. First of all, I am deeply indebted to my parents for teaching me to be curious and always supporting me. I also can not thank my supervisor Francesco Piazza enough for his guidance. His excellent physical intuition has taught me to appreciate that deep insight is not binary but a spectrum where each part deserves to be valued. While his deep understanding of physics has been invaluable, I have also been spoiled by his unbreakable positivism and his ever-present support regarding all aspects of my Ph.D.

While Francesco always has been able to maintain a grand view of both goal and path as a true expedition coordinator, Johannes Lang took on the role of the local mountain guide that knew all the hidden in's and out's of the mountain. In this sense, he truly holds the KOM, and I doubt that this title will be taken any time soon. His deep technical insight and great spirit have been vital both for the projects and my ever-continuing curiosity about non-equilibrium field theory.

While the academic journey was full of unknowns, I was able to truly enjoy it thanks to the unwavering support of Stephanie Matern. Our countless adventures in the great outdoors in either water or on rock, the many hours spent chatting about everything from caterpillars to open systems, and just hanging out are among the main reasons why I will always think back to the last four years with joy.

I also want to thank the great people at the institute with whom I spent my last four years. The many discussions about life outside of physics made everyday life at the institute a joy, and our climbing adventures made Dresden a lot more exciting!

Finally, a big thanks to SM, JL, MSM, LHJ, and NL that looked through different parts of the thesis and helped comb through both typos, mistakes, and convoluted sentences.



## Erklärung

Hiermit versichere ich, dass ich die vorliegende Arbeit ohne unzulässige Hilfe Dritter und ohne Benutzung anderer als der angegebenen Hilfsmittel angefertigt habe; die aus fremden Quellen direkt oder indirekt übernommenen Gedanken sind als solche kenntlich gemacht. Die Arbeit wurde bisher weder im Inland noch im Ausland in gleicher oder ähnlicher Form einer anderen Prüfungsbehörde vorgelegt.

Die vorliegende Dissertation wurde am Max-Planck-Institut für Physik komplexer Systeme unter der wissenschaftlichen Betreuung von Dr. Francesco Piazza angefertigt. Ich erkenne die Promotionsordnung des Bereichs Mathematik und Naturwissenschaften der Technischen Universität Dresden vom 23.02.2011 an.

Christian Høj Johansen

Dresden, 10. Oktober 2022